Simulations of Dry Friction between Rough Surfaces and Corresponding Nonlinear Problems at Nano and Microscales

by

Ovidiu Savencu

Thesis submitted in candidature for the degree of

Doctor of Philosophy at Cardiff University

Tribology and Contact Mechanics Research Group

Institute of Mechanics and Advanced Materials

School of Engineering

Cardiff University

April 2016

(Intentionally blank)

Declaration

This work has not been submitted in substance for any other degree or award at this or any other university or place of learning, nor is being submitted concurrently in candidature for any degree or other award.

Signed …….…… (Ovidiu Savencu) Date ……

Statement 1

This thesis is being submitted in partial fulfilment of the requirements for the degree of Philosophy Doctor.

Signed …….…… (Ovidiu Savencu) Date ……

Statement 2

This thesis is the result of my own independent work/investigation, except where otherwise stated. Other sources are acknowledged by explicit references. The views expressed are my own.

Signed …….…… (Ovidiu Savencu) Date ……

Statement 3

I hereby give consent for my thesis, if accepted, to be available for photocopying and for inter-library loan, and for the title and summary to be made available to outside organisations.

Signed …….…… (Ovidiu Savencu) Date ……

Statement 4

I hereby give consent for my thesis, if accepted, to be available for photocopying and for inter-library loans after expiry of a bar on access previously approved by the Academic Standards & Quality Committee.

Signed …….…… (Ovidiu Savencu) Date ……

(Intentionally left blank)

Summary

The work is devoted to modelling of dry sliding friction between contacting surfaces and related problems of contact mechanics. To limit the number of physical phenomena involved, the studies are targeted to systems used in vacuum conditions, hence there is no need to consider environmental parameters, such as humidity or oxidation films. Although friction has been studied over many years, challenges remain for obtaining a comprehensive understanding and a quantitative description of influence of nanometre scale effects on friction at micro/macro levels. Many existing models are critically re-examined using ideas of nanoscience.

The studies start from the classic Zhuravlev model well-known as the Greenwood - Williamson model representing rough surfaces as collections of spherical elastic asperities. Contact problems for bodies of various shapes are investigated using the Galin solution along with the Borodich rescaling formulae. The rescaling method is applied to indentation experiments by spherical and nominally sharp punches and then a way to model dry friction following Zhuravlev's arguments is outlined.

New ways for numerical simulations of dry sliding friction are presented assuming the friction force is defined by the total energy dissipated over the sliding distance. Novel hierarchical, multiscale, multilevel structural models for simulation of sliding dry friction are presented. The models reflect the physical mechanisms which are most relevant to dry friction at the specific length scales: the chemical interactions at the atomic scale, the adhesive (van der Waals) interactions at the nanoscale, and the mechanical interlocking of asperities and their coupling at the micro and macroscales. Although the models include some features of known models, the nanotribological interpretation of the features is novel. It is argued that the nano-asperities do not deform plastically due to the so-called Polonsky-Keer effect. The obtained results are in good agreement with the experimental observations found in literature.

Acknowledgements

This work was funded by the "Austrian COMET-Program" within the framework of the COMET K2 Excellence Centre of Tribology (project XTribology, no. 824187 and no. 849109) via the Austrian Research Promotion Agency (FFG) and the provinces of Niederösterreich, Vorarlberg and Wien The financial support is very much appreciated.

The fact that I can be in the privileged position to complete such a work is largely due to the people that have invested in me over the years. Therefore thanks are due.

First, I am grateful for the help I received from my supervisors, Prof. F.M. Borodich and Prof. H. P. Evans. Their effort, patience and encouragement have been invaluable and their character inspiring.

I am thankful for the useful discussions and stimulating debates I had with my colleagues Dr. Ingram Weeks and Dr. Anton Manoylov. Getting to know them was a great joy.

It has also been a pleasure to share the office with my colleagues Sergey Khaustov, Nabeel Almuramady and Maasi Al-Mayali. Each of them has been a pleasure to know and work alongside on a daily basis.

Thanks are also due to Dr. Emmanuel Brousseau for his help with the AFM and illuminating discussions about the nano-world.

Lastly, I am grateful to my family and friends for their constant support and many prayers for a work I doubt they will ever read.

To the Ground of all reason

(Intentionally left blank)

Contents

(Intentionlly left blank)

Chapter 1 - Background and literature review

1.1 Introduction

It is well known that friction phenomena play a central role in a rich variety of physical systems (see, e.g. Kragelsky et al. 1982, Berger 2002, Popov 2010) and therefore they have been the topic of studies in an enormous number of papers and books (e.g. Bowden and Tabor 1956, 1973, Kragelsky and Schedrov 1956, Derjaguin 1963).

The concern of the current thesis is the modelling of dry friction. This chapter will start with an accurate account of the classic laws of friction. Basic mechanisms of friction will be discussed and classic contact mechanics and friction models will be presented. The structure of the thesis is also given.

Usually friction of solids is described by the Amontons-Kotelnikov law that is quite often confused with Coulomb's law. The rest of this section is an attempt to accurately trace the development of the classic laws of friction.

1.1.1 Classic laws of friction

The books on tribology (Bowden and Tabor 1956, Kragelsky and Schedrov 1956, Dowson 1979) usually attribute the priority on studies of friction to Leonardo da Vinci. However, it is quite clear that, although the genius understood a lot about friction, he had just satisfied his curiosity and his unpublished studies had no influence on his contemporaries.

Amontons (1699)

The first paper on friction phenomena was published by the French physicist Amontons (1699) who worked on the manufacturing of optical lenses. Using an extremely primitive polishing element, in which the pressure of the optical lens on a plate was established by means of a curved flexible element, he presented his observations as three friction laws that can be formulated as (see e.g. Kragelsky et al. (1982):

I. The polishing force is independent of the dimensions of the lens.
II. The polishing force is proportional to the applied force.

III. The ratio of these forces is independent of the combination of tool and component material and under boundary lubrication conditions is equal to 0.3.

The first law of friction presented by Amontons was so counterintuitive for his colleagues that Philippe de la Hire immediately decided to check the findings, and the new experiments confirmed Amontons' results (Dowson 1979, Kragelsky and Schedrov 1956).

The first two Amontons' laws are of great practical importance and they were used in a number of friction models. However, the third law is in general not correct and these observations are related only to a particular case of his experiments.

Kotelnikov (1774)

As we have seen, Amontons (1699) gave only a descriptive formulation of the friction laws. Kotelnikov (1774), one of eight former students of Euler, studied friction under external compressing force *P*. He wrote: 'If the friction content *F* to the mentioned force *P* one puts as unknown that is equal to μ:1, then the friction will be $F = \mu P$.' Hence, Kotelnikov not only dismissed the third Amontons' law but he also introduced the notion of the coefficient of friction μ, and presented the law as a formula. The Amontons-Kotelnikov law for the frictional force F_f can be written as

$$F_f = \mu P \tag{1-1}$$

Coulomb (1785)

In 1785, Coulomb proposed a two-term formula for the force of friction (Dowson 1979, Kragelsky et al. 1982, Kragelsky and Schedrov 1956):

$$F_f = A + \mu P \tag{1-2}$$

where *A* is a characteristic of adhesiveness for two contacting bodies. It follows from Coulomb's law (1-2) that the coefficient of friction (COF) does not remain constant and it depends on the applied load. In addition, Coulomb stated that sliding kinetic friction is independent of the sliding velocity *v* for ordinary sliding velocities.

Derjaguin (1934a)

Unfortunately the two-term Coulomb law (1-2) was forgotten for a rather long time. For instance, Hardy and Bircumshaw (1925) had difficulties describing their experimental results employing the Amontons-Kotelnikov law (1-1). Due to this, there are still many confusing statements in literature that, for example, refer to the one-term friction law (1-1) as the Coulomb law or the Amontons-Coulomb law.

Several researchers who rediscovered the two-term relation, including Derjaguin (1934a, 1934b) thought that they introduced a new relation. As it was noted by Akhmatov (1963), only Kragelsky's historical studies allowed attributing the two-term relation (1-2) to Coulomb.

After Derjaguin had learnt from Kragelsky about the Coulomb two-term law (1-2), he gave corresponding reference (see Derjaguin 1963), and noted that Coulomb (1785) had not mentioned the connection between the term *A* of his empirical law and the true area of contact. Derjaguin (1934a) gave a molecular meaning to Coulomb's force *A*. He expressed the force of friction F_f as

$$F_f = \mu(P + S\, p_0) \qquad (1\text{-}3)$$

In relation (1-3), *S* is the true area of the interacting surface, and p_0 is the specific attractive force. Hence the term $A = \mu\, S\, p_0$ represents the tangential component of the force of molecular interactions. Derjaguin (1934a,b) suggested distinguishing between the true friction coefficient μ_t and the apparent friction coefficient μ_a, where

$$\mu_t = \frac{F_f}{P + Sp_0} \qquad and \qquad \mu_a = \frac{F_f}{P}$$

The real value of the COF depends on many factors and, therefore, it may seem as an astounding fact that the Amontons-Kotelnikov law of friction (1-1) is so often in a very good agreement with experimental tests. As Akhmatov (1963, 1966) noted, both (1-1) and (1-2) laws of friction belong to statistical laws of nature whose apparent simplicity is based on the rather high internal complexity of the phenomenon.

Therefore, any serious attempt at modelling dry friction will need to take into account the main mechanisms underlying the phenomenon. We will discuss dry friction and the corresponding mechanisms of energy dissipation in the following section.

1.2 Dry Friction and Corresponding Mechanisms of Energy Dissipation

Usually it is possible to distinguish between dry and lubricated friction. Lubricated friction has been the favourite topic of tribological studies for many years. However, the amount of effort put into the study of dry friction has increased rapidly. Indeed, the conditions encountered in various fields render lubrication as ineffective or inapplicable. For example, mechanisms and components used in aerospace industry, along with other high-vacuum systems, are applications working under dry friction. Further miniaturization of devices, including micro-electromechanical systems (MEMS), makes extensive use of low-friction solid lubricants, which also work under dry friction.

It is also known that, at the nanoscale, friction, adhesion and bonding can be so strong that they may greatly limit MEMS reliability, or they will not allow micro-devices to work at all (Maboudian et al. 2002). In addition, conventional microscopic tribology deals with the phenomenological processes (such as plastic deformation, lubrication, etc.) when the asperities of the rough surface are microns in size, comparable to the size of some modern micro-electronic devices. Nonlinear contact problems are rather complex even at the microscale, and traditional models need to be improved to achieve a major impact in studying interactions at the nanoscale. The objective of the work presented in this thesis is to develop an effective multiscale modelling and analysis scheme of dry friction at the micro and nanoscale.

Although friction and wear of non-lubricated solids were studied very intensively, challenges remain for obtaining a thorough understanding of the corresponding phenomena at various scales, together with a rigorous theoretical description for the majority of nanotribological effects.

One of the main features of nanotribology and nanomechanics is that these branches of science have to study interactions between physical objects using equations

adjusted to the specific character of the nanometre length scale (Borodich et al. 2012). These interactions that act at the short distances include molecular adhesion caused by van der Waals (vdW) forces and various surface forces, and are one of objects of the present work.

Tomlinson (1929), introducing his molecular theory of friction, noted that his theory of friction is '*admittedly somewhat abstract and speculative. It is remarkable fact, however, that a phenomenon so universal and important as the friction between solid bodies has so far received no satisfactory explanations*.' Bowden and Leben (1938) noted that 'we have, as yet, no clear understanding of the mechanism of friction of sliding solids.' Later, Akhmatov (1963) noted that there is no universal theory of friction. The best theories of friction can take into account only some causes of the friction phenomenon and describe just particular situations of similar physical nature. The situation is still the same. As Blau (2001) noted, '*while friction coefficients are relatively easy to determine in laboratory experiments, the fundamental origins of sliding resistance are not as clear. In fact, some of the greatest scientists and philosophers have contemplated friction without managing to produce a universal, predictive theory. This striking lack of success is due to the many potential factors that can influence friction in a wide spectrum of physical situations*.' Thus studies of the nanotribological processes have to account for the underlying chemical and physical mechanisms of interaction between the opposite surfaces, including temporary chemical bonding, van der Waals forces, and capillary forces. The adsorption and mechanical desorption of oxygen and other gases, the combination of various environmental parameters (e.g. humidity) are other factors which, along with parameters such as surface morphology, sliding direction, contact area, micro/nano structure and material properties of coating layers and substrate, also play significant roles in the tribological processes.

1.3 Chemical and van der Waals Interactions. Cold welding phenomenon

Chemical and molecular interactions play a very important role in energy dissipation during friction. It is therefore fitting to define what we mean by these terms, give a classification of the primary and secondary bonds, and then interact with relevant literature on the subject. The books we will rely on are Smith (2011), Butt and Kappl (2010), Chung (2007) and Israelachvili (1992).

1.3.1 Primary bonds

The primary bonds between atoms are the strongest (the typical energy per bond is of the order of 10^{-19} to 10^{-18} Joules) and they are established due to the atoms seeking a lower energy state. There are three possible types of bonds between atoms: metal-nonmetal, nonmetal-nonmetal, and metal-metal.

a) Ionic bonds

Ionic bonds are formed between metals and nonmetals through electron transfer. Usually the bond is between reactive metals (group 1A or 2A of the Mendeleev Table of Elements) and reactive nonmetals (group 6A or 7A), thus having large differences in their electronegativities. In the ionic bond between Li and F, for example, Li loses an electron which is gained by F. Li becomes the cation Li^+, and F becomes the anion F^-. The electrostatic forces then hold the ions together to form an ionic bond.

b) Covalent bonds

Covalent bonds are established usually between nonmetals, through sharing of electrons. The covalent bonding between two H atoms can be considered as an example. First, the nucleus of one H atom is attracted to the electron cloud of the other. After they come closer, their electron clouds start to interact, and both atoms take ownership of both electrons. Both atoms will complete their outer electronic structure, and they will reach an equilibrium distance as a result of the balancing between the attraction and repulsion forces (see e.g. Smith (2011). Due to the fact that covalent bonds result from atoms sharing electrons, they are directional bonds, while

ionic bonds are not. Therefore the atoms in covalent bonds prefer specific orientations, which gives molecules definite shapes.

c) Metallic bonds

Metallic atoms can establish strong covalent bonds. However, the result will be a gaseous material, with weak bonds between molecules. In solid metals, the atoms are held together by metallic bonds. The result is a repetitive and organized structure of nuclei, in a 'sea of electrons.' This sea of electrons is made of delocalised electrons from the metal atoms that become, as a result, positive cores (metal cations). The atoms are held together in solid metals by the attraction forces between the metal cations and the sea of electrons.

Metallic bonds are similar to the covalent bonds in that the participating atoms share their valence electrons. The major difference between them however is that, in the metallic bonding, the electrons do not belong to any specific atom, but are delocalized.

It should be mentioned that atoms can be involved in more than one type of primary bonds. The following mixed-bonds may result: ionic-covalent, metallic-covalent, metallic-ionic, and ionic-covalent-metallic (see e.g. Smith (2011)).

1.3.2 Secondary bonds (van der Waals)

While the primary bonds between atoms are due to the interaction of their valence electrons in the process of finding a lower energy state, the secondary bonds are caused by the attraction of the electric dipoles contained in atoms or molecules, and the nature of the attraction forces is electrostatic (Coulombic). The secondary bonds are much weaker than the primary bonds, reaching energies of about 4 to 42 kJ/mol (Smith 2011, p.72).

These secondary bonds are collectively known under the name of van der Waals forces. They are long-range interactions and their energy decays with the inverse sixth power of the distance. The van der Waals forces can be grouped under three distinct components (see e.g. Israelachvili 1992, Parsegian 2005):

a) Induction forces (Debye)

The induction force is also known as Debye force, and arises between a polar molecule and a non-polar molecule. The polarizing field of the polar molecule transforms the non-polar molecule into an induced dipole. This will give rise to an attractive force between the polar molecule and the induced dipole.

b) Orientation forces (Keesom)

Permanent dipoles are molecules with an asymmetric structure, and thus an asymmetric distribution of electrostatic charges, which makes them able to bond with other molecules. One case of a permanent dipole-dipole interaction is the *hydrogen bond*, which occurs when a O-H or N-H bond interacts with the atoms O, N, F or Cl. The interaction between these entities appears because the bond containing the hydrogen atom is polar (the H end of the bond is slightly positive, while the O or N ends are slightly negative), and the atoms O, N, F and Cl are electronegative.

The permanent dipoles are often able to move freely. In doing so, their charges will interact with each other and orient the dipoles so that a maximum interaction is achieved. If the fluctuations were random, the average interaction would be null (Butt and Kappl 2010). However, they are not random, but the orientations with lower potential energy will be favoured over the ones with higher potential energy. The net interaction can be calculated by integration over all possible orientations, each orientation being weighted with a Boltzmann factor. This averaged interaction between two permanent dipoles is usually called the Keesom or orientation interaction.

c) Dispersion forces (London)

The dispersion forces are also known as London forces, charge-fluctuation forces, electrodynamic forces and induced-dipole-induced-dipole forces. The dispersion forces are always present, regardless of the properties of the molecules, being maybe the most important component of the van der Waals forces.

The dispersion forces are long-range forces (from interatomic spacings of about 2 Å, to distances larger than 10 nm), they can be repulsive or attractive, and are affected by

the presence of other bodies (property also known as non-additivity). The dispersion forces are originated by the interaction between a fluctuating dipole and an induced dipole. The fluctuating dipole is created due to the fact that the electron charge cloud changes with time: at a given moment, there could be a higher electron density at one side of the atom than the other. The electric field thus created affects the neighbouring atoms, inducing them to form dipoles as well. The interaction between the two dipoles generates an instantaneous attractive force.

When the atoms are further apart, the dispersion forces are subject to retardation effects. The separation is meaningfully large when the time for the electric field to travel from one atom to the other atom and back is comparable to the period of the fluctuating dipole itself. In this case, by the time the field gets back to the atom, the configuration of the other atom has changed in a less favourable disposition to an attractive interaction. This is called the 'retardation effect', and it applies only to dispersion forces between molecules and particles at large separation. Due to this, the dispersion energy between two atoms begins to decay faster than $-1/r^6$, approaching $-1/r^7$ at separations greater than 100 nm (see e.g. Israelachvili 1992, Parsegian 2005, Butt and Kappl 2010).

1.3.3 Adhesion

In the beginning of his book, before defining molecular adhesion, Kendall (2001) takes some time to clarify what adhesion is not. He says molecular adhesion is not to be confused with friction, gravitational attraction, electrostatic and magnetic attractions and adhesion between nuclear particles. He then defines molecular adhesion as 'the force experienced when bodies make contact at the molecular level, with gaps near molecular dimensions.'

We need to also note that, after reading relevant literature, one can see that there is ambiguity around the use of the term *adhesion*. Indeed, to show 'adhesion' is loosely used, Pollock (1992) identifies 6 different concepts it denotes in literature, and their corresponding measurement units, as follows:

a. Adsorption (by which a solid surface attracts individual gas molecules onto itself), in electron-volts per molecule

b. The macroscopic force of attraction between two surfaces in contact, in newtons
c. The externally-applied pull-off force, in newtons
d. The thermodynamic work or free energy of adhesion, in joules per square metre
e. Various quantities used to quantify the performance of coatings and glued joints
f. The adhesion component of friction, in newtons

Further, Pollock (1992) underlines that the van der Waals force is different from the pull-off force that many authors have measured, as this experimental force has a much longer range than the inverse square dependence (for a sphere against flat geometry). He speculates the reason is that, in laboratory conditions, the experiments are compromised by electrostatic surface effects.

As indicated by Borodich et al. (2014), 'adhesion' is also used to refer sometimes to the strong chemical bonds between surfaces, or the weak connections due to van der Waals forces, or the contact boundary conditions in the no-slip case.

The American Society for Testing and Materials (ASTM) also has a very broad definition of adhesion that includes multiple mechanisms: 'Adhesion is the state in which two surfaces are held together by interfacial forces which may consist of valence forces or interlocking forces or both' (ASTM D907-70).

In this work, the term 'adhesion' will be used to refer strictly to the van der Waals forces described in the previous section.

1.3.4 Cold welding

Although 'cold welding' is usually associated with Bowden and Tabor, the concept can be found in an earlier paper by Bowden and Leben (1939). Their experiments showed for the first time that, for dissimilar materials, unlubricated friction is not a constant process, but it is made of smaller stick-slip events. The authors have explained the sticking together of the surfaces by 'a local welding together and a formation of metallic junctions between the metals' due to high pressures at the very small points

of contact. These metallic junctions have to be broken for relative motion to be maintained, resulting in tears and distortions in the metal to a considerable depth beneath the surface. Their theory was supported by many experimental investigations (for e.g., Bowden et al. 1943, Cocks 1962, Moore 1948, Rabinowicz 1951, Rabinowicz and Tabor 1951).

Based on these assumptions, the force of friction F_f can be expressed as (Bowden et al. 1943):

$$F_f = A_t\,\tau + A'p$$

where A_t is the true contact area and τ is the shear strength of the material, A' is the cross section of the torn track, and p is the pressure to cause plastic flow in the softer metal. Therefore, the force of friction is expressed as a sum between the force required to shear the metallic junctions and the force required to remove the softer metal from the path of the slider.

Cold welding occurs between surfaces when there is intimate contact between clean metals. It is not a common phenomenon in our usual experience because, in the presence of air, metals are covered by an oxide layer that prevents surfaces from welding together. However, in space, cold welding is a phenomenon that has to be taken into account, because it can lead to the failure of metallic mechanisms when coatings are damaged by impact or fretting. One well-known documented case is the failure of the deployment mechanism of an antenna on the Galileo spacecraft in 1991 (Johnson 1994). Investigations have shown the cause of the deployment failure was cold welding due to fretting during transport and lift-off (Merstallinger 2009).

The experiments performed by Lu et al. (2010) show that, at the nanoscale where adhesive forces become more important, gold nanowires are cold welded only by being brought into contact. In their experiments the single crystalline nanowires, with diameters between 3 and 10 nm, achieved welds with the same crystal orientation, strength and conductivity as the nanowires themselves just by being brought together head-to-head or side-to-side. It has to be mentioned that the experiments were performed in the Transmission Electron Microscope chamber, under high vacuum, between perfectly clean surfaces.

Ferguson et al. (1991) report the cold welding of thin (approximately 20 nm thick) gold films under ambient laboratory conditions and low loads. This is remarkable because under ambient conditions the gold surfaces are not clean, due to adsorbed organic impurities. Because cold welding occurs between atomically clean surfaces, the authors hypothesise that the impurities are laterally displaced to allow contact, possible due to the compliant elastomeric supports.

1.4 Specific features of micro and nanoscale deformations. The Polonsky-Keer effect

With the development of the technological means to measure and manipulate nanoscale size bodies and to build more powerful computational units, we now have a wealth of evidence showing the properties of materials at the nanoscale are not as predicted by the laws derived at the macroscale.

For example, Kelly et al. (2015) report anomalous imbibition of various liquids in silica nano-channels, that cannot be explained by macroscopic descriptions. They show the reason these macroscopic descriptions are not adequate is because they do not take into account the deformation of the menisci caused by the long-range intermolecular forces, effective pore deformation due to thin films, elastocapillarity and surface stresses.

In the field of hardness measurement it is known that, in some conditions, materials may show higher hardness when the indentation size is smaller (Moreau et al. 2005). Although this may be due to poor sample preparation or failure to take into account other processes (e.g. the formation of surface layers due to technological processing or environmental exposure, the bluntness of the indenter, the pile-up effect, etc.), the indentation size effects may be caused by material-related mechanisms, i.e. the reduction of dislocation density, the curvature of the dislocation requiring higher loads for propagation, or changes in grain size near the surface region (Bull 2003).

Research done in the area of conductors show that, at the nanoscale, Ohm's law breaks down, due to the fact that the small distances between the atoms make the resistance independent of their length (Agrait et al. 2003). The authors of the study note this is asking for a conceptual redefinition of resistance that would use the wave nature of the electrons.

Not only the electrical resistance has to be redefined at the nanoscale, but the mechanical properties are also different: the yield stress of the atomic-size metal wires is one or two orders of magnitude larger than for the corresponding bulk materials (Agrait et al. 2003). Even more impressively, Greer et al. (2005) reported that single crystalline Au nano-pillars subjected to uniaxial compression shows strengths 50 times

higher than in bulk. The 'ultra-strength' of nano samples is now a well-known fact, so much so that there is a commonly-known term for this phenomenon: 'smaller is stronger' (Greer and De Hosson 2011). There are many investigations, both experimental and numerical, that have reached this conclusion (see, for example, Shan et al. 2008, Uchic et al. 2004, Zhu and Li 2010). Volkert et al. (2012) explain that the nano-structures are stronger than the bigger samples because their failure is controlled by the nucleation of dislocations in usually perfect crystals, whereas the larger scale samples have crystal defects that cause an earlier failure. If the nano-sample is larger and contains defects, its super-strength is explained by a process coined 'dislocation starvation', by which the defects inside the structure move to the surface (Hemker and Nix 2008). This phenomenon has been observed experimentally by Shan et al. (2008) testing nickel nano-columns, with diameters between 150 and 400 nm. They obtained images showing that, after applying a small compressive load, the dislocation density was reduced by 15 orders of magnitude, making the columns defect free; the authors call this 'mechanical annealing.'

Let us address the question of what is the size threshold where special scale-effects begin to appear? The discussion is more complex, taking into account not only the size of the sample, but also the grain size. The well-known Hall-Petch equation (1-4) has been used to express empirically the relation between the yield stress σ_y and the average grain diameter d (see e.g. Smith 2011, p.254).

$$\sigma_y = \sigma_0 + \frac{k}{d^{1/2}} \qquad (1\text{-}4)$$

In (1-4), σ_0 and k are material constants. However, Smith (2011) notes that the Hall-Petch equation does not apply in the case of extremely coarse or extremely fine grain sizes. Indeed, this can be seen in Figure 1-1.

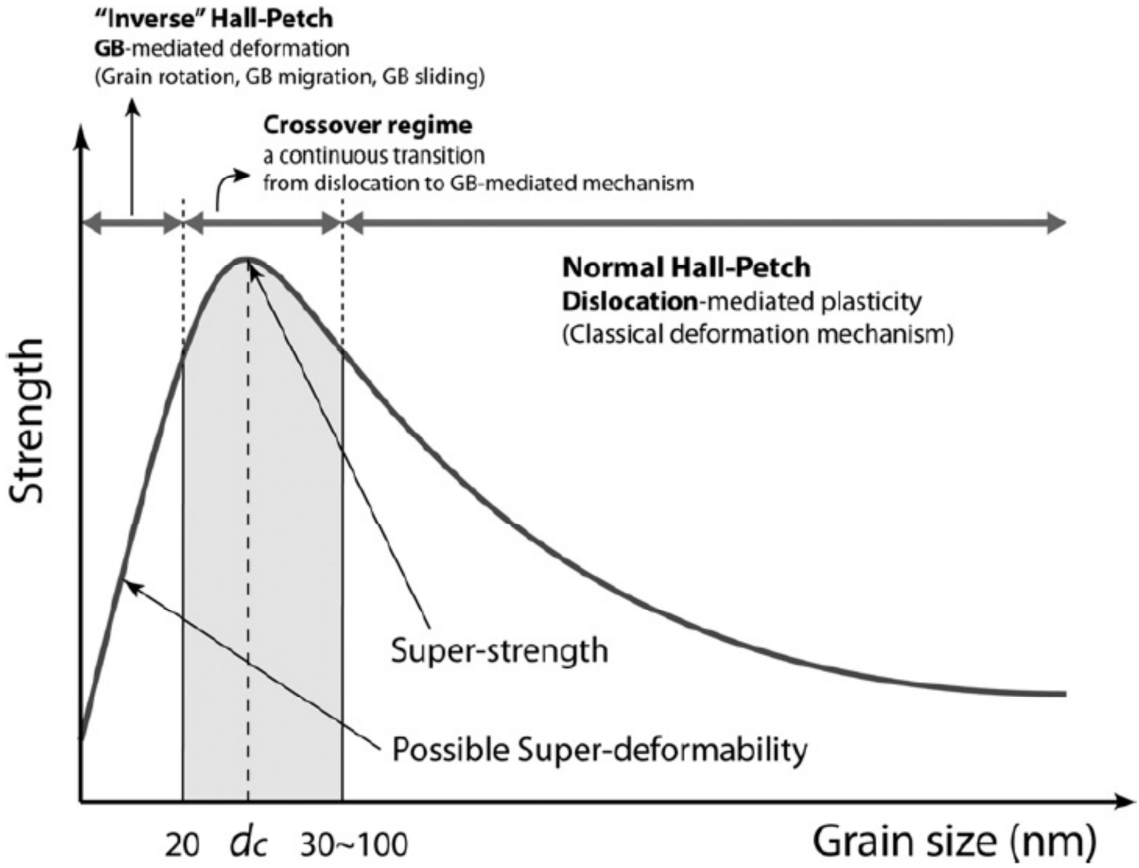

Figure 1-1 – Strength of polycrystalline materials as a function of grain size: Hall-Petch relation and transition to 'inverse' Hall-Petch (Greer and De Hosson, 2011)

The chart presented by Greer and De Hosson (2011) confirms the trend given by the Hall-Petch relation down to a grain size of about 30-100 nm. As the grain size becomes smaller, the material becomes stronger, so 'smaller is stronger.' But decreasing the grain size even more causes the material to become 'weaker', an effect called 'inverse' or 'negative' Hall-Petch (Greer and De Hosson 2011).

The diagram presented by Meyers et al. (2006) gives more information, and shows not only the general trend, but also the experimental data (see Figure 1-2). This diagram is a plot of the yield stress against the square root of the grain size so that a larger number on the abscissa means a smaller grain size. Grain size values for positions of interest are added to the top of the figure.

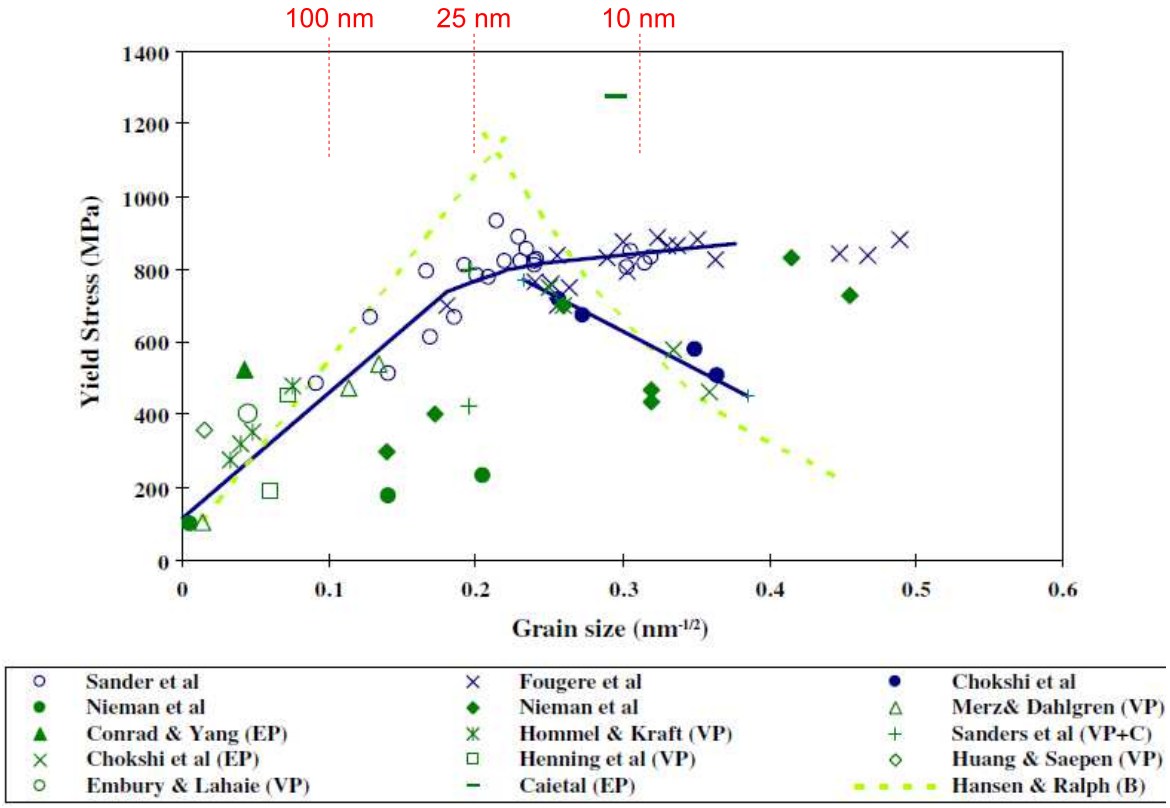

Figure 1-2 – Yield stress versus grain size plot for Cu from various sources ranging from coarse to nanograin size (Meyers et al. 2006)

It can be seen that, if the grain size is below approximately 25 nm, the trend in yield stress is ambiguous. Indeed, in some cases, if the grain size is below the threshold of 30 to 100 nm, the yield stress is followed by a plateau, whereas in other cases, the material becomes 'weaker', in the sense that it will have lower yield stress.

There are different proposed explanations for the breakdown of the Hall Petch law for grain size below a critical value. As reported by Meyers et al. (2006), Chokshi et al. (1989) explained it by the occurrence of creep at room temperature (phenomenon similar to grain-boundary sliding in macroscopic materials at high temperature), while Weertman (1993) attributes it to the presence of flaws. The numerical simulations performed by Koslowski et al. (2011) show that the transition from Hall Petch to inverse Hall Petch is due not only to grain size, but also to the energy of the grain boundary, as the threshold grain size decreases when the grain boundary energy is increased. In their simulations, the samples with higher values of cohesive energy at the sliding interface between the grains do not show inverse Hall Petch. Koslowski et al. (2011) argue that the variation in the grain boundary energy could be the reason for

the apparently conflicting experimental results (i.e. some experiments show inverse Hall Petch, others do not).

Therefore, it can be clearly seen that conventional laws of plasticity theory developed for macroscopic samples cannot be applied across the scales, to nano-samples.

This is also true for the laws of contact mechanics. Indeed, as noted by Polonsky and Keer (1996b), when the size of contact becomes comparable to the characteristic microstructural length, the material can no longer be treated as a homogeneous continuum. Molecular dynamics simulations of atomic-scale contacts have also shown that their behaviour is significantly different from the behaviour of the macroscopic contacts (Kallman et al. 1993, Mordehai et al. 2011).

Polonsky and Keer (1996a, 1996b) developed a numerical model to study scale effects in the ploughing of a flat elastic-plastic surface by a hard asperity. The plasticity representation they used is based on discrete crystal dislocations and they found their simulations 'show that plastic deformation at an asperity micro-contact becomes difficult and then impossible when the asperity size decreases below a certain threshold value of the order of the microstructural length.' The reason for this is that, when the contact is below the size of the microstructural length, the dislocated volume is not large enough to cause plastic flow.

Polonsky and Keer say their conclusion seems to support the findings of Kuhlmann-Wilsdorf (1981), who has maintained in a number of papers that, in the case of contact scenarios with a large number of contact spots per unit area, the very small contacts will undergo only elastic deformation (Kuhlmann-Wilsdorf 1981, 1991, 1996a, 1996b). However, Kuhlmann-Wilsdorf (1996b) clearly stated that her experiments show only elastic deformation because the load is distributed to a large number of contact spots, and the stress per contact spot is kept below Meyer impression hardness, and not because of a physical particularity that the nano-contacts may have. Indeed, one of her conclusions was that 'there is every indication that dislocations in tribology behave exactly the same way as in bulk material', or, to use her metaphor, 'there are no mermaids.' Therefore, the results of Polonsky and Keer seem to show that there may be 'mermaids' after all, when the contact becomes comparable in size to the

characteristic macrostructural length, i.e. plastic deformation becomes very difficult, or even impossible. This effect will be referred to as the 'Polonsky-Keer effect'.

1.5 Surface Topography and Corresponding Statistical Models and parameters

Even though some surfaces may look smooth to the human eye, observing it under a magnifying instrument will reveal a complex structure. Summits of different heights may be identified, which are points that are higher than the closest neighbouring points, and can be situated at different distances from one another. Summits are points of interest because these are the points where contact will be initiated, or which are very close to contact initiation points.

The properties of rough surfaces can be a consequence of a number of factors, for example manufacturing method, crystal structure, coatings, wear, and so on. The properties of surfaces in contact will greatly influence their interaction; therefore the performance of many processes can be improved by controlling these characteristics. For example, in the experiments of Krantz et al. (2001), reducing the average roughness of a steel gear by about a factor of 5 increased the life of the gear by a factor of 4.

Rough surfaces are usually characterized by analysing line profiles, which are line measurements across the surface. The profile obtained is a series of peaks and valleys, which requires a number of parameters to describe different aspects of the analysed profile. Due to the increasing computational possibilities in recent years, there has been a 'parameters rash', most of which are useless, as argued by Whitehouse (1982). Borodich et al. (2015) also note that the existence of more than 30 parameters and functions to characterize rough surfaces suggests there is no clear understanding of which characteristics are meaningful for tribology.

1.5.1 Surface texture parameters defined by the British Standard EN ISO 4287:1998+A1:2009

There are eleven statistical parameters of roughness profiles that are commonly used, and that have been defined and published by the International Organization for

Standardization. Nine of these parameters are amplitude parameters (calculated based on the measured heights of the profile), one is a spacing parameter (involving the ordinates of the measured points), and one is a hybrid parameter. We will mention them briefly in this section. The heights and depths involved in these definitions are measured from the mean-line of the profile, which is established using a Gaussian profile filter with a prescribed cut-off length.

a) Maximum profile peak height (R_P)

The maximum profile peak height is defined as the largest peak height of the profile within the sampling length.

b) Maximum profile valley depth (R_V)

The maximum profile valley depth is the depth of the deepest valley of the profile within the sampling length.

c) Maximum height of the profile (R_Z)

The maximum height of the profile is defined as the sum of the maximum profile peak height (R_P) and the maximum profile valley depth (R_V) within the sampling length. Note that confusion may arise from the fact that, in ISO 4287-1:1984, R_z was used to denote the 'ten point height of irregularities'.

d) Mean height of profile elements (R_C)

The mean height of profile elements is defined as the mean value of the profile heights within the sampling length, computed by:

$$R_c = \frac{1}{m}\sum_{i=1}^{m} z_{t_i}$$

Where m is the number of heights in the sampling length and z_{ti} are the heights of the profile elements, as shown in Figure 1-3.

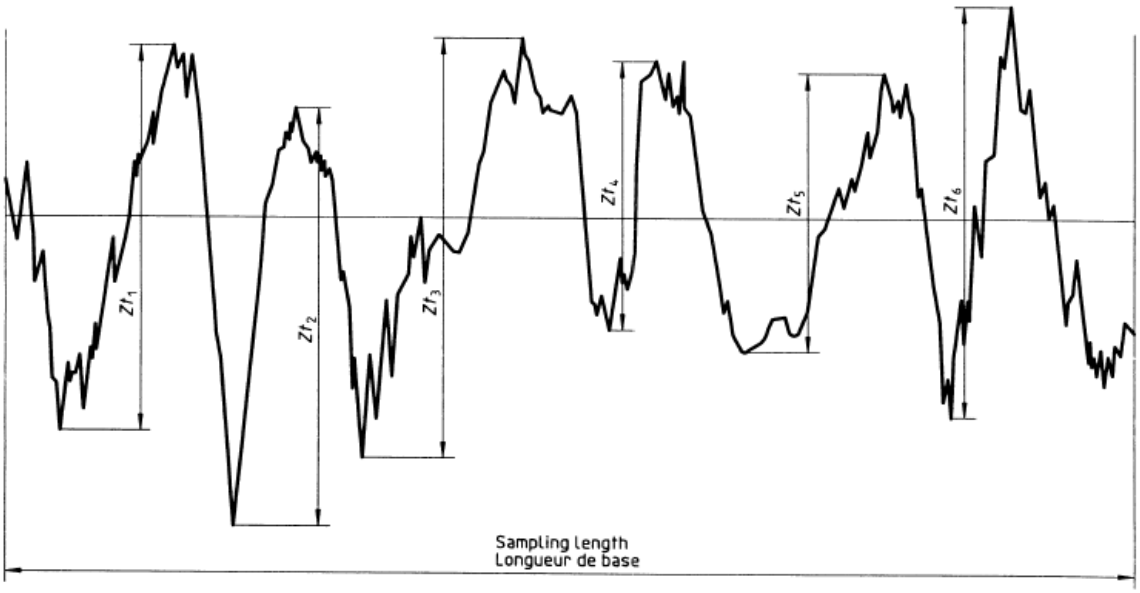

Figure 1-3 – Height of profile elements (from BS EN ISO 4287:1998+A1:2009)

e) Total height of profile (R_T)

The total height of profile is defined as the sum of the maximum profile peak height (Z_P) and the maximum profile valley depth (Z_V) within the evaluation length. When the evaluation length coincides with the sampling length, R_T coincides with R_Z. The standard defines the sampling length as the length '*used for identifying the irregularities characterizing the profile under evaluation*', and the evaluation length as the length '*used for assessing the profile under evaluation*'.

f) Arithmetical mean deviation of the assessed profile (R_a)

The arithmetical mean deviation of the assessed profile is defined as the arithmetic mean of the absolute ordinate values $Z(x)$ within the sampling length (l), as is calculated by:

$$R_a = \frac{1}{l}\int_0^l |Z(x)|dx$$

g) Root mean square deviation of the assessed profile (R_q)

The root mean square deviation of the assessed profile is defined as the root mean square of all heights within the sampling length l, and it is computed as:

$$R_q = \sqrt{\frac{1}{l}\int_0^l Z^2(x)dx} \quad (1\text{-}5)$$

h) Skewness of the assessed profile (R_{sq})

The skewness of the assessed profile is a measure of the asymmetry of the probability density function of the profile heigths, and it is defined as:

$$R_{sq} = \frac{1}{R_q^3}\left[\frac{1}{l}\int_0^l Z^3(x)dx\right]$$

i) Kurtosis of the assessed profile (R_{ku})

The kurtosis of the assessed profile is a measure of the sharpness of the probability density function of the profile heights, and is strongly influenced by isolated peaks of isolated valleys. It is defined as:

$$R_{sq} = \frac{1}{R_q^4}\left[\frac{1}{l}\int_0^l Z^4(x)dx\right]$$

j) Mean width of the profile elements (RS_m)

The mean width of the profile elements is defined as:

$$RS_M = \frac{1}{m}\sum_{i=1}^{m} X_{S_i}$$

Where m is the number of profile elements in the sampling length and the meaning of the width of profile elements X_{Si} is illustrated in Figure 1-4.

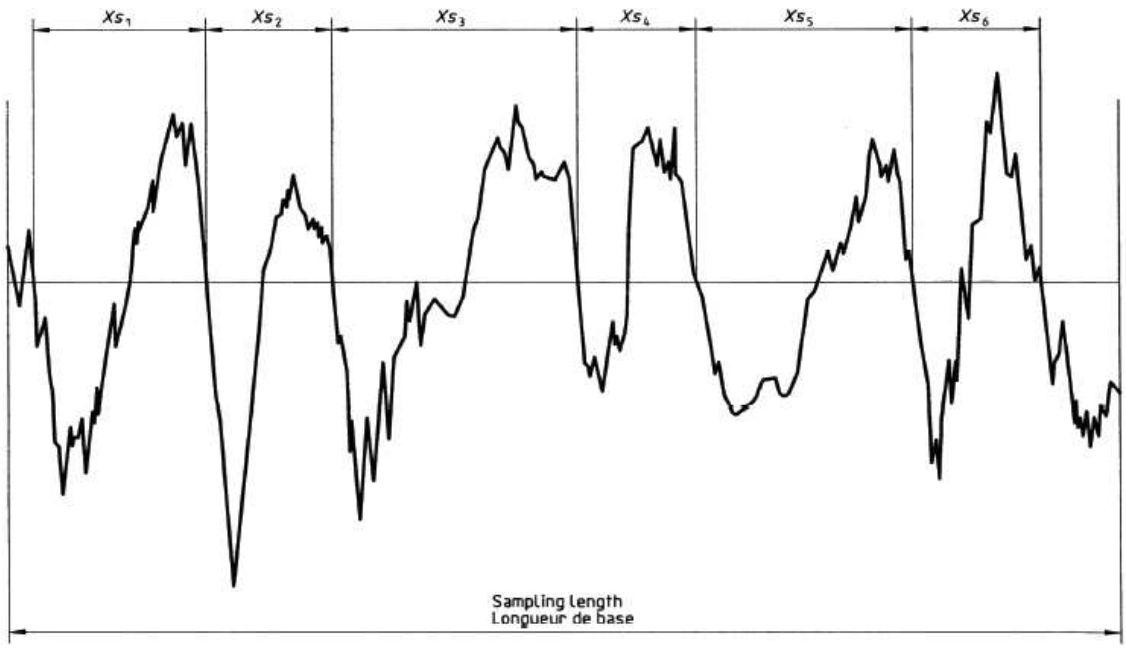

Figure 1-4 – Width of profile elements (from BS EN ISO 4287:1998+A1:2009)

k) Root mean square slope of the assessed profile ($R_{\Delta q}$)

The root mean square slope of the assessed profile is defined as the root mean square of the slopes dZ/dX within the sampling length:

$$R_{\Delta q} = \sqrt{\frac{1}{l}\int_0^l \left(\frac{d}{dx}Z(x)\right)^2 dx}$$

One source of errors in calculating some of the above parameters (R_a, R_q, $R_{\Delta q}$, R_{sk} and R_{ku}) is that they are defined using definite integrals. However, the measured surface profiles come in a series of discrete points. Therefore the obtained results will be approximate, and will depend on the method used for integration. A discussion of this issue and proposal of new integration methods can be found in the thesis of Brennan (2010).

It is worthy to note that the parameters mentioned above are defined for line profiles and not rough surfaces. As Maugis (2000) notes, it is quite difficult to pass from the statistical characteristics of a profile to the statistical characteristics of the surface. One theory to correlate properties of profiles to properties of surfaces was introduced by Nayak (1971), and it is called 'the theory of random processes.' His theory expresses the density of peaks per unit length in terms of the density of summits per unit area,

the mean height of peaks as function of the mean height of summits, and the mean curvature of peaks in terms of the mean curvature of summits (Maugis 2000, p.321). To obtain these results, Nayak assumed the surface is isotropically random with a Gaussian height distribution. Although Gaussian is a widely used heights distribution, we will see later that this is not an accurate distribution for most surfaces.

One widely used curve that ISO 4287:1998 defines is the material ratio curve of the profile, also known as the Abbott and Firestone (1933) curve. As illustrated in Figure 1-5, the curve represents the material ratio of the profile as a function of depth.

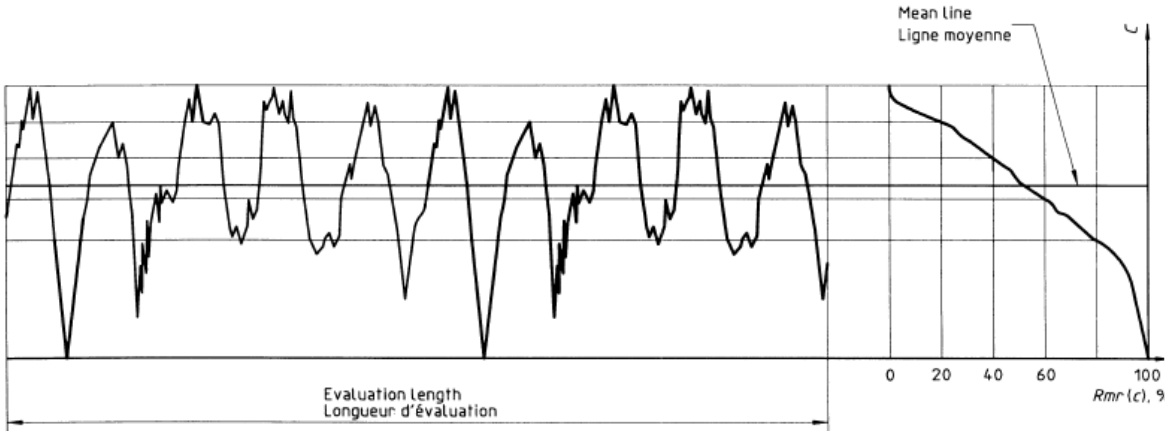

Figure 1-5 – Material ratio (Abbott-Firestone) curve (from BS EN ISO 4287:1998+A1:2009)

1.5.2 Autocorrelation function

Applied to roughness profiles, the autocorrelation function shows the distance over which a correlation in the asperity heights exists. The autocorrelation function $R_z(\delta)$ can be defined as:

$$R(\delta) = \lim_{T\to\infty} \frac{1}{2T} \int_{-T}^{T} [z(x+\delta) - \bar{z}][z(x) - \bar{z}]dx \qquad (1\text{-}6)$$

In (1-6), the length of the analysed sample is $2T$ and $\bar{z}$ is the mean-line of the profile $z(x)$. There exists a Fourier transform relation between the autocorrelation function $R_z(\delta)$ and the power spectral density $G(\omega)$:

$$G(\omega) = \frac{2}{\pi} \int_{0}^{\infty} R(\delta) \cos \omega\delta \, d\delta \qquad (1\text{-}7)$$

Whitehouse and Archard (1970) treated the surface profile as a random signal and they defined it using only two characteristics: the height distribution and the autocorrelation function. They assume a Gaussian distribution of asperity heights and an exponential autocorrelation function.

It is fitting to say here, as argued by Borodich et al. (2015), that contact models relying only on the autocorrelation function to represent the roughness cannot give reliable results. Their mathematical argument is straightforward and short enough to be given here. It will be shown that the autocorrelation function and corresponding power spectral density are the same for a profile, in both positive and negative directions. That is to say an inverted roughness profile has the same autocorrelation function as the original profile.

For the autocorrelation function expressed in (1-6), we can choose $\bar{z} = 0$, without any loss of generality. This is equivalent to shifting the system of coordinates on the mean-line. (1-6) then becomes:

$$R(\delta) = \lim_{T\to\infty} \frac{1}{2T} \int_{-T}^{T} z(x+\delta)z(x)dx \tag{1-8}$$

Let us now consider the inverted profile, defined by $y(x) = -z(x)$. If the mean line $\bar{z}$ is defined by

$$\bar{z} = \lim_{T\to\infty} \frac{1}{2T} \int_{-T}^{T} z(x)dx$$

Then the mean-line of the inverted profile will be

$$\bar{y} = \lim_{T\to\infty} \frac{1}{2T} \int_{-T}^{T} y(x)dx = -\lim_{T\to\infty} \frac{1}{2T} \int_{-T}^{T} z(x)dx = 0$$

Then the autocorrelation function for the inverted profile $y(x) = -z(x)$ will be

$$\begin{aligned} R_y(\delta) &= \lim_{T\to\infty} \frac{1}{2T} \int_{-T}^{T} [y(x+\delta) - \bar{y}][y(x) - \bar{y}]dx \\ &= \lim_{T\to\infty} \frac{1}{2T} \int_{-T}^{T} y(x+\delta)y(x)dx = \lim_{T\to\infty} \frac{1}{2T} \int_{-T}^{T} z(x+\delta)z(x)dx \\ &= R_z(\delta) \end{aligned} \tag{1-9}$$

Relation (1-9) shows that the profile $z(x)$ and the inverted profile $y(x) = -z(x)$ have the same auto-correlation function and, as follows from (1-7), the same power spectrum. Just to illustrate this result we can say that, if the autocorrelation function is the only roughness characteristic used to model a surface in contact with a flat, the two contact scenarios depicted in Figure 1-6 and Figure 1-7 should yield the same result, which is not correct.

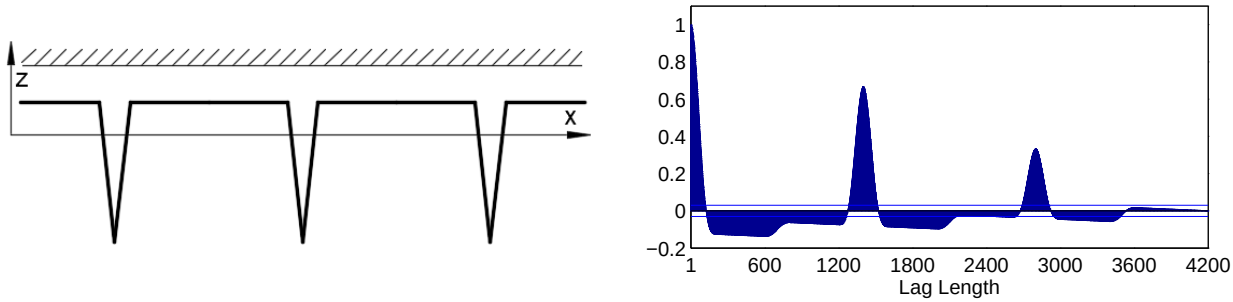

Figure 1-6 – Profile $z(x)$ and the corresponding autocorrelation function for 4200 lags (the roughness data has 4200 points)

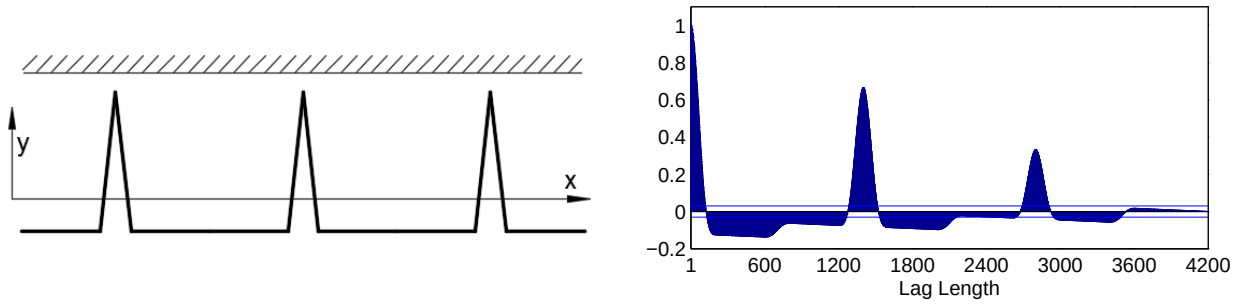

Figure 1-7 – Inverted profile $y(x) = -z(x)$ and the corresponding autocorrelation function for 4200 lags (the roughness data has 4200 points)

1.5.3 Fractal representation of rough surfaces

Sayles and Thomas (1978) presented the variation of the power spectral density with wavelength for many different surfaces. In logarithmic coordinates, these results span along a line, suggesting that many different surfaces have a similar form of power spectrum.

In a reply to the claims of Sayles and Thomas, Berry and Hannay (1978) were the first to connect the concept of fractals to surface representation. They argued that the findings of Sayles and Thomas (1978) are a particular case of 'the statistically isotropic surfaces which have no scale and whose height function is well defined but non-

differentiable,' with geometric properties 'discussed in detail by Mandelbrot (1977) who calls them *fractals*.'

As noted by Borodich and Onishchenko (1999), Roques-Carmes et al. (1988) were the first in a long line of researchers to use the Weierstrass-Mandelbrot function $W(x;p)$:

$$W(x;p) = \sum_{n=-\infty}^{\infty} p^{(D-2)n}(1 - \cos p^n x)$$

Where p is the scaling parameter and D is the fractal dimension. A truncated version of the function was proposed by Majumdar and Bhushan (1990), but extensive studies have shown that parameter A, which determines the position of the spectral density along the log$G$ axis, and the fractal dimension D depend on the resolution and the instrument used for surface measurement (Bhushan 1995, Borodich and Onishchenko 1999).

To address the question of whether the fractal dimension alone can characterize a surface in contact, Borodich and Onishchenko (1993) have carried out a theoretical experiment, similar to the one given above, which invalidates using solely the autocorrelation function for surface characterization. They divide a solid in two parts along a boundary defined by the Cantor-Borodich profile (see a more detailed description in section 5.4.2), as illustrated in Figure 1-8. The fractal dimension of this profile is

$$\dim_B C_B = 1 + \frac{\ln(2\beta)}{ln\frac{1}{\alpha}}$$

Where the similarity constants α and β satisfy the following relations: $0 < \alpha < ½$, $½ < \beta < 1$.

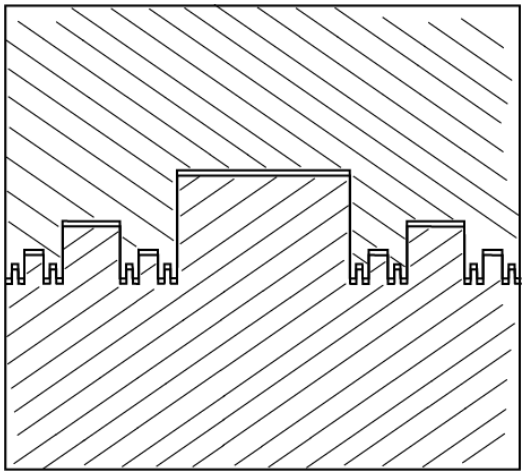

Figure 1-8 – Solid divided along the boundary defined by the Cantor-Borodich profile

Borodich and Onishchenko (1993) then calculate the contact force when the upper and the lower part are brought in contact with a Winkler elastic foundation, as shown in Figure 1-9 and Figure 1-10.

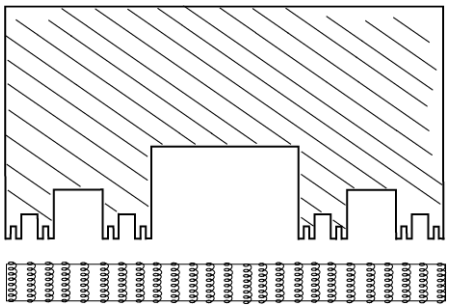

Figure 1-9 – Upper part of the solid in contact with a Winkler elastic foundation (after Borodich and Onishchenko 1993)

They showed that in the case described in Figure 1-9 the relation between the approach h and the external load P is

$$P(h) = \mathrm{A}\left(\frac{h}{h_0}\right)^{1+\frac{\ln(2\alpha)}{ln\beta}} \tag{1-10}$$

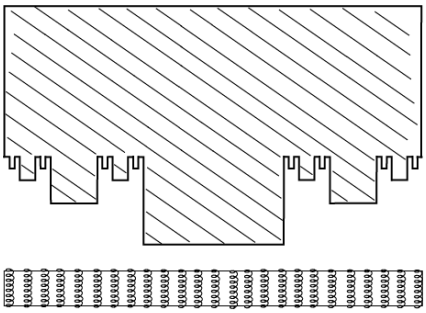

Figure 1-10 – Lower part of the solid in contact with a Winkler elastic foundation (after Borodich and Onishchenko 1993)

In the case described in Figure 1-10 the corresponding *P-h* relation is

$$P(h) = A\left[\left(1 - \frac{h}{h_0}\right)^{1+\frac{\ln(2\alpha)}{ln\beta}}\right] + B\frac{h}{h_0} \quad (1\text{-}11)$$

We can see in (1-10) and (1-11) that the solution obtained for the two contact scenarios is significantly different, even though the surfaces are defined by the same fractal profile. Therefore the authors conclude the fractal dimension alone cannot characterize the contact between two surfaces.

This conclusion was supported by further work (see e.g. Borodich 1993a). Borodich gave rigorous arguments about trends of force-penetration curves for punches described by smooth and fractal parametric-homogeneous functions (Borodich 1998a, 1998b, 2013a, 2013b, 2014). The parametric-homogeneous functions have been introduced in contact mechanics applications by Borodich (1992). For a description of these functions the reader is referred to the above mentioned works.

1.5.4 Representative Elementary Pattern of Roughness (REPR)

Due to the increasing availability of computational power, the friction models developed in recent years work directly with the measured roughness of the surfaces involved, rather than with the statistical interpretation of the measured profiles (see, for example the model developed by Bora et al. (2013) also described in section 5.3.9, or the model developed by the author, described in Chapter 6). However, the searching and interpolation operations involving long arrays of roughness data can lead to great computational cost. Pepelyshev (2015) has introduced a method to simplify the roughness data by finding a 'representative elementary pattern of roughness,' and was first presented by Borodich et al. (2015). The method makes use of the Kolmogorov-Smirnov test for two samples to determine which section of the roughness profile best represents the entire profile. The resulting representative profile is obtained by replication of the representative pattern and will be equivalent to the original profile in terms of height distribution. For example, the algorithm finds the 52 points profile section in Figure 1-12 as the most representative 52 points section for the profile in Figure 1-11 made of 668 points. The equivalent profile obtained by replication of the most representative pattern is shown in Figure 1-13.

Besides being equivalent in terms of height distribution, a visual comparison of the original and the equivalent profiles also shows that there is reasonable similarity between them. The equivalent profile is computationally easier to handle than the original profile, since it is a replication of just 52 points.

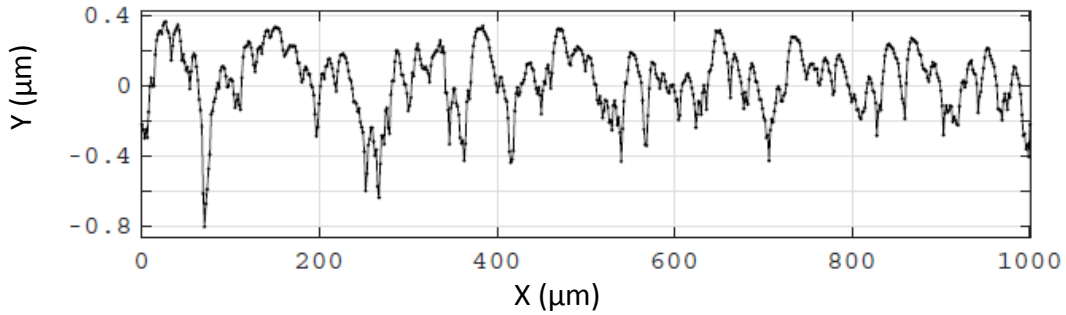

Figure 1-11 – Original measured profile (668 points)

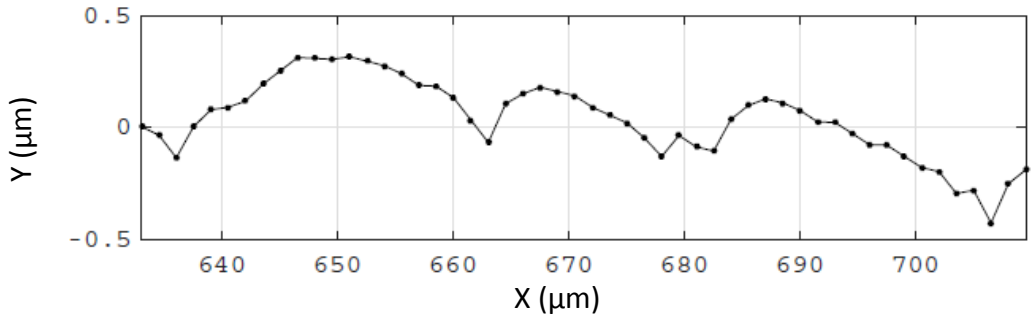

Figure 1-12 – The most representative pattern (52 points)

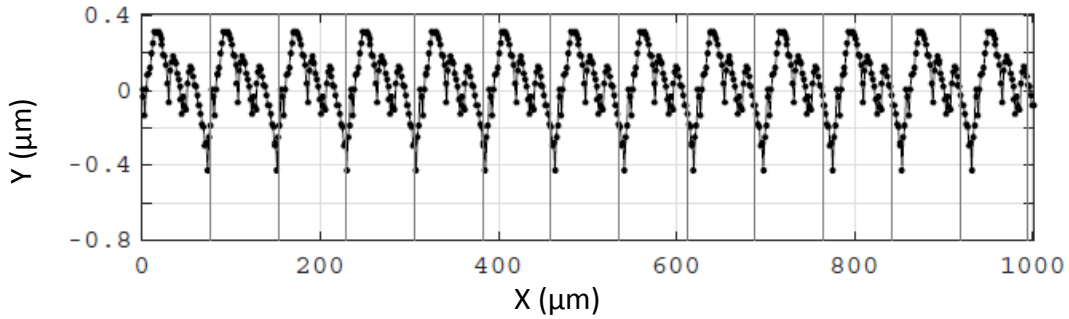

Figure 1-13 – Equivalent profile in terms of height distribution obtained by replication of the most representative pattern

Other proposed models of roughness exist that have not been considered in this section, but they will be encountered in the following material. The models of Archard (1957), Zhuravlev (1940), and Greenwood and Williamson (1966) will be described in the next sections of the current chapter. Models like the Kragelsky (1948) rod assembly model, the Cantor-Borodich profile, and others will be analysed in 0.

1.6 The Hertz Contact Theory and Archard's model

The classic contact mechanics theory begins with Heinrich Hertz, who solved the contact problem between two elastic bodies with curved surfaces at the age of 23, over his 1880's Christmas holiday (Johnson 1985). The work was published two years later (Hertz 1882a). The Hertzian contact model does not take into account the force of adhesion and it builds on the following assumptions:

- The curvature radii of the contacting bodies and their dimensions are large compared to the radius of the contact area; small strains are assumed.
- The bodies are involved in frictionless contact.
- The surfaces of the bodies in contact are continuous and nonconforming.

For a mathematical formulation of the full list of assumptions of the Hertz contact problem as given by Borodich (1989), the reader can see section 3.2.1.

A full treatment of the Hertz contact problem for paraboloid shape bodies can be found in Johnson (1985). In the current work the solution for the contact between solids of revolution will be used. In this case, if the origin of the system of coordinates is at the point of first contact, with the *xy* axes in the tangent plane common to both bodies, and axis *z* along the common normal, directed through the lower body, the shapes of the bodies can be approximated as:

$$z_1 = \frac{1}{2R_1}(x_1^2 + y_1^2) \tag{1-12}$$

$$z_2 = -\frac{1}{2R_2}(x_2^2 + y_2^2) \tag{1-13}$$

Where R_1 and R_2 are the radii of curvature of the two surfaces.

The Hertz contact problem can be stated as follows:

a) There is no displacement at infinity (when $x^2 + y^2 + z^2 \rightarrow \infty$)
b) There are no tangential stresses in the contact region (frictionless condition)
c) The boundary condition for displacements within the contact can be expressed as

$$u_{z1} + u_{z2} = \delta - \frac{1}{2R} r^2, \qquad r^2 = x^2 + y^2$$

Where u_{z1} and u_{z2} are the deformations of the two bodies, respectively, δ is the penetration depth, and R is the combined radius of curvature and is defined by:

$$\frac{1}{R} = \frac{1}{R_1} + \frac{1}{R_2} \tag{1-14}$$

The radius of curvature is positive for a convex surface and negative for a concave one. Either one of R_1 and R_2 can be negative, as long as R is positive, as it represents the radius of a sphere in contact with a plane.

For the contact of two general shape bodies, the boundary condition for displacements within the contact region can be expressed as:

$$u_z = \delta - f(x, y)$$

Where f(x,y) represents the effective shape of contact.

d) There are no applied surface stresses outside of the contact region
e) The integral of the normal stresses σ_{zz} over the contact region is equal to the external force applied P.

The solution obtained by Hertz for the contact radius a, penetration depth δ and maximum contact pressure p_0 is:

$$a = \left(\frac{3PR}{4E^*}\right)^{\frac{1}{3}} \tag{1-15}$$

$$\delta = \frac{a^2}{R} = \left(\frac{9P^2}{16RE^{*2}}\right)^{\frac{1}{3}} \tag{1-16}$$

$$p_0 = \frac{3P}{2\pi a^2} = \left(\frac{6PE^{*2}}{\pi^3 R^2}\right)^{\frac{1}{3}} \tag{1-17}$$

In the above relations E^* is the contact modulus, and it is defined by:

$$\frac{1}{E^*} = \frac{1 - \nu_1^2}{E_1} + \frac{1 - \nu_2^2}{E_2} \tag{1-18}$$

E_1 and E_2 are the Young's moduli for the two bodies in contact, and ν_1 and ν_1 are the corresponding Poisson's ratios. E^* then comprises the properties of both bodies, 1 and 2, and has the form of the equivalent stiffness for an ensemble of two springs connected in series.

Equation (1-15) reflects a weak dependence (in power 1/3) of the contact radius on the compressive force, combined radius of curvature and contact modulus. The contact radius increases when the force or the combined radius increases, and decreases when increasing the contact modulus.

Many contact and friction models use or are an extension of the Hertz contact theory, as it will be shown further.

1.6.1 Galin's solution for axisymmetric contact for power law shape punches

Galin (1946) obtained the solution for axisymmetric contact for punches described by power law functions (see also Galin 1961, 2008)

$$f(r) = B_d r^d, \qquad d \geq 1 \tag{1-19}$$

Here B_d is the shape constant and d can be called the 'bluntness factor'. In the case of cone indentation, d = 1 and B_d = cotγ, where γ is the half-angle of the cone. For spherical indentation, d = 2 and B_d = 1/(2R), where R is the radius of the indenter. For 1 < d < 2, equation (1-19) defines blunter cones. If the shape of an indenter is described by (1-19), the relation between the force P and the contact radius a, and the relation between the penetration δ and the contact radius a, are as follows:

$$P = E^* B_d \frac{d^2}{d+1} 2^{d-1} \frac{\left[\Gamma\left(\frac{d}{2}\right)\right]^2}{\Gamma(d)} a^{d+1} \tag{1-20}$$

$$\delta = B_d d 2^{d-2} \frac{\left[\Gamma\left(\frac{d}{2}\right)\right]^2}{\Gamma(d)} a^d \tag{1-21}$$

In the above relations, $\Gamma(d)$ is the Euler gamma function. From (1-20) and (1-21), the following relation between force and indentation depth can be obtained:

$$P = E^* \left[B_d^{-\frac{1}{d}} 2^{\frac{2}{d}} d^{\frac{d-1}{d}} \frac{1}{d+1} \left[\Gamma\left(\frac{d}{2}\right) \right]^{-\frac{2}{d}} [\Gamma(d)]^{\frac{1}{d}} \right] \delta^{\frac{d+1}{d}} \quad (1\text{-}22)$$

1.6.2 Archard's model

Using Hertz contact theory, Archard (1957) introduced the first hierarchical model of roughness, popularly referred to as the "bump on bump" or "asperity on asperity" model. Experimental studies later confirmed Archard's observation, by showing that, at some intervals, the power spectral density functions of real surfaces have power-law character (Sayles and Thomas 1978). They interpret this to mean that surfaces are statistically similar to themselves under successive magnifications. As depicted in Figure 1-14, the apparent contact is at the level of the protuberances of the surface having radius R_1. But the real contact area is the sum of the local contacts for every protuberance of radius R_2 touching the surface, that is superimposed on the radius R_1 asperity. But if we further magnify the profile, each of these R_2 protuberances has its own protuberances; the model thus reflects the multiscale nature of the surface that is found from the macroscale down to the atomic scale.

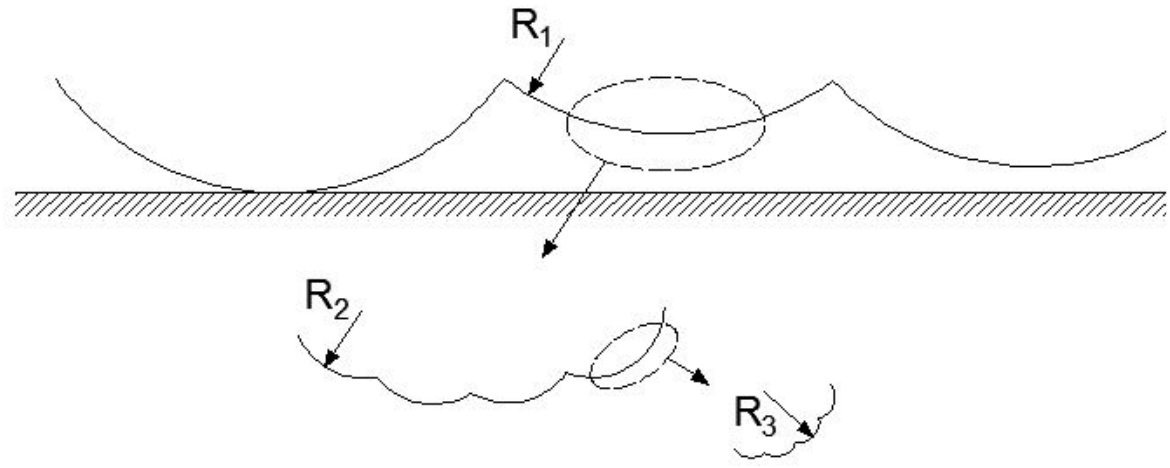

Figure 1-14 – Archard model (1957)

The model is hierarchical because the asperities of generation *k* are located on the asperities of generation *k*-1. As a consequence, the deformation of the asperity at generation *k* will influence its neighbours, as well as the asperities at previous generations. Even though it is hierarchical and multi-level, Archard's model is not

multi-scale as it takes into account only one physical contact mechanism, namely the elastic deformation of asperities.

In order to describe the contact between the surfaces, the Hertzian pressure under a sphere of radius R_1 was considered external load for the spheres of radius R_2 on top of it. Further, the pressure on the sphere of radius R_2 was considered external load for the spheres of radius R_3 on top of it, and so on. In doing so, it was assumed that the Hertz solution for pressure is valid for rough solids. However, it was later showed that this is not true (Greenwood and Tripp 1967).

1.7 The classic Zhuravlev and Greenwood-Williamson Models

After Prandtl-Tomlinson model was introduced in 1928 (a description of Prandtl-Tomlinson model can be found in section 5.3.1), Zhuravlev was concerned with trying to explain the Amontons-Kotelnikov friction law. In 1940 he introduced a model of dry friction for nominally flat surfaces where asperities were represented as independent elastic spherical caps, of the same radius, with random height distribution, that deform according to Hertz theory (Zhuravlev 1940). Figure 1-15 offers a schematic representation of the model.

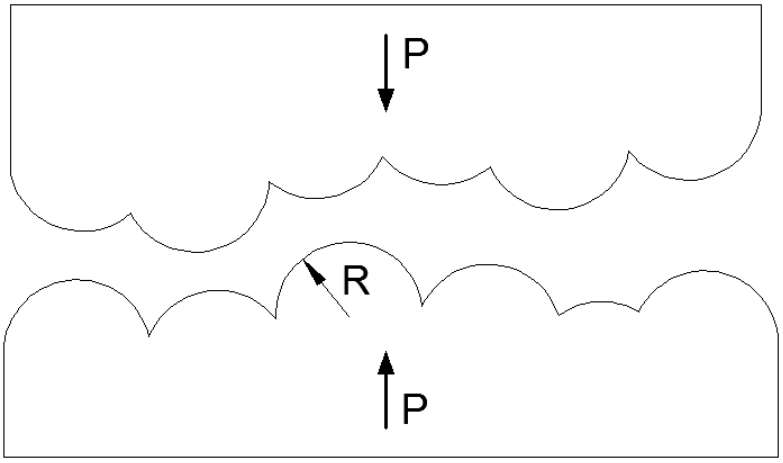

Figure 1-15 - Zhuravlev model (1940) presenting two rough surfaces as statistically identical collections of spheres located at different heights

Zhuravlev's findings were that the true contact area and the friction force are approximately proportional to the external compressing force, and the influence of the load on the coefficient of friction is very small. Let us briefly go through the argument

of Zhuravlev's paper. The meaning of the terms involved will be both explained and illustrated in Figure 1-16.

Using Hertz's solution for elastic contact, the compressing force *P* and the true contact area *S* are expressed as follows:

$$P = \frac{\sqrt{2R}}{3\pi k}\int_0^{x/2}\int_0^{x/2}[x-(\xi_1+\xi_2)]^{3/2}\,\frac{n(\xi_1)n(\xi_2)d\xi_1 d\xi_2}{N} \tag{1-23}$$

$$S = \frac{\pi R}{2}\int_0^{x/2}\int_0^{x/2}[x-(\xi_1+\xi_2)]\,\frac{n(\xi_1)n(\xi_2)d\xi_1 d\xi_2}{N} \tag{1-24}$$

It is obvious that the two integrals in (1-23) and (1-24) are to calculate the total sum penetration for all the contacting asperities within the $d\xi_1$ and $d\xi_2$ layers. The term $\frac{n(\xi_1)n(\xi_2)d\xi_1 d\xi_2}{N}$ expresses the expected number of contacting asperities within these layers because $\frac{n(\xi_2)d\xi_2}{N}$ gives the probability for an asperity on surface *A* to meet an asperity of surface *B* in the layer $d\xi_2$. $N = \int_0^x n(\xi)d\xi$ is the total number of asperities from the level of the tallest asperity down to the depth *x,* and *n(ξ)* is the distribution function of the spherical caps summits. The meaning of these notations is also illustrated in Figure 1-16.

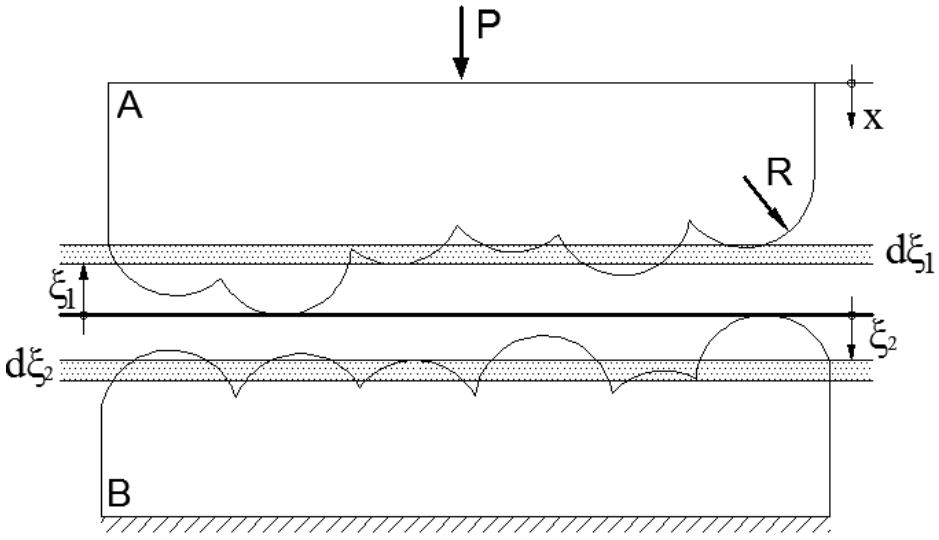

Figure 1-16 - Zhuravlev model (1940) – illustration of notations used

In order to be able to integrate analytically the expressions (1-23) and (1-24), Zhuravlev assumes the distribution function is linear: $n(\xi) = \beta\xi$. Therefore the

integral $\int_0^{x/2}\int_0^{x/2} n(\xi_1)n(\xi_2)d\xi_1 d\xi_2$ is equal to β^2. After solving the integrals in (1-23) and (1-24), the following expressions are obtained for the total compressing force and true contact area, where C_1 and C_2 are integration constants:

$$P = \frac{\sqrt{2R}\,\beta^2}{3\pi kN} C_1 x^{11/2} \tag{1-25}$$

$$S = \frac{\pi R\,\beta^2}{2N} C_2 x^5 \tag{1-26}$$

On the assumption that the friction force F is proportional to the number of molecular contacts and thus to the true contact area, Zhuravlev expresses friction force as:

$$F = \alpha S = \frac{\alpha\pi R\,\beta^2}{2N} C_2 x^5 \tag{1-27}$$

Where α is a coefficient depending on the cohesive forces. Eliminating x from equations (1-25) and (1-27) the relation between the friction force and the normal compressing force is obtained:

$$F = C\frac{\alpha R^{1/11}\,\beta^2}{N^{1/11}} k^{10/11} P^{10/11} \tag{1-28}$$

The coefficient of friction can be further expressed as:

$$\mu = C\frac{\alpha R^{1/11}\,\beta^2}{N^{1/11}} k^{10/11} P^{-(1/11)}$$

The criticism brought to this model was directed to a number of features and a summary can be found in Borodich (2007). Kragelsky (1948) noted that the natural height distribution of asperities is Gaussian rather than linear, as considered by Zhuravlev. However, Zhuravlev choose a linear asperity height distribution as an initial approximation, as this allowed him to solve analytically the integrals to express the compressive force and the true area of contact. Any heights distribution function can be used in the expressions (1-23) and (1-24).

Greenwood and Williamson (1966) improve on Zhuravlev's model and introduce a Gaussian asperity height distribution, as well as plastic deformation of asperities. The assumption that the asperities have the same radius of curvature was left unchanged.

Greenwood and Williamson consider the contact between a rough surface and a plane (Figure 1-17), but their approach is very similar to that of Zhuravlev. We note that the Hertzian elastic contact between two spheres of radius R_1 and R_2 is mathematically equivalent to the contact between a half-space and a sphere of radius $\frac{1}{R} = \frac{1}{R_1} + \frac{1}{R_2}$.

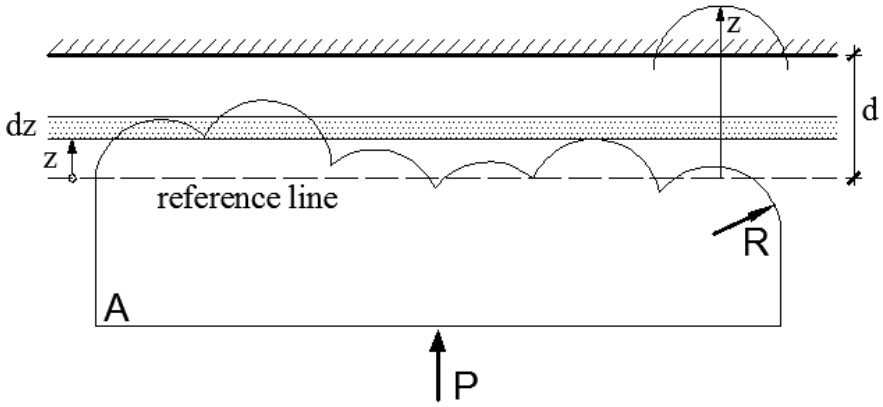

Figure 1-17 - Greenwood-Williamson model (1966)

The expected total compressive force and the expected total area of contact are expressed as follows:

$$P = \frac{4}{3} N E^* R^{1/2} \int_d^\infty (z-d)^{\frac{3}{2}} \phi(z) dz \tag{1-29}$$

$$A = \pi N R \int_d^\infty (z-d) \phi(z) dz \tag{1-30}$$

In these expressions *N* is the total number of asperities, $\phi(z)$ gives the probability that an asperity is within a layer *dz* and E* is the contact modulus. The term $N \int_d^\infty \phi(z) dz$ expresses the number of asperities that are expected to make contact when the surfaces are at a distance *d* apart.

Greenwood and Williamson (1966) have solved numerically the integrals for a Gaussian asperity height distribution and showed that the area of contact is almost proportional to the load (Figure 1-18). Two curves are plotted, for a 1 cm^2 (dashed curve) and 10 cm^2 (solid curve) nominal contact area. The fact that they are so close shows that the contact area does not depend on nominal pressure, but on the load.

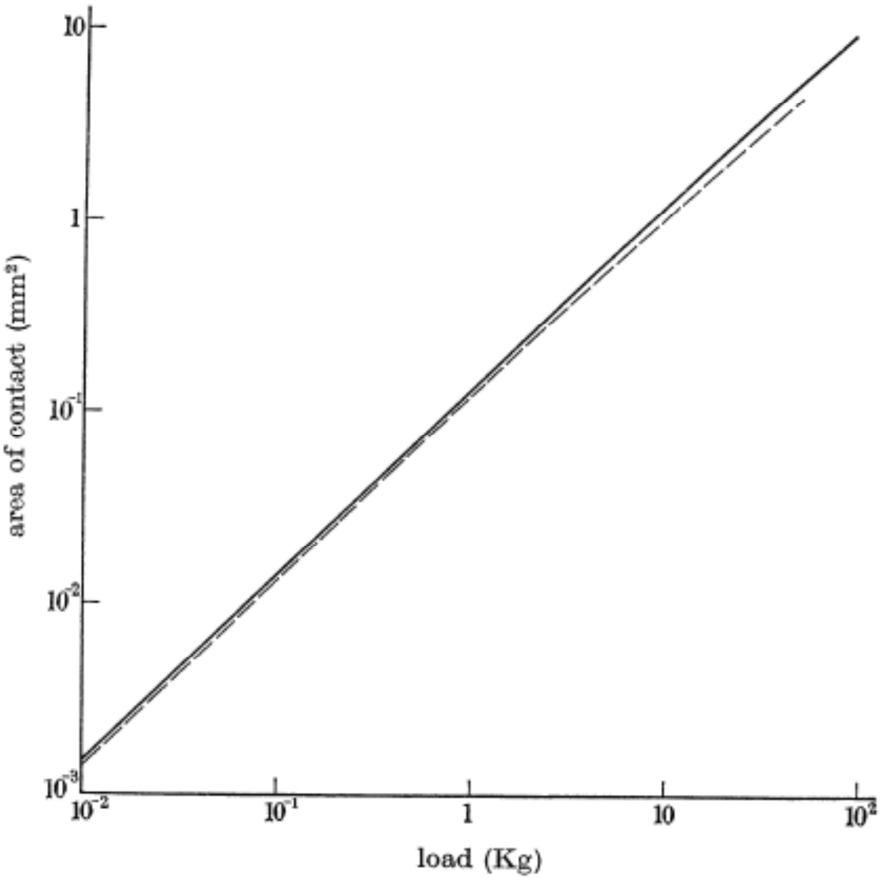

Figure 1-18 - Relation between area of contact and load (from Greenwood and Williamson, 1966)

To determine the critical load at which the surface will reach the elastic deformation limit, the plasticity index is defined as:

$$\psi = \frac{E^*}{H}\sqrt{\frac{\sigma}{R}} \tag{1-31}$$

Here H stands for hardness and σ stands for the standard deviation of the height distribution. It might be surprising that the plasticity index does not depend on the external load. In other words, the system will deform elastically or plastically, independent of the external load. Therefore, depending on the properties of the material and on the nature of the surface profile, the contact can be in a plastic state of deformation even for very small loads (for example ground surfaces); whereas other surfaces can be in an elastic state of deformation even for very high loads (for example highly polished surfaces).

The Zhuravlev / Greenwood – Williamson model has found good agreement with a variety of experimental systems. However, the model has several drawbacks. One of

the most important drawbacks is that the asperities are uncoupled; in reality the asperities are connected through the bulk and influence one-another. The resulting friction force is constant for the pair of rubbing surfaces and does not reflect the local effects and interplay between the asperities of the interacting surfaces.

1.8 Mechanics of adhesive contact

The first calculation of adhesive forces between two rigid spheres was done by Bradley (1932). He performed a very cumbersome calculation of the attractive forces as a point-wise summation of the interaction stresses between all the elements of the bodies.

1.8.1 Derjaguin approximation

Two years later Derjaguin (1934a, 1934b) introduced an extension of the Hertz model to take into account the force of adhesion in an approximate manner. Rather than pair-wise consideration of the interactions between all the elements of the bodies (as in Bradley's model), surface interactions were considered between corresponding surface elements along the vertical line. So each surface element on body 1 is attracted to the closest surface element on body 2, along the vertical line (Figure 1-19).

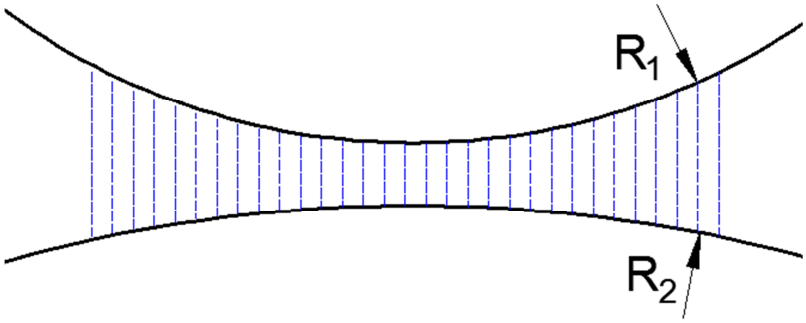

Figure 1-19 – Adhesive interactions in Derjaguin approximation (1934)

Almost all common adhesive contact models are based on Derjaguin's assumption and do not calculate the force of adhesion as the interaction between all the points in the volume of the interacting bodies.

Another assumption of Derjaguin approximation is that the interaction energy per unit area between small elements of the curved surfaces is equal to the interaction energy per unit area between two parallel planar surfaces. Derjaguin's 1934 theory is an

approximation because the contact stresses and the relation between the contact area and penetration, as well as the deformed shape of the bodies, are calculated according to Hertz theory. It does not take into account the effect of adhesion on the pressure distribution (Kendall 2001, p.183).

Since it is not lengthy, we can give here Derjaguin's approach to calculate the separation force P_c. If the sphere of radius R is replaced by a paraboloid of revolution $f(r)=B_2 r^2$, with $B_2 = 1 / (2R)$, the separation force can be expressed as:

$$P_c = \int_0^{2\pi} \int_0^{\infty} p_a[z(r)] r dr d\phi = 2\pi R \int_0^{\infty} p_a(z) dz = 2\pi w R$$

$$w = \int_0^{\infty} p_a(z) dz, \qquad z = \frac{r^2}{2R} \tag{1-32}$$

In the above equations, w is the energy spent in separating one unit area of contacting surfaces, and $p_a(z)$ is the adhesive force per unit area between two flats at a distance z apart.

1.8.2 Johnson-Kendall-Roberts (JKR)

Johnson attempted to explain why the experimentalists found the contact radius for small loads does not obey Hertz predictions (Johnson 1958). His approach was to overlap the Hertzian contact stress with the Boussinesq stress distribution for a flat punch, which gave infinite stress at the edge of the contact area. The idea was very fruitful, however the conclusion that the particles would not adhere due to the stress singularity is wrong. Thirteen years later, the same approach, together with Derjaguin's idea to equate the work done by surface attraction against the work of deformation in the elastic bodies (Kendall 2001, p.186), produced what is now known as the JKR theory of adhesive contact (Johnson et al. 1971). A balance between the elastic, potential and surface energies was used for a two-step indentation problem, illustrated in Figure 1-20.

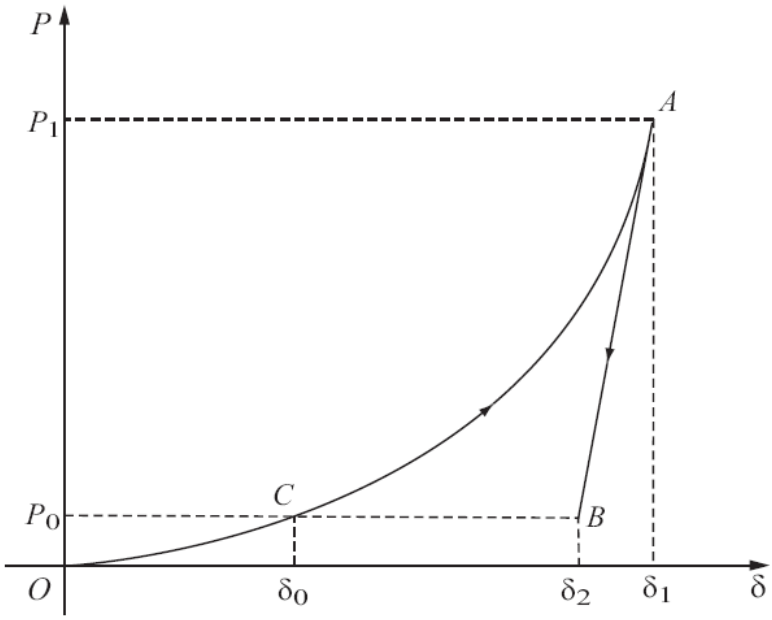

Figure 1-20 – Loading – unloading diagram explaining JKR model of adhesive contact

Point *C* on the loading diagram is obtained by Hertzian contact of a sphere and a half-space. At point *C* the system has a corresponding force P_0, penetration δ_0, and contact radius a_0. But if the surface attractive forces are considered, the contact radius would be $a_1 > a_0$. To obtain the contact radius a_1 that would characterize the system in the real adhesive case for force P_0 and δ_0, the compressive force between the sphere and the half-space is increased under Hertzian assumptions, reaching to point *A*. At point *A* the system has the correct radius a_1 to reflect adhesive interactions for P_0 and δ_0, but wrong values for force and penetration, P_1 and δ_1. In order to keep the correct contact radius a_1 and obtain the correct force P_0, the force is decreased under Boussinesq contact solution for a flat cylindrical punch (reflected in the unloading branch AB). The variation of the penetration in the unloading branch is:

$$\Delta\delta = \frac{P_1 - P_0}{2a_1 E^*} \tag{1-33}$$

From applying the equilibrium condition to the total energy written for point *B*, JKR obtained:

$$P_1 = P_0 + 3\gamma\pi R + \sqrt{6\gamma\pi R P_0 + (3\gamma\pi R)^2} \tag{1-34}$$

If K is $\frac{4}{3}\left(\frac{1-\nu_1^2}{E_1}+\frac{1-\nu_2^2}{E_2}\right)$ and R is the combined radius from Hertzian contact, and γ is the surface energy, then the expression for the contact radius becomes:

$$a^3=\frac{R}{K}\left(P+3\gamma\pi R+\sqrt{6\gamma\pi RP+(3\gamma\pi R)^2}\right) \tag{1-35}$$

In JKR theory, the stresses at the edge of contact are tensile and infinite, due to the adhesive forces, and the connection between the surfaces is normal rather than tangential. The contact ends abruptly when the pulling force reaches the separation force equal to:

$$P_{snap-off}=\frac{3}{2}\pi wR \tag{1-36}$$

We have to note that the formulae (1-35) and (1-36) were derived earlier by Sperling (1964) in his doctoral dissertation using a totally different and less elegant approach.

1.8.3 Generalization of the JKR theory and extension to non-slipping boundary conditions

Galanov (1993) used Galin (1946) expressions to formulate an extension of the JKR theory of adhesive frictionless contact for axisymmetric bodies of revolution. The same year Borodich suggested an alternative derivation for Galanov's solution, however the solution was published much later (see, Borodich 2008).

For punches described by (1-19), relation (1-34) between the real load P_0 and the real contact area a_1 becomes (Borodich 2014):

$$P_0=P_1-\sqrt{8\pi wE^*a_1^3}=C(d)B_dE^*a_1^{d+1}-\sqrt{8\pi wE^*a_1^3} \tag{1-37}$$

Here $C(d)=\frac{d^2}{d+1}2^{d-1}\frac{\Gamma^2\left(\frac{d}{2}\right)}{\Gamma(d)}$ and w is the Dupré energy of adhesion $w=\gamma_1+\gamma_2-\gamma_{12}$. $\Gamma(d)$ is the Euler gamma function. The real displacement of the punch $\delta_2=\delta_1-\Delta\delta$ can be written as:

$$\delta_2=B_dC(d)\frac{d+1}{2d}a_1^d-\left(\frac{2\pi wa_1}{E^*}\right)^{\frac{1}{2}} \tag{1-38}$$

For the non-slipping case, the relations (1-37) and (1-38) become (Borodich 2014):

$$P_0 = P_1 - \sqrt{8\pi w E^* C_{NS} a_1^3} = \frac{C_{NS} C(d) B_d E^*}{d I^*(d)} a_1^{d+1} - \sqrt{8\pi w E^* C_{NS} a_1^3} \tag{1-39}$$

$$\delta_2 = B_d C(d) \frac{d+1}{2d} \frac{1}{d I^*(d)} a_1^d - \left(\frac{2\pi w a_1}{E^* C_{NS}}\right)^{\frac{1}{2}} \tag{1-40}$$

In the above relations $C_{NS} = \frac{(1-\nu)\ln(3-4\nu)}{1-2\nu}$ and $I^*(d) = \int_0^1 t^{d-1} cos\left[\frac{\ln(3-4\nu)}{2\pi} ln\frac{1-t}{1+t}\right] dt$.

1.8.4 Derjaguin-Muller-Toporov (DMT) theory

A few years after the JKR paper had been published, Derjaguin et al. (1975) introduced a different theory of adhesive contact that followed from the Derjaguin approximation. In this theory the adhesive forces act around the contact area, but they do not change the deformed shape of the body, which remains as described by Hertz theory of contact. As opposed to JKR theory, there is no stress singularity at the edge of the contact area, and the connection between the surfaces is tangential. The contact breaks when it is reduced to a point, under the force:

$$P_{snap-off} = 2\pi w R \tag{1-41}$$

1.8.5 The JKR-DMT transition

The JKR and DMT theories seem to contradict each-other. The snap-off force found by JKR $\left(\frac{3}{2}\pi w R\right)$ is different to the one found by DMT $(2\pi w R)$. In JKR theory, adhesion is considered inside the contact area and contributes to the deformation of the bodies in contact, whereas in the DMT theory adhesion is considered outside the contact area and does not cause the deformation of the surface profile of the bodies in contact. Upon analysing the two theories, Tabor (1977) proposed that they should be applied for two different contact conditions, and a transition could be made between them based on a parameter μ_T defined as:

$$\mu_T = \left(\frac{w^2 R}{E^{*2} Z_0^3}\right)^{\frac{1}{3}} \tag{1-42}$$

The parameter in expression (1-42) is obtained as a ratio between an approximation of the variation of penetration in JKR theory (see equation (1-33), and the equilibrium interatomic distance Z_0. After a heated exchange with Tabor (Maugis 2000, p.205), Muller et al. (1980) presented a numerical adhesive contact model that gave up the assumption that the surface profiles of the bodies in contact deform according to Hertzian theory, and introduced a μ parameter (proportional to the one introduced by Tabor) to make a continuous transition between the JKR and DMT theories. So, for contact between hard solids, with small radius of curvature and weak adhesion energy, μ would be much less than unity, and the DMT theory would be applied. Values for μ would be much larger than unity for softer solids, with large curvature radius and energy of adhesion, where JKR theory would be more appropriate. The transition is also discussed by Johnson (1996) and Maugis (1992).

1.8.6 The Maugis-Dugdale model of adhesive contact

Maugis (1992) used an idea from fracture mechanics and represented the adhesive forces as a Dugdale cohesive zone at the tip of the crack. In a cohesive zone model, fracture is a gradual process where the separation of the surfaces is opposed by cohesive forces. Dugdale (1960) introduced the idea that the cohesive stress is equal to the yielding stress of the material under consideration, and is constant over a distance determined by the cancellation of stress intensity factors (Maugis 1992).

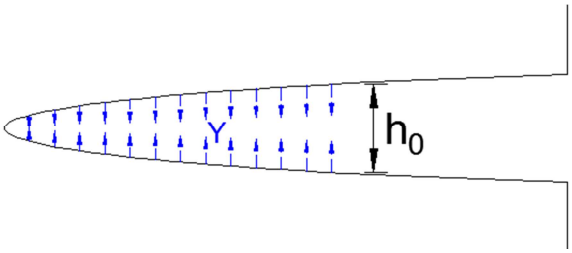

Figure 1-21 - Dugdale cohesive zone model

The work of adhesion can be written as:

$$w = \sigma_0 h_0 \tag{1-43}$$

Here h_0 is the crack opening at the end of the cohesive zone. In Maugis approximation, h_0 can be obtained by matching the areas under the Maugis approximation and Lennard-Jones curves (illustrated in Figure 1-22).

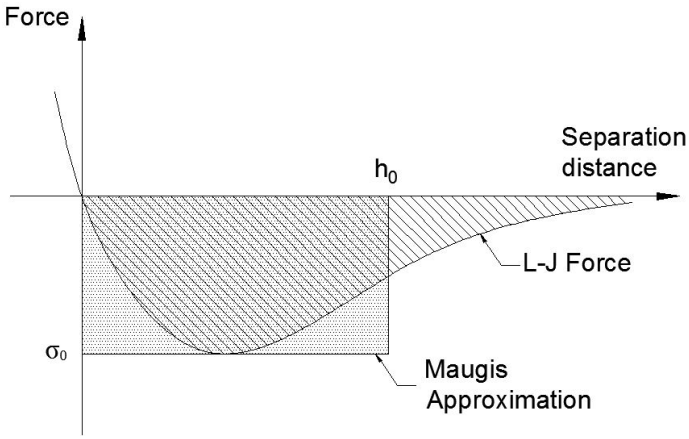

Figure 1-22 - Lennard-Jones force and Maugis-Dugdale Approximation

In Dugdale's model, σ_0 is the yielding stress of the material (denoted *Y* in Figure 1-21). Instead of the yielding stress of the material, Maugis (1992) uses the theoretical stress σ_{th} which, for a Lennard-Jones potential, is:

$$\sigma_{th} = 1.03\frac{w}{z_0} \tag{1-44}$$

In (1-44), z_0 is the equilibrium separation of the atoms.

The adhesive forces are constant for the interval $z \in [z_0, z_0 + h_0]$, as illustrated in Figure 1-23.

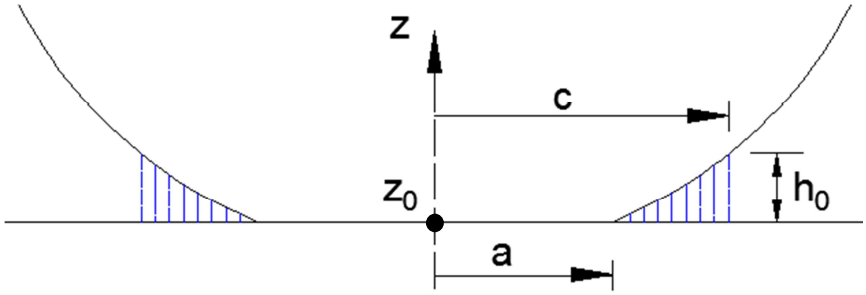

Figure 1-23 – Sketch of the contact area in the Maugis-Dugdale model

Contact is established on an area of radius $r = a$, and the adhesive forces act on the interval $r \in [a, c]$. When $r = a$ the separation between surfaces is null; when $r = c$, the separation between surfaces is h_0.

1.9 Thesis Layout

The concern of this work is the modelling of dry friction. Two approaches have been used in this thesis.

The first approach follows the classic formulation of Zhuravlev (1940) in order to develop an analytical model of dry friction for elastically non-linear materials and asperities modelled as axisymmetric bodies of revolution. In this, the formulation of contact problems for axisymmetric punches introduced by Galin (1946) has been used together with the rescaling formulae introduced by Borodich (1989). The rescaling formulae have been obtained by rigorous mathematical derivation, but they have not been used in many practical applications until now. Therefore, after a brief review of literature on the indentation of linear and non-linear materials in Chapter 2, Chapter 3 seeks to apply the rescaling method to a number of indentation experiments by spherical and nominally sharp punches and then it outlines a way to model dry friction following the argument of Zhuravlev (1940).

The second approach in this thesis is to use structural multi-scale models to simulate dry friction. Chapter 4 describes a novel way to calculate the force of friction as the energy dissipated, by different mechanisms, over the sliding distance. The method models the physical mechanisms which are specific to the length scales most relevant to dry friction. It takes into account the chemical interactions between surfaces at the atomic scale, the adhesive (van der Waals) interactions at the nano-scale, and the mechanical interlocking of asperities and their coupling at the micro and macro-scale. The assumption that the nano-asperities do not deform plastically (here called the Polonsky-Keer effect) is also used.

Chapter 5 is a critical discussion of existing dry friction models, with an emphasis on the question of whether models are multi-scale, multi-level or hierarchical. Two original models are part of the discussion, i.e. the multi-scale single-asperity model in section 5.2, and the multi-scale hierarchical model in section 5.6.

Using the formulation of the force of friction presented in chapter 4 and building on features of some models described in chapter 5, a new multi-scale, multi-level, hierarchical model is introduced in chapter 6.

Finally the conclusions to the thesis and some recommendations for future development are given in chapter 7.

(Intentionally left blank)

Chapter 2 - Contact and indentation of spheres and cones into linear and nonlinear materials

2.1 Introduction

As mentioned before, one approach to model dry friction introduced in this work follows the classic formulation of Zhuravlev (1940), which will be extended for elastically non-linear materials and asperities modelled as axisymmetric bodies of revolution. In this we will use the formulation of an axisymmetric punch introduced by Galin (1946), together with the rescaling formulae introduced by Borodich (1989). Therefore Chapter 2 will lay the theoretical ground we will later use in Chapter 3, and give a brief literature review on the contact and indentation of spheres and cones into linear and nonlinear materials.

2.2 The Linear and Nonlinear Elastic Deformation theory

For an elastic body under infinitesimal deformations, the second-order terms can be neglected and the strain-displacement relations can be written in a single equation, using index notation (Timoshenko and Goodier 1951):

$$\varepsilon_{ij} = \frac{1}{2}\left(\frac{\partial u_i}{\partial x_j} + \frac{\partial u_j}{\partial x_i}\right) \tag{2-1}$$

Equation (2-1) can also be written as a matrix (tensor):

$$\varepsilon = \begin{bmatrix} \frac{\partial u_1}{\partial x_1} & \frac{1}{2}\left(\frac{\partial u_1}{\partial x_2} + \frac{\partial u_2}{\partial x_1}\right) & \frac{1}{2}\left(\frac{\partial u_1}{\partial x_3} + \frac{\partial u_3}{\partial x_1}\right) \\ \frac{1}{2}\left(\frac{\partial u_1}{\partial x_2} + \frac{\partial u_2}{\partial x_1}\right) & \frac{\partial u_2}{\partial x_2} & \frac{1}{2}\left(\frac{\partial u_2}{\partial x_3} + \frac{\partial u_3}{\partial x_2}\right) \\ \frac{1}{2}\left(\frac{\partial u_1}{\partial x_3} + \frac{\partial u_3}{\partial x_1}\right) & \frac{1}{2}\left(\frac{\partial u_2}{\partial x_3} + \frac{\partial u_3}{\partial x_2}\right) & \frac{\partial u_3}{\partial x_3} \end{bmatrix} \tag{2-2}$$

Under the same assumptions, the state of stress on a surface at a specific point is expressed using the classic Cauchy stress tensor:

$$\boldsymbol{T}^{(n)} = \boldsymbol{n}\,\boldsymbol{\sigma} \tag{2-3}$$

In (2-3) **n** is a unity direction vector, $\mathbf{T}^{(n)}$ is the stress vector on the surface perpendicular to **n**, and

$$\sigma = \begin{bmatrix} \sigma_x & \tau_{xy} & \tau_{xz} \\ \tau_{yx} & \sigma_y & \tau_{yz} \\ \tau_{zx} & \tau_{zy} & \sigma_z \end{bmatrix} \tag{2-4}$$

The theory of non-linear elasticity often assumes that stresses are large and we cannot use equations (2-1) and (2-3) to describe strains and stresses. However, in geometrically linear models it can be assumed that strains are still small, so the small strains tensor and the Cauchy tensor can still be used.

For physically non-linear materials we can use (2-1) and (2-3), and the constitutive stress-strain relation is described by a non-linear functional $\mathcal{F}$:

$$\sigma_{ij} = \mathcal{F}(\varepsilon_{kl}) \tag{2-5}$$

If the material is elastic, then the mechanical work along the closed path is equal to zero. This means that there exists a potential (elastic energy) W and the stress-strain relation is

$$\sigma_{ij} = \frac{\partial W(\varepsilon_{kl})}{\partial \varepsilon_{ij}} \tag{2-6}$$

If $W = \frac{1}{2} C_{ijkl} \varepsilon_{ij} \varepsilon_{kl}$, then we obtain the classic equation of anisotropic Hooke's law.

The difference between a non-linear elastic behaviour and elastic-plastic material may be seen only under unloading of the material. If, when unloading, the stress-strain relation differs from the σ - ε relation for loading, the material undergoes plastic deformations (see Figure 2-1 and Figure 2-2).

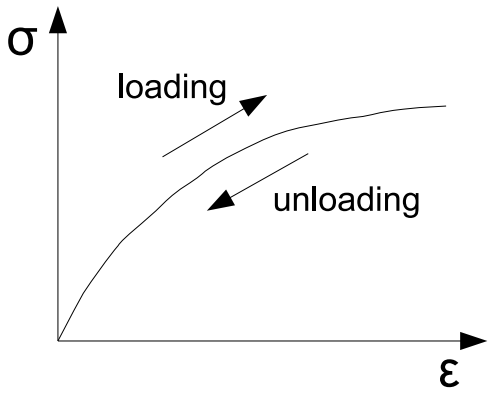

Figure 2-1 – Physically non-linear elastic relations

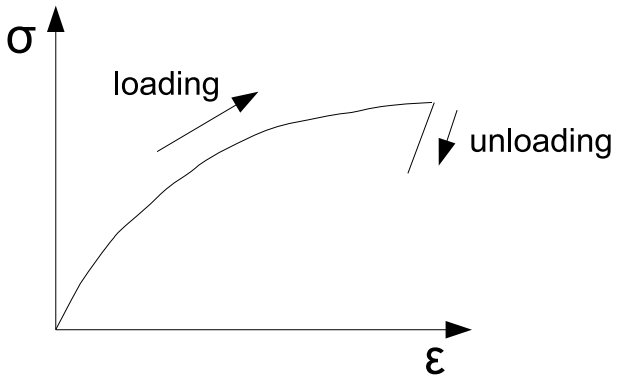

Figure 2-2 – Elastic-plastic material

If the properties of the material change with time, then it shows viscoelastic or viscoplastic behaviour, depending on whether or not it recovers after it has been stressed. If the material comes back to the initial shape, it is called viscoelastic, or hereditary-elastic. If the material does not recover, it is viscoplastic.

Strictly speaking, viscoelasticity should be described using Volterra equations. However, in the one dimensional case, the material behaviour is often modelled using Maxwell or Kelvin- Voigt spring-damper models, or combinations of the two.

2.3 Hardness tests

According to Tabor (1951), hardness can be generally defined as 'the resistance to deformation.' He continues by making the qualification that, because materials can have very different behaviours (he compares rubber with steel), it is important to specify whether we refer to the elastic or plastic deformation. Rubber is more resistant to plastic deformation than steel, but there is no doubt steel is more resistant to elastic deformation. In the case of metals, the deformation is often outside of the elastic range, and therefore the hardness of metals is primarily related to their plastic properties. Indeed, in a paper published in the same year as the famous paper presenting the well-known theory of elastic contact discussed in section 1.6, Hertz (1882b) proposes '*The hardness of a body is to be measured by the normal pressure per unit area, which must act at the center of a circular surface of pressure in order that at some point of the body the stress may just reach the limit consistent with perfect elasticity*'. However, this is a rather complicated task because, as reported by Borodich (2014), Dinnik showed in 1908 that, for a circular contact region, the first yielding point is beneath the contact surface (see Dinnik (1952)). Belyaev (1924) showed the same is true for an elliptic contact region. These findings are also confirmed by Johnson (1985). Therefore, Hertz' idea of determining the hardness of materials based on the pressure corresponding to the limit of perfect elasticity is impracticable, because this pressure is rather difficult to find experimentally.

While there are different approaches for hardness measurement, i.e. scratching, static indentation, and rebound or dynamic indentation, here we are concerned only with static indentation hardness.

Brinell (1900) introduced a hardness test based on the indentation of a hard ball in the surface of the metal. The Brinell hardness number (B.H.N.) is given by equation (2-7), where *W* is the load, *D* is the diameter of the ball, and *d* is the projected diameter of the imprint (Tabor 1951). It can be seen that the Brinell hardness number is the ratio between the load and the curved surface of the impression.

$$B.H.N. = \frac{2W}{\pi D^2 \left[1 - \sqrt{1 - \left(\frac{d}{D}\right)^2}\right]} \tag{2-7}$$

A few years later, Meyer (1908) proposed expressing the hardness as the ratio between the load and the projected area of indentation (Tabor 1951):

$$H_{Meyer} = \frac{4W}{\pi d^2} \tag{2-8}$$

The so-called Meyer scaling law was also introduced, which is an empirical formula relating the load and diameter of the imprint:

$$W = kd^n \tag{2-9}$$

In (3-2), *k* and *n* are material constants. For an analysis of Meyer's law, see Tabor (1951). A scaling law was derived by Borodich (1989) using similarity approach and is described in section 3.1.

It was Ludwik (1908) who first introduced the hardness measurement by a diamond cone indentation (Tabor 1951). He computed the hardness in a similar way to Brinell, dividing the load by the surface area of the indentation, and the Ludwik hardness number (L.H.N.) is expressed in (2-10).

$$L.H.N. = \frac{4W}{\pi D^2 \sqrt{2}} \tag{2-10}$$

But just as the Brinell hardness number, the Ludwik hardness number does not have any physical meaning. The pressure between the cone and the material imprint in the absence of friction is given by the ratio between the load and the projected area, as in the Meyer hardness (Tabor 1951):

$$H_{cone} = \frac{4W}{\pi d^2} \quad (2\text{-}11)$$

Smith and Sandland (1922) introduced the hardness tests by a diamond pyramidal indenter (Williams 1942). The shape of the indenter is a square pyramid, with an angle of 136° between the opposite faces (the Vickers indenter), which was chosen by analogy with the Brinell test; if we have a spherical indenter which penetrates the material to the depth where the impression diameter is 0.375*D,* the tangents to the sphere at the contact edges make an angle of 136° (Tabor 1951). To determine the projected area of the indentation, the diagonals are measured. If the mean value of the diagonals is *d*, the projected area is $d^2/2$. But, similarly to Brinell hardness, the Vickers hardness is the ratio between the load and the full surface of the impression. Knowing from the geometry of the pyramid that the surface of the faces is equal to the area of the base multiplied by sin(136°/2), the Vickers hardness number (V.H.N.) is expressed as (Tabor 1951):

$$V.H.N. = \frac{2W}{d^2} sin\frac{136°}{2} = 0.927\frac{2W}{d^2} \quad (2\text{-}12)$$

A special feature of the Vickers hardness number revealed by experiments is the geometrical similarity of the problem, i.e. it does not depend on the indentation size, and consequently on the load (Lea 1936).

A spheroconical indenter was introduced by Rockwell (1922), but the hardness measurement technique is quite different, as it relies on the measurement of the depth of penetration. According to Tabor (1951), there are greater chances the hardness determined based on the depth of indentation will contain errors, due to the elastic recovery of the material when load is removed.

Another pyramidal indenter has been introduced by Knoop et al. (1939). The Knoop indenter has one edge longer than the other, resulting from the different angles between the opposing faces, of 172°30’ and 130° respectively. Because of the geometry, the Knoop indentation has some specific properties (Tabor 1951). The longer diagonal of the imprint changes very little in length after the load is removed, making a more reliable basis for computing the area of indentation. On the other

hand, due to elastic recovery, the shorter diagonal of the imprint is considerably reduced in length, and can be used as a measure of the elastic properties of the indented material.

For more detailed descriptions of indenters and hardness measurement techniques, the reader can see Williams (1942), O'Neill (1934), Tabor (1951), Fischer-Cripps (2011), Herrmann (2011), or other books on hardness tests.

2.4 Depth-sensing Nanoindentation

The idea of continuously monitoring the displacement of the indenter has revolutionized material characterisation techniques. The force (P) – displacement (δ) diagram obtained has been called the 'mechanical fingerprint' of the material, due to the wealth of information it can provide (Hainsworth et al. 1996). In many cases other techniques are rather impracticable. A good example is the testing of very thin coatings, with thickness less than 1 μm, when depth sensing nanoindentation could be the only viable approach (Chen and Bull 2009).

As noted by Borodich (2014), Kalei was the first to build a depth-sensing indenter in 1966; the techniques were described in his PhD thesis and in a paper (Kalei 1968). We also find that Kalei was supervised by Khrushchov who, together with Berkovich, introduced a three sided pyramidal indenter that has the same projected area to depth ratio as a Vickers indenter, and which is now known as the Berkovich indenter (Khrushchov and Berkovich 1950). The need for this new indenter was raised by the difficulty of manufacturing a four-sided Vickers pyramid so that the sides meet in a point (Mott 1956). Because of its geometry, the Berkovich indenter allows more precise control over the indentation and for this reason it is widely used in nanoindentation testing (Fischer-Cripps 2011).

2.4.1 Evaluation of material properties by depth-sensing indentation

As was already mentioned, the $P - \delta$ diagram obtained by depth-sensing indentation can be treated as a 'mechanical fingerprint' of the material, provided it can be correctly interpreted to reveal useful properties of the studied material. As noted by Borodich (2014), Bulychev, Alekhin and Shorshorov developed a method to determine

Young's modulus from the $P - \delta$ diagram in 1975, and it was first published in Bulychev et al. (1975, 1976), Shorshorov et al. (1981). They assumed that the material has elastic behaviour during unloading, and they applied the elastic contact solution for the flat-ended punch, for a cone, and for a sphere. In all three cases they obtained the slope of the unloading curve as

$$S = \frac{dP}{d\delta} = 2aE^* \tag{2-13}$$

In (2-13) a is the contact radius and E^* is the reduced elastic modulus. Relation (2-13) was later confirmed by Pharr et al. (1992) for any body of revolution. Considering the contact area $A = \pi a^2$, another proposed form of relation (2-13) was (2-14), also known as the BASh formula.

$$S = \frac{dP}{d\delta} = \frac{2\sqrt{A}}{\sqrt{\pi}} E^* \tag{2-14}$$

Considering the expression of the reduced elastic modulus (1-18), Bulychev et al. (1976) expressed the elastic modulus for the tested material as in (2-15), which, together with (2-14), they argued is applicable to imprints with both circular and square in-plane shapes (Borodich 2014):

$$E = \frac{1 - \nu^2}{\frac{2\sqrt{A}}{S\sqrt{\pi}} - e_2}, \qquad e_2 = \frac{1 - \nu_i^2}{E_i} \tag{2-15}$$

In (2-15) E_i and ν_i are the elastic constants of the indenter.

Borodich (2014) explains that BASh formula (2-14) is a semi-empirical approximation for the exact expression (2-13), and it is a particular case of (2-16), which, as he shows, follows from the Hertz contact problem between an axisymmetric indenter and a material with rotational symmetry.

$$\frac{dP}{d\delta} = \frac{1}{2aK^*} \tag{2-16}$$

In (2-16) K^* is the reduced contact modulus of the materials. For isotropic materials, $K^* = E^*$. Relation (2-16) is valid also for nonlinear elastic uniformly prestressed solids,

when K^* is obtained by multiplying the reduced modulus E^* by a constant coefficient, and for contact between a transversely isotropic indenter and a prestressed half-space, when

$$(K^*)^{-1} = \left(E_{Transversely\ Isotropic}\right)^{-1} + \ (E_{Prestressed})^{-1}.$$

For a full treatment of the problem see Borodich (2014).

2.5 The effective shape of indenters (the Galanov effect)

The loading indentation curve has elastic-plastic behaviour, while it is generally assumed that the material recovery during unloading is purely elastic, the resulting imprint reflecting the plastic deformation of the specimen (see Figure 2-3). It was found that the plastic imprint produced by spherical indenters is spherical, with a larger radius, and conical indenters produce conical imprints, with larger half-angles (Stilwell and Tabor 1961, Tabor 1948).

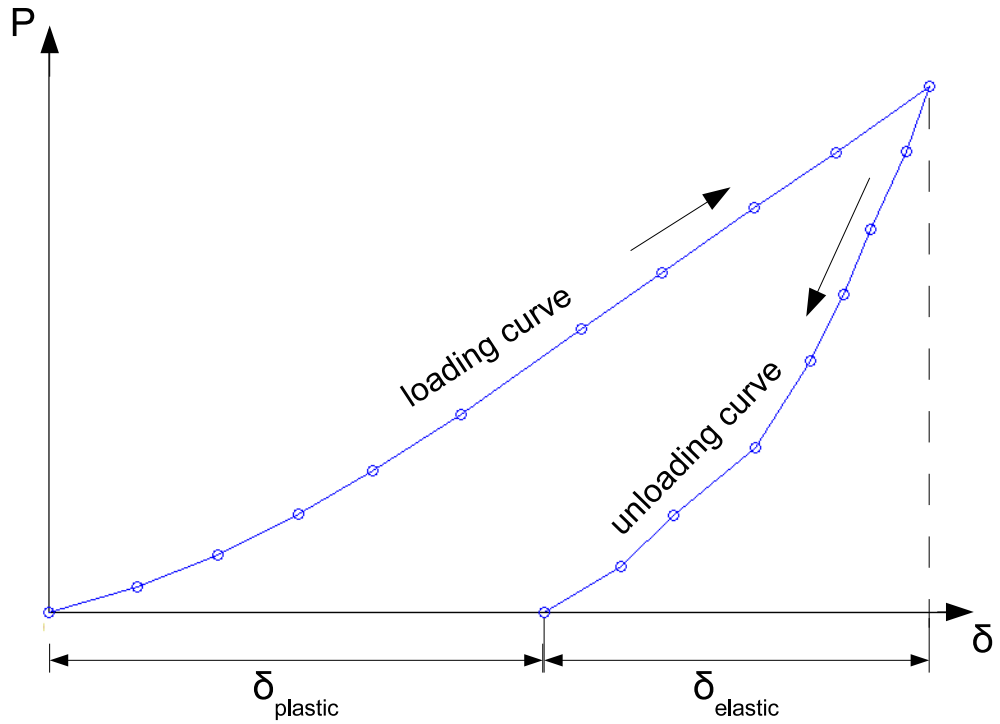

Figure 2-3 – Force-penetration diagram; experimental data from Goldsmith and Lyman (1960)

The first one to take into account the plastic imprint in indentation models was Galanov et al. (1983), (1984). They showed that, in order to account for the deformed

shape of half-space in the solution obtained by Love (1939) for a cone indentation, equation (2-17) should become (2-18).

$$P = \frac{2E^*}{\pi}\frac{1}{cot\gamma}\delta^2 \tag{2-17}$$

In (2-17), γ is the half-angle of the cone.

$$P = \frac{2E^*}{\pi}\frac{1}{cot\gamma_i - cot\gamma_f}\delta^2 \tag{2-18}$$

In (2-18), γ_i is the semi-angle of the indenter and γ_f is the semi-angle of the imprint, as Figure 2-4b illustrates.

a)

b)

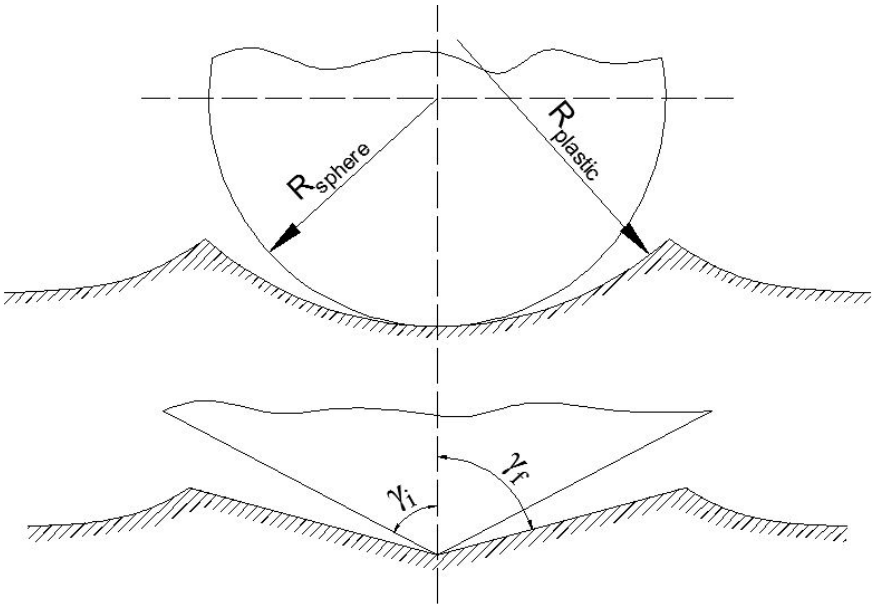

Figure 2-4 – Diagram of elastic deformation of residual imprints made by: a) a sphere, and b) a conical indenter

In the case of Galin's solution for an axisymmetric punch, $B_1 = cot\gamma$ (see section 1.6.1) becomes $B_1 = cot\gamma_i - cot\gamma_f$.

Galanov et al. (1983) considered the case of spherical indentation as well. When the contact is between a sphere and a spherical crater, the combined radius from (1-14) becomes:

$$\frac{1}{R} = \frac{1}{R_{sphere}} - \frac{1}{R_{plastic}} \tag{2-19}$$

The significance of R_{sphere} and $R_{plastic}$ in (2-19) is illustrated in Figure 2-4a.

A similar concept of an effective indenter shape was introduced much later by Pharr and Bolshakov (2002) (see also a discussion by Borodich (2011)).

2.6 Conclusions

We have seen that the small strains tensor and the Cauchy tensor can still be used in the case of non-linear elasticity, if the problem is geometrically linear. We have also seen how the depth-sensing indentation tests have followed historically from the hardness tests and the material properties they can reveal.

It has been shown that the Hertz type problem used to describe the contact between the indenter and the tested material sample is self-similar (Galanov (1981a, 1981b), Borodich (1983, 1988, 1989, 1993a)).

The rescaling approach developed by Borodich (1989, 1993a) has been obtained by rigorous mathematical derivation, but it has not been used in many practical applications until now. Therefore the next chapter seeks to apply the rescaling method to a number of indentation experiments by spherical and nominally sharp punches and then it outlines a way to model dry friction following the argument of Zhuravlev (1940).

Chapter 3 Applications of the rescaling approach to Hertz-type contact problems and indentation of materials

3.1 Introduction

Models like Zhuravlev-Greenwood-Williamson, where the asperities are modelled as spheres of the same radius, are still widely used. However, the shape of the asperities is closer to paraboloids than perfect spheres, and they have different curvatures. The current chapter proposes a straight-forward way to model the interaction between asperities whose shape is described by the revolution of a power-law curve, using rescaling methods. In the rescaling methods presented in this chapter, the contact solution for any parameter value (applied force, depth of indentation, size of indenter, radius of contact) can be found by simple algebraic calculations involving the solution for a known set of parameters. Having one experimental indentation curve, we can easily find the compressing force for any penetration between asperities and any size of the asperities involved.

3.2 Rescaling of Hertz-type contact problems

In self-similar problems the solution for any value of the parameter (force or penetration for a Hertz-type problem) can be found by elementary calculation from a known solution corresponding to another value of the parameter. Self-similarity thus presents important applications to practical problems. For example, after one has obtained experimental data from the indentation of a material with a sphere, one does not have to perform another series of experiments if the radius of the sphere is changed. For a number of indentation media the solution for the new contact conditions can be obtained by simple calculations using rescaling formulae. Self-similarity also gives the possibility of constructing numerical algorithms for contact problems. For instance, the problem of contact between two rough surfaces where the asperities are represented as spheres situated at different heights, having different radii, can be elegantly solved using rescaling methods. This is the end to which the indentation problems have been studied in the current work. However, due to time

constraints, the contact model has not been developed to the point where results could be shown, it being one of the subjects for future work.

3.2.1The mathematical justification for the rescaling of Hertz-type contact problems

As it has been mentioned above, the self-similarity of the 3D problems for indentation of isotropic elastic solids was discovered independently by Galanov (1981b, 1981a) and Borodich (1983). It was later shown by Borodich (1988, 1989, 1993a) that the self-similarity approach is valid also for non-linear anisotropic materials in both frictionless and frictional cases.

Statement of a Hertz contact problem

Borodich (1989) formulates the conditions characterizing a Hertz contact problem as follows (for simplicity, we will not formulate the conditions as a function of time, assuming the properties of the medium do not change with time):

a) The displacement vector goes to zero at infinity

$$u(\boldsymbol{x}, P) \to 0, \quad (x_1^2 + x_2^2 + x_3^2) \to \infty \tag{3-1}$$

b) In the plane $x_3 = 0$ the following boundary conditions are fulfilled:

$$\sigma_{3\beta}(x_1, x_2, 0, P) = 0, \quad (x_1, x_2) \in R^2, \quad \beta = 1, 2 \tag{3-2}$$

$$u_3(x_1, x_2, 0, P) = \delta(P) - f(x_1, x_2), \quad (x_1, x_2) \in G(P) \cup \partial G(P) \tag{3-3}$$

$$\sigma_{33}(x_1, x_2, 0, P) = 0, \quad (x_1, x_2) \in R^2 \backslash G(P) \tag{3-4}$$

$$\iint_{G(P)} \sigma_{33}(x_1, x_2, 0, P) dx_1 dx_2 = -P \tag{3-5}$$

In the above relations, $\boldsymbol{u}$ is the displacement vector, P denotes the applied force, f is the function describing the shape of the indenter, σ stresses, G denotes the contact region, and $\partial G(P)$ is the boundary of the open contact area G. $x_1x_2x_3$ is the Cartesian coordinate system, with the origin in the point of initial contact between the indenter and the half-space, and axis x_3 coinciding with the line of action of force P and directed in the depth of the indented medium.

General transformation of self-similarity

Borodich (1989) shows that, **if** the solution for the Hertz contact problem described above is known for a punch described by f_1 and a pressing force P_1 for the given set of parameters u_1, $(\sigma_{ij})_1$, δ_1, G_1, **then** the solution for pressing an indenter f with a force P is given, for any positive λ, by the following set of parameters:

$$u_i(x,P) = \lambda^{-d} u_i(\lambda x, P_1) \tag{3-6}$$

$$\varepsilon_{ij}(x,P) = \lambda^{1-d} \varepsilon_{ij}(\lambda x, P_1) \tag{3-7}$$

$$\sigma_{ij}(x,P) = \lambda^{-\mu(d-1)} \sigma_{ij}(\lambda x, P_1) \tag{3-8}$$

$$\delta(P) = \lambda^{-d} \delta(P_1) \tag{3-9}$$

$$[(x_1, x_2) \in \mathrm{G}(P)] \Leftrightarrow [(\lambda x_1, \lambda x_2) \in \mathrm{G}(P_1)] \tag{3-10}$$

$$\lambda = \left(\frac{P_1}{P}\right)^{\frac{1}{2+\mu(d-1)}} \tag{3-11}$$

For the above parameters to fulfil the conditions and be a solution for the Hertz type problem, the following must be true also:

- the relationship between the tensor of small strain ε_{ij} and the medium's displacement vector is:

$$\varepsilon_{ij}(x,t,P) = \frac{1}{2}\left[\frac{\partial u_i(x,t,P)}{\partial x_j} + \frac{\partial u_j(x,t,P)}{\partial x_i}\right] \tag{3-12}$$

- the components σ_{ij} of the stress tensor are quasi-homogeneous functions
- the function f describing the shape of the indenter is a homogeneous function of degree d, i.e. $f(kx, ky) = k^d f(x,y)$ or $f(\theta, r) = B_d(\theta) r^d$.

A full treatment of the problem can be found in Borodich (1988, 1989, 1993a, 2014).

3.2.2 Fundamental rescaling relations for indentation

As a consequence of the general self-similarity transformation described above, the following relations are valid for indentation, if the function describing the shape of the

indenter and the stress-strain relation are expressed as power-law functions (Borodich 1993a):

$$\delta(\lambda, P) = \lambda^{\frac{2-\kappa}{2+\kappa(d-1)}} \left(\frac{P}{P_1}\right)^{\frac{d}{2+\kappa(d-1)}} \delta(1, P_1) \tag{3-13}$$

$$a(\lambda, P) = \lambda^{\frac{-\kappa}{2+\kappa(d-1)}} \left(\frac{P}{P_1}\right)^{\frac{1}{2+\kappa(d-1)}} a(1, P_1) \tag{3-14}$$

Where δ is depth of indentation, a is the linear dimension of the contact region, P is the external load, and κ is the work-hardening exponent of the constitutive relationship for the material ($\sigma \sim \varepsilon^{\kappa}$). Parameter λ reflects any change in the shape of the indenter. If the indenter is spherical, then

$$\lambda = \frac{R_1}{R_2} \tag{3-15}$$

where R_1 is the effective radius for the known solution of the contact problem and R_2 is the new effective radius. For conical and pyramidal indenters

$$\lambda = \frac{cot(\gamma_1)}{cot(\gamma_2)} \tag{3-16}$$

where γ_1 and γ_2 are the half angles of the shape of the indenter for the known and required solution, respectively. If no change is produced to the geometry of the indenter then, obviously, $\lambda = 1$. For the particular case of a spherical indenter (d=2), by substituting (3-15) in (3-13) and (3-14), we obtain (Borodich 1989):

$$\delta(P, R_1) = \left(\frac{R_1}{R_2}\right)^{\frac{2-\kappa}{2+\kappa}} \left(\frac{P}{P_1}\right)^{\frac{2}{(2+\kappa)}} \delta(P_1, R_1) \tag{3-17}$$

$$a(P, R_2) = \left(\frac{R_2}{R_1}\right)^{\kappa/(2+\kappa)} \left(\frac{P}{P_1}\right)^{\frac{1}{2+\kappa}} a(P_1, R_1) \tag{3-18}$$

3.3 The influence of the indenter bluntness and strain hardening index on the force-displacement diagrams

It is well known that all nominally sharp indenters have tips which are not perfectly sharp but are rounded, due to manufacturing difficulties. Furthermore, the tips of such indenters become blunter when they are used. For example, Bull (2002) reports the tip radius of a Berkovich indenter, being ~50nm when new, increased 1nm per 50 performed indentations, over a period of 6 months. The deviations from the ideal shape can therefore be important and taking them into account is essential when trying to describe experimental data.

For the purpose of illustrating how the bluntness of the indenter influences the P-δ curve, we will plot the loading indentation curve for a material having Young's modulus E = 204 GPa and Poisson's ratio ν = 0.286. The value of the work hardening index κ is set to 0.9 and the value for the bluntness varies from 1.0 (cone) to 2.0 (sphere), with an increment of 0.1. The resulting curves are shown in Figure 3-1. It can be clearly seen that, for blunter indenters, the indentation curve becomes steeper, greater force being necessary to reach the same indentation depth.

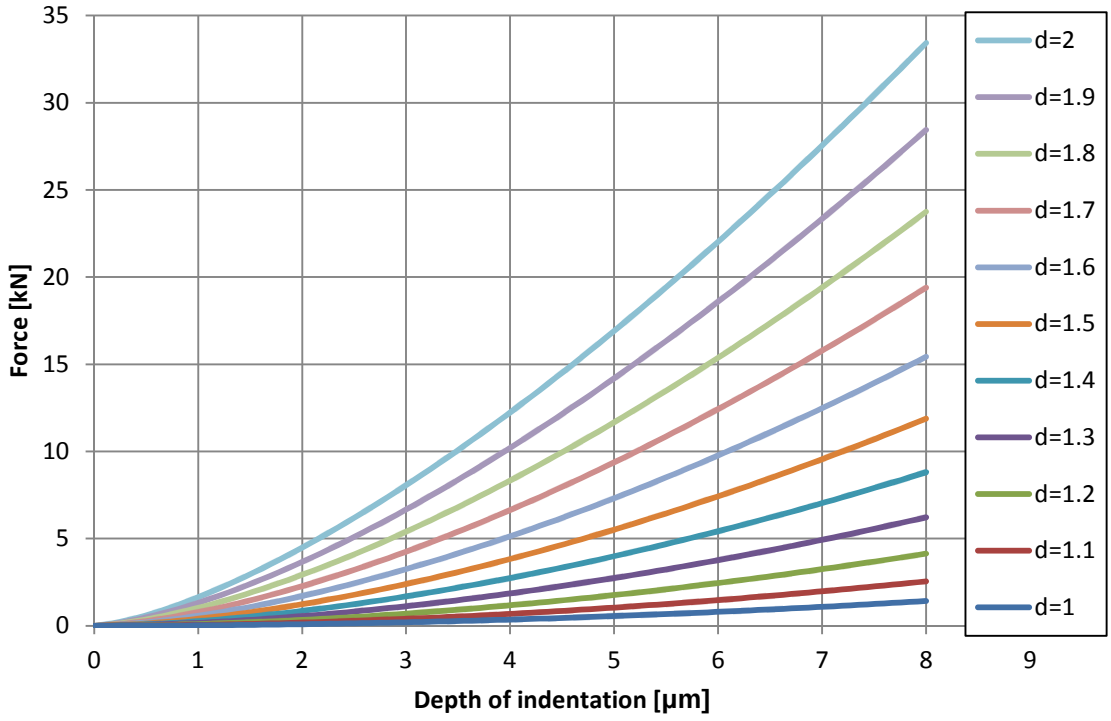

Figure 3-1 – Influence of the tip bluntness on the P-δ curve, with bluntness index varying from d=1 (cone) to d=2 (sphere)

To study the influence of the strain hardening index on the *P-δ* curve, a similar exercise is shown in Figure 3-2. The curves are obtained for *κ* taking values from 0.1 to 1, with an increment of 0.1, while the value of the bluntness index is fixed to *d*=2. It is evident that the indentation curves for softer materials (with lower values for *κ*) are less steep, requiring a smaller force to achieve the same depth of penetration.

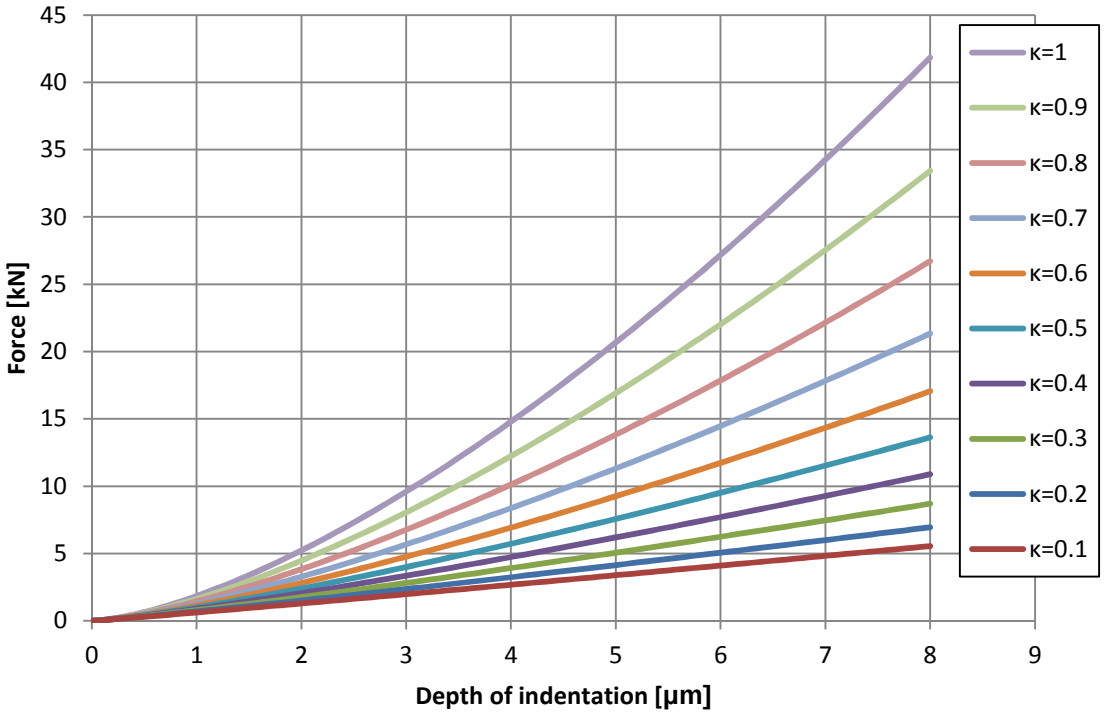

Figure 3-2 – Influence of the hardening exponent on the P-δ curve, varying from κ=0.1 to κ=1

One can see that both the shape of the indenter (asperity) and the hardening index *κ* may have a great influence on the force-displacement diagram of contacting surfaces.

3.4 Applications to Experimental Data

It is important to note that although the Borodich rescaling formulae (3-13) and (3-14) follow from rigorous mathematical analysis of contact problems, the formulae are not universal. The rescaling methods described above are valid if the indenter and the indented material are either made of the same material (and have the same *κ* in the approximation), or one of them has to be significantly harder than the other, so that it can be assumed that it is not deformable (rigid). If one material is described by $\sigma_1 \propto \varepsilon_1^{\kappa_1}$ and the counterpart is described by $\sigma_2 \propto \varepsilon_2^{\kappa_2}$, the method is not applicable.

3.4.1 The method used

Let us divide the P - δ indentation curve in two branches and discuss them separately, as they will be modelled using different methods. In the loading branch the material goes through elastic and plastic deformation, so we will use the rescaling method described above to fit the experimental data.

In order to use the rescaling method, two parameters have to be known: the bluntness index and the hardening exponent. In some cases we know the value of one of these parameters. For example, when it is assumed the unloading branch reflects the recovery of the elastic deformation, we know κ = 1, for any material with the constitutive curve $\sigma \sim \varepsilon^{\kappa}$. Knowing κ = 1, we can extract the value for the bluntness factor d from the experimental data and use it for the loading branch. Another case when one of the parameters is known is the case of spherical indentation for which d = 2. We can then easily extract the value of the strain hardening index from the experimental loading branch.

Let us exemplify how the rescaling formulae may be applied to describe an experimental indentation curve.

A. Taljat et al. (1998): spherical indentation of A533-B steel

Here we will use the experimental data from Taljat et al. (1998), shown in Figure 3-3, without engaging with the argument of their paper. Let us then apply the rescaling approach on the indentation of A533-B steel experiment. The authors specify the indenter is a 1.576mm diameter tungsten carbide spherical indenter. We will use a value of 600*GPa* for the elastic modulus (AZO Materials 2000). The elastic modulus of the A533-B steel was 210GPa with a Poisson's ratio of 0.3.

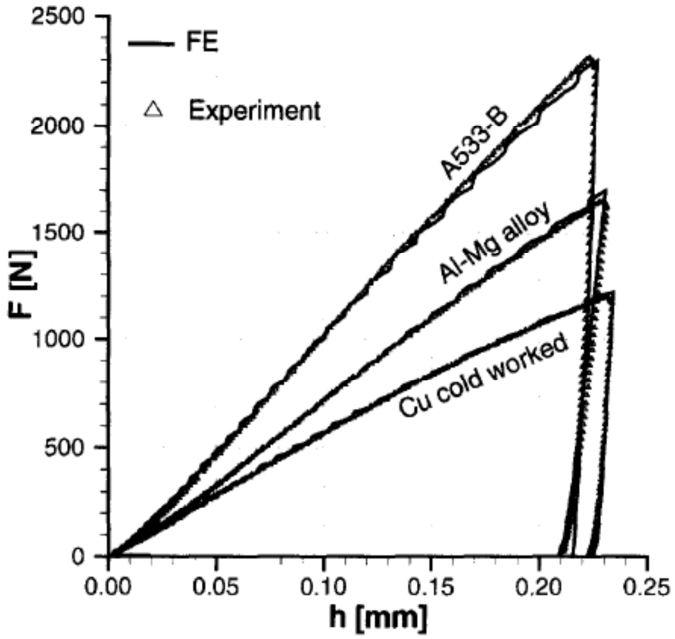

Figure 3-3 – Comparison between FE and experimental results in Taljat et al. (1998)

The result of trying to fit the experimental data for the indentation of A533-B steel is shown in Figure 3-4. Let us explain how these curves have been obtained.

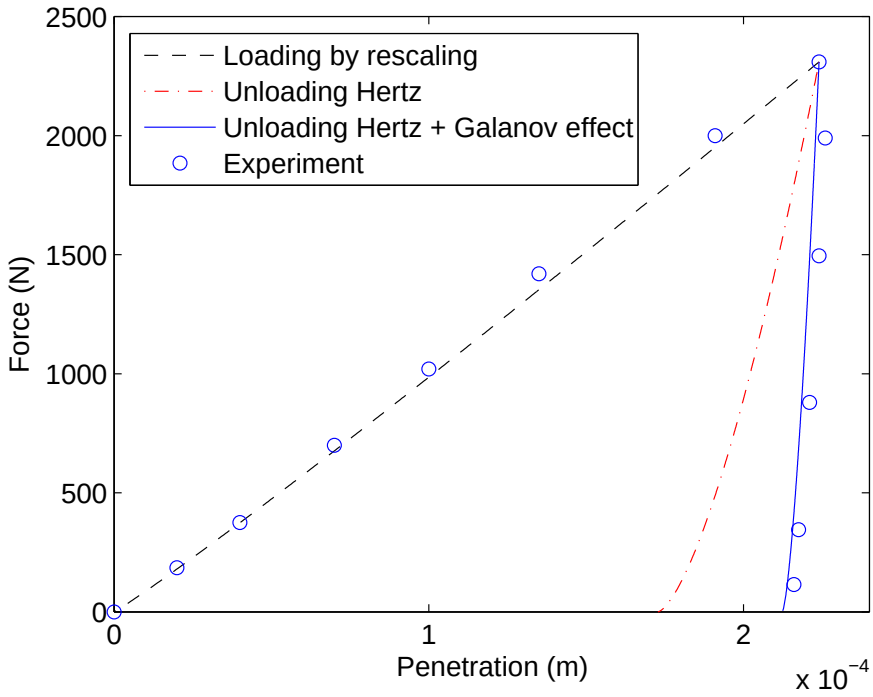

Figure 3-4 –Fitting the experimental results in Taljat et al. (1998) for A533-B steel by rescaling formulae and Hertz contact theory

Loading branch

For the loading branch relation (3-17) has been used. We assume the geometry of the indenter does not change during loading, so the ratio R_1/R_2 = 1. Expressing force P in terms of penetration δ, the relation becomes:

$$P = \left(\frac{\delta}{\delta_1}\right)^{\frac{2+\kappa}{2}} P_1 \tag{3-19}$$

In the above formula, P_1 and δ_1 are the parameters of the known contact solution. We assume the known contact solution is the maximum point of indentation where P_{max} = $2.31kN$ and δ_1 = $0.224mm$. The value of κ can be obtained from a log-log representation of the experimental data for the loading branch. If we take logarithm of both sides of (3-19), we get:

$$\log P = \frac{2+\kappa}{2} \log\left(\frac{\delta}{\delta_1}\right) + \log P_1 \tag{3-20}$$

So, if we plot the experimental data for the loading branch in logarithmic coordinates and fit it by a straight line (see Figure 3-5), the slope of the line will be $\frac{2+\kappa}{2}$, from which we can easily calculate κ, as shown in (3-21).

$$\frac{2+\kappa}{2} = 1.056 \rightarrow \kappa = 0.112 \tag{3-21}$$

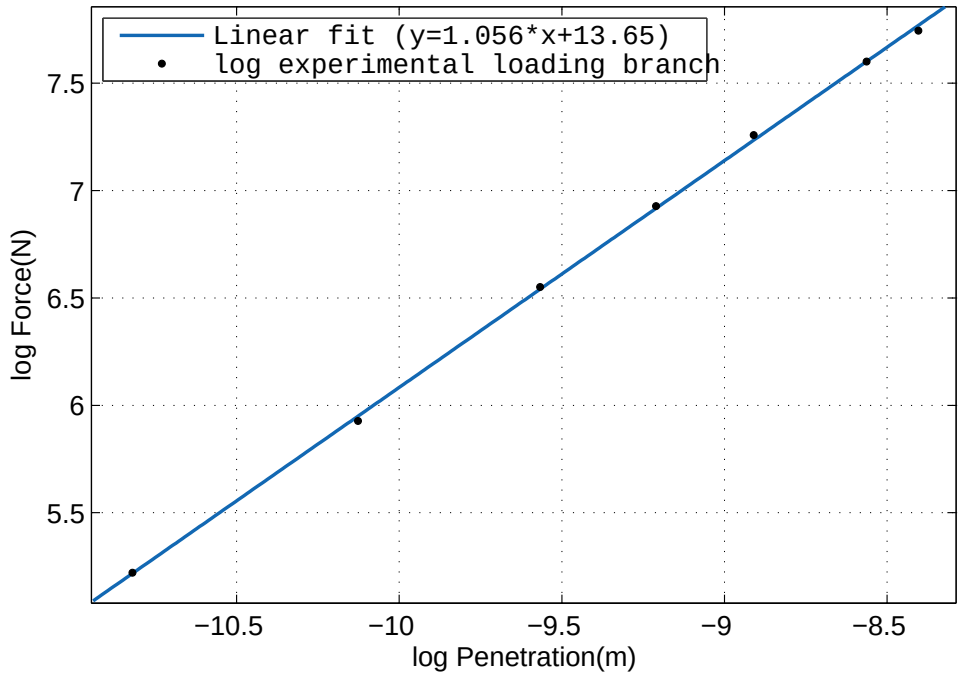

Figure 3-5 – Finding the strain hardening index for the indentation loading branch

It should be mentioned that the value obtained for κ as described above (κ=0.11) is very close to the value of κ=0.15, that is obtained by fitting the stress-strain curve for the indented material by a power law function (see Figure 3-6).

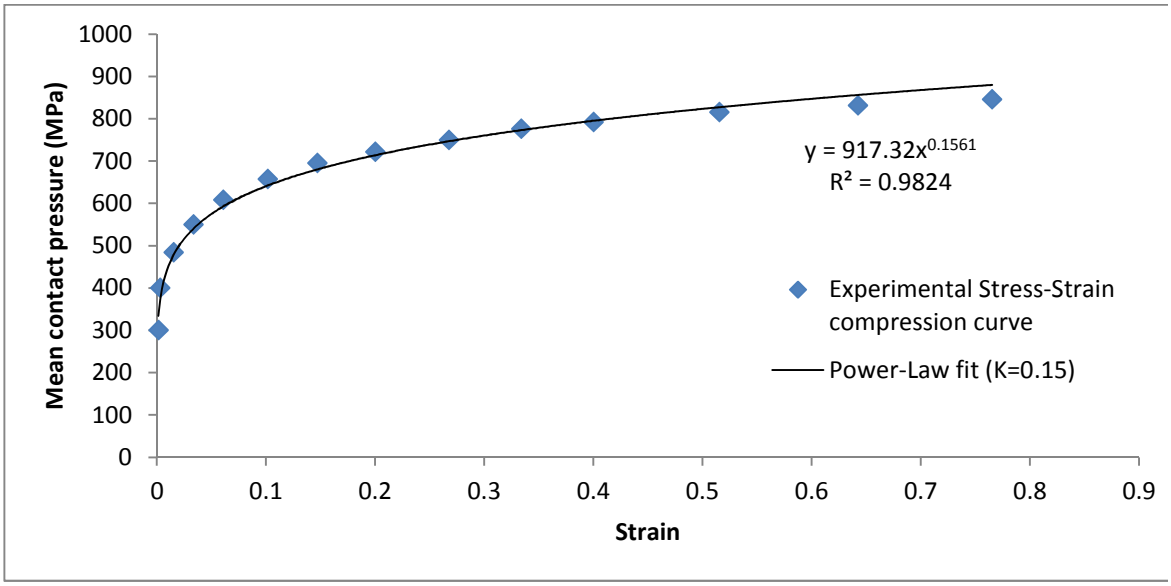

Figure 3-6 – Power law fitting of the experimental stress-strain curve for A533-B steel as given by Taljat et al. (1998)

Unloading branch

Figure 3-4 shows that the Hertz equation for an initial punch does not describe the unloading branch of the experiment very well, even though unloading is elastic. We assume the reason for the disagreement is the Galanov effect. That is, because the material does not recover fully after the plastic deformation, the unloading branch of the indentation becomes like the contact between a sphere and a negative radius (concave) sphere. So, after we find the solution for the unloading branch using Hertz solution, we use the rescaling relation (3-17) with $\kappa = 1$ (linear elasticity) to find the new effective radius:

$$R_2 = R_1 \left(\frac{P}{P_1}\right)^2 \left(\frac{\delta_1}{\delta}\right)^3 \tag{3-22}$$

Substituting the effective radius R_2 in the obtained Hertz solution, we obtain the unloading branch taking into account the Galanov effect, as shown in Figure 3-4. We can find the radius of the deformed medium from:

$$\frac{1}{R_2} = \frac{1}{R} - \frac{1}{R_{medium}} \tag{3-23}$$

For the experiment under discussion with an indentation sphere of radius R = 0.788mm, the calculated radius of the deformed shape of the indented medium is R_{medium} = 0.798mm.

3.5 Comparison with experimental results

Let us examine a few more experiments found in literature and try to describe them in the manner explained above. The indentation by a sphere and the indentation by a sharp die will be addressed separately.

3.5.1 Spherical indenter

B. *Taljat et al. (1998): spherical indentation of Al-Mg alloy*

The same spherical indenter is used in all 3 indentation experiments presented in Taljat et al. (1998). The diameter of the indenter is 1.576mm and it is made of tungsten carbide (E = 600GPa, ν=0.2). The elastic modulus of the indented Al-Mg alloy was 70GPa and the Poisson's ratio was 0.3. The calculated radius of the deformed shape of the indented medium is R_{medium} = 0.816mm (for an indenter radius of 0.788mm). The

loading curve obtained by rescaling from the solution for the maximum point of indentation (P_{max} = 1.65kN and δ_{max} = 0.23mm) with κ = 0.18 is shown in Figure 3-7.

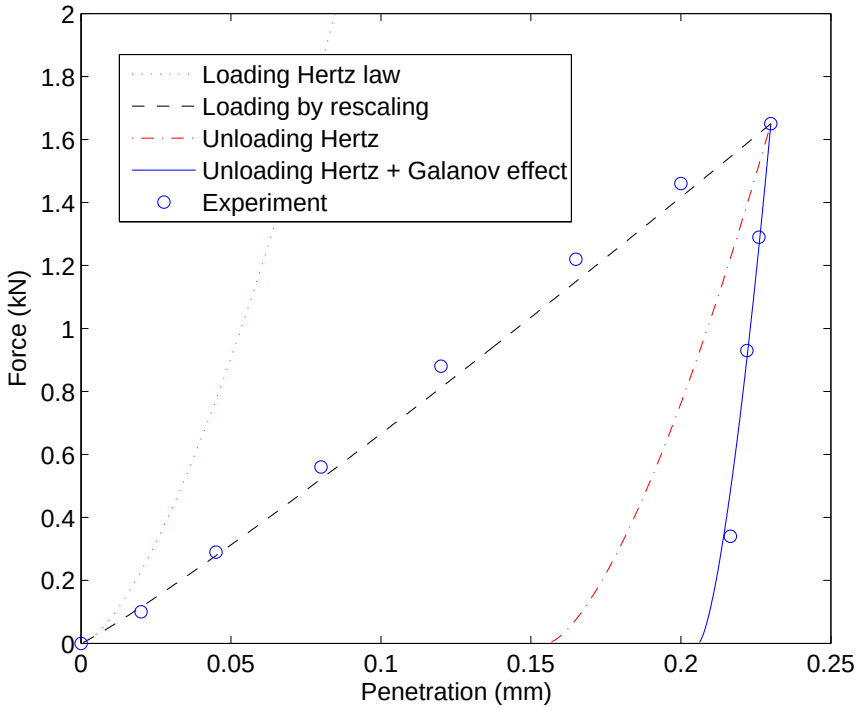

Figure 3-7 - Fitting the experimental results in Taljat et al. (1998) for Al-Mg alloy by rescaling formulae and Hertz contact theory

The value κ=0.18 obtained from the slope of the loading branch of the experiment in logarithmic coordinates is confirmed by the value that is obtained by fitting the experimental stress-strain curve of the material by a power-law function ($\sigma \sim \varepsilon^{K}$), as it can be seen in Figure 3-8.

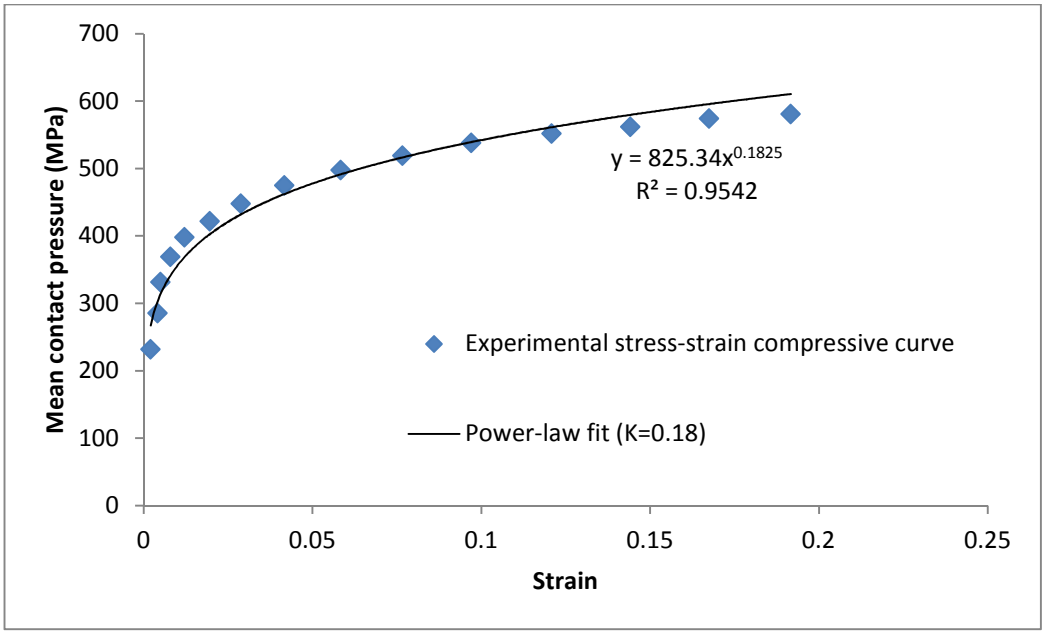

Figure 3-8 - Power law fitting of the experimental stress-strain curve for Al-Mg alloy as given by Taljat et al. (1998)

C. Taljat et al. (1998): spherical indentation of Cold-worked Cu

The characteristics of the materials involved in the experiments are as follows:

- Indenter: tungsten carbide (E = 600GPa, v=0.2), spherical, R = 0.788mm.
- Indented medium: Cold-worked Cu (E = 117GPa, v=0.3), as given by Taljat et al. (1998).

The calculated radius of the deformed shape of the indented medium on the unloading branch is $R_{medium} = 0.794mm$.

The loading curve obtained by rescaling from the solution for the maximum point of indentation ($P_{max} = 1.21kN$ and $\delta_{max} = 0.234$mm) and $\kappa = 0.0318$ is shown in Figure 3-9.

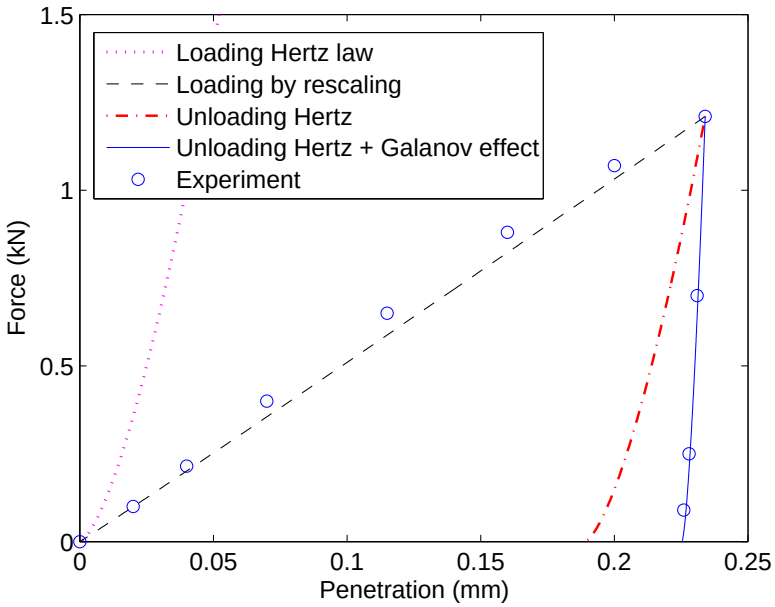

Figure 3-9 - Fitting the experimental results in Taljat et al. (1998) for cold-worked Cu by rescaling formulae and Hertz contact theory

As for the previous two cases, the value of the strain hardening index (κ) obtained from the slope of the loading branch of the experiment in logarithmic coordinates is confirmed by the value that is obtained by fitting the experimental stress-strain curve of the material by a power-law function ($\sigma \sim \varepsilon^{\kappa}$). Indeed, the experimental loading branch showed κ=0.0318 and the fit of the experimental compressive stress-strain curve showed κ=0.0311, as it can be seen in Figure 3-10.

We have seen that, for all the experiments performed by Taljat et al. (1998), there is very good agreement between the κ value extracted from the experimental data using the rescaling formulae, and the κ value obtained by fitting the experimental stress-strain curve for the indented materials. However, strictly speaking, these experiments are outside of the assumptions of the rescaling method presented by Borodich (1983), because the materials involved are non-linear and distinct. The method is mathematically justified if the indenter and the indented medium are made of the same material, or one of them is not-deformable (rigid). We assume the reason that the theory describes the experiment so well is that there is a large enough difference between the hardness of the indenter and the hardness of the indented materials to assume the indenter is not-deformable. In terms of elastic modulus, the ratios

between the properties of the indenter and the indented materials are of about 3:1 for steel, 8:1 for Al-Mg, and roughly 6:1 for cold-worked Cu.

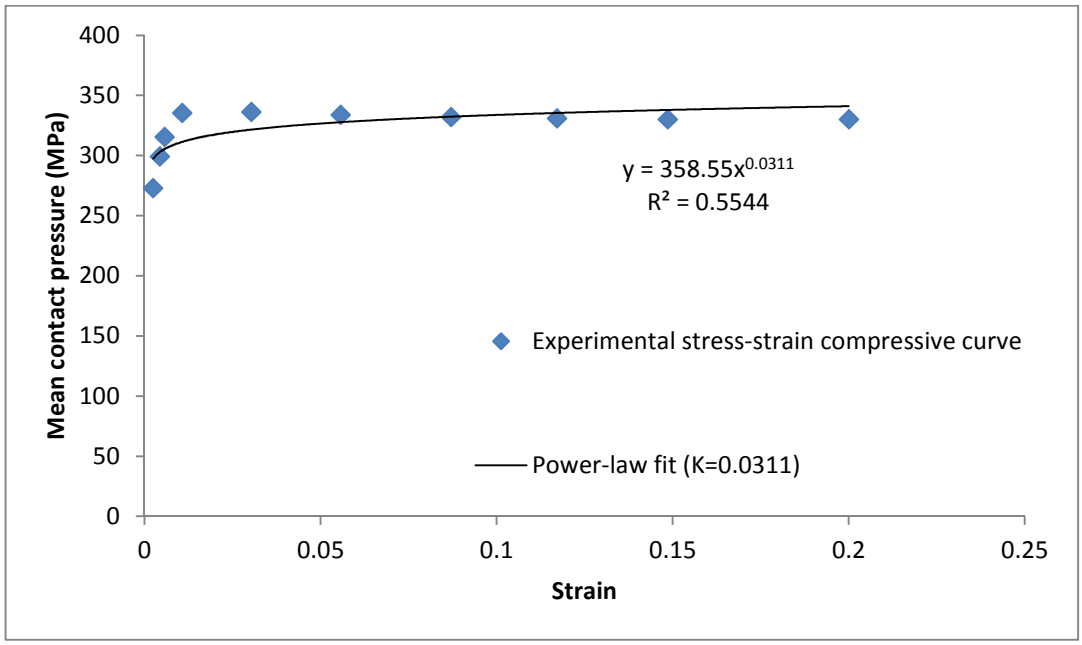

Figure 3-10 - Power law fitting of the experimental stress-strain curve for cold-worked Cu as given by Taljat et al. (1998)

D. Harsono et al. (2011): spherical indentation of Aluminium 7075

The spherical indentation experiments in Harsono et al. (2011) were performed using a diamond indenter with a tip radius of 5µm. The authors do not provide information about the mechanical properties of the indenter or of the indented materials. In the finite element analyses that Harsono et al. conduct to explain the experiments, they adopt the material properties of Al7075 (E = 70.1GPa, ν=0.33) used by Dao et al. (2001), that we will also use. For the diamond indenter, we use elastic modulus E = 1200Gpa and Poisson's ratio ν = 0.2 (Klein and Cardinale 1992, Spear and Dismukes 1994).

The unloading branch of the indentation test showed a radius of the deformed shape of the specimen equal to R_{medium} = 5.79µm (Figure 3-11).

The loading branch was obtained by rescaling from the maximum indentation point for a value of κ = 0.05 for the hardening index. It has to be mentioned that this value was extracted considering only the last 4 points of the experimental loading branch (see Figure 3-11). The reason for this is that points 2-4, counting from the origin, slightly

deviate from the general trend of the curve. This is reflected in all the spherical indentation experiments performed by Harsono et al. (2011), and they explain it by the presence of a thin oxide layer formed on the surface of the specimens. This explanation seems to be confirmed by the fact that the loading indentation curves have a greater deviation when indenting Cu than when indenting Al7075 (compare the experimental loading branches in Figure 3-12 to the ones in Figure 3-13), due to the thicker oxide layer that is easier to form on Cu than on Al7075. Furthermore, there is no apparent deviation in their Berkovich indentation experiments, as one will be able to see in Figure 3-14, due to the fact that it is easier for a sharper indenter to cut through the oxide layer, as Harsono et al. make the case.

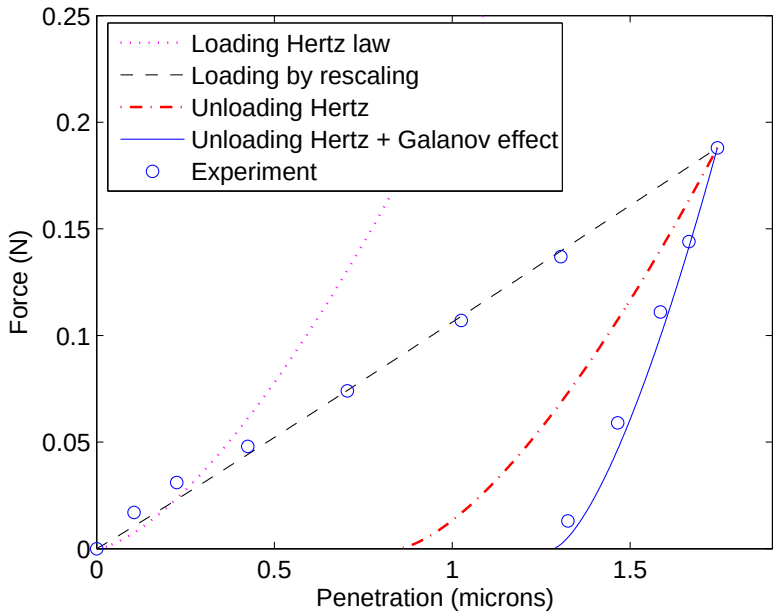

Figure 3-11 - Fitting the experimental results in Harsono et al. (2011) for Al7075 by rescaling formulae and Hertz contact theory

The experiments presented in Figure 3-12 to Figure 3-14 show a plateau at the end of the loading branch that is due to the fact that, before unloading, the indenter was held under the same force for a time and therefore some time-dependent (viscoelastic or viscoplastic) effects could be observed. It is interesting to note that this effect was observed in the first-ever paper on depth sensing indentation (Kalei 1968). When describing the experiment (Figure 3-11) using the rescaling methods, the plateau was removed by shifting the unloading branch. Alternatively, we could have used two points in our rescaling approach: one for the loading branch (for instance, the

maximum indentation point on the loading branch) and a different one for the unloading branch (for instance, the maximum indentation point on the unloading branch). This does not affect the agreement between the experimental data and the results obtained by rescaling.

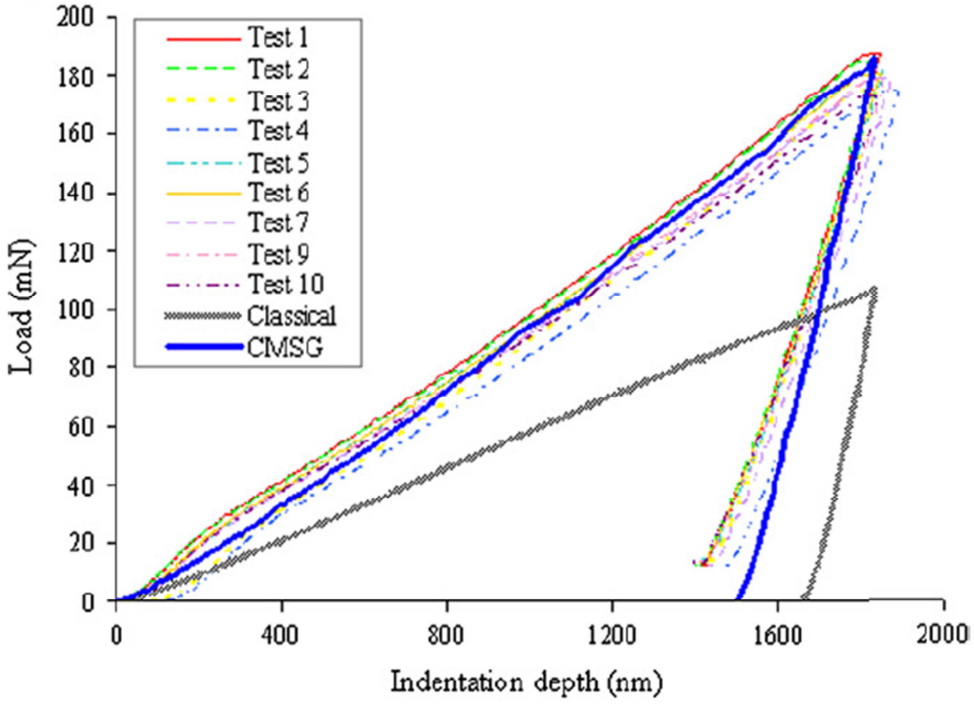

Figure 3-12 - Test results using spherical indenter tip for Al7075 in Harsono et al. (2011)

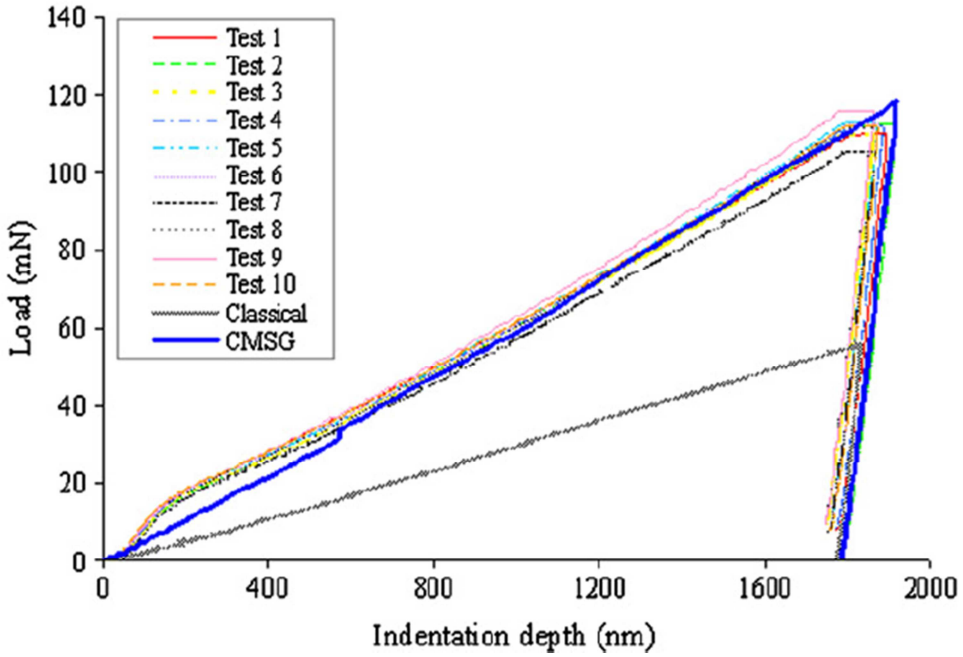

Figure 3-13 - Test results using spherical indenter tip for Cu in Harsono et al. (2011)

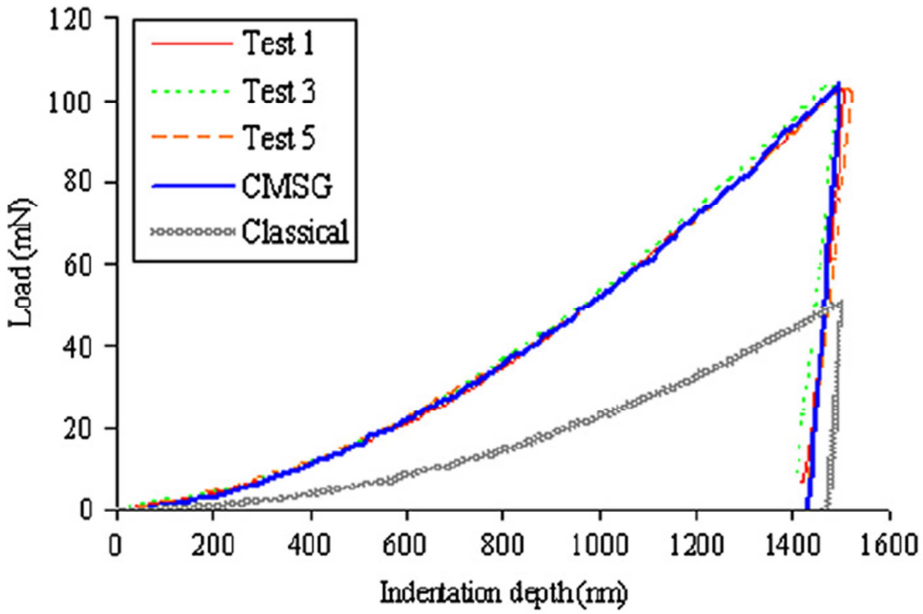

Figure 3-14 - Test results using Berkovich indenter tip for Ni in Harsono et al. (2011)

E. Harsono et al. (2011): spherical indentation of Copper

The indentation test of Cu was performed using the same indenter as described for the previous experiment (diamond indenter with a tip radius of 5µm), and the same mechanical properties will be used (E = 1200Gpa and ν = 0.2), based on Spear and Dismukes (1994). We will use the same elastic modulus of the Cu specimen that Harsono et al. say they adopt from (Qiu et al. 2003), i.e. E = 109.2GPa. However, this value is not to be found in the paper they refer to.

We can see that the results obtained using the rescaling formula for the loading branch and the Hertz solution taking into account the Galanov effect for the unloading branch are in satisfactory agreement with the experiment (Figure 3-15). The unloading branch of the indentation test showed a radius of the deformed shape of the specimen equal to R_{medium} = 5.123µm.

The loading branch was obtained by rescaling from the maximum indentation point for a value of κ = 0.024 for the hardening index. In the same way as above, this value was extracted considering only the last 4 points of the experimental loading branch, and the deviation at the beginning of the experimental loading curve was neglected. Harsono et al. explain this deviation through the existence of an oxide layer on the surface of the specimen, as explained at greater length in the description of the previous experiment, at point D.

As was done for the previous experiment, the unloading branch was shifted to remove the plateau due to holding the indenter under the maximum load before unloading, visible in the experimental curves in Figure 3-13.

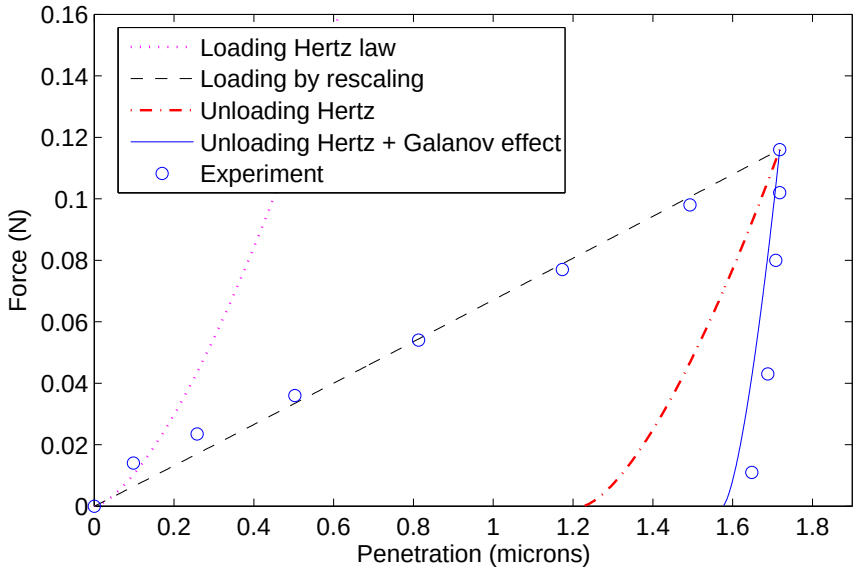

Figure 3-15 - Fitting the experimental results in Harsono et al. (2011) for Cu by rescaling formulae and Hertz contact theory

F. Goldsmith and Lyman (1960): spherical indentation of Al1100F

The spherical indentation experiments in Goldsmith and Lyman (1960) were performed using a hard-steel sphere with a diameter of 0.5in (R=6.35mm). The only mechanical property of the indenter provided by the authors is the hardness of 67 Rockwell C. We use the following values for the elastic modulus and Poisson's ratio: E = 200GPa, ν=0.3. However, they measure the mechanical properties of the tested specimens; for Al1100F, the given values are E = 73GPa (10.6 x 10^6psi), ν=0.33 and a hardness of 24 Rockwell B.

Discussion

In order to find the strain hardening index for the loading branch, we represent the experimental loading branch in logarithmic coordinates and fit it by a straight line (see Figure 3-16). As shown in section 3.4.1, the slope of this line is equal to $\frac{2+\kappa}{2}$, as follows from the rescaling formulae (equation (3-20), from which we can find the value of κ. However, for the experiment under consideration, one can see that the resulting κ is negative ($\kappa = 2 \text{ x } 0.766 - 2 = -0.467$), which does not have any physical meaning.

This is because we are outside of the applicability of the rescaling theory. As mentioned before, the rescaling formulae may be used if the indenter and the indented material are either made of the same material, or one of them is significantly harder than the other (so that we could assume one is not deformable, as was possible for experiments at points A to E). However, in the current experiment the materials involved in contact are nonlinear and have different properties. This issue will be discussed again in section 3.6. In such cases we will show the rescaling curve for several values of κ, trying to plot the best fit of the experimental data. It should be mentioned that this is the case only for the loading branch of the experiment, as the unloading is assumed to be totally elastic ($\kappa = 1$).

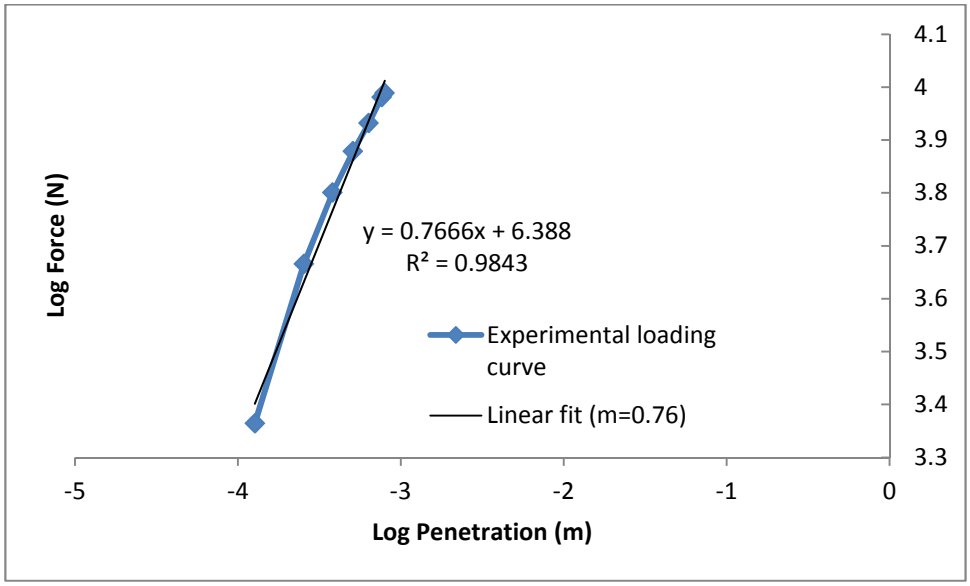

Figure 3-16 - Indentation loading branch in logarithmic coordinates, for Al1100F, from Goldsmith and Lyman (1960)

The loading curve was plotted using the rescaling approach for κ = -0.5, 0.05, 0.35 (Figure 3-17). The negative value of the strain hardening index has no physical meaning and the curves for the positive values are quite far from the experimental data.

The unloading branch was described by Hertz' solution, taking into account the Galanov effect for a radius of the surface of the specimen R_{medium} = 6.38mm (compared to the original radius of the indenting sphere R = 6.35mm). We can see that the difference between the radius of the deformed shape of the surface and the radius of the undeformed sphere is very small, suggesting the indented specimen is very plastic.

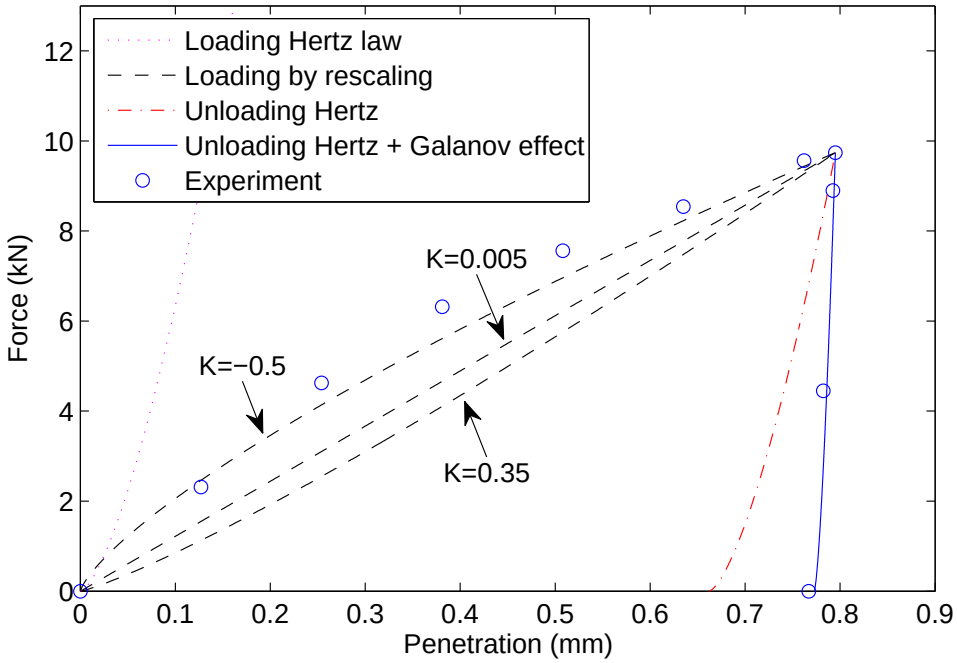

Figure 3-17 - Fitting the experimental results in Goldsmith and Lyman (1960) for Al1100F by rescaling formulae and Hertz contact theory

G. Goldsmith and Lyman (1960): spherical indentation of partially annealed tool steel

The characteristics of the materials involved are as follows:

- Indenter: hard-steel sphere with a diameter of 0.5in (R=6.35mm), E = 200GPa, ν=0.3, 67 Rockwell C hardness.
- Specimen: partially annealed tool steel (E = 204GPa, ν=0.286, 17-32 Rockwell C hardness).

The interpretation of the given experimental loading data using the rescaling formula (3-20) gives a strain hardening index κ = 0.28, and the resulting curve is plotted in Figure 3-18. Unlike the previous experiment where we have obtained a negative value for κ without any physical meaning, here we have a good agreement between the loading curve resulted by rescaling (κ = 0.28) and the experimental data. The explanation for this is that the characteristics of the materials for the indenter and the specimen are virtually the same, even though non-linear, which is within the bounds of the mathematical framework of the rescaling problem.

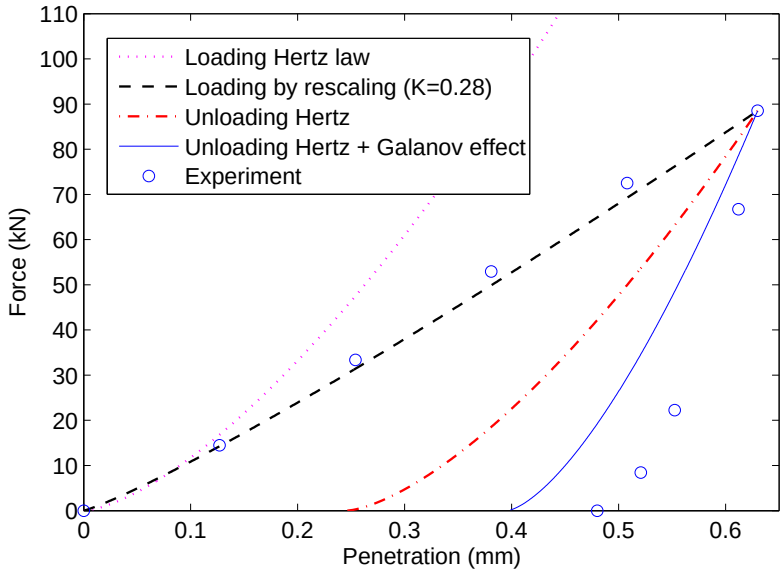

Figure 3-18 - Fitting the experimental results in Goldsmith and Lyman (1960) for partially annealed tool steel, by rescaling formulae and Hertz contact theory

We can see in Figure 3-18 that, in this case, the Hertzian theory produces an unloading curve with a considerable deviation from the experimental data, and even taking into account the deformation of the surface of the specimen (Galanov effect) does not completely rectify it. The calculated radius of the deformed surface was R_{medium} = 8.22mm, compared to the 6.35mm radius of the indenter. This shows the indented steel is less compliant than the specimen in the previous experiment which was made of a softer material (Al1100F, R_{medium} = 6.38mm).

H. Goldsmith and Lyman (1960): spherical indentation of quench-hardened tool steel

The characteristics of the materials involved are as follows:

- Indenter: hard-steel sphere with a diameter of 0.5in (R=6.35mm), E = 200GPa, ν=0.3, 67 Rockwell C hardness.
- Specimen: quench-hardened annealed tool steel (E = 204GPa, ν=0.286, 60-64 Rockwell C hardness).

The interpretation of the given experimental loading data using the rescaling formula (3-20) gives a strain hardening index κ = 0.69, and the resulting curve is plotted in Figure 3-19. It can be seen that there is a satisfactory agreement with the experimental data for the loading branch.

Let us also notice that the Hertz solution for the loading branch is closer to the experimental data for this indentation case, compared to the previous experiments. A reasonable explanation could be that, being a harder material, this specimen suffers less deformation, thus being closer to the assumptions of Hertz theory. Indeed, the radius of the deformed surface is 24.04mm, which is quite large compared to the radius of the indenter (6.35mm) and to the radius of the deformed surface for the previous indentation test of annealed steel (8.22mm).

However, it is evident that, for unloading, there is a great deviation from the experimental data, even when taking into account the deformation of the indented specimen.

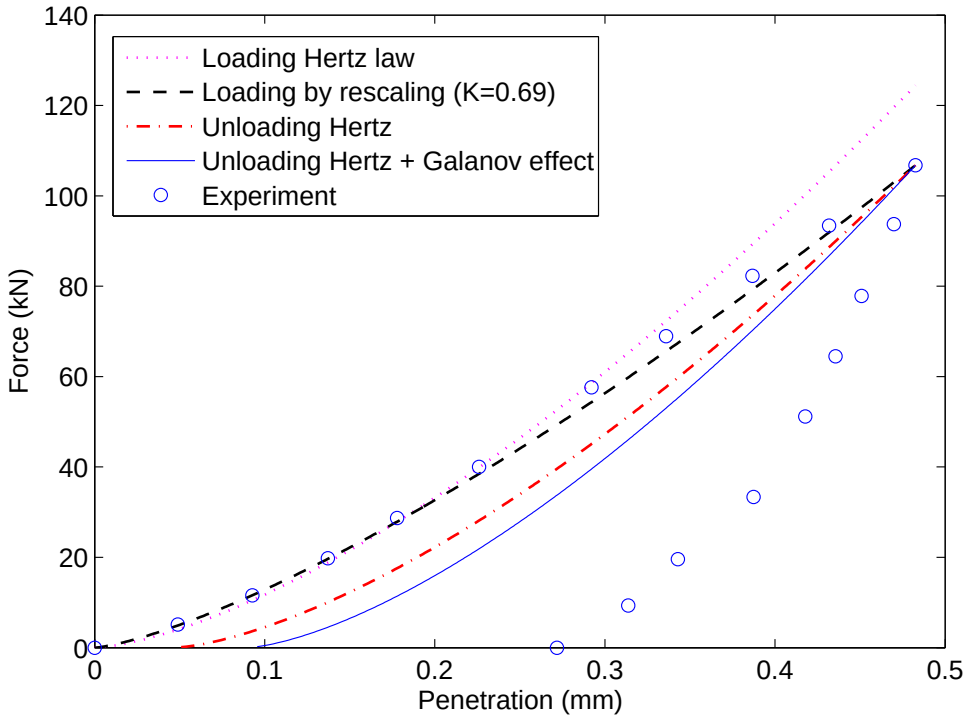

Figure 3-19 - Fitting the experimental results in Goldsmith and Lyman (1960) for quench-hardened tool steel, by rescaling formulae and Hertz contact theory

I. Bartier et al. (2010): spherical indentation of AISI 1035 spheroidized steel

Bartier et al. (2010) carried out experimental indentation tests on spheroidized steels. The AISI 1035 steel was treated under the temperature of 710°C for 10 hours, from an initial normalized state. The same treatment was applied to the AISI 1065 and AISI 4135 steels that will be analysed in the following sections. The mechanical properties

provided by the authors are E = 210GPa and ν = 0.3 for the indented steel, and E = 600GPa and ν = 0.28 for the tungsten carbide spherical indenter of radius R = 1.25mm.

There is a good agreement between the rescaling theory and the experimental points for this indentation test, as it can be seen in Figure 3-20. The rescaling approach was applied for a strain hardening index κ = 0.224, extracted from the experimental loading curve. The point from which the solution was obtained by rescaling was the maximum indentation point (in this case, P = 920.8N and δ = 0.1033mm), as for all the experiments described in the present work.

For the unloading branch of the experiment, a radius of 1.27mm was calculated.

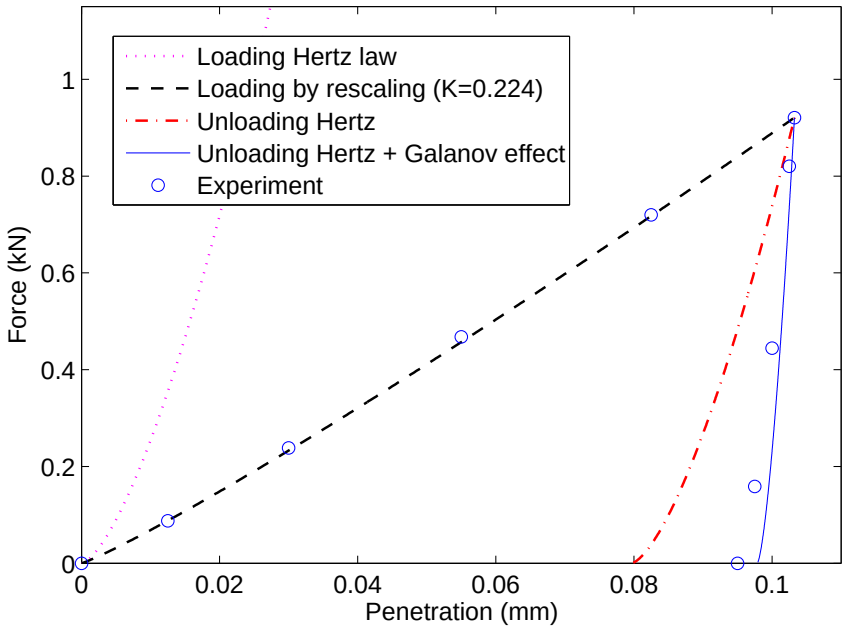

Figure 3-20 - Fitting the experimental results in Bartier et al. (2010) for AISI 1035 steel, by rescaling formulae and Hertz contact theory

J. Bartier et al. (2010): spherical indentation of AISI 1065 spheroidized steel

The characteristics of the materials involved are as follows:

- Indenter: tungsten carbide spherical indenter, R = 1.25mm, E = 600GPa, v=0.28.
- Specimen: AISI 1065 spheroidized steel, E = 210GPa, v=0.3.

The rescaling approach was applied for the loading branch for a strain hardening index κ = 0.43, extracted from the experimental loading curve, and good agreement with the experimental data was obtained, as shown in Figure 3-21. The point from which the

loading curve was obtained by rescaling was the maximum indentation point (in this case, P = 465N and δ = 0.051mm).

The unloading branch obtained using Hertz contact theory with an effective radius calculated using the rescaling formulae also shows good agreement with the experimental curve. The calculated radius of the deformed surface of the specimen was 1.282mm (compared to 1.25mm radius of the indenting sphere).

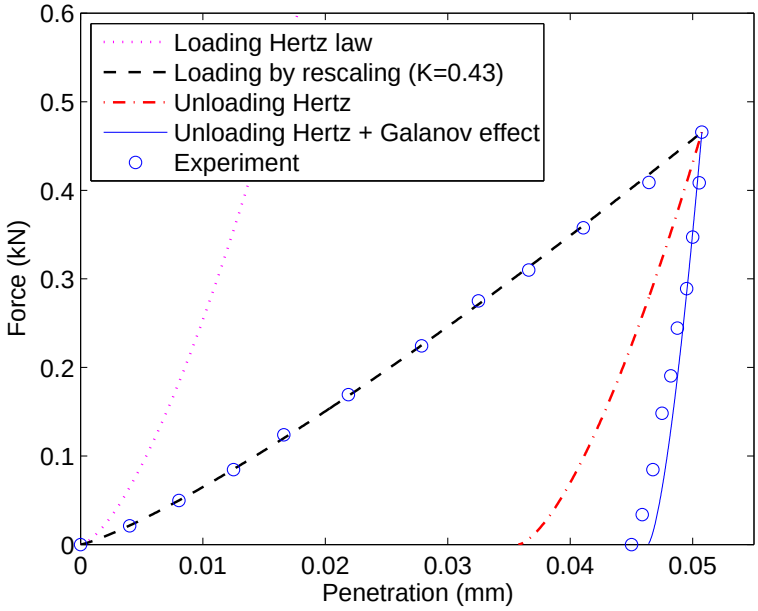

Figure 3-21 - Fitting the experimental results in Bartier et al. (2010) for AISI 1065 steel, by rescaling formulae and Hertz contact theory

K. Bartier et al. (2010): spherical indentation of AISI 4135 spheroidized steel

The characteristics of the materials involved are as follows:

- Indenter: tungsten carbide spherical indenter, R = 1.25mm, E = 600GPa, ν=0.28.
- Specimen: AISI 4135 spheroidized steel, E = 210GPa, ν=0.3.

The rescaling approach was applied for the loading branch for a strain hardening index κ = 0.23, extracted from the experimental loading curve, and good agreement with the experimental data was obtained, as shown in Figure 3-22. The point from which the loading curve was obtained by rescaling was the maximum indentation point (in this case, P = 920.8N and δ = 0.081mm).

The unloading branch obtained using Hertz contact theory with an effective radius calculated using the rescaling formulae also shows reasonable agreement with the experimental curve. The calculated radius of the deformed surface of the specimen was 1.281mm (compared to 1.25mm radius of the indenting sphere).

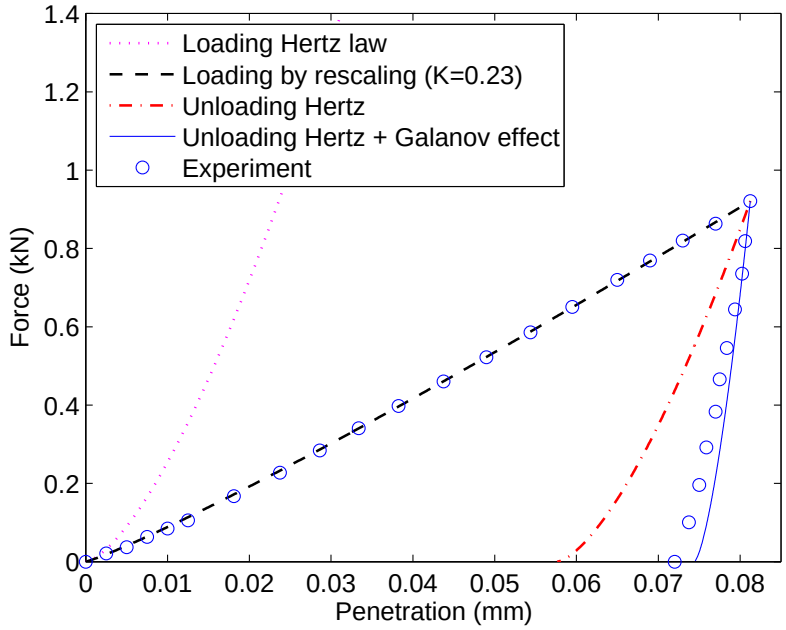

Figure 3-22 - Fitting the experimental results in Bartier et al. (2010) for AISI 4135 steel, by rescaling formulae and Hertz contact theory

L. Beghini et al. (2006): spherical indentation of work-hardened Cu, 7075 Al alloy and C40 steel

Beghini et al. (2006) have performed indentation tests for two types of steels, two types of Cu, and two types of Al alloys. We will try to describe the experimental data for one material out of each pair, namely C40 steel (Figure 3-23), work-hardened Cu (Figure 3-24), and 7075 Al alloy (Figure 3-25). These figures only show the loading curves because the authors studied only the loading branch of the experiments.

It can be seen that in all three cases there is very good agreement between the curves obtained by rescaling and the experimental data. In all cases the rescaling was performed using the point of maximum indentation as the known solution.

The values of the strain hardening index for the three indentations have been calculated from the experimental curve. We have found $\kappa = 0.38$ for steel, $\kappa = 0.197$ for Cu, and $\kappa = 0.15$ for Al.

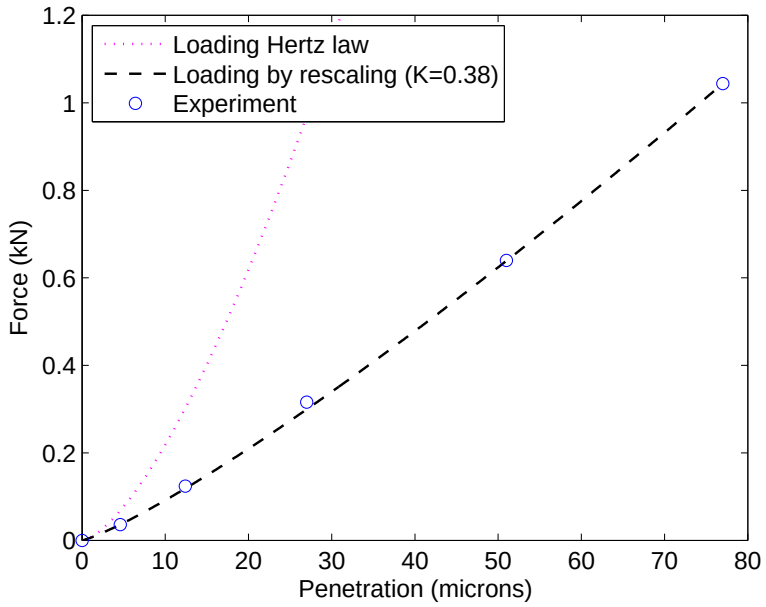

Figure 3-23 - Fitting the experimental results in Beghini et al. (2006) for C40 steel, by rescaling formulae and Hertz contact theory

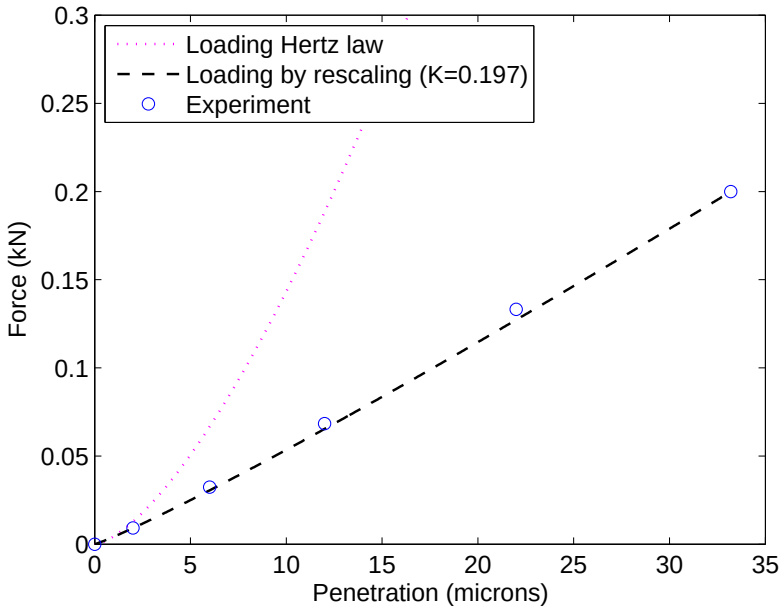

Figure 3-24 - Fitting the experimental results in Beghini et al. (2006) for work-hardened Cu, by rescaling formulae and Hertz contact theory

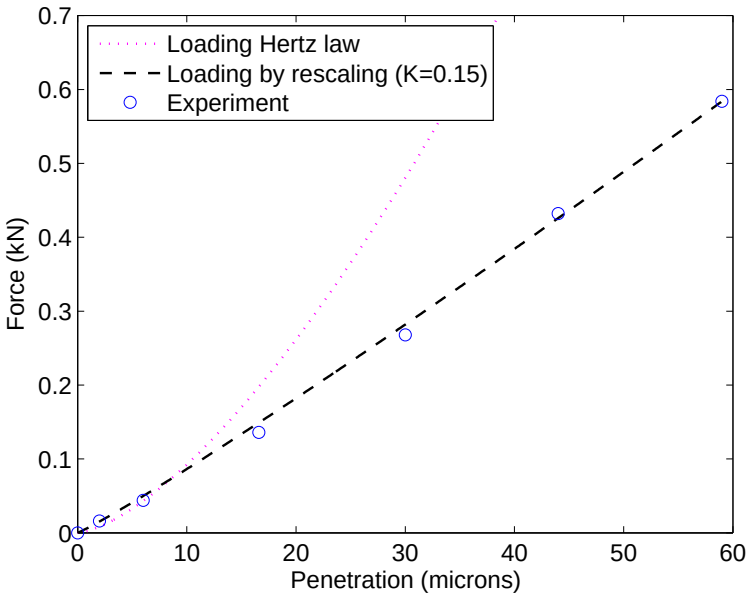

Figure 3-25 - Fitting the experimental results in Beghini et al. (2006) for 7075 Al alloy, by rescaling formulae and Hertz contact theory

In this section, we have tried to describe a considerable number of spherical indentation tests using the Borodich rescaling method. An analysis of the results will follow in section 3.6.3, and a discussion and conclusions in section 3.7.

3.5.2 Sharp indenter

Let us now analyse some indentation experiments that use nominally sharp indenters. The case of indentation using a nominally sharp die is more complicated than using a spherical indenter, both physically, because of the stress singularity under the tip, and theoretically, because we do not know the actual shape of the indenter. When the indenter was spherical, all the information we needed about its geometry was the radius, whereas all nominally sharp indenters have a certain deviation from the ideal shape that we will call bluntness, which is usually not known. Therefore, for the indentation loading branch, the rescaling formulae will depend both on the material hardening exponent (κ) and on the indenter bluntness index (d).

It is common for a sharp indenter to be modelled as a cone (called equivalent cone) because analytical solution for the problem of indentation of a half space by a cone is available (first obtained by Love (1939), although many authors attribute the result to Sneddon (1948)). Therefore we will use Galin's approach to describe the cone as an

axisymmetric punch by a power law, as shown in equation (1-19), section 1.6.1. For convenience, we will give the formula below.

$$f(r) = B_d r^d, \qquad d \geq 1$$

B_d is the shape constant which, for a cone, is equal to the cotangent of the half-angle. This representation of the shape of the indenter allows us to take into account the bluntness of the indenter when index $d > 1$.

The half-angle of the equivalent cone for the pyramidal indenters is found by equating the projected area of the pyramidal indenter with that of the cone, at the same height. So, as illustrated in Figure 3-26, the half-angle ϑ of the cone is found from the equivalence of projected areas, at the same height h, for the known half-angle ψ of the pyramidal indenter. As given by Fischer-Cripps (2011), the angle ψ of the Berkovich indenter is 65.3°, for Vickers indenter 68°, and for the cube corner indenter 35.26°. Thus the calculated half-angle ϑ of the equivalent cone is 70.3° for Berkovich and Vickers indenters, and 42.3° for the cube corner indenter. The Berkovich and Vickers indenters have the same angle of the equivalent cone because, for nanoindentation, the Berkovich indenter has been designed to have the same ratio of projected area to indentation depth as the Vickers indenter (Fischer-Cripps 2011, p.27).

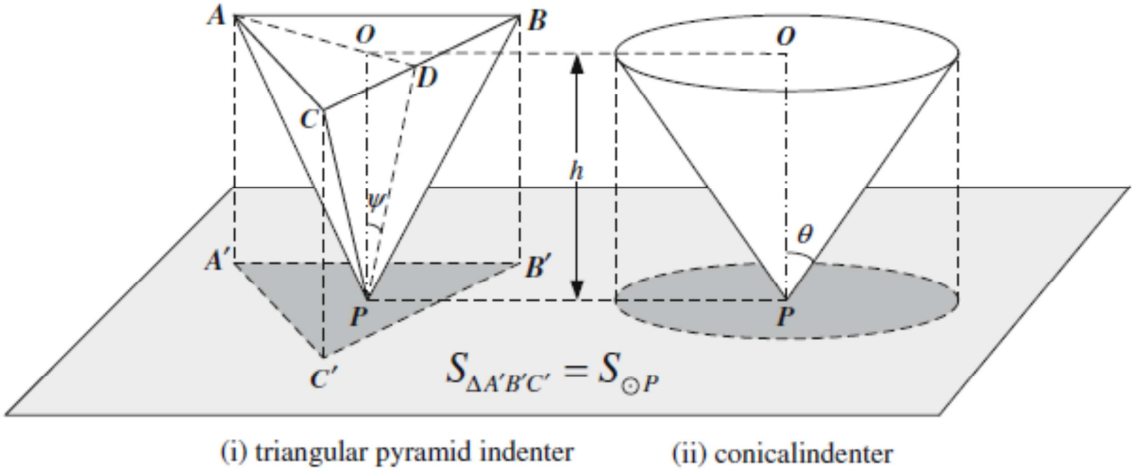

Figure 3-26 - Schematic of a pyramidal indenter of angle ψ and its equivalent axisymmetric indenter of angle θ, based on the equivalence of the projected area, from Shi et al. (2010)

Let us analyse some experiments presented in literature and attempt to describe them using the rescaling approach. The first experiment discussed will comprise a more

detailed explanation of the method applied, and the other experiments will follow the same methodology, unless stated otherwise.

M. Gadelrab et al. (2012b): Berkovich indentation of fused silica

We will use the experimental data provided by Gadelrab et al. (2012b) for the indentation of fused silica by a Berkovich tip. The material of the indenter is industrial diamond with an elastic modulus of 865GPa and Poisson's ratio of 0.2. The estimated elastic modulus for the fused silica specimen is 70.3GPa and Poisson's ratio is 0.17.

In the case of indentation by an axisymmetric indenter we work with rescaling formula (3-13) which, for convenience, we will give below.

$$\delta(\lambda, P) = \lambda^{\frac{2-\kappa}{2+\kappa(d-1)}} \left(\frac{P}{P_1}\right)^{\frac{d}{2+\kappa(d-1)}} \delta(1, P_1)$$

When expressing force P in terms of penetration δ, we get (3-24):

$$P(\lambda, \delta) = \lambda^{\frac{\kappa-2}{d}} \left(\frac{\delta}{\delta_1}\right)^{\frac{2+\kappa(d-1)}{d}} P(1, \delta_1) \qquad (3\text{-}24)$$

If we do not take into account the plastic deformation of the indented specimen (called here the Galanov effect), then $\lambda = 1$ and (3-24) becomes:

$$P(\lambda, \delta) = \left(\frac{\delta}{\delta_1}\right)^{\frac{2+\kappa(d-1)}{d}} P(1, \delta_1) \qquad (3\text{-}25)$$

We can see that there are two unknowns if we try to use rescaling relation (3-25) for the loading branch, namely the strain hardening index κ and the bluntness factor d. However, for unloading, the material is assumed to have an elastic behaviour, so $\kappa = 1$. Therefore (3-25) can be used for the unloading branch to find the bluntness index d of the indenter, which can then be substituted in the rescaling equation for the loading branch to find the strain hardening index κ.

In order to find d from the loading branch, we take logarithm of both sides of relation (3-25):

$$\log P(\lambda,\delta) = \frac{2+\kappa(\mathrm{d}-1)}{\mathrm{d}} \log\left(\frac{\delta}{\delta_1}\right) + \log P(1,\delta_1) \qquad (3\text{-}26)$$

Therefore, if we represent the logarithm of the experimental unloading data and fit it by a straight line, the slope of the linear fit will be $\frac{2+\kappa(\mathrm{d}-1)}{\mathrm{d}}$. For the experiment discussed here, it can be seen in Figure 3-27 that the slope is m = 1.24, and the resulting d is 4.24.

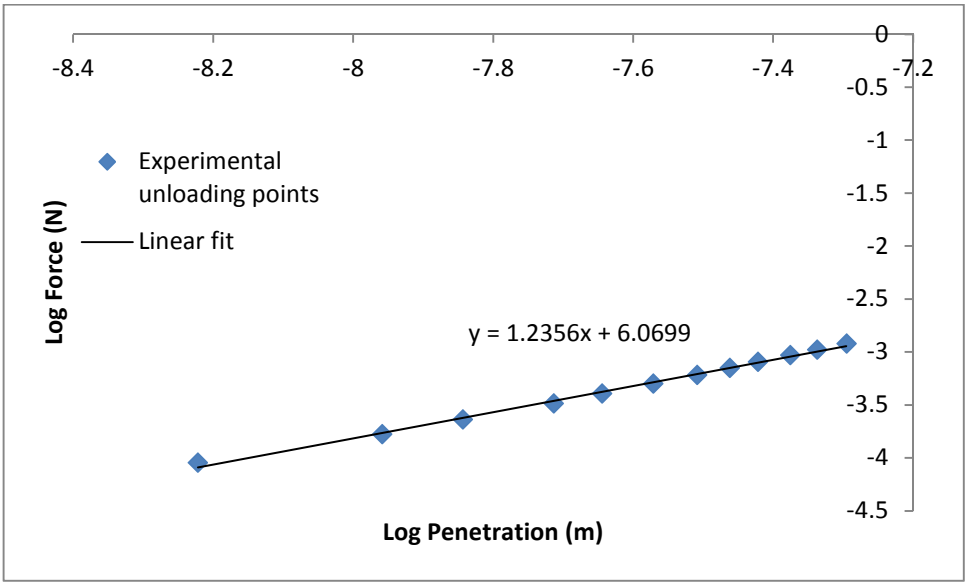

Figure 3-27 – Linear fit of the logarithm of the experimental data for the unloading branch, to find the bluntness factor *d*, assuming the strain hardening index *κ* = 1

Following the same procedure to find the slope of the linear fit of the logarithm of the loading experimental data gives m = 1.43. Knowing from the above that the bluntness index of the indenter is d = 4.24, we can find κ from

$$m = \frac{2+\kappa(4.24-1)}{4.24} = 1.43$$

The resulting strain hardening index κ for the loading branch is 1.25.

Discussion

Let us now discuss the values obtained for the κ and d parameters. d = 4.24 describes a very blunt indenter. For a better understanding of its shape, Figure 3-28 shows the half-shape of the axisymmetric indenter defined by d = 4.24 and the half-angle γ = 70.3°, using Galin's formula (1-19).

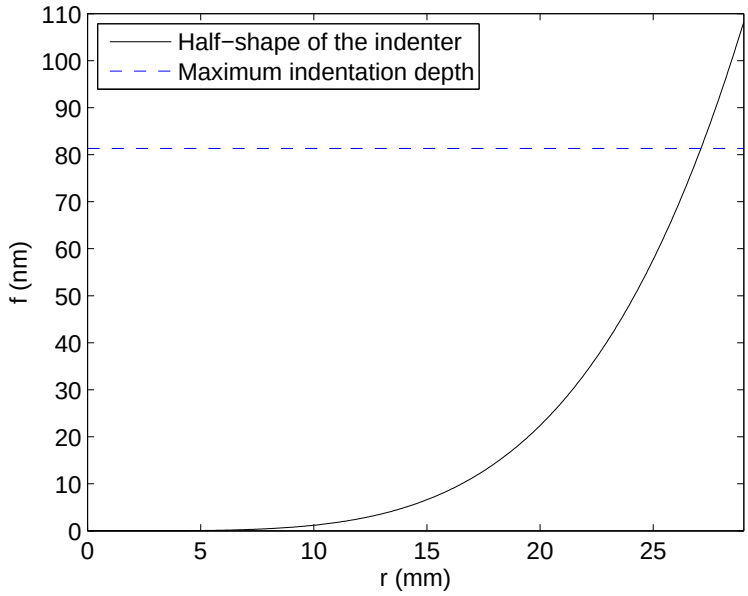

Figure 3-28 - Sketch of the half-shape of the axisymmetric indenter defined by d = 4.24 and the half-angle of the Berkovich equivalent cone (70.3°)

This plot confirms the calculated shape of the indenter is very blunt. It should also be mentioned that the figure does not show the real aspect ratio, as the axes have different scales, so the indenter is even blunter than the impression given in the plot of its shape.

Regarding the strain hardening index κ, it is remarkable that it is greater than unity. Indeed, in all the experiments in the previous section, where the indenter was a sphere, the calculated value for κ was less than unity. A value of the strain hardening index greater than unity reflects the behaviour of a material that becomes harder when stressed. It is known that fused silica is such a material (Bertoldi and Sglavo 2004, Kermouche et al. 2008, Perriot et al. 2006). Due to the fact that it is an amorphous material, with a low Poisson's ratio (0.17), fused silica is one of the 'anomalous' glasses that is more prone to densification (Gadelrab et al. 2012a).

However, even though the special nature of fused silica qualitatively justifies the resulting $\kappa > 1$, there are factors that make the method unreliable for calculating the hardening exponent κ and the bluntness index d. Firstly, the modelling of the Berkovich indenter as a cone is only an approximation. Studies show that the edges of the pyramidal indenter significantly change the pressure distribution under the tip (Galanov 1981b, 1981a). Secondly, it was assumed that the unloading branch of the

indentation curve is as for an elastic half-space, while in the case of a nominally sharp indenter there are unknown residual stresses. Another assumption we make is that the contact is between an indenter and half-space but, strictly speaking, the contact is between the indenter and the deformed shape of the imprint. In addition, we do not take into account the strain rate effects, which become more important in the case of sharp indentation.

The curves obtained for the calculated parameter values are shown against the experimental data in Figure 3-29. We can see the agreement is reasonably good.

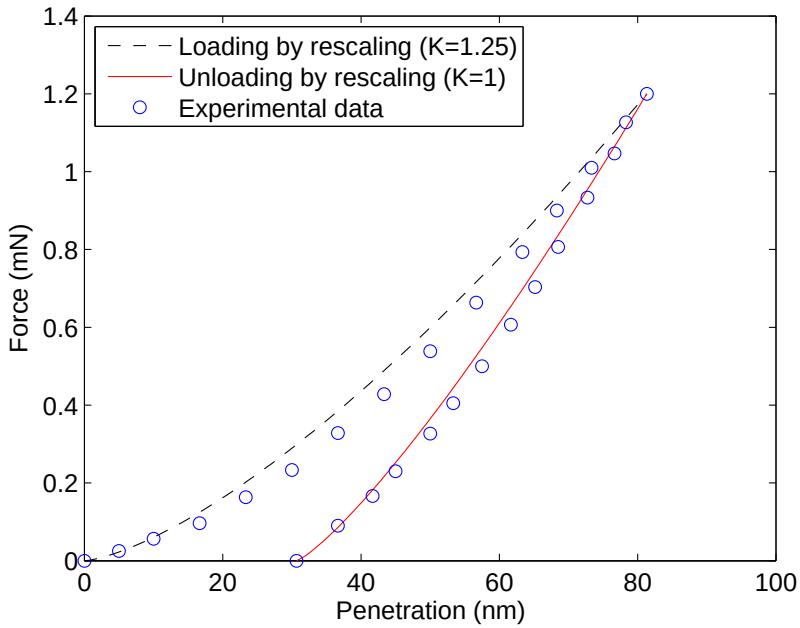

Figure 3-29 - Rescaling curves for fused silica indentation experiment by A Berkovich tip. Experimental data from Gadelrab et al. (2012-b)

N. *Krier et al. (2012): Berkovich indentation of Si*

Krier et al. (2012) studied the influence of the tip defect on the $P - \delta$ diagrams and found that, for indentation depths less than 50 nm, the influence of tip defect is significant and has to be considered. One of the more relevant diagrams in their paper is shown in Figure 3-30.

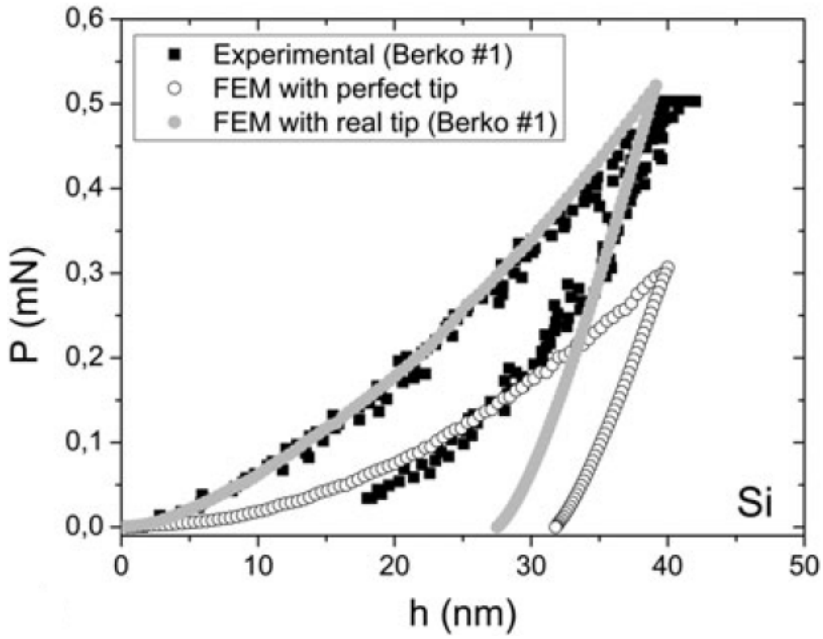

Figure 3-30 – Comparison between indentation curves on Si showing the influence of modelling the tip defect (9 nm), from Krier et al. (2012)

Krier et al. (2012) perform an indentation test with a Berkovich tip that has a 9 nm defect and plot it using black square symbols. The 9 nm defect is the distance from the tip of the real shape to the tip of the ideal shape (see Figure 3-31 - a).

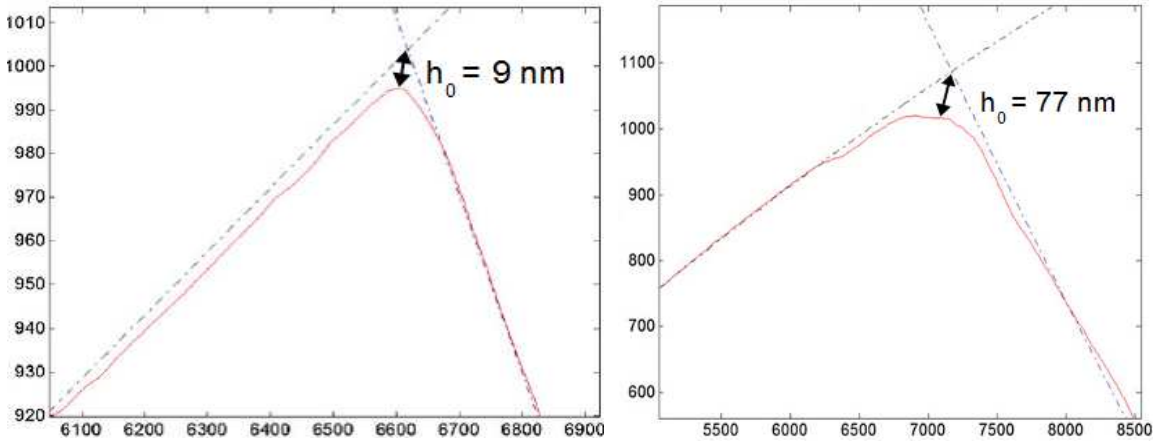

(a) **(b)**

Figure 3-31 – Real shape of the indenters versus the ideal geometry, from Krier et al. (2012). h_0 is the gap between the ideal and the real shape at the tip. The units on the ordinate are nanometres and the units on the abscissa are Angstroms.

They measure the real shape of the indenter by AFM and perform a FEM simulation with the real geometry, and represent the result in grey circles. We can see there is good agreement for the loading branch, but there is quite a significant deviation from the unloading experimental data. They also perform FEM simulations with the ideal tip

geometry and represent the resulting curves in white circles. It can easily be seen in Figure 3-30 that considering the real geometry of the indenter has important effect in the $P - \delta$ diagrams. This is confirmed by our analysis, as will be explained further.

We have followed the same idea and the result is shown in Figure 3-32. First, with regards to the indentation test by the Berkovich tip with a 9 nm defect, it can be seen there is reasonable agreement between the experimental data and the curves obtained by rescaling. One could see that the rescaling approach gives a closer description of the experiment than the AFM simulations performed by Krier et al. (2012) for the unloading branch.

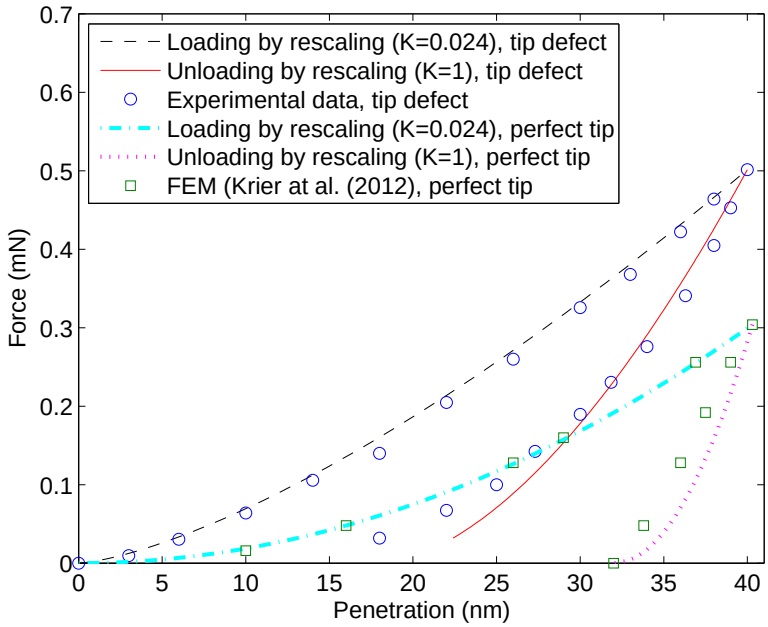

Figure 3-32 – Comparison between indentation curves obtained by rescaling, for a 9 nm defect tip and an ideal Berkovich tip. Experimental data and FEM simulations from Krier et al. (2012)

The parameters involved in rescaling have been obtained as follows. Assuming $\kappa = 1$, from the experimental unloading data, the bluntness factor of the tip was found to be $d = 1.4$. With this known bluntness factor, $\kappa = 0.024$ was obtained for the loading branch. For both the case of the ideal indenter and the case of the imperfect one, the known solution for rescaling was the point of maximum indentation.

Secondly, with regards to the comparison between the FEM simulations performed by Krier et al. (2012) and the rescaling approach, it can be seen in Figure 3-32 that there is

good agreement. The rescaling curves have been plotted for the κ values indicated above and d = 1, for both loading and unloading, to model a perfect cone.

Krier et al. (2012) also compare results for another Berkovich tip, with a greater deviation from the ideal geometry: 77 nm between the tip of the real shape and the tip of the ideal shape (see Figure 3-31 - b).

The indentation curves obtained by Krier et al. (2012) for the 77 nm defect tip are shown in Figure 3-33. It can be seen that their FEM simulations are closer for the loading part of the experiment, than for the unloading part. It is explained that the disagreement in the case of the unloading branch is due to simplistic assumptions regarding the material modelling of the specimen, as it is considered to have elastic-perfectly plastic behaviour.

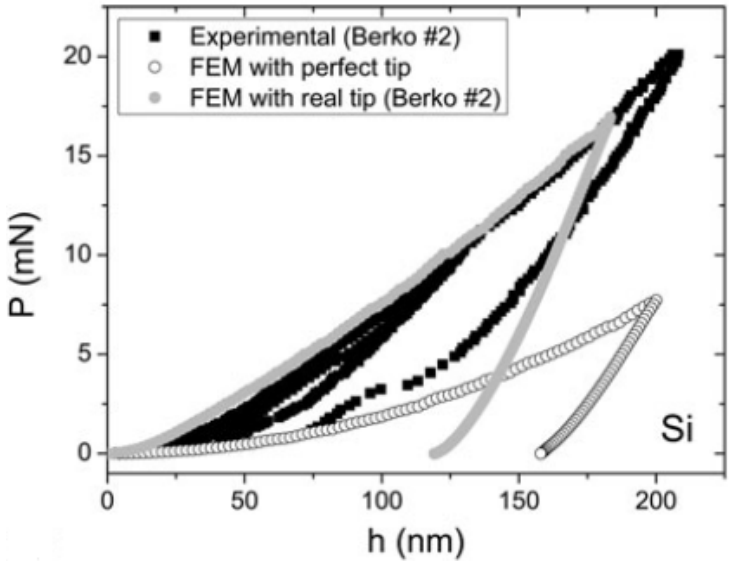

Figure 3-33 – Comparison between indentation curves on Si showing the influence of modelling the tip defect (77 nm), from Krier et al. (2012)

It is not clear why the authors have not performed the simulation to the experimental indentation depth, but have stopped at about 180 nm. However, it can be seen again that taking into account the real shape of the indenter has a great impact on the $P - \delta$ diagrams. Indeed, from comparing Figure 3-33 to Figure 3-30, it is evident that for the blunter tip (77 nm defect) there is a greater deviation from the perfect-tip simulation curve than for the 9 nm defect tip.

Let us use the similarity approach to describe the experimental curve for the 77 nm defect tip, to see whether our results indicate a blunter tip. The resulting curves are

plotted in Figure 3-34. Our analysis shows a bluntness index d = 4.89, which is indeed greater than d = 1.4 obtained for the 9 nm defect tip.

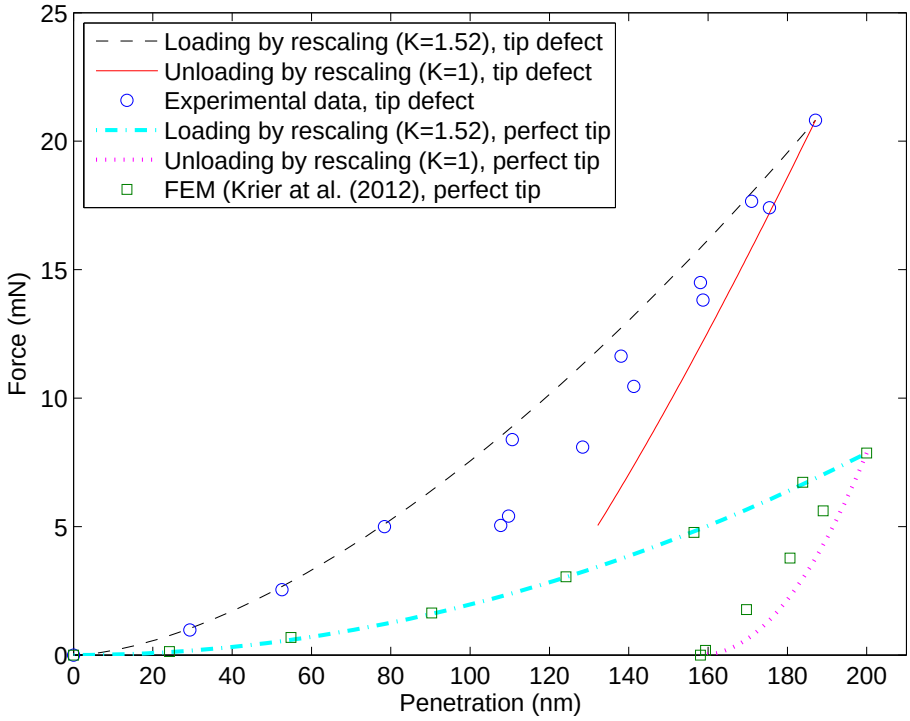

Figure 3-34 – Comparison between indentation curves obtained by rescaling, for a 77 nm defect tip and an ideal Berkovich tip. Experimental data and FEM simulations from Krier et al. (2012)

However, Figure 3-34 shows quite a significant divergence from the experimental data for the unloading curve obtained by rescaling. This can be, as stated before, due to the approximation of the Berkovich indenter by an equivalent cone disregarding stress singularities, not taking into account the Galanov effect, or not considering residual stresses.

O. Lichinchi et al. (1998): Berkovich indentation of titanium nitride (TiN)

Lichinchi et al. (1998) have obtained very good results applying the FEM to study the nanoindentation of thin hard coatings by a Berkovich tip. In their simulations the tip was modelled as a cone with the same contact area as the Berkovich indenter. In order to validate their results, experiments have been performed.

As Figure 3-35 shows, the experimental data provided by Lichinchi et al. (1998) is described very well using the rescaling approach. Satisfactory agreement with the experiment has been obtained for both loading and unloading branches.

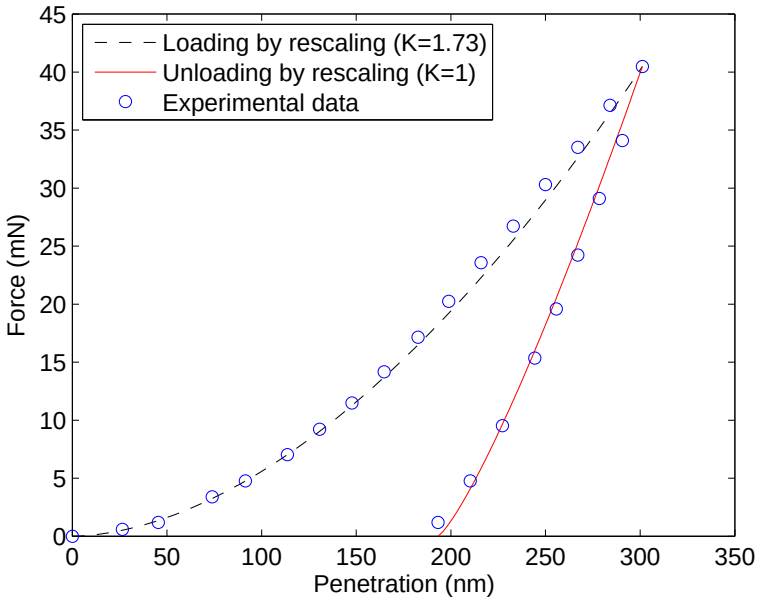

Figure 3-35 –Rescaling curves for TiN indentation experiment. Experimental data from Lichinchi et al. (1998)

The bluntness index *d*, characterising the indenter, has been obtained from the unloading branch and it is equal to 4.11. With this value of *d* we have obtained $\kappa = 1.73$ from the loading branch. As was the case for the experiment at point *M*, a hardening index greater than unity reflects a material that becomes harder when stressed. Figure 3-36 shows the experiments done by Paar (2006) confirm TiN is such a material. It is clear that the first part the TiN stress-strain curve is concave, showing hardening.

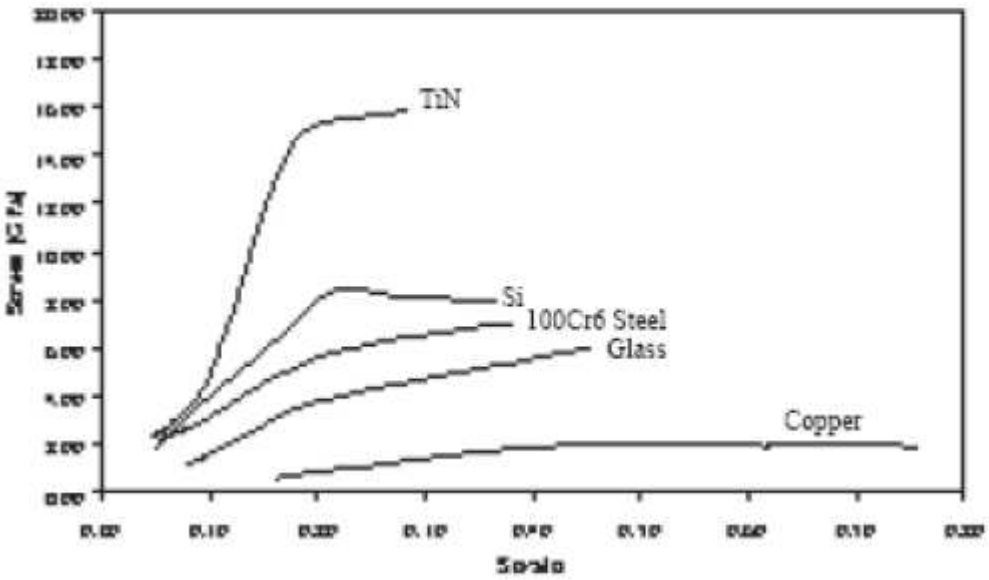

Figure 3-36 –Stress-strain data for TiN (3 µm thick coating). Experimental data from Paar (2006)

P. *Taylor et al. (2005): cube corner indentation of gallium arsenide (GaAs)*

Here we will apply the rescaling approach to describe the experimental data provided by Taylor et al. (2005) for the indentation of vertical gradient freeze (VGF) GaAs(100) by a diamond cube corner indenter. The mechanical properties given by the authors are E = 1140 GPa and ν = 0.17 for the diamond indenter, and E = 116.62 GPa and ν = 0.3 for the substrate material (GaAs).

The bluntness index d, characterising the indenter, has been obtained from the experimental data for the unloading branch and it is equal to 1.43. With this value of d we have obtained κ = 0.96 from the experimental loading data. The rescaling curves obtained for the experiment can be seen in Figure 3-37.

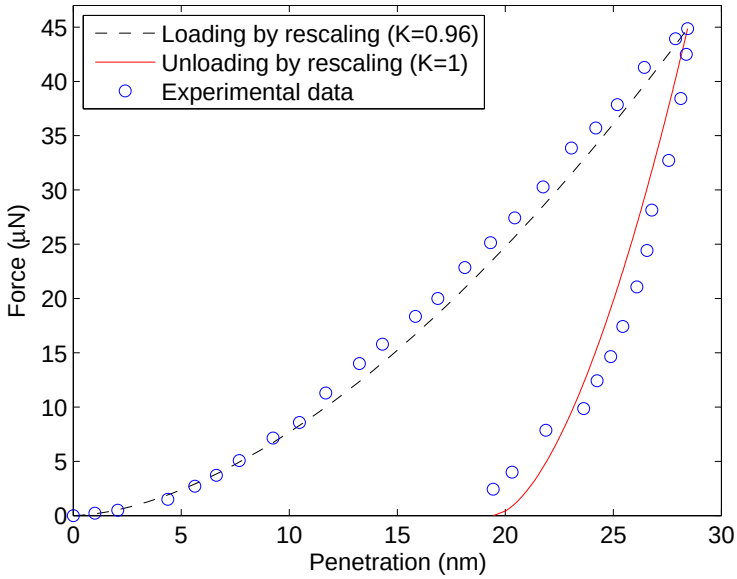

Figure 3-37 –Rescaling curves for VGF GaAs indentation experiment. Experimental data from Taylor et al. (2005)

The experimental unloading branch presented in Figure 3-37 shows a shift in displacement for a force of about 10 μN. This shift may be due to an irregular shape of the indenter that could create a sudden jump in the contact area. Such a tip defect could not be modelled as a power law function and therefore would make the rescaling approach inapplicable. In the case when the tip shape is not continuous one could try a piecewise approximation of the geometry.

Q. *Jayaraman et al. (1998): Berkovich indentation of silicon nitride (Si_3N_4)*

Jayaraman et al. (1998) provide experimental data for indentation tests of 1070 steel and Si_3N_4 using Berkovich and cube corner indenters. Let us analyse the indentation test of Si_3N_4 using a Berkovich indenter. The authors use an elastic modulus of 315 GPa and Poisson's ratio of 0.25 for the silicon nitride. The mechanical properties of the indenter tip are E = 1141 GPa and ν = 0.07.

From the experimental data we have obtained a value of κ = 0.82 for the strain hardening index and a value of d = 1.51 for the indenter bluntness index. The resulting rescaling curves for these parameters are shown in Figure 3-38. It can be seen that, for the unloading branch, there is excellent agreement with the experimental data. However, there is considerable deviation for the loading branch. Indeed, the strain hardening index that Jayaraman et al. (1998) obtain from their study using FEM does not coincide with what we have obtained here using the rescaling approach. Using the value of κ = 0.22 that they have calculated, we obtain a bluntness index d = 1.3 and the resulting curves are plotted in Figure 3-39, but the curves are identical as they are obtained by fitting the same experimental data.

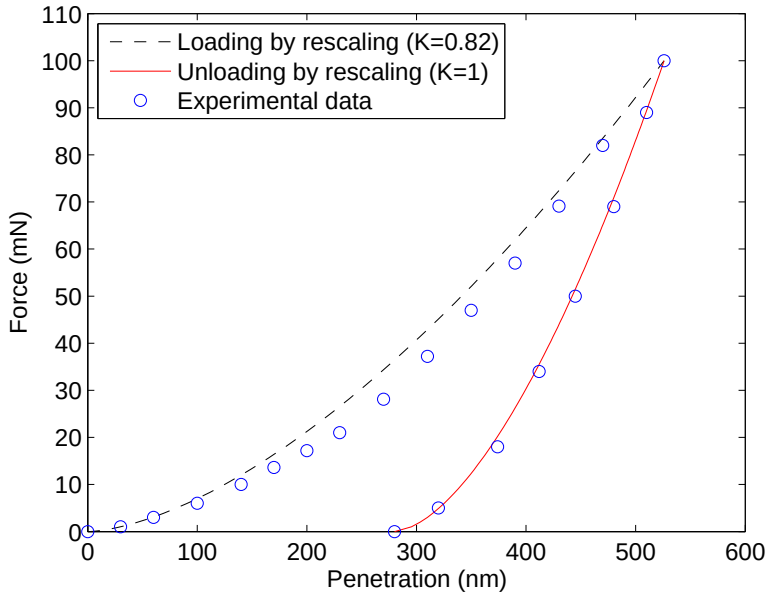

Figure 3-38 –Rescaling curves for silicon nitride indentation experiment using a Berkovich tip. Experimental data from Jayaraman et al. (1998)

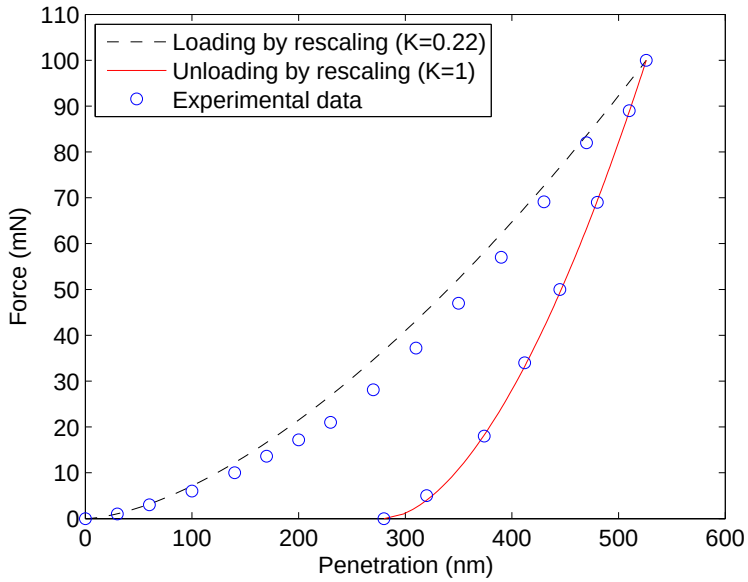

Figure 3-39 –Rescaling curves for silicon nitride indentation experiment using a Berkovich tip, with κ provided by Jayaraman et al. (1998)

Let us analyse the other experiments presented by Jayaraman et al. (1998) and compare their results to the results obtained using the rescaling approach.

R. Jayaraman et al. (1998): cube corner indentation of silicon nitride (Si_3N_4)

The materials involved in this indentation test are the same as for the previous experiment ($E_{indenter}$ = 1141 GPa, $\nu_{indenter}$ = 0.07, $E_{specimen}$ = 315 GPa, $\nu_{specimen}$ = 0.25).

Let us apply the procedure described above for fitting the experimental results. First, we consider the unloading branch, assuming that κ = 1. From fitting the experimental points we obtain d = 2.43. Then, from the loading branch, we obtain κ = 1.31.

There is a great discrepancy between our result and the value κ = 0.22 obtained for the hardening index by Jayarman et al. If we use the rescaling approach for κ = 0.22, the bluntness factor d becomes 1.3. A diagram showing the rescaling curves for both sets of parameters is presented in Figure 3-40. It can be seen that the loading curves for the two sets of parameters almost coincide, while for the unloading curves there is a slight deviation. The analysis of these results is given in section 3.6.

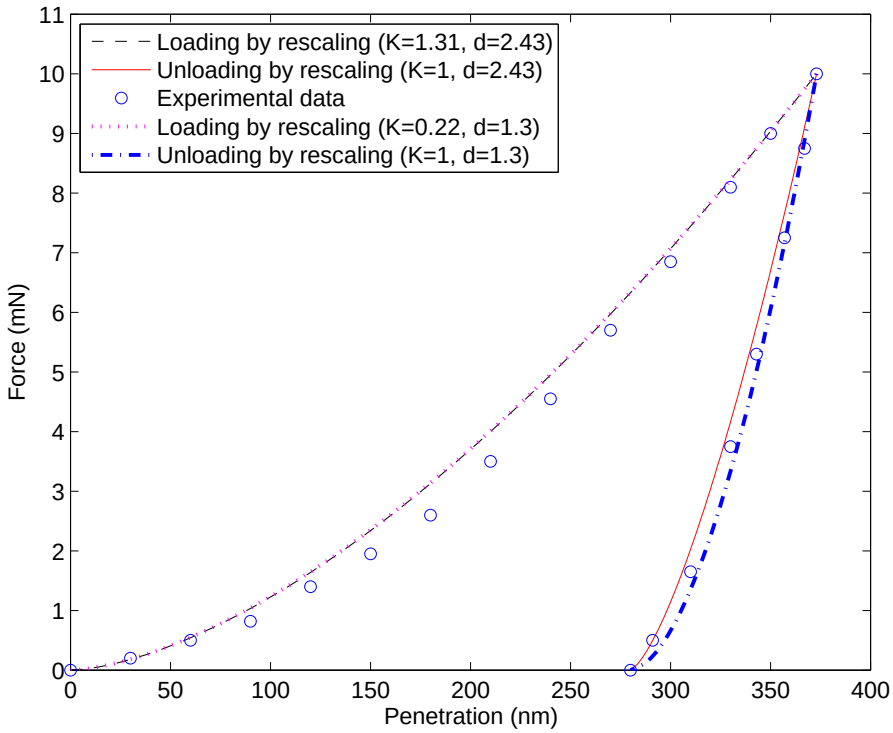

Figure 3-40 – Rescaling curves for silicon nitride indentation experiment using a cube corner tip, with parameters obtained from experimental indentation data using rescaling formula (κ = 1.31, d = 2.43), and κ = 0.22 provided by Jayaraman et al. (1998) from which d = 1.3 was calculated using rescaling formula

S. Jayaraman et al. (1998): Berkovich indentation of 1070 Steel

Specimens made of 1070 Steel are indented using a Berkovich tip. The properties of the indented steel, as given by the authors, are $E_{specimen}$ = 207 GPa, $\nu_{specimen}$ = 0.3. The indenter has the same properties as for the previous experiment, namely $E_{indenter}$ = 1141 GPa, $\nu_{indenter}$ = 0.07.

Applying the rescaling formulae for the experimental data, we have obtained d = 3.91 (from the unloading curve) and κ = 1.53 (from the loading curve), whereas the value of the hardening exponent obtained by Jayarman et al. is 0.12. Using their value of κ = 0.12, and the value of the slope of the linear fit of the loading branch in logarithmic coordinates, we obtain d = 1.23. A diagram showing the rescaling curves for both sets of parameters is presented in Figure 3-41.

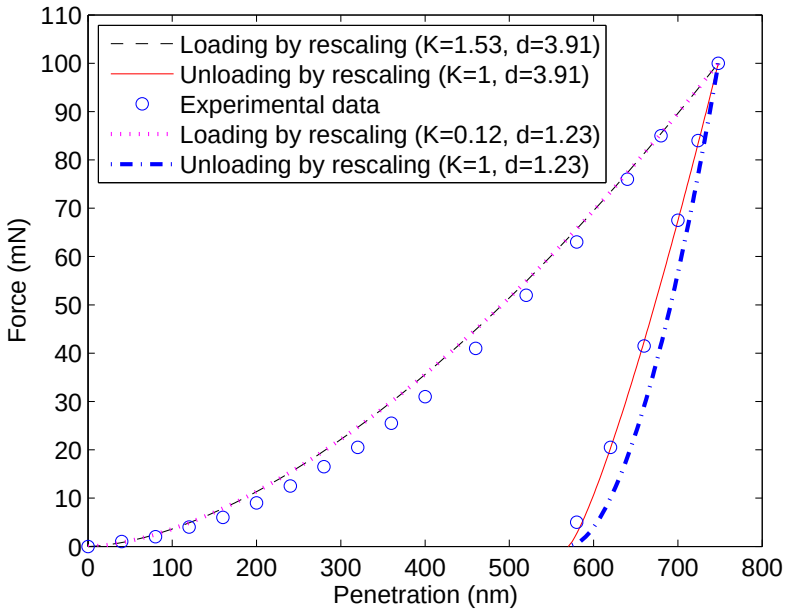

Figure 3-41 – Rescaling curves for 1070 steel indentation experiment using a Berkovich tip, with parameters obtained from experimental indentation data using rescaling formula (κ = 1.53, d = 3.91), and κ = 0.12 provided by Jayaraman et al. (1998) from which d = 1.23 was calculated using rescaling formula

It can be seen that the result is very similar to what we have seen before in Figure 3-40: identical loading curve, and a slight deviation between the unloading curves. The results are similar for cube corner indentation, as it can be seen in the next section.

T. Jayaraman et al. (1998): cube corner indentation of 1070 Steel

The same materials are involved, as for the last experiment. So we have $E_{indenter}$ = 1141 GPa, $\nu_{indenter}$ = 0.07 and $E_{specimen}$ = 207 GPa, $\nu_{specimen}$ = 0.3.

Applying the rescaling formulae for the experimental data, we have obtained d = 3.91 (from the unloading curve) and κ = 1.53 (from the loading curve), whereas the value of the hardening exponent obtained by Jayarman et al. is 0.12. Using their value of κ = 0.12, and the value of the slope of the linear fit of the loading branch in logarithmic coordinates, we obtain d = 1.23. A diagram showing the rescaling curves for both sets of parameters is presented in Figure 3-42.

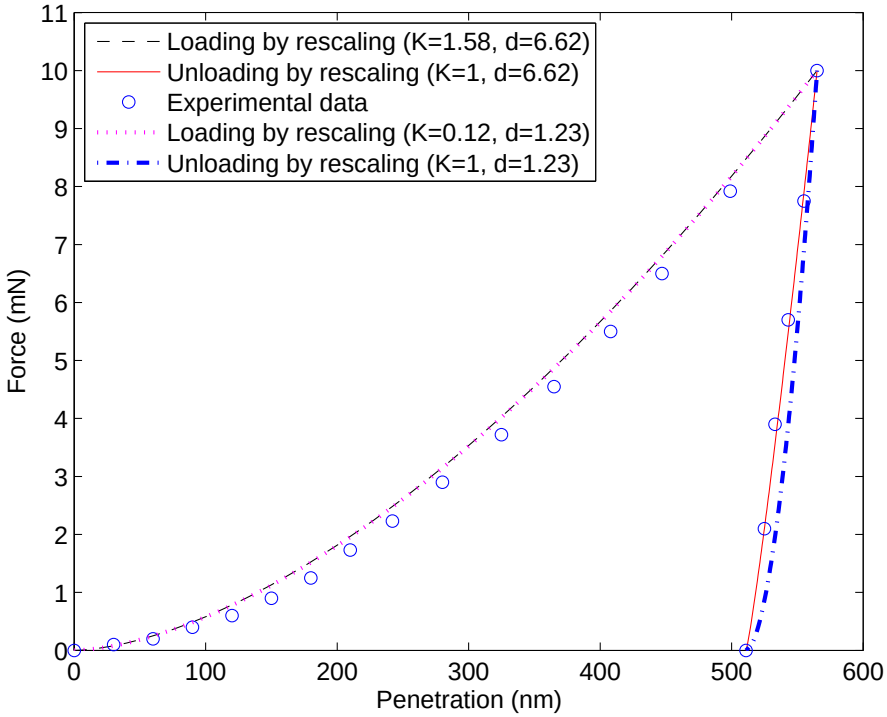

Figure 3-42 – Rescaling curves for 1070 steel indentation experiment using a cube corner tip, with parameters obtained from experimental indentation data using rescaling formula (κ = 1.58, d = 6.62), and κ = 0.12 provided by Jayaraman et al. (1998) from which d = 1.23 was calculated using rescaling formula

The result is very similar to what we have obtained for all experiments presented in Jayaraman et al. (1998).

Discussion

Let us explain the shape of the resulting curves. Firstly, it can be seen that the loading curves are identical, even for different values of κ. This is so because the values of d are different as well, keeping the exponent constant in the rescaling relation. Let us explain in more detail. The rescaling curves are obtained using relation (3-25), which we give below, for convenience.

$$P(\lambda,\delta)=\left(\frac{\delta}{\delta_1}\right)^{\frac{2+\kappa(d-1)}{d}}P(1,\delta_1)$$

In the approach we have used, we first found d from the unloading branch, assuming κ = 1, from the equation $\frac{2+\kappa(d-1)}{d}=m_u$, where m_u is the slope of the linear fit of the unloading data in logarithmic coordinates.

$$\frac{2+\kappa(\mathrm{d}-1)}{\mathrm{d}} = \frac{d+1}{d} = m_u \Rightarrow d = \frac{1}{m_u - 1}$$

With the *d* thus obtained, we then find the hardening index from the loading branch from equation $\frac{2+\kappa(\mathrm{d}-1)}{\mathrm{d}} = m_l$, where m_l is the slope of the linear fit of the loading data in logarithmic coordinates.

$$\kappa = \frac{d\, m_l - 2}{d - 1}$$

In order to obtain the second set of curves, we substituted the hardening exponent provided by Jayaraman et al. in equation $\frac{2+\kappa(\mathrm{d}-1)}{\mathrm{d}} = m_l$, to obtain a new *d*. However, we obtained the same curve even if we changed *κ* and *d* because the ratio $\frac{2+\kappa(\mathrm{d}-1)}{\mathrm{d}} = m_l$ was the same, and was given by the experimental data for the loading branch.

Therefore, the different unloading branches are due to the fact that only *d* changes, while *κ* remains equal to unity. Thus the exponent in the rescaling relation changes producing a different unloading curve.

The hardening index presented by Jayaraman et al. is backed up experimentally and it is physically consistent. We have obtained *κ* = 1.58 > 1, and we know steel does not have a concave stress-strain curve. In addition to this, an indenter with *d* = 6.62 is unrealistically blunt. As explained above, these results were obtained assuming *κ* = 1 for the unloading curve and assuming the effective angle of the pair indenter-specimen does not change.

In addition to this, the Borodich rescaling formulae need the Hertz assumption to be true. But all experiments presented in this section clearly break the Hertzian assumptions. Therefore, for the case of indentation by sharp punches, the method is not reliable to extract the parameters *d* and *κ* only from the experimental indentation data, as was previously stated.

U. Mata and Alcala (2004): Vickers indentation of annealed copper

Mata and Alcala (2004) study the effect of friction on sharp indentation of metallic materials, undertaking FEM simulations, which are then validated by indentation

experiments. In this section we will use the data they provide for the indentation of annealed copper by a Vickers indenter.

The properties of the specimen, as given by the authors, are $E_{specimen}$ = 110 GPa, $\nu_{specimen}$ = 0.3. The indenter is made of diamond, so $E_{indenter}$ = 1141 GPa, $\nu_{indenter}$ = 0.07.

Applying the rescaling formulae for the experimental data, we have obtained d = 9 (from the unloading curve) and κ = 2 (from the loading curve), whereas the value of the hardening exponent obtained by Mata and Alcala is 0.52. A diagram showing the rescaling curves obtained for the resulting parameters is presented in Figure 3-43. Even though the curves follow the experimental data very well, for reasons presented in the discussion of the previous experiment, the resulting unrealistically large parameters κ and d cannot reflect the physical properties of the system.

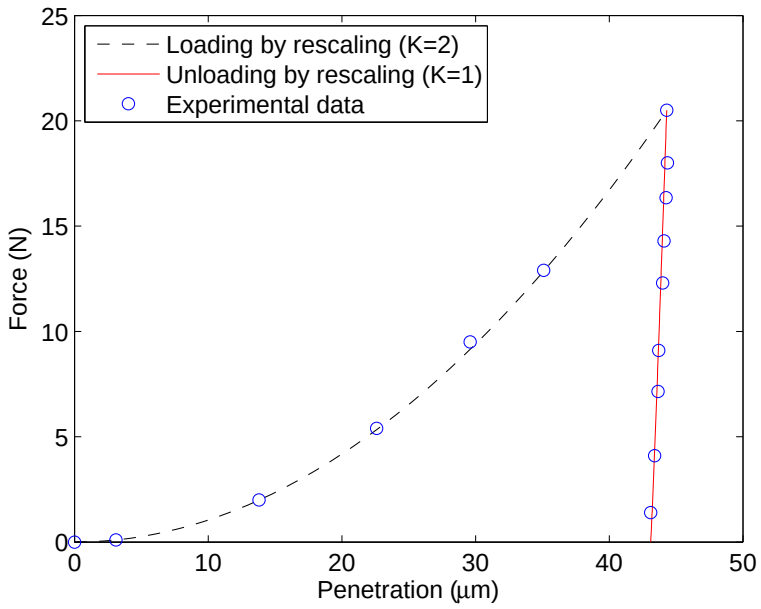

Figure 3-43 – Rescaling curves for annealed copper indentation experiment using a Vickers tip; experimental data from Mata and Alcala (2004)

V. *Mata and Alcala (2004): Vickers indentation of SAF 2507 duplex stainless steel*

In this section we will use the data provided by Mata and Alcala (2004) for the indentation of SAF 2507 steel by a Vickers indenter.

The properties of the specimen, as given by the authors, are E_{SAF} = 200 GPa, ν_{SAF} = 0.3. The same type of diamond indenter is used, so $E_{indenter}$ = 1141 GPa, $\nu_{indenter}$ = 0.07.

Applying the rescaling formulae for the experimental data, we have obtained d = 1.45 (from the unloading curve) and κ = 1.8 (from the loading curve). A diagram showing the rescaling curves obtained for the resulting parameters is presented in Figure 3-44. Even though the curves follow the experimental data very well, the resulting parameter κ cannot reflect the physical properties of the system, because it is too large. Indeed, the value of the hardening exponent obtained by Mata and Alcala is 0.19.

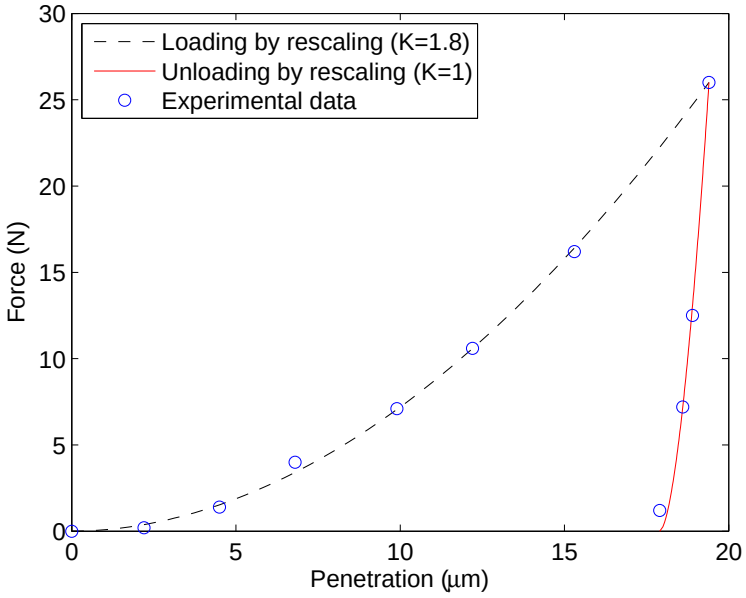

Figure 3-44 – Rescaling curves for SAF 2507 duplex stainless steel indentation experiment using a Vickers tip; experimental data from Mata and Alcala (2004)

Let us now discuss the outcomes of our investigation in section 3.6.

3.6 Analysis of the results

Here it will be shown that the rescaling approach may be successfully used for describing experimental loading and unloading indentation curves. This was confirmed by application to 15 spherical indentation experiments (sections *A* to *L*) and 10 indentation experiments using a nominally sharp indenter (sections *M* to *V*). However, the original approach introduced by Borodich (1988, 1989, 1993b, 2003) needs to be further developed.

3.6.1 Influence of the chosen starting point for rescaling

Let us begin with a discussion about some general features of the method applied.

Theoretically, any known point of indentation can be used to obtain the rescaling curve. However, it is advantageous to use the maximum indentation point. The reason for this is that choosing a point closer to the end of loading curve allows us to be more precise than choosing a point closer to the beginning of the curve, due to the fact that the rescaling formula is a power law relation. This is illustrated in Figure 3-45.

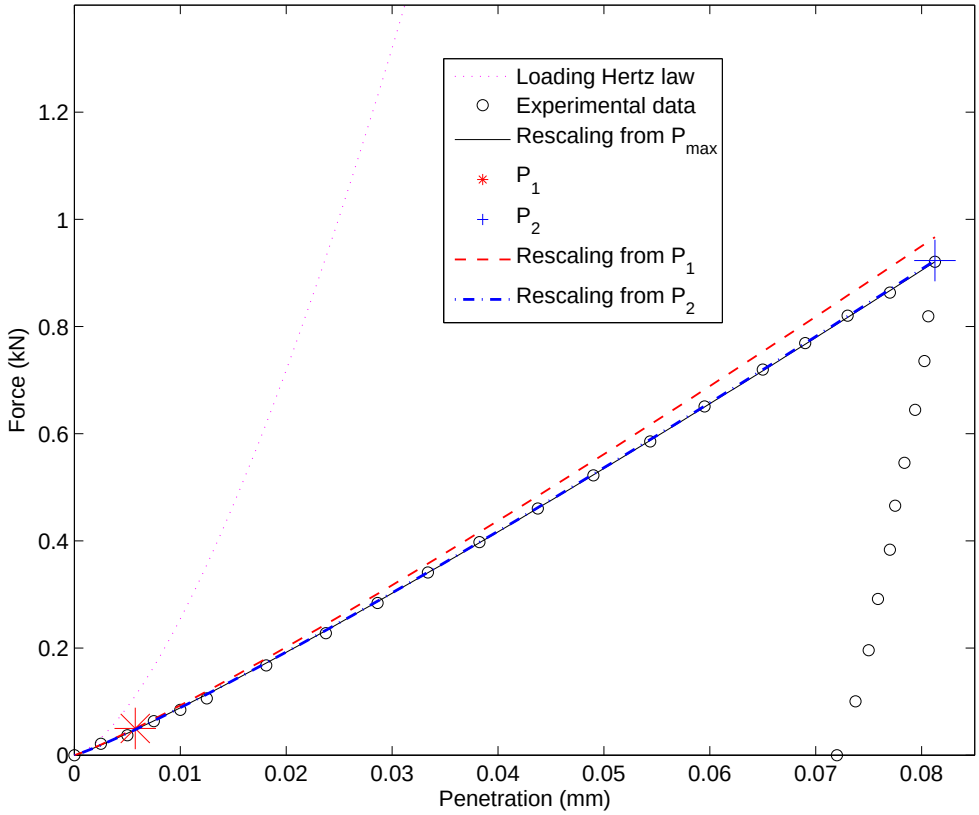

Figure 3-45 – Rescaling curves from different known points. Experimental data for indentation of AISI 4135 steel, from Bartier et al. (2010)

The full (black) line is the curve obtained by rescaling from the maximum point of indentation, the dashed (red) line is obtained by rescaling from point P_1 (red asterisk) at the beginning of the curve, and the dash-dot line is obtained by rescaling from point P_2 (blue cross) close to the maximum point of indentation. The points P_1 and P_2 have been chosen so that they are just above the black rescaling line (from P_{max}) by the same offset. The force at P_1 is 5% greater than the force obtained by rescaling from P_{max} for the same penetration. So,

$$P_1(\delta_1) = 1.05P(\delta_1)$$

The force at P_2 has the same offset as the force at P_1, namely

$$P_2(\delta_{max}) = P_{max} + 0.05P(\delta_1)$$

The plot in Figure 3-45 clearly demonstrates that, for a power-law relation, a small error in choosing the known solution close to the beginning of the curve determines a

greater deviation of the rescaling curve than the same error in choosing the known solution at the end of the loading curve. For this reason all our rescaling curves have been obtained from the point of maximum indentation.

3.6.2 The case of indentation by nominally sharp punches

Let us now analyse the results we have obtained using the rescaling approach to describe the experiments *M* to *V* (sharp indenters).

For the materials tested in the experiments *M* and *O*, we have obtained a hardening index κ greater than unity. At first sight, this looks like a controversial result because usually $\kappa < 1$ for elastic-plastic materials with $\sigma \sim \varepsilon^{\kappa}$. However, $\kappa > 1$ was found in literature for fused silica, which shows densification when subjected to high pressures, and titanium nitride, which is a very hard coating that hardens when it is stressed.

Another positive result was obtained for experiment *N*, where we have obtained a greater bluntness index for the tip with a greater defect. For the 9 nm defect tip, the calculated bluntness index was 1.4, whereas for the 77 nm tip the calculated bluntness index was 4.89. However, even if qualitatively the result of a blunter tip was justified by a measured geometry with a greater defect, quantitatively, a bluntness index of 4.89 is hard to explain. Even in the cases where the obtained hardening index greater than unity was confirmed by experiments found in literature (experiments *M* and *O*), the value obtained for the bluntness index was quite high (d = 4.24). Indeed, even accepting that none of the pyramidal indenters has ideal sharpness, it is hard to believe that the indenter used in experiment *M* was as blunt as shown in Figure 3-28.

As stated at the beginning of the section describing the indentation by sharp indenters, one difficulty is that we have too many unknowns and only one rescaling equation. In order to obtain reliable results, either the bluntness index or the hardening exponent has to be provided in addition to the indentation data. In order to solve this, we have worked on the assumptions that, for the unloading branch κ = 1, and the effective angle of the contact system does not change. This allowed for the bluntness index d to be found from the rescaling equation for the unloading branch, and then be substituted in the equation for the loading part, to find κ. The resulting values for κ were not confirmed by the results of Jayaraman et al. (1998) (which were backed up

experimentally). In addition to not being in agreement with experimental data, our results were not physically consistent because we have obtained $\kappa > 1$ for materials that we know do not get harder when stressed.

By way of conclusion, we can say that the information given by the experimental indentation curve is not sufficient to be able to obtain reliable results using the rescaling approach for sharp indenters. In addition to experimental indentation data, either the real shape of the indenter (the bluntness index) or the hardening exponent of the material has to be provided. We have to also mention that the case of sharp indenters is out of the bounds of the Hertzian assumptions, and other simplifying assumptions (the indenter being approximated as a cone, not taking into account the Galanov effect, not accounting for strain rate effects, or disregarding residual stresses when unloading) can introduce important discrepancies.

However, our results have shown that the bluntness index of the indenter has a very important effect on the $P - \delta$ indentation diagrams, and it should be taken into account. This is shown again in Figure 3-46, where the influence of considering the bluntness of the indenter can be seen, compared to the case when the indenter is considered ideally sharp.

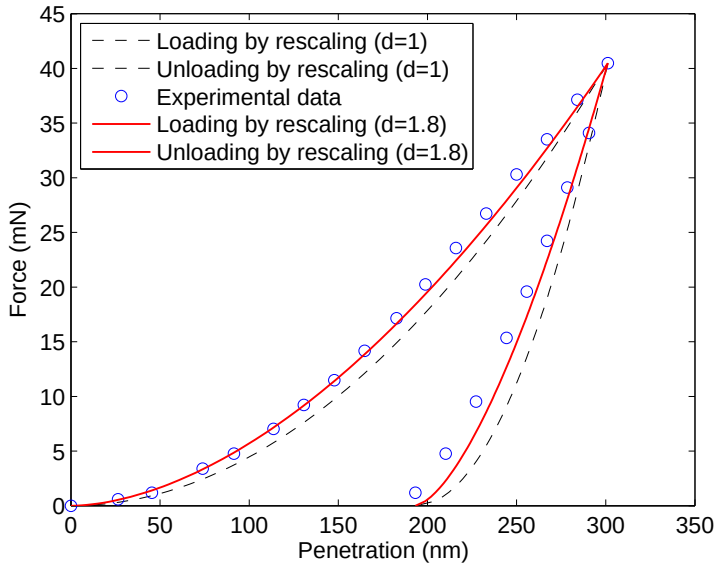

Figure 3-46 – Comparison between rescaling curves for ideal indenter geometry (d = 1) and blunter shape (d = 1.8). Experimental data from Lichinchi et al. (1998)

3.6.3 The case of indentation using a spherical indenter

In this section we will analyse the results we have obtained using the rescaling approach to describe the experiments *A* to *L*, where specimens have been penetrated using spherical tips of various radii.

One observation that needs to be made is that we have treated the indentation experiments as quasi-static, without accounting for effects that might appear due to the loading speed. However, the strain rate plays an important role for some of the materials involved (e.g. Aluminium) and can greatly influence the results obtained.

Unlike in the indentation experiments by sharp tips, the spherical indenters were not always made of very hard materials. In most cases a very rigid indenter has been used (tungsten carbide or diamond), but in the experiments by Goldsmith and Lyman (1960) the indenter was made of steel. Table 3-1 contains a list of the materials involved in the indentation tests we have analysed.

Test	Authors	Spherical indenter material	Specimen material	Loading rate
A	Taljat et all (1998)	tungsten carbide (E = 600 GPa)	steel (E = 210 Gpa)	Not specified
B	Taljat et all (1998)	tungsten carbide (E = 600 GPa)	Al-MG alloy (E = 70 GPa)	Not specified
C	Taljat et all (1998)	tungsten carbide (E = 600 GPa)	cold-worked Cu (E = 117 GPa)	Not specified
D	Harsono et all (2011)	diamond (E = 1200 GPa)	Al 7075 (E = 70.1 GPa)	1 mN/s
E	Harsono et all (2011)	diamond (E = 1200 GPa)	Cu (E = 109.2 GPa)	1 mN/s
F	Goldsmith and Lyman (1960)	hard steel (E = 200 GPa)	Al1100F (E = 73 GPa)	'static'
G	Goldsmith and	hard steel (E = 200 GPa)	Partially annealed tool	'static'

	Lyman (1960)		steel (E = 204 GPa)	
H	Goldsmith and Lyman (1960)	hard steel (E = 200 GPa)	Quench-hardened tool steel (E = 204 GPa)	'static'
I	Bartier et al. (2010)	tungsten carbide (E = 600 GPa)	AISI 1035 spheroidized steel (E = 210 GPa)	2 µm/s
J	Bartier et al. (2010)	tungsten carbide (E = 600 GPa)	AISI 1065 spheroidized steel (E = 210 GPa)	2 µm/s
K	Bartier et al. (2010)	tungsten carbide (E = 600 GPa)	AISI 4135 spheroidized steel (E = 210 GPa)	2 µm/s
L1	Beghini et al. (2006)	tungsten carbide (E = 534 GPa)	C40 steel (E = 211 GPa)	50 µm/min
L2	Beghini et al. (2006)	tungsten carbide (E = 534 GPa)	Work-hardened Cu (E = 121 GPa)	50 µm/min
L3	Beghini et al. (2006)	tungsten carbide (E = 534 GPa)	7075 Al alloy (E = 72 GPa)	50 µm/min

Table 3-1 – Materials of the indenter-specimen pair for the analysed spherical indentation tests

The question about what materials are involved is a very important one, as it is one of the factors that can set the experiment outside of the assumptions of the rescaling method. In order for the rescaling formulae to be mathematically justified, the material of the indenter and the material of the specimen either have to be identical (thus having the same hardening exponent in the power-law approximation of the constitutive curve) or one of them has to be considerably harder than the other, as hard as to assume it is not deformable. It can be seen in Table 3-1 that this condition has been fulfilled for all spherical indentation tests, except the experiments by Goldsmith and Lyman (1960). The fact that the experiment was outside the assumptions of the rescaling method because of the materials involved is reflected in

the results we have obtained. Indeed, it can be seen that experiments *F, G* and *H* are the only ones where we have not obtained rescaling curves in very good agreement with the experimental data. In all other cases the agreement between the rescaling curves and the experimental data was at least satisfactory.

To conclude, we can say that the rescaling approach was proven to be consistently reliable for the experiments we have analysed, and it can be used to model the contact between nominally flat rough surfaces with asperities modelled as spheres of different radii. However, in order for the approach to be valid, the experiment giving the known contact solution for rescaling has to be performed within the assumptions of the rescaling theory. The materials for the contacting pair have to be chosen so that they are either identical, or one of the counterparts is very hard, as to be assumed it is perfectly rigid.

3.7 Discussion and conclusions

The results obtained are of interest for both materials science and tribology. We have seen the rescaling method is reliable when the considered indentation is within the bounds of the assumptions of the theory.

Applied to tribology, the rescaling method can be used for the Zhuravlev and Greenwood-Williamson models to be extended to non-spherical shapes of the asperities and non-linear stress-strain relation. For linear elastic materials and asperities described as $B_d r^d$, using Zhuravlev's approach and Borodich's rescaling formulae, one can obtain:

$$P = \lambda^{\frac{-1}{d}} \frac{P_1}{\delta_1^{\frac{d+1}{d}}} \frac{1}{N} \int_0^{\frac{x}{2}} \int_0^{\frac{x}{2}} [x - (\xi_1 + \xi_2)]^{\frac{d+1}{d}} n(\xi_1)\, n(\xi_2)\, d\xi_1\, d\xi_2 \qquad (3\text{-}27)$$

For physically non-linear materials, one cannot use the above formula because the stress-strain relations are not linear. However, as it was shown above, one can still employ the rescaling approach if materials have the same non-linearity of the stress-strain curve (the work hardening index is the same) or one of the materials is much harder than the counterpart and, therefore, we can describe its asperities as

absolutely non-deformable punches of $B_d r^d$ shape. In these two cases, one can again employ Zhuravlev's approach and the rescaling formulae. Then one has

$$P = \lambda^{\frac{\kappa-2}{d}} \frac{P_1}{\delta_1^{\frac{2+\kappa(d-1)}{d}}} \frac{1}{N} \int_0^{\frac{x}{2}} \int_0^{\frac{x}{2}} [x - (\xi_1 + \xi_2)]^{\frac{2+\kappa(d-1)}{d}} n(\xi_1)\, n(\xi_2)\, d\xi_1\, d\xi_2 \quad (3\text{-}28)$$

Chapter 4 - Physical and chemical mechanisms of energy dissipation corresponding to different scales of the models

In the dry friction models introduced by the author (which are described in sections 5.2, 5.6 and Chapter 6) friction is calculated as the dissipated energy over the sliding distance (4-1).

$$F_f = \frac{U_{dissipated}}{x} \quad (4\text{-}1)$$

Many mechanisms contribute to the amount of energy dissipated during frictional processes. Depending on the materials of the counterparts, roughness, and magnitude of stresses, the surfaces can undergo irreversible changes by ploughing, chipping of the asperities, scratching, and so on, which dissipate energy. Depending on the nature of the surfaces, their contamination, the presence of coatings, and the ambient chemical composition, the surfaces can engage in chemical interactions, leading to more energy being dissipated when sliding. The mechanical interactions between asperities, the propagation of acoustic waves, the presence of the molecular forces and capillary effects are other processes that increase the energy spent in friction. Therefore, we can express the dissipated energy by its different components (4-2).

$$F_f = \frac{U_{dissipated}}{x} = \\ = \frac{U_{chemical} + U_{vdW} + U_{mechanical} + U_{acoustic} + U_{capillary} + \cdots}{x} \quad (4\text{-}2)$$

However, as this work concerns modelling friction in vacuum, three sources of energy dissipation are taken into account:

- Breaking of metallic bonds – corresponding to the atomic scale
- Breaking of Van der Waals bonds – corresponding to the nano-scale
- Mechanical interlocking of asperities – corresponding to the micro-scale

The behaviour of the micro-asperities will reflect the mechanical interlocking component of the dissipated energy, while the behaviour of the nano-asperities will reflect the energy dissipated by breaking of chemical bonds and engaging in the van der Waals interactions. The energy lost in chemical and van der Waals interactions is modelled in a new way, and its novelty will be discussed in sections 4.1 and 4.2.

To calculate the coefficient of friction (COF), one can choose a relation that accounts for the molecular forces or one that does not. So the COF can be expressed using the one-term Amontons-Kotelnikov law $\left(\mu = \frac{F_f}{P}\right)$ or a two-term formulation following Coulomb $\left(\mu = \frac{F_f - A}{P}\right)$ or Derjaguin $\left(\mu = \frac{F_f}{P + S\,p_0}\right)$. A discussion of these classic laws of friction can be found in section 1.1.1. We need to adopt one of the two-term relations in order to account for the van der Waals forces.

Coulomb's term *A* did not have the meaning of adhesion, but if we used it in that sense, it seems like it would emphasize the contribution of adhesion tangentially to the surface. Even though our model accounts for the role adhesion has both tangentially and normally to the surface, as it will be shown further, its normal contribution is more important, thus justifying the use of Derjaguin's formulation. The friction coefficient can then be expressed as:

$$\mu = \frac{F_f}{(N + A)} = \frac{U_{dissipated}}{(N + A)\ x} \tag{4-3}$$

Where *N* is the normal force and *A* is the force of adhesion. We can further divide the COF into its different components:

$$\mu = \frac{U_{chemical}}{(N + A)\,x} + \frac{U_{vdW}}{(N + A)\ x} + \frac{U_{mechanical}}{(N + A)\ x} + \frac{U_{acoustic}}{(N + A)\ x} + \frac{U_{capillary}}{(N + A)\ x} + \cdots \tag{4-4}$$

or

$$\mu = \mu_{chemical} + \mu_{vdW} + \mu_{mechanical} + \mu_{acoustic} + \mu_{capillary} + \cdots \tag{4-5}$$

4.1 Energy dissipation by breaking of chemical bonds

Let us first discuss the dissipation of energy through the breaking of chemical bonds. Our model works on the assumption that surfaces establish chemical bonds over very small contacts, a process named cold welding. Whereas Bowden and Leben (1938) were the ones who introduced the concept of cold welding and interpreted the phenomenon at the macro-scale, the current approach uses it at the atomic scale.

Bowden and Leben considered the strength of the bonds established by cold welding is equal to the shear strength of the material. In our formulation, the dissociation of the chemical bonds corresponds to the atomic scale of the model. For very small contacts, the participating atoms engage in chemical interactions. When the body slides, these bonds are broken and a significant amount of energy is dissipated. In the model introduced in this work it is considered that only the tip of the contacting nano-asperities will be engaged in chemical bonds, whereas a greater number of atoms in the nano-asperity will be engaged in van der Waals bonds. This is the reason why the nano-asperity will be approximated as two slabs of different dimensions (see Figure 4-1).

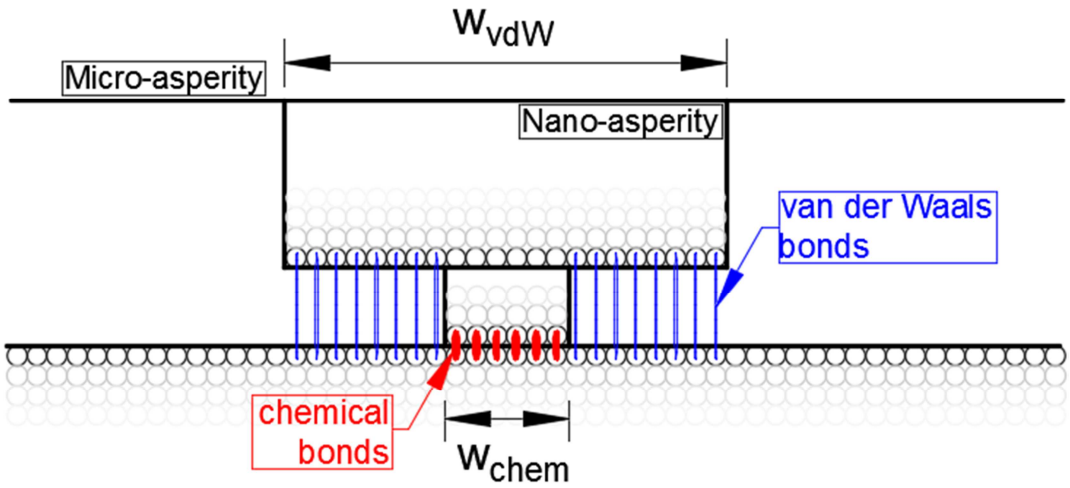

Figure 4-1 - Bonds established at nano-scale (figure scaled up vertically by a considerable factor)

The wider slab represents the van der Waals reactive area of the nano-asperity, and the smaller slab represents the tip of the nano-asperity, the chemically reactive area of the nano-asperity, where chemical contact is established. A number of n_{chem} atoms will be engaged in chemical bonds with the surface, calculated as in Equation (4-6).

$$n_{chem} = \left(\frac{w_{chem}}{D_{chem}}\right)^2 \quad (4\text{-}6)$$

where D_{chem} is the diameter of the metallic bond between the atoms of the slider and the surface. Then the energy dissipated by breaking all the chemical bonds established by the surface atoms of one nano-asperity will be:

$$U_{chem_{nano}} = n_c \, U_{chem_1} \quad (4\text{-}7)$$

where U_{chem1} is the energy dissipated by the dissociation of one chemical bond.

4.2 Energy dissipation by breaking of Van der Waals bonds

Evidently, the van der Waals forces have been considered in many models. The novelty of our approach lies in the fact that adhesion plays a double role. Firstly, in the direction normal to the surface, adhesion acts by increasing the area of true contact. Secondly, tangentially to the surface, molecular adhesion represents a resistance that has to be overcome when sliding occurs, leading to energy dissipation. The contribution of the van der Waals forces to the shearing of the bonds between particles is a very recent concern for the physical chemists (Carrasco et al. 2013).

Adhesion is described using an approach similar to the Maugis-Dugdale step-function description of the adhesive zone (Figure 4-2) (a more detailed description of the Maugis-Dugdale model can be found in section 1.8.6).

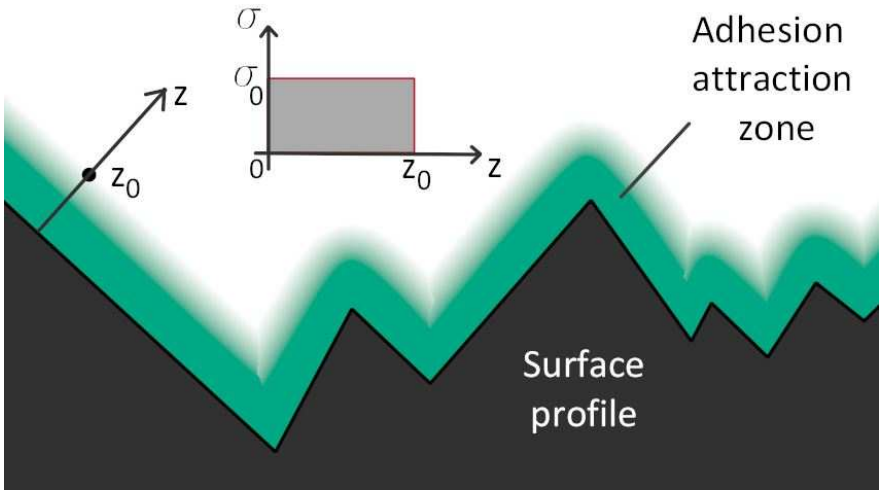

Figure 4-2 - The adhesive layer

Concerning the thickness of the adhesive layer, there is experimental evidence of the force of adhesion influencing friction and the jump-off forces up to 150nm from the surface (Lessel et al. 2013). It is also known that when the pair potentials corresponding to the London, Keesom and Debye forces are summed up, the result is significant even for separations of 100nm or more (Pollock 1992). However, the magnitude of the force of adhesion rapidly decays over this distance. One way to model this using the idea of Maugis would be to consider a 'multi-step' adhesion function, i.e. to consider more than one layer with varying intensity of the force of attraction. However, to minimise the computational cost, in the current work only the bottom layer will be considered, where adhesion is the greatest and can cause nano-asperities to snap into contact. Therefore the thickness of the adhesive layer is assumed here to be 5nm.

As stated before, one of the effects of the van der Waals forces is the attraction between the surfaces. Therefore, whenever one nano-asperity enters into the range of the van der Waals forces, it will snap into contact. As a consequence, the tip of the nano-asperity will engage in chemical interactions, as described in the previous section. Due to adhesion, the nano-asperity will also be attracted to the counter-surface with a force equal to the snap-off force calculated using the Boussinesq-Kendall solution for a flat punch. In the current model it is assumed that, while the tip of the nano-asperity is within the adhesive layer, the attraction force is constant. When the nano-asperity leaves the range of the van der Waals forces, it snaps out of contact.

The second role of the van der Waals forces, manifested tangentially to the sliding, is the resistance to relative motion. We consider that while the nano-asperity is within the adhesive layer it engages also in molecular interactions. In a simplistic manner, we calculate the number of atoms engaged in these interactions as we have calculated the number of atoms engaged in chemical interactions. As illustrated in Figure 4-1, we consider one layer of atoms on the width w_{vdW} of the nano-asperity interacts with the corresponding atom layer on the counter-surface. The number n_{vdW} of atoms involved is calculated using equation (4-8).

$$\mathrm{n}_{vdW} = \left(\frac{w_{vdW}}{D_{chem}}\right)^2 \quad (4\text{-}8)$$

We consider the molecular interactions between these atoms oppose the relative motion between the counterparts. Because of this resistance, additional energy is dissipated when sliding. Knowing $U_{vdW,1}$ is the energy spent to tangentially break the attraction between two atoms, we calculate the total energy dissipated per nano-asperity due to van der Waals interaction $U_{vdW,nano}$ as shown in equation (4-9).

$$U_{vdW\,nano} = n_{vdW}\, U_{vdW\,1} \quad (4\text{-}9)$$

4.3 Energy dissipation by mechanical interlocking of asperities

The dissipated energy by mechanical interlocking of asperities is the energy lost when the asperities of the contacting counter-parts deform mechanically. The mechanical behaviour of the micro and nano-asperities will be discussed in sections 4.3.1 and 4.3.2. The description of the way we calculate the total energy spent in mechanical interlocking of asperities will follow in section 4.3.3.

4.3.1Mechanical behaviour of the micro-asperities

Due to the small dimensions and deformations of the nano-asperities, the greatest part of the energy lost in mechanical deformation comes from the micro-asperities. As it will be shown in the section about the mechanical behaviour of the nano-asperities, their deformation before reaching the incompressibility threshold is insignificant compared to the deformation that the micro-asperities experience.

In our models, the micro-asperities will have elastic-perfectly plastic behaviour; a sketch of the material curve is given in Figure 4-3.

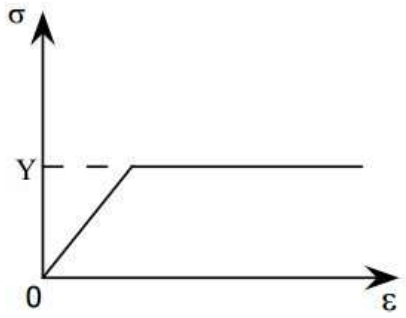

Figure 4-3 - The stress-strain curve for the micro-asperities

The micro-asperities are modelled as rods subjected to compression and deform elastically by:

$$\delta = \frac{PL}{EA} \qquad if \quad \frac{P}{A} \leq \sigma_y \tag{4-10}$$

where *P* is the force to which a micro-asperity is subjected, *L* is its length, *E* the corresponding elastic modulus and *A* is the area of its cross section.

After reaching the yield strength the micro-asperities will behave perfectly plastically; constant stress is assumed even if strain increases. In this way, the excess load of the collapsing asperity is taken by the other asperities in contact.

We assume that when a micro-asperity is stressed beyond its yield strength, the contact with the counter surface is very intimate and all nano-asperities on its tip establish full contact, engaging in both chemical and van der Waals interactions.

4.3.2 Mechanical behaviour of the nano-asperities

The mechanical behaviour of the nano-asperities reflects the **Polonsky-Keer effect** presented also in section 1.4. The finding of Polonsky and Keer (1996a, 1996b) is that, in the case of a very small micro-contact, its behaviour becomes purely elastic. Based on this assumption, the nano-asperities will have no plastic deformation and will always return to their initial shape. So, after reaching the incompressibility threshold, the load is transferred to the micro-asperity and, after the load is removed, the nano-asperity comes back to the initial shape. This incompressibility threshold is calculated based on the bilinear approximation of the stress-strain curve obtained based on the Lennard-Jones potential, as it will be shown below.

We will use the 12-6 Lennard-Jones potential, which describes the interaction between two molecules (atoms), separated by distance *r*:

$$U_{LJ12-6}(r) = 4\varepsilon\left[\left(\frac{\sigma}{r}\right)^{12} - \left(\frac{\sigma}{r}\right)^{6}\right] \qquad (4\text{-}11)$$

In (4-11), σ and ε are the specific Lennard-Jones parameters that are different for different interacting atoms and are chosen to fit the physical properties of the material. ε is the minimum value of the potential and it is a measure of how strong is the interaction between two particles. At this point of minimum potential, the interaction force is zero. The distance that corresponds to minimum potential is thus the equilibrium separation ρ. σ is the separation between two particles when the potential is null (note that in this use of the symbol σ has the dimension of distance). A plot of the 12-6 potential curve is shown in Figure 4-4.

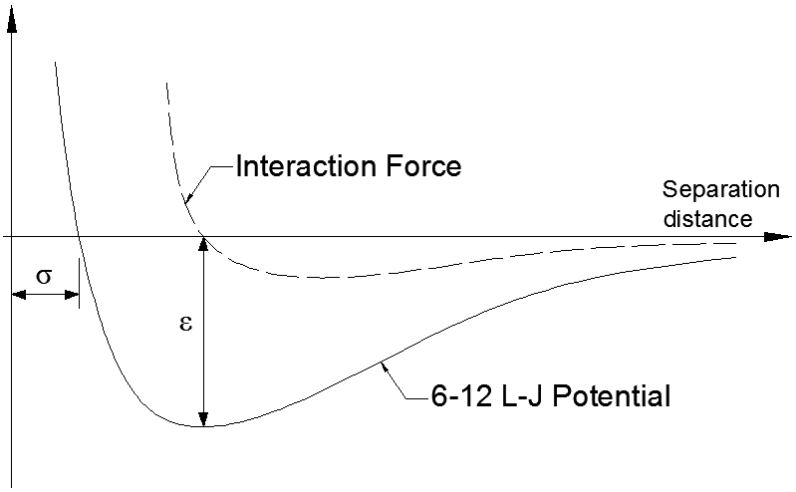

Figure 4-4 - Schematic representation of the 6-12 Lennard-Jones potential

The behaviour of the interaction between two particles as described by the 12-6 Lennard-Jones potential can be summarized as: two particles will be attracted to one another until they reach an equilibrium separation; if they are brought even closer, the particles will experience repulsion.

The interaction force can be obtained by differentiation of the potential with respect to the separation distance *r* (equation (4-12).

$$F_{LJ}(r) = 24\varepsilon\left[\frac{2\sigma^{12}}{r^{13}} - \frac{\sigma^{6}}{r^{7}}\right] \qquad (4\text{-}12)$$

To obtain the stress-strain curve for the nano-asperities, we will use the 12-6 Lennard-Jones potential to model the interaction between two metallic atoms. Let us take 2 copper atoms as an example. We know the radius of one copper bond is 1.28 Angstrom (Wells 1984). Thus, the diameter of one metallic bond is D_{chem} = 2.56Å, which can be considered the equilibrium separation ρ where the force is zero. Knowing this we can easily find the separation where the potential is null from the following relation:

$$F_{LJ}(D_{chem}) = 24\varepsilon\left[\frac{2\sigma^{12}}{D_{chem}^{13}} - \frac{\sigma^{6}}{D_{chem}^{7}}\right] = 0 \qquad (4\text{-}13)$$

From (4-13), we obtain $\sigma = D_{chem}\sqrt[6]{\frac{1}{2}} = 2.28\text{Å}$.

We obtain the stress Σ resulting from the total compression force between two half-spaces by multiplying the force obtained for a single atom-pair by the number of atoms per unit area N_A (square meter). The average area A_1 corresponding to one atom is $A_1 = 1/N_A$. We can express stress Σ as:

$$\Sigma = F_{LJ_{12-6}} N_A \qquad (4\text{-}14)$$

Young's modulus is equal to the slope of the stress-strain curve:

$$E = \frac{d\sum U_{LJ12-6}}{de} = \frac{d\sum U_{LJ12-6}/dz}{de/dz}$$

when the separation distance equals the equilibrium distance ρ.

Because the strain e is

$$e = -\frac{(z-\rho)}{\rho}$$

with z denoting the current position and ρ denoting the equilibrium distance, one can obtain

$$\frac{de}{dz} = -\frac{1}{\rho}$$

We can then express Young's modulus E as follows:

$$E = \frac{72\varepsilon/\rho^2}{1/\rho} N_A = \frac{72\varepsilon}{\rho} N_A = 120 \cdot 10^9 Pa$$

From the above we can easily find the depth of the potential for a Cu-Cu atom pair, as shown below:

$$\varepsilon = \frac{120 \cdot 10^9}{72 N_A} 2.56 \cdot 10^{-10} = \frac{120 \cdot 10^9}{1.53 \cdot 10^{19} \cdot 72} 2.56 \cdot 10^{-10} = 2.79 \cdot 10^{-20} J$$

We can now plot the potential curve modelling the interaction between two Cu atoms (Figure 4-5).

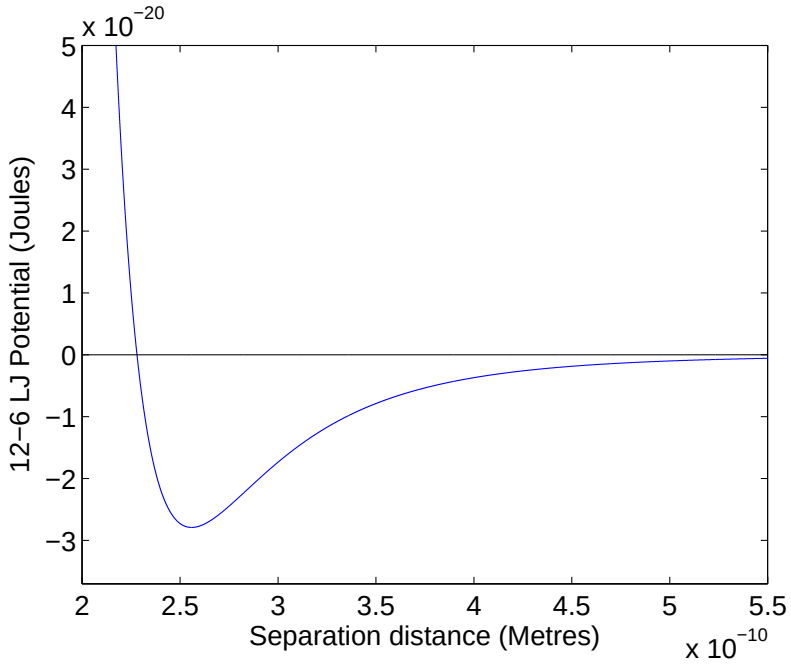

Figure 4-5 – The 12-6 Lennard-Jones potential for two Cu atoms

The resulting stress-strain curve and the approximation used are plotted in Figure 4-6.

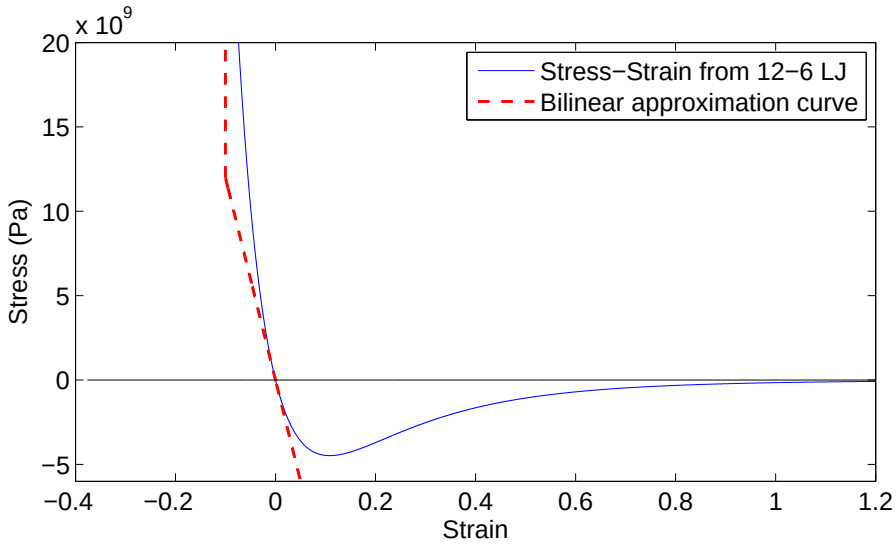

Figure 4-6 – The stress-strain curve for nano-asperities

It can be seen that the stress-strain curve is approximated as a bilinear elastic – perfectly rigid curve. When compression starts, the nano-asperity deforms according to Hook's law. When it reaches a certain strain threshold, the linear approximation of stress-strain relation becomes meaningless and the load is transferred from the nano-asperity to the micro-asperity. For the considered case of copper nano-asperities, the threshold strain is 10%, as illustrated in Figure 4-6.

4.3.3 Calculation of the energy dissipated by mechanical deformation of asperities

We have seen in the previous sections that the mechanical behaviour of the micro-asperities follows an elastic - perfectly plastic stress-strain curve, while the behaviour of the nano-asperities follows an elastic - perfectly rigid stress-strain curve.

Let us suppose that the slider moves from point A to point B. If one asperity is compressed due to the mechanical interaction between the counter-parts, without reaching the yielding limit, the elastic strain energy is computed according to (4-15).

$$\Delta U_{elastic,1} = \frac{1}{2}\frac{EA_c}{L}\delta_e^2 \qquad (4\text{-}15)$$

In (4-15) δ_e is the change in the state of deformation for one asperity, when the slider moves from point A to point B, A_c is the cross-sectional area of the asperity and L is its

length. If the asperity is compressed beyond its elastic limit, to the elastic strain energy we have to add the energy:

$$\Delta U_{plastic,1} = \sigma_y \, \varepsilon_p \, V_d \qquad (4\text{-}16)$$

In (4-16) ε_p is the plastic strain and V_d is the volume of deformed material.

The total energy dissipated in mechanical deformation will be the sum of all the strain energies of all asperities that are compressed. The energy dissipated by interlocking of asperities will be calculated for every time-step, when a change in the deformation state of the asperities occurs.

4.4 A hand-calculation of the apparent coefficient of friction for one yielded micro-asperity

For the sake of clarification of the main concepts used, we will consider an example and calculate the coefficient of friction for one plastically deformed micro-asperity, considering that all the nano-asperities on its tip engage in chemical and van der Waals bonds.

A surface is measured by profilometer to obtain the micro-scale roughness and by AFM to obtain the nano-scale roughness. After calculating the geometry of the nano-asperities as described in section 6.2.1, the following characteristics are obtained:

The width of the micro-asperity	$w_{micro} = 13.5\mu m$
The van der Waals interaction width of one nano-asperity	$w_{vdW} = 430nm$
The chemical interaction width of one nano-asperity	$w_{chem} = 161nm$
The number of nano-asperities per micro-asperity	$N_{nm} = 100$

Table 4-1 - Statistical geometrical charactersitics of the copper surface

We assume that both the interacting counterparts are made of copper with a yield strength $\sigma_y = 276\ MPa$.

The energy lost by dissociation of one mole of Copper is 202 kJ/mole (Darwent 1970). Since one mole of Copper contains 6.0221413 x 10^{23} atoms, the energy lost when breaking one metallic bond between two Copper atoms is $U_{chemDissoc}$ = 3.3543 x 10^{-19} Joules.

It is hard to find any record of the energy of one van der Waals 'bond' between the copper atoms. Usually the energy of the van der Waals interaction is estimated to about 2 to 4 kJ/mol. Therefore the energy released by breaking one van der Waals 'bond', $U_{vdWdissoc}$, will be considered 100 times less than the chemical bond dissociation energy. Then, in our case $U_{vdWDissoc}$ = 3.3543 x 10^{-21} Joules.

The radius of one Copper metallic radius is 1.28 Angstrom (Wells 1984). Thus, the diameter of one metallic bond is D_{chem} = 2.56 *Angstrom*.

If we consider the tip of the nano-asperity has the width w_{chem} = 161 nm (see Table 4-1), the number of metallic bonds per one such nano-asperity is:

$$N_{chem} = \left(\frac{W_{chem}}{D_{chem}}\right)^2 = 395.523$$

In order to find the number of vdW bonds per nano-asperity, we divide the width of the van der Waals contact to the diameter of the chemical bond; the density of the atoms that create vdW bonds is the same as the density of the atoms involved in metallic bonds. Therefore the average number of van der Waals bonds per one nano-asperity is:

$$N_{vdW} = \left(\frac{W_{vdW}}{D_{chem}}\right)^2 = 2.819.906$$

If the micro-asperity moves over the length *x*, the breaking of metallic and vdW bonds will dissipate the energy:

$$U_{dissip} = N_{nm}\left(N_{chem}U_{chemDissoc} + N_{vdW}U_{vdWDissoc}\right)\frac{x}{D_{chem}}$$

This is the energy dissipated by the force of friction when moving over a distance *x*. So we can write:

$$U_{dissip} = F_f\, x \rightarrow F_f = \frac{U_{dissip}}{x}$$

where F_f is the force of friction. But the force of friction can be written as:

$$F_f = \mu_{aparr}(F_{ext} + F_{adh})$$

where F_{ext} is the external force compressing the micro-asperity and F_{adh} is the force of adhesion. Then the apparent coefficient of friction can be expressed as:

$$\mu_{appar} = \frac{U_{dissip}}{(F_{ext} + F_{adh})\, x}$$

Because it was assumed the micro-asperity is compressed beyond its elastic limit and the mechanical behaviour of the micro-asperity is elastic/perfectly plastic, the external force is:

$$F_{ext} = f_y\, W_{micro}^2 = 50.3\, mN$$

The force of adhesion for one nano-asperity is calculated as the pull-off force according to non-slip Boussinesq-Kendall theory:

$$F_{adh1} = \sqrt{8\,\pi\,w_{12}\,E^{*}C_{NS}\,a_1^3} = 4.36\,\mathrm{x}\,10^{-5}N$$

W_{12} is the van der Waals energy between two plates calculated as (Israelachvili 1992, Hamaker 1937):

$$w_{12} = \frac{A_{12}}{12\,\pi\,D_0^2} = 0.502\,J/m^2$$

Here A_{12} is the Hamaker constant and D_0 is the separation distance (in this case, when the nano-asperities are smashed against the counter surface, the separation distance is the dimeter of the metallic bond). For Copper, $A_{12} = 2.7\,\mathrm{x}\,10^{-19}\,J$ (Eichenlaub et al. 2002, Leite et al. 2012, Matope et al. 2013) and $D_0 = 2.56$ Å.

Hamaker constant is defined as (Hamaker 1937):

$$A_{12} = \pi^2\rho_1\rho_2 C$$

Where ρ_1 and ρ_2 are the number of atoms per unit volume, and C is the London-van der Waals constant. Hamaker's approach of calculating the van der Waals energy between bodies was based on pairwise integration, as Bradley (1932) had done before him for spherical particles. Hamaker (1937) presents the results in a manner suitable for numerical calculations, and extends the method for other surfaces. Hamaker's approach assumes the forces are additive and non-retarded.

Young's modulus for Copper is E = 120 GPa, and Poisson's ration is ν = 0.355, thus the reduced modulus is:

$$E^{*} = \frac{E}{2\,(1-\nu^2)} = 68.7\,GPa$$

The no-slip coefficient (Borodich et al. 2014) is:

$$C_{NS} = \frac{(1-\nu)\,ln(3-4\,\nu)}{1-2\,\nu} = 1.017376$$

The radius of contact a_1 is approximated as half the width of the vdW interaction step of the nano-asperity:

$$a_1 = \frac{W_{vdW}}{2} = 215\ nm$$

Knowing the force of adhesion for one nano-asperity F_{adh1}, the total force of adhesion can be calculated, since it is assumed that all nano-asperities on the tip of the micro-asperities are in close contact with the counter surface:

$$F_{adh} = N_{nm}\, F_{adh1} = 4.36 \text{ x } 10^{-3} N$$

The apparent coefficient of friction can now be calculated:

$$\mu_{appar} = \frac{U_{dissip}}{(F_{ext} + F_{adh})\, x}$$

$$\mu_{appar} = \frac{N_{nm}(N_{chem} U_{chemDissoc} + N_{vdW} U_{vdWDissoc}) \frac{x}{D_{chem}}}{(F_{ext} + F_{adh}) x}$$

$$\mu_{appar} = \frac{N_{nm}(N_{chem} U_{chemDissoc} + N_{vdW} U_{vdWDissoc})}{(F_{ext} + F_{adh}) D_{chem}} = 1.0156$$

4.4.1 Discussion

The estimation of the apparent COF is in very good agreement with the experimental apparent coefficient of sliding friction between copper and copper. As found in literature, the experimental apparent coefficient of sliding friction between copper and copper is in the range 0.8 - 1.2 (Holmberg and Matthews 2009). However, the agreement could be due to compensation between the dissipation mechanisms we did not consider and the fact that we considered the nano-asperities establish chemical bonds on their whole contact area, whereas in reality the contamination of surfaces reduces the area of chemical interaction.

As it can be seen, our result shows that the greatest contribution to the dissipated energy in friction is the energy lost in breaking the chemical bonds. This is closely dependent on the width of the chemical interaction step of the nano-asperity, w_{chem}, because we find the number of broken metallic bonds by dividing w_{chem} to the diameter of one chemical bond. So the way the nano-surface is interpreted has the greatest impact on the resulting coefficient of friction.

The approach described used to calculate the friction force is incorporated in the models developed by the author, which are described in sections 5.2, 5.6, and Chapter 6.

(Intentionally left blank)

Chapter 5 - Hierarchical, multi-scale and multi-level models of dry friction

5.1 Introduction. Basic definitions: multi-scale, hierarchical and multi-level

This chapter will discuss existing and original models with frequent reference to whether or not they are multi-scale, multi-level or hierarchical. Therefore it is appropriate to begin by defining the meaning of these terms, as they will be used from here on.

Meaning of scale and multi-scale

The term 'scale' is related to the capabilities of the system to model different physical-chemical mechanisms of interactions between surfaces. For instance, a model where the nano-scale asperities are mainly responsible for molecular and chemical interactions and the micro-scale asperities are responsible for modelling the mechanical interlocking of asperities in friction would be multi-scale, because the system is capable of modelling more than one mechanism of interaction. The scale considered can be changed by changing the considered characteristic length of the processes involved in friction. The following distinctions will be used:

1. Atomic scale reflects the phenomena specific to the characteristic length $l \leq 1nm$, namely chemical interactions between surfaces.
2. Nanoscale reflects phenomena specific to the characteristic length $1nm \leq l \leq 1\mu m$, namely the van der Waals bonds involved in the interaction between surfaces.
3. Microscale reflects phenomena specific to the characteristic length $1\mu m \leq l \leq 1mm$, namely the mechanical interlocking of asperities.
4. Macroscale reflects phenomena specific to length scale over $1mm$, including the behaviour of the bulk of the body, which will couple the micro-asperities together.

Meaning of multilevel

The question of whether a surface topography model may be characterized as multilevel is related to its structure and to whether the asperities of the k^{th} generation have the same height of not. If all asperities of the same generation have the same height, then the model would be single-level, even if it was multi-scale, i.e. the configuration of the model would allow the single-level asperities to be engaged in mechanisms of interactions between surfaces specific to at least two length-scales. If the asperities of the k^{th} generation have different heights, then the model is multi-level.

Meaning of hierarchical

A model will be called hierarchical if it has at least two asperity generations, and the 'parent' asperities have at least two descendants. It is thus not enough for the asperities to be situated on top of each other to have a hierarchy. In order for the model to be hierarchical there has to be at least one subdivision in the asperity generation.

Section 5.2 will start a discussion about different models of roughness and the above definitions will then be illustrated. The discussion will span over the remainder of this chapter and will include two models developed by the author, namely the single-asperity model, described in section 5.2, and the multi-scale hierarchical model described in section 5.6. These models use an original formulation of the force of friction and the energy dissipated in sliding, which are described in Chapter 4.

5.2 Simulations of friction by multi-scale non-hierarchical model surface asperity

This section will start a critical discussion of existing dry friction models illustrating the scale, level and hierarchy concepts that have been introduced in section 5.1.

We will start with the simple example of a single-asperity model, represented by a rod consisting of different scales having the same width but no subdivision from scale to scale, as shown in Figure 5-1. The model is multiscale, but it is not multilevel, as the asperities of the same generation are on the same level (being only one). Also, this

model is not hierarchical. To be called hierarchical the model needs to have more than one micro-asperity or more than one nano-asperity.

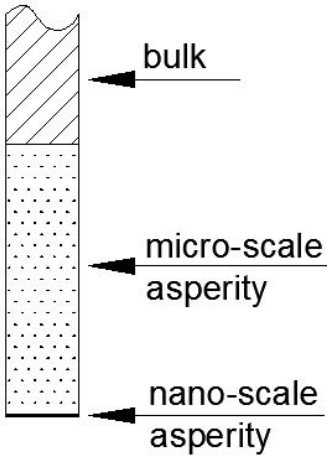

Figure 5-1 - Multiscale, single-level, non-hierarchical model example

This can be a model of one asperity rubbing against a counter-surface that can be easily formulated for elastic deformation using Hooke's law. Suppose the model is formulated for a fixed gap between the top of the rod and the mean-line of the counter-surface. The known parameters are:

- H_1, H_2, H_3 - the heights of the nano-asperity, micro-asperity and the considered bulk section of the slider
- E_1, E_2, E_3 - the values of the Young's modulus of the nano-asperity, micro-asperity and the considered bulk of the slider
- A - the cross-sectional area of the three sections of the slider
- G - the gap between the top of the slider and the mean-line of the counter-surface
- h - the height of the asperity of the counter-surface

A sketch of the deformed shape of the asperity at contact with the counter-surface can be seen in Figure 5-2.

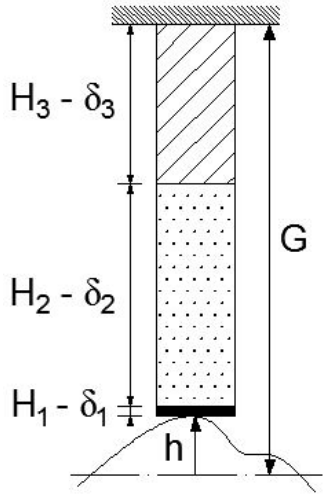

Figure 5-2 - Deformed state of a single-asperity model at contact with the counter-surface

From the deformed geometry, it can be written:

$$\mathrm{h} + (\mathrm{H}_1 - \delta_1) + (H_2 - \delta_2) + (H_3 - \delta_3) = G \tag{5-1}$$

The force equilibrium equation can be written as:

$$\delta_1 \frac{E_1 A}{H_1} = \delta_2 \frac{E_2 A}{H_2} = \delta_3 \frac{E_3 A}{H_3} \tag{5-2}$$

From equation (5-2) δ_2 and δ_3 can be expressed in terms of δ_1 and substituted in equation (5-1) to obtain:

$$\delta_1 = \frac{h + H_1 + H_2 + H_3 - G}{1 + \frac{E_1 H_2}{E_2 H_1} + \frac{E_1 H_3}{E_3 H_1}} \tag{5-3}$$

If δ_1 is known, δ_2 and δ_3 can be found by:

$$\delta_2 = \delta_1 \frac{E_1 H_2}{E_2 H_1} \text{ and } \delta_3 = \delta_1 \frac{E_1 H_3}{E_3 H_1} \tag{5-4}$$

This model can be further developed by incorporating the Polonsky-Keer effect, the influence of the force of adhesion and the energy dissipated by breaking the chemical and van der Waals bonds, as described in Chapter 4.

Let us implement these features and run the single-rod model against a surface under a fixed load. The material for the rubbing surfaces is copper. A force has been applied at the top of the slider, compressing the rod. In order to remain in the elastic domain with the deformation at all the scales, the magnitude of the load has been chosen as *P*

= 0.9 σ_y A_n, where σ_y and A_n are the yielding strength and the cross-sectional area of the nano-asperity. The bulk section of the slider is considered to have the Young's modulus equal to copper's Young's modulus, and the material at the micro and nano-scale is considered to have the contact modulus.

The resulting coefficient of friction has a value of 6.23 and is constant for all the simulation time. Firstly, the magnitude of the coefficient of friction may seem very high. However, such a high magnitude is to be expected, as all the atoms on the tip of the nano-asperity are considered to be engaged in chemical bonds; when these chemical bonds are broken, large amounts of energy are dissipated. In real life, surfaces are contaminated with oxides, water vapours or other particles, so surfaces will not perfectly clean to allow all atoms to establish chemical bonds. Furthermore, 6.23 is the value of the real coefficient of friction, rather than the apparent coefficient of friction, as there is no distinction between the nominal and the true contact area. All nano-asperities of the slider (being just one) are engaged in contact with the counter-surface at all times.

Secondly, it is reasonable to expect a constant coefficient of friction because all the components of the dissipated energy remain constant during friction. There is no variation in the state of deformation of the slider, as it is subject to the same compressing force through all the simulation, and there are no other asperities to which to shift the load due to different heights of asperities on the counter-surface. The energy dissipated by dissociation of chemical bonds and molecular attraction does not introduce any variation in the dissipated energy either, as the same area (the nano-asperity tip) is always engaged in chemical and van der Waals interactions. The plot in Figure 5-3 confirms the dissipated energy is constant for all mechanisms taken into account.

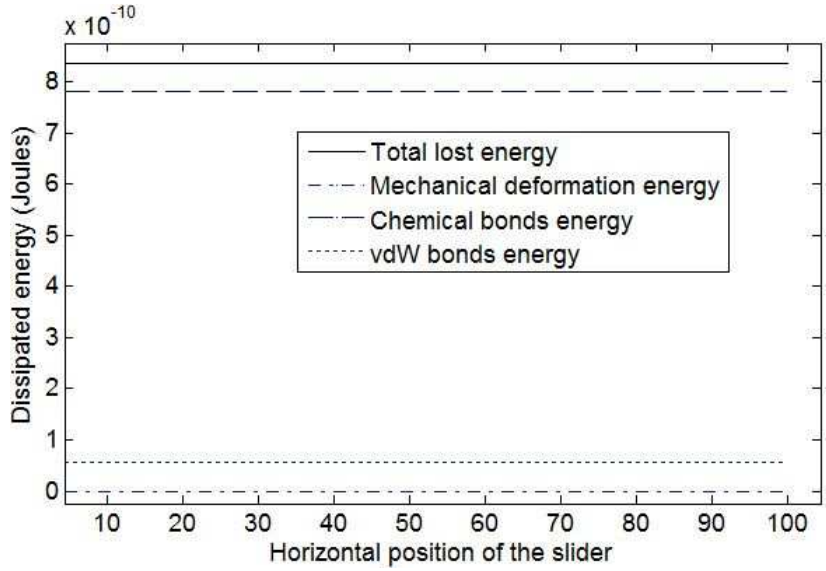

Figure 5-3 - Contribution of the different energy dissipation mechanisms

It can also be seen that there is no energy dissipation through mechanical interlocking of asperities as there is no change in the deformation state of the slider because the external load is constant. The greatest contribution to friction is the energy lost by breaking of the chemical bonds, while the breaking of the van der Waals bonds accounts for roughly 10% of the total energy loss.

Even though very simple, this model can be valuable for describing the interaction between a single asperity and a counter-surface. However, it cannot reflect the interaction between two real rubbing surfaces as it cannot model the interplay between their asperities. In the following sections multi-asperity models will be analysed.

5.3 Multi-asperity models of surface roughness

5.3.1 Prandtl-Tomlinson model

Even though widely attributed to Tomlinson (1929), the model about the contribution of molecular forces to friction we are going to discuss here cannot be found in his paper. As Popov (2010) notes, the model has been introduced by Prandtl (1928) and was first used to model plastic deformations in crystals. For this reason we will refer to it as the 'Prandtl-Tomlinson model.' The simplest formulation describes the movement of a point mass in a periodic potential, pulled by a constant force (Figure 5-4).

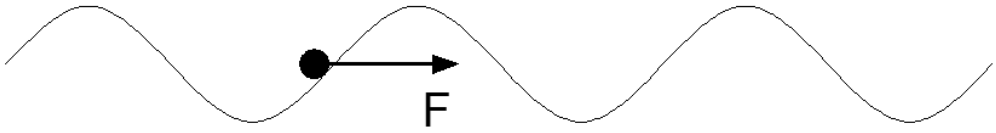

Figure 5-4 - Tomlinson model

The equation of motion of the point mass is:

$$m\ddot{x} = F - \eta\dot{x} - N\sin kx \tag{5-5}$$

where x is the coordinate of the body, m is the mass of the body, F is the external constant force, η is the damping factor, N is the amplitude of the periodic force and k is the wave number. The Prandtl-Tomlinson model reflects the distinction between static and kinetic friction. The minimum force that will produce movement of the point mass is the force of static friction (N in (5-5)). After the body starts to move it will keep sliding even for a smaller force (the force of kinetic friction), because of the energy it already possesses due to its inertia and due to the damping component.

The model thus offers a qualitative description of the friction phenomena. The point mass would represent a surface asperity and the periodic potential would represent the resistance that the asperity has to overcome rubbing against a counter-surface. Because such a uniform roughness profile can hardly be met in a real life scenario, Filippov and Popov (2007) have extended the model for a more general shape.

Prandtl (1928) also introduced another version of the model where the mass is not pulled by a constant force but through a spring moving horizontally. In this case the equation of motion becomes (Popov 2010):

$$m\ddot{x} = c(x_0 - x) - \eta\dot{x} - \frac{\partial U}{\partial x} \tag{5-6}$$

Where c is the stiffness of the pulling spring, x_0 is the position of the free end of the spring, and U is the periodic potential.

The spring-generalization of the Prandtl-Tomlinson model has been often used in nanotribology to model the friction between an AFM tip and a surface. The spring takes into account the stiffness of the cantilever of the AFM. But this model has been further extended in order to account for both the stiffness of the cantilever and the

stiffness of the tip by introducing another spring and mass in the system, as it can be seen in Figure 5-5.

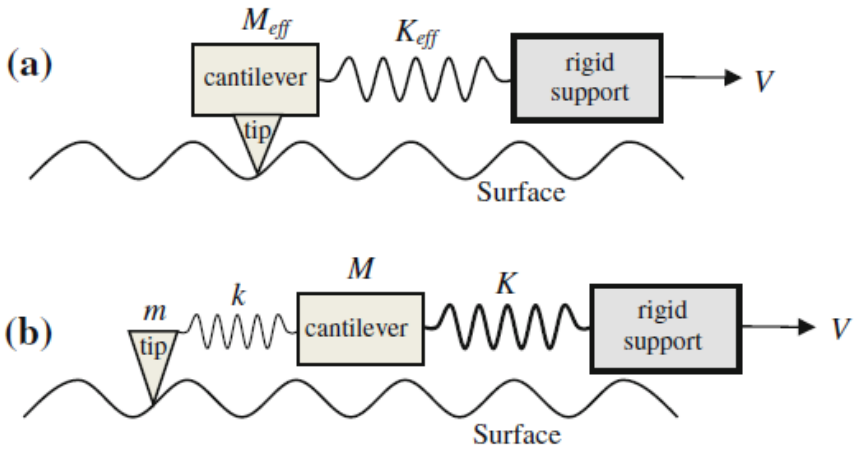

Figure 5-5 - One spring and two springs versions of Tomlinson model (from Lu et al. 2011)

By a straight-forward analytical comparison of these two models under quasistatic conditions, one can conclude that the solutions given by the two models are identical (Lu et al. 2011).

5.3.2 Zhuravlev and Greenwood-Williamson models

After Tomlinson's model was introduced, Davidenkov, the supervisor of Zhuravlev, assigned to him the task of explaining the Amontons-Kotelnikov friction law (Borodich 2007). In 1940 he introduced a model of dry friction for nominally flat surfaces where asperities were represented as independent elastic spherical caps, of the same radius, with random height distribution, that deform according to Hertz theory (Zhuravlev 1940).

Greenwood and Williamson (1966) improved on Zhuravlev's model and introduced a Gaussian asperity height distribution, as well as plastic deformation of asperities. The assumption that the asperities have the same radius of curvature was left unchanged. Greenwood and Williamson (1966) consider the contact between a rough surface and a plane, but their approach is very similar to that of Zhuravlev.

A more detailed description of the Zhuravlev and Greenwood-Williamson models is given in section 1.7. A Zhuravlev-Greenwood-Williamson type model is an uncoupled multi-asperity, multi-level model. The model is not multi-scale, as it does not consider

multiple physical mechanisms of energy dissipation, and it is not hierarchical as it has only one asperity generation.

5.3.3 Bush, Gibson and Thomas (BGT) model

Bush et al. (1975) have further extended the multi-asperity model introduced earlier by Zhuravlev (1940) and then improved by Greenwood-Williamson (1966). In the BGT model the asperities are represented as paraboloids and their statistical characteristics (height distribution, radii of curvature) are interpreted using the statistical theory of isotropic random rough surfaces developed by Longuet-Higgins (1957) and Nayak (1971). Consequently, the multi-scale nature of the surface roughness is taken into account and the linear dependence between the real area of contact and the load is obtained only for small loads. However, the asperities are not coupled and they deform only elastically, following Hertzian contact theory. A thorough description of the model and comparison with other multi-asperity models is given by Carbone and Bottiglione (2008).

We have to note that, even though the BGT model accounts for the multi-scale nature of the rough surfaces, it cannot be considered multi-scale in the sense defined in section 5.1 because it does not model any other physical phenomena than the elastic deformation of the asperities. The model is however multi-level, but it is not hierarchical.

5.3.4 The Kragelsky rod-assembly model

Kragelsky developed a multi-asperity model using an assembly of elastic rods of constant cross section (Kragelsky et al. 1982), as illustrated in Figure 5-6. According to the definitions that opened the current chapter, this model of uncoupled asperities is not multi-scale (because only one physical mechanism is considered, i.e. the deformation of the rods) and thus it cannot be hierarchical, as it has only one generation of asperities. However, the model can be considered multi-level because the asperities of the same generation have different heghts.

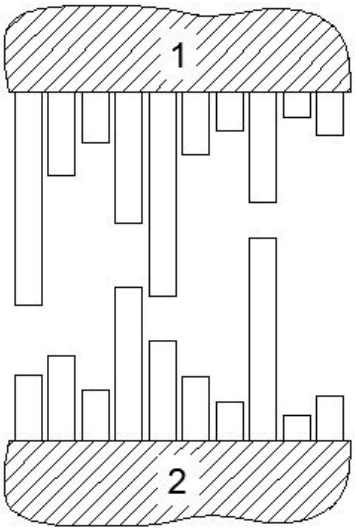

Figure 5-6 - Kragelsky rod assembly model

Kragelsky derives the formula by which the approach between the surfaces relates to load and obtains:

$$N = A_c \gamma_1 \gamma_2 \frac{K a^3}{6} \tag{5-7}$$

N is the normal load, A_c is the contact area and a is the approach between surfaces. γ_1 and γ_2 are factors that depend on the representation of the distribution function of the asperities, and K stands for the stiffness of the rods. Kragelsky (1948) stated that the asperity heights distribution has to be Gaussian.

Equation (5-7) also shows that the contact area depends on the load in a linear fashion. However each asperity deforms independently, without any influence on the neighbouring asperities.

5.3.5 Sergienko - Bukharov model

Building on the work of Kudinov (1980), Sergienko and Bukharov (2015) developed a model that reflects the interrelation of normal and tangential micro-oscillations between two rubbing surfaces. The model consists in a rigid body resting on an assembly of springs which simulate the asperities (see Figure 5-7). The model reflects oscillations both normally and tangentially to the movement direction because any horizontal impulse given to the rigid body will be accompanied by oscillations in the normal direction. As the body descends, due to the normal oscillations, it will come in contact with more springs. Greater normal oscillations will give smaller friction force,

due to the higher mean level of the mass and the decrease in the number of contacting springs.

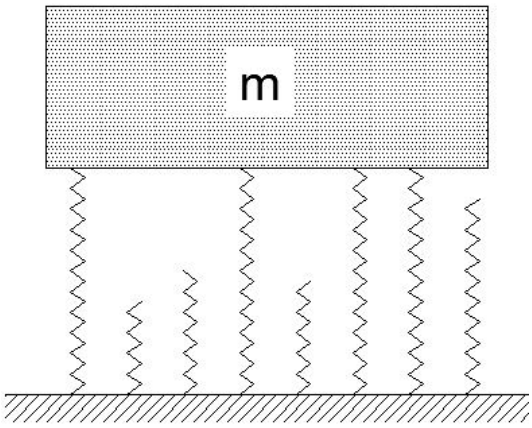

Figure 5-7 – Sergienko - Bukharov model

One good feature of this model is that it takes into account the dynamic lift of the slider, which is an important phenomenon, as first noted by Tolstoi (1967). Like the one developed by Kragelsky (1948), this is a multi-level model, but not multi-scale, nor hierarchical. The asperities are uncoupled as well, because the springs deform independently.

5.3.6 The Bristle Model

Haessig and Friedland (1991) have introduced a model where the interaction between the surfaces is modelled as interaction between bristles extending from the rubbing counter-parts (Figure 5-8). The bristles do not represent asperities, but the bonds created between the surfaces. The bristles on one of the surfaces are rigid, whereas the bristles on the counter-surface are deformable. When the slider moves the energy in the contacting bristles increases. When an individual bristle reaches a critical deflection, it snaps off contact, and a new bond is created between the rigid bristle and another deformable bristle. The friction force is the resistance that the slider experiences due to all the bristles in contact and can be expressed as:

$$F_f = \sum_{i=1}^{N} k(x_i - b_i) \tag{5-8}$$

Where N is the total number of bristles, k is the stiffness of the bristles, x_i is the position of the bristles, and b_i is the position where the bond with the rigid bristle was

formed. It is evident that the behaviour of one deformable bristle is very similar to the behaviour of the elastic pile in the model introduced by Borodich and Onishchenko (1993) and discussed in section 5.4.2.

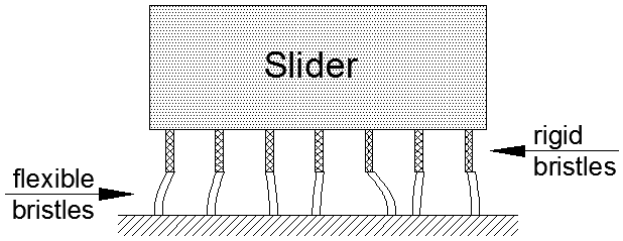

Figure 5-8 - The Bristle Model

The Bristle model can be considered a multi-asperity model, but it is not multi-scale, multi-level nor hierarchical model.

It is worth noting that the above scheme is quite similar to the model of boundary friction presented by Akhmatov (1963) where, instead of bristles, chain macromolecules were considered. Some ideas of the Bristles model can be traced back to classic papers by Euler and Coulomb (see discussions of the models presented by Kragelsky and Schedrov (1956) and Dowson (1998).

5.3.7 Borodich and Kryukova model

The model introduced by Borodich and Kryukova (1997) is a numerical simulation of the dynamics of friction during sliding taking into account only the elastic deformation of the asperities. It consists of a block, fixed through a spring, sliding with friction over a moving conveyor belt (Figure 5-9). The system allows the motion of the sliding block both horizontally and vertically.

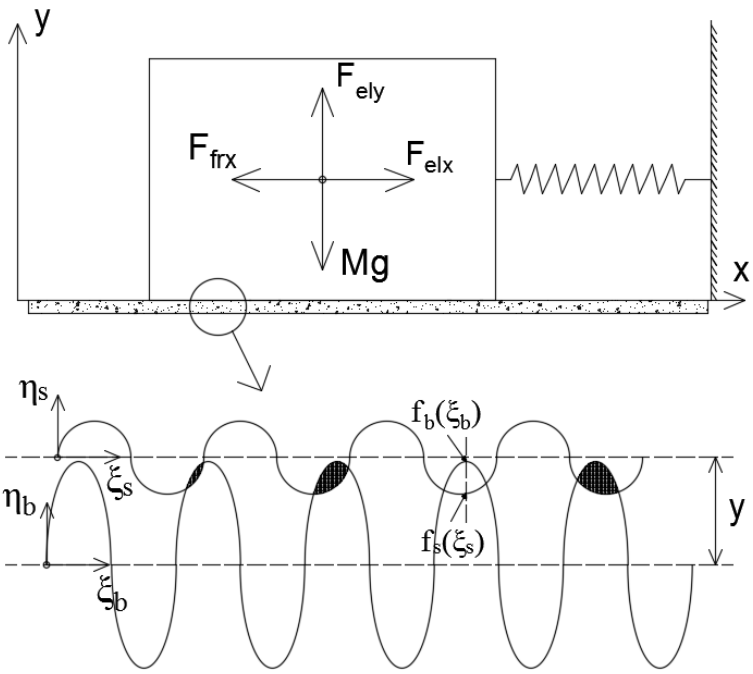

Figure 5-9 – Borodich-Kryukova (1997) model

The length of the sliding block is 2*a*, it has unit mass *M*, and it is lying on a belt moving with constant velocity *U*. As it moves, the block pulls a horizontal spring with stiffness k_x. Two systems of coordinates are used, namely a global coordinates system (x, y) and a local coordinates system for each of the bodies: (ξ_b, η_b) for the belt and (ξ_s, η_s) for the slider.

It is assumed that the block and the belt are rigid and planar, but both surfaces are covered with a deformable rough layer consisting of linearly elastic springs, all with the same stiffness ϵ. The force of elastic interaction F_{ely} will be equal to the integral of all the local elastic interaction forces over the entire length of the block:

$$F_{ely} = \int_{-a}^{a} \Phi(\xi) d\xi$$

where

$$\Phi(\xi) = b\epsilon_s \Psi(f_b(\xi + x - Ut) - f_s(\xi) - y)$$

Here Ψ is the local deformation function, t is the time variable, y is the distance between the mean lines of the two roughness profiles, f_s and f_b are the functions describing the shape of the surface profile of the slider and of the belt, respectively. Function Ψ takes the following values:

$$\Psi(x) = x \; for \; x > 0, \qquad \Psi(x) = 0 \; for \; x < 0$$

The sign of the coefficient of friction changes depending on the relative velocity between the slider and the belt.

The dynamic behaviour of the system is described by the following system of equations:

$$\ddot{x}(t) = F_{frx} - F_{elx}$$

$$\ddot{y}(t) = F_{ely} - g, \qquad g = 9.81 \times 10^3, \qquad (M = 1)$$

Here F_{elx} is the elastic resistance force of the spring and F_{frx} is the force of friction. As it can be seen, one very important drawback of the model formulation is that it does not have any energy dissipation mechanisms in the vertical direction.

The model developed by Borodich and Kryukova (1997) takes into account only one interaction mechanism, namely the elastic deformation of the contacting asperities; therefore it is not a multi-scale model. In the formulation presented, sinusoidal profiles have been used for both of the interacting surfaces, which makes the model single-level and non-hierarchical. However, any roughness profile can be used for the counter-surfaces.

5.3.8 Al-Bender et al. model

Al-Bender et al. (2004) introduced a multi-asperity model of friction able to generically reflect mechanisms of creep, adhesion and elastic-plastic deformation. The model has been developed to phenomenologically describe other mechanisms like pre-sliding behaviour, lift-up hysteresis (Al-Bender et al. 2012) and wear (De Moerlooze et al. 2011). A schematic representation of the model is shown in Figure 5-10.

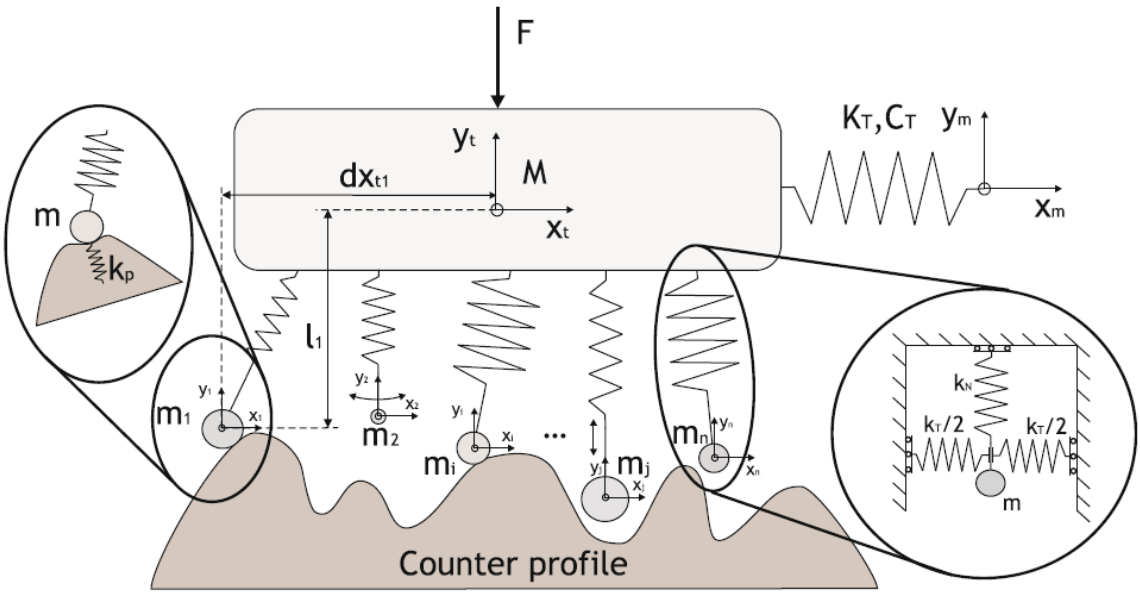

Figure 5-10 - Al-Bender model (from De Moerlooze et al. 2010)

The model is comprised of a slider and a counter-profile. The slider is perfectly rigid and it contains the flexible surface made of a representation of asperities. One asperity is modelled as a mass connected to the slider through a spring with a certain normal and tangential stiffness, damping and length. The system of uncoupled normal and tangential springs used to model the asperity (shown in the snippet in Figure 5-10) is equivalent to the elastic pile connected through a torsion spring of Borodich and Onishchenko (1993), discussed in section 5.4.2. The asperities deform independently without any interaction with each other and they are given a length distribution which reflects the original surfaces. The counter-surface has a much higher stiffness than the asperities and its geometry reflects the overlap between asperities during contact. In order to model the elastic-plastic behaviour, the springs are modelled as individual Maxwell-Slip elements. The equations of motion for the main mass *M* are as follows:

$$M\ddot{x}_t = K_T(x_m - x_t) + C_T(\dot{x}_m - \dot{x}_t) + \sum_{i=1}^{N} k_{T,i}\left(x_i - x_t - dx_{T,i}\right) + \cdots \sum_{i=1}^{N} c_{T,i}(\dot{x}_i - \dot{x}_t) \tag{5-9}$$

$$M\ddot{y}_t = \sum_{i=1}^{N} k_{N,i}\left(y_i - y_t + l_i\right) + \sum_{i=1}^{N} c_{N,i}(\dot{y}_i - \dot{y}_t) - F \tag{5-10}$$

In (5-9) and (5-10), K_T and C_T are the tangential stiffness and the tangential damping of the main spring, respectively; $k_{T,I}$ and $k_{N,I}$ are the tangential and normal stiffness of the *i*-th asperity, and $c_{T,I}$ and $c_{N,I}$ are the tangential and normal damping of the *i*-th asperity; x_m and y_m express the position of the free end of the main spring, x_t and y_t express the position of the main mass, and x_i and y_i express the position of the mass of the *i*-th asperity; *F* is the vertical load, l_i is the asperity length, and $dx_{T,I}$ is the horizontal asperity distribution. The meaning of the terms involved in the above equations is also illustrated in Figure 5-10. The equations for the asperity masses m_i are given below, in (5-11) and (5-12).

$$m_i\ddot{x}_i = k_{T,i}(x_t - x_i + dx_{T,i}) + c_{T,i}(\dot{x}_t - \dot{x}_i) + \gamma k_{p,i}(x - x_i) + F_{adh,i,x} \quad \text{(5-11)}$$

$$m_i\ddot{y}_i = k_{N,i}(y_t - y_i - l_i) + c_{N,i}(\dot{y}_t - \dot{y}_i) + \gamma k_{p,i}(y - y_i) + F_{adh,i,y} \quad \text{(5-12)}$$

In the above expressions, the value of γ is 1 if the asperity is in contact and 0 otherwise. The terms $F_{adh,i,x}$ and $F_{adh,I,y}$ are the tangential and normal components of the force of adhesion acting upon asperity *i*.

We have to note that some of the features of the model lack physical meaning; hence the model describes friction only qualitatively. For example, the force of adhesion in the model of Al-Bender et al. is not exactly the force of molecular adhesion, but a local, asperity level, tangential resistance force, that the asperity has to overcome to be set in motion. But this force is not physically connected to any chemical or inter-molecular phenomena and, therefore, the model cannot be considered multiscale. The damping coefficients also are artificially imposed parameters that lack physical meaning.

Concluding, this is a multi-asperity, multi-level model, without features of multi-scale or hierarchy. Due to the fact that it offers only a qualitative description of friction, it cannot be applied directly for modelling friction between real surfaces.

5.3.9 Real nano-topography model - Bora et al. (2013)

The contact model introduced by Bora et al. (2013) is shown in Figure 5-11.

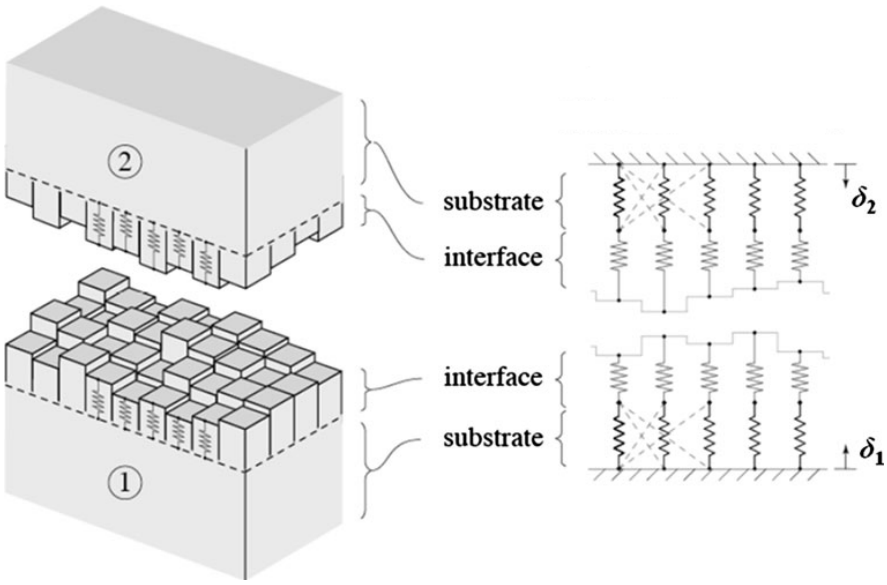

Figure 5-11 – Bora et al. model (from Bora et al. 2013)

The counter-parts involved in contact are represented by two regions: the substrate and the interface. The interface consists of individual uncoupled springs that extend from the substrate. The substrate is an elastic half-space that deforms according to the Boussinesq solution when the springs are compressed.

The role of the substrate is also to couple the springs on top of it. The springs have heights according to the real topography of the surface measured by AFM; to every height of the profile corresponds one spring.

Some of the drawbacks of the model are that the nodes are allowed only normal displacement, the interface and the substrate are purely elastic, and adhesion is not taken into account. Because the deformation of the asperities represented by springs and their coupling through the substrate are the only mechanisms taken into account, this is not a multi-scale model. The model is not hierarchical either because the substrate is a half-space, therefore it cannot reflect any asperity interplay at the micro-scale. The nano-asperity generation has different heights, hence the model can be called multi-level.

In conclusion, this is a coupled multi-asperity, multi-level model of contact between rough surfaces. We have to note that the idea of reflecting discretely the real surface is valuable, and we will use it later on.

5.4 Hierarchical models of roughness

We have seen a number of multi-asperity models that are multi-level but feature uncoupled asperities. A class of models that offer asperity coupling is that of the hierarchical models, as we shall see in the current section.

5.4.1 Archard model

The model has been described in section 1.6.2, but here it will be discussed under the current task of analysing models to discover features of multi-scale, multi-level and hierarchy.

Archard (1957) has introduced the first hierarchical model: the asperities of generation *k* are on top of the asperities of generation *k*-1. As a consequence the deformation of the asperity at generation *k* will influence its neighbours, as well as the asperities at previous generations. Even though it is hierarchical and multi-level, Archard's model is not multi-scale as it takes into account only one physical contact mechanism, namely the elastic deformation of asperities.

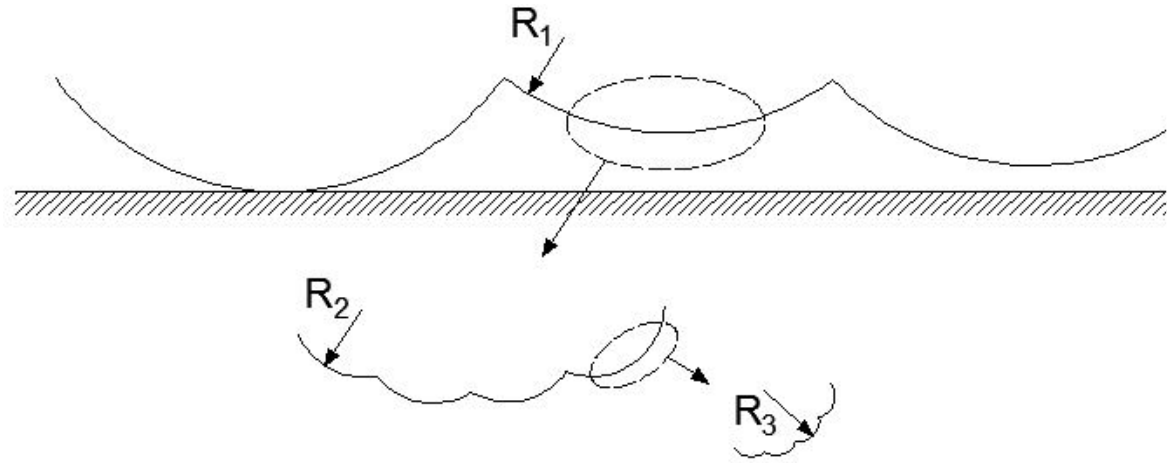

Figure 5-12 – Archard model (1957)

5.4.2 Cantor-Liu and Cantor-Borodich profile

A number of scientists have suggested that fractals are a good representation of topography (Berry and Hannay 1978, Brown and Scholz 1985). Liu et al. (1986)introduced a model of fractal roughness, known by the name of Cantor-Liu model. The main drawback of this model is that the asperities have the same height at every generation and therefore the surface is not bounded. The Cantor-Borodich profile (Borodich and Mosolov 1991, Borodich and Mosolov 1992) is a modification of this model, with decreasing heights for every asperity generation. The authors say that such a surface could result after unidirectional polishing or wearing leading to this system of parallel scratches of different depths, as can be seen in Figure 5-13. The profile creates always just two asperities every next generation of the hierarchy. However, it is evident that the generation can be such that an asperity can produce any number of descendants in the next generation. Warren and Krajcinovic (1995) suggested using three descendants. The model has been used to study contact between elastic and plastic bodies. Borodich and Onishchenko (1993) have solved indentation problems of a Winkler-Fuss elastic spring foundation by the Cantor-Borodich profile. Their conclusion was that fractal dimension alone cannot be used to describe the contact between rough surfaces.

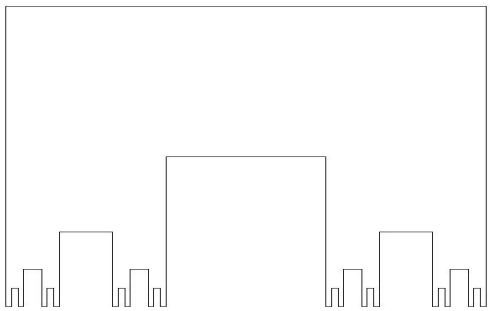

Figure 5-13 - The Cantor-Borodich profile

In the same paper another model using the Cantor-Borodich profile as support surface is introduced (Figure 5-14). The asperities of the sliding surface are modelled as telescopic piles with a certain rotational stiffness of the connection with the top body. The model seems to account for interlocking of asperities and stick-slip mechanisms of friction. The following stages can be observed in the motion of the pile:

- The pile 'catches' the asperity of the Cantor profile.
- The pile rotates with respect to its connection with the top body, gathering elastic energy in the connection, leading to an increase in the resistance force.
- When the pile moves past the asperity, the elastic energy in the connection is released and the resistance force decreases, until it catches another asperity.

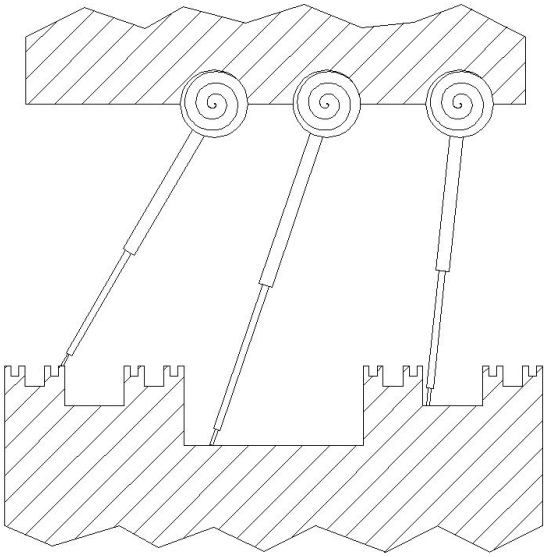

Figure 5-14 - Elastic pile model

The authors propose to modify the Cantor-Borodich profile and construct multilevel hierarchical profiles where asperities or gaps of the next generation lie on the tops of all asperities of the previous generations, as it can be seen in Figure 5-15. The

multiscale nature of friction is implied when they say they 'expect that some subset of the surface profile would be responsible for the adhesive component of the contact interaction while another one, having possibly a different fractal dimension, determines the deformational component.'

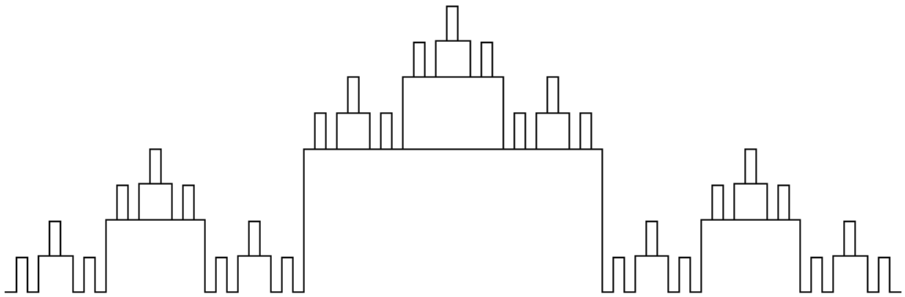

Figure 5-15 - Variation of the Cantor profile

To study the normal stiffness of the interface, Plesha and Ni (2001) developed an analytical model (Figure 5-16) based on the Cantor-Borodich profile and its modification by Warren and Krajcinovic (1995). In this model the asperities are considered elastic springs. When subjected to a compressive load *P*, the model undergoes a deflection *Δ* which is given by summation of the deformation at each *i* layer:

$$\Delta = P \sum_{i=0}^{\infty} \frac{z_i}{A_i E_i} \tag{5-13}$$

A_i, E_i and z_i are the cross-sectional area, the elastic modulus and the height of layer *i*.

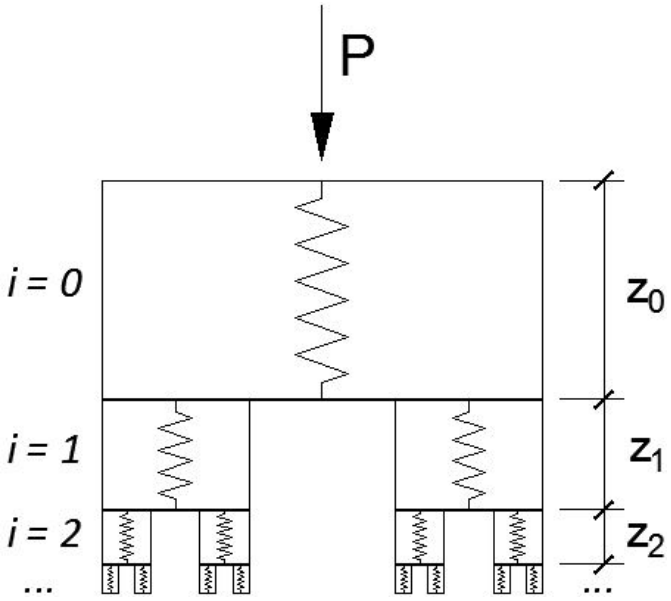

Figure 5-16 - Plesha and Ni analytical model

Abuzeid and Eberhard (2007) have used the Cantor-Borodich profile to develop a linear viscoelastic creep model of contact. They used Radok's technique of replacing the elastic constants in the elastic solution by the corresponding operators in the stress-strain equation for the standard-linear-solid model describing the viscoelastic behaviour of the material.

5.4.3 Schmittbuhl hierarchical model

Schmittbuhl et al. (1996) developed a hierarchical model to account for the interaction at the contact between geologic plates. As the sketch in Figure 5-17 shows, the body is discretized in rigid elements – finer close to the interface, to capture the small details of the slip, and coarser farther away because the stress and strain fields are expected to be smoother. These rigid elements interact through horizontal springs with the elements at the same level, and are coupled with the previous level by vertical springs. The element size increases in geometric series with the distance to the interface (the element size is multiplied by a fixed ratio N) and all the physical parameters describing the elastic interaction are rescaled accordingly.

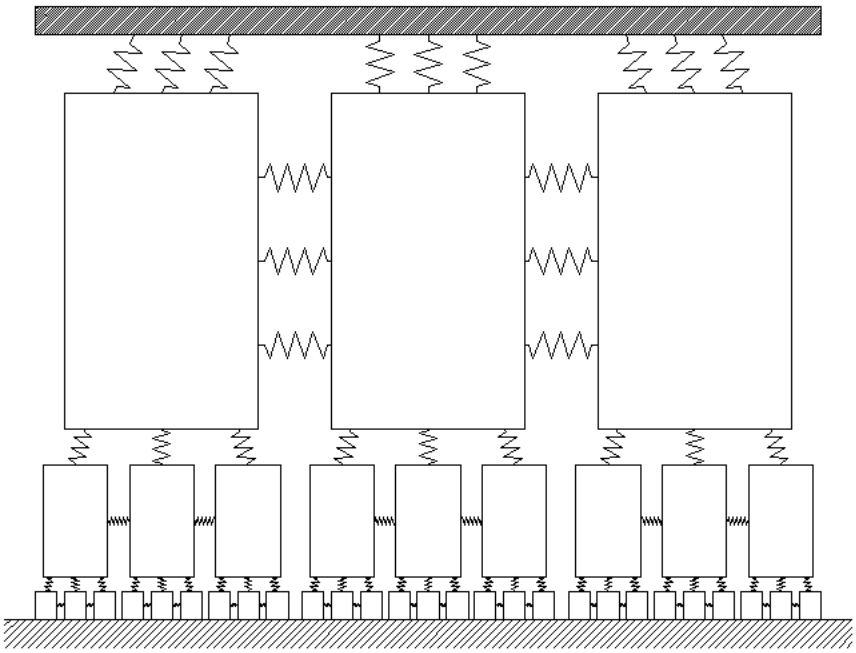

Figure 5-17 - Schmittbuhl hierarchical model

The friction problem is solved in a recursive manner, reducing each step to a Burridge-Knopoff problem.

Burridge and Knopoff (1967) have proposed a model to describe the mechanics of the earthquake faults. As illustrated in Figure 5-18, the interface consists in a number of blocks of mass m_i, resting on a surface and connected by springs. The blocks are also connected to the moving body by another series of springs, which is the driving geological plate.

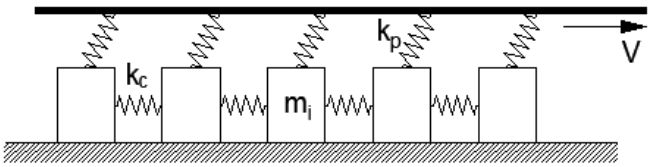

Figure 5-18 - Burridge-Knopoff model

The equation of motion of the i^{th} block would then be:

$$m\ddot{x}_i = k_c(x_{i+1} - 2x_i + x_{i-1}) - k_p(x_i - Vt) - F_f(\dot{x}_i) \quad (5\text{-}14)$$

Where k_c is the stiffness of the horizontal springs, k_p is the stiffness of the driving springs, and V is the velocity of the moving plate. F_f is a velocity weakening friction force, which means the system will show stick-slip behaviour; the individual block will stick to the surface until the pulling force matches the static friction threshold. After the block will be set in motion, the friction force will decrease.

The procedure developed by Schmittbuhl et al. (1996) may be described as follows. They initially impose a velocity weakening friction law for the interaction between the rigid interface and the elastic slider. Then the Burridge-Knopoff model is used to solve the problem at this generation and the obtained results are used to formulate the friction law for the next iteration at the superior block generation. Therefore, the problem is reduced to iterative solving of the Burridge-Knopoff problems for the chain of blocks at every generation.

One can see that in essence the Schmittbuhl profile is a version of the Cantor-Borodich profile with 3 descendants for every generation. Figure 5-19 shows a rearrangement of the Cantor-Borodich profile using blocks and springs to show the similitude in the hierarchical structure between the two models.

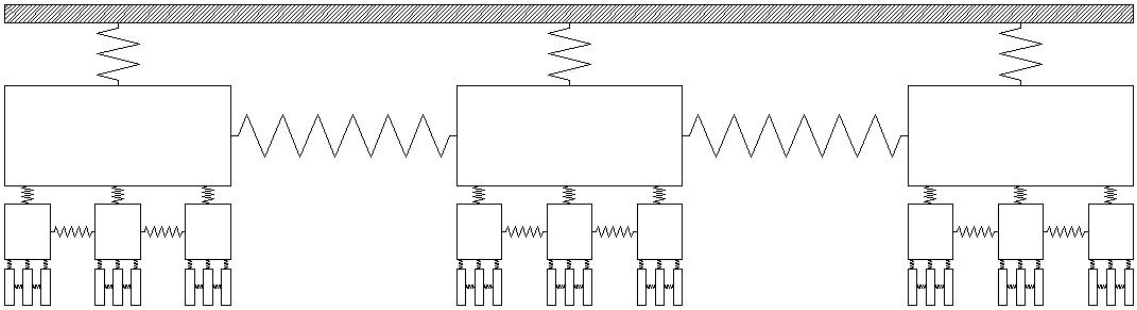

Figure 5-19 - Cantor-Borodich profile using blocks and springs

This hierarchical structure takes into account the lateral stiffness of the system, modelling the coupling between the bulk elastic response of the slider and the friction at the interface level.

Even though it is hierarchical, according to the definitions that opened the current chapter, the model is not multi-scale nor is it multi-level. It is not multi-scale because the model does not feature other physical phenomena than the deformation of the sliding body, and it is not multi-level as every block generation has constant height. Another drawback of Schmittbuhl's model is that the friction law is artificially imposed and does not follow from the physical mechanisms involved in friction.

5.5 Summary

In the previous sections of this chapter, a significant number of dry friction models have been analysed critically. Borrowing elements from these models, the author has developed a multi-scale hierarchical model, which will be described in the following section.

Most obviously, the original model draws on the model of Kragelsky (1948) in representing the asperities as elastic rods, while the geometrical configuration of the model is very similar to the Cantor-Borodich profile.

5.6 Simulations of friction by multi-scale hierarchical model of rough surfaces

In this section, a quasistatic, multi-scale, hierarchical model of friction between two surfaces is proposed. The bottom surface is considered perfectly rigid and contains information about geometry. Its profile is the measurement of a copper surface by a profilometer (curtesy of Weeks (2015)). The top surface is represented by a body, from here on referred to by the term 'slider'. The slider contains information about both the geometry of the sliding surface and the mechanical properties of the counterparts, and represents the bulk of the sliding body with its micro and nano-asperities.

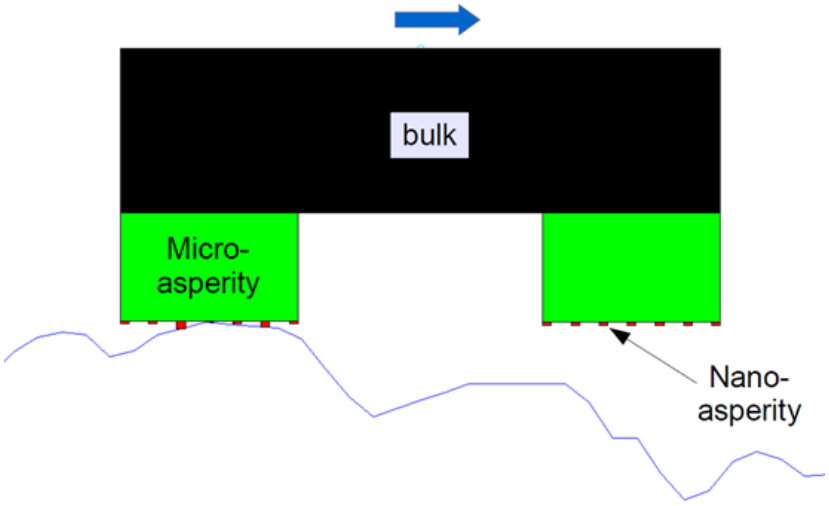

Figure 5-20 - Multiscale, single-level, hierarchical model (note: the scale of the vertical axis is about 1000 times smaller than the scale of the horizontal axis)

5.6.1 Geometry of the slider

As it can be seen in Figure 5-20, the geometry of the slider combines ideas from the Cantor-Borodich profile and the Kragelsky (1948) rod assembly model, as the asperities are represented as elastic rods. However, as Figure 5-21 shows, the aspect ratio of the asperities is quite different from Kragelsky's model. The measured surfaces that the slider approximates are quite smooth, therefore the statistical interpretation of the roughness profile has resulted in the asperities being more like slabs, rather than vertical rods. The height and width of the micro-asperities, as well as the distance between them were determined by analysing the slider's surface at micro-level, using a profilometer. The geometric characteristics of the nano-asperities, as well as their density, were determined by analysing the slider's surface at nano-level, using an AFM.

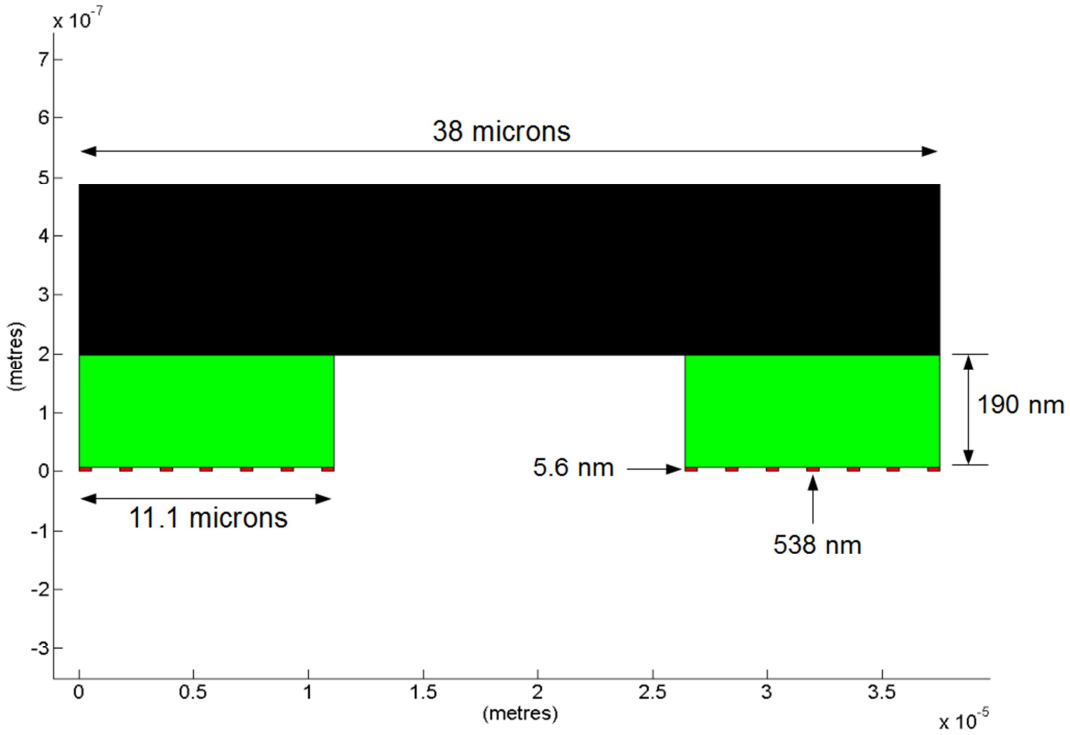

Figure 5-21 – Geometry of the slider (note the different scales of the axes)

The height of the asperities was computed using root mean square of all asperity heights, with respect to the mean-line of the profile, using equation (1-5). For a curve made of discrete points, relation (1-5) can be written as:

$$\mathrm{R}_q = \sqrt{\frac{1}{n}\sum_{i=1}^{n} h_i^2} \tag{5-15}$$

Where h_i are the heights of the discrete points of the measured nano-roughness, and n is the number of points.

The width of the asperities was computed as the arithmetic average of the widths of all the asperities reaching to the root mean square level computed beforehand. The method will be illustrated below.

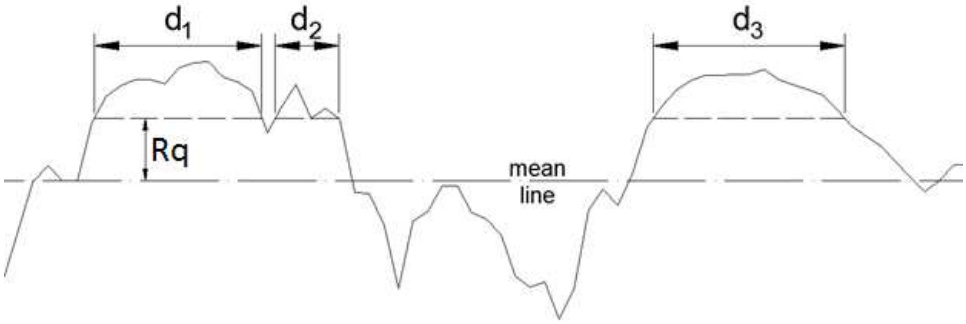

Figure 5-22 – Calculation of the width of asperities

R_q is the root mean square of all asperity heights obtained using formula (5-15). The lengths d_1, d_2, d_3 are the widths of the asperities at the height R_q. Thus the width of the asperities for the slider was calculated as an average of these widths. If the sampling length was just as long as in Figure 5-22, then the resulting width of the asperities would be obtained by:

$$\mathrm{d}_\mathrm{a} = \frac{d_1 + d_2 + d_3}{3} \tag{5-16}$$

A general formula can be written as:

$$\mathrm{d}_\mathrm{a} = \frac{1}{n}\sum_{i=1}^{n} d_i \tag{5-17}$$

The distance between asperities is computed according to Equation (5-18).

$$\lambda_\mathrm{q} = 2\pi\frac{R_q}{\Delta_q} \tag{5-18}$$

Where Δ_q is the root-mean-square average slope of the profile within the sampling length, and is calculated according to Equation (5-19).

$$\Delta_q = \sqrt{\frac{1}{n-1}\sum_{i=1}^{n} s_i^2} \tag{5-19}$$

Where s_i is the gradient of the profile at every point computed as the ratio between the change in height and the change in the horizontal position, $s_i = \frac{dy_i}{dx_i}$.

It should be mentioned that the geometrical characteristics for both the micro-asperities and the nano-asperities were obtained using the procedure described above applied to the corresponding roughness profiles. This means that, for the nano-asperities, the geometry was obtained by analysing the nano-roughness, whereas the geometry for the micro-asperities was obtained by analysing the micro-roughness. However, the determination of the geometry of the nano-asperities has one further step, due to the fact that they have two characteristic widths, corresponding to the van der Waals interaction domain and the chemical interaction domain (according to the description in Chapter 4). So the geometry of the chemically active part of the nano-asperities is obtained by uniformly distributing the material above the R_q height of the asperities to the asperities already represented using the above procedure.

The force of friction and the energy dissipation mechanisms that have been taken into account are as described in Chapter 4.

5.6.2 Simulation results

The apparent coefficient of friction is presented in Figure 5-23, and we have to address two obvious features of the curve, namely the sharp shape and the low magnitude, compared to the single-asperity model (described in section 5.2).

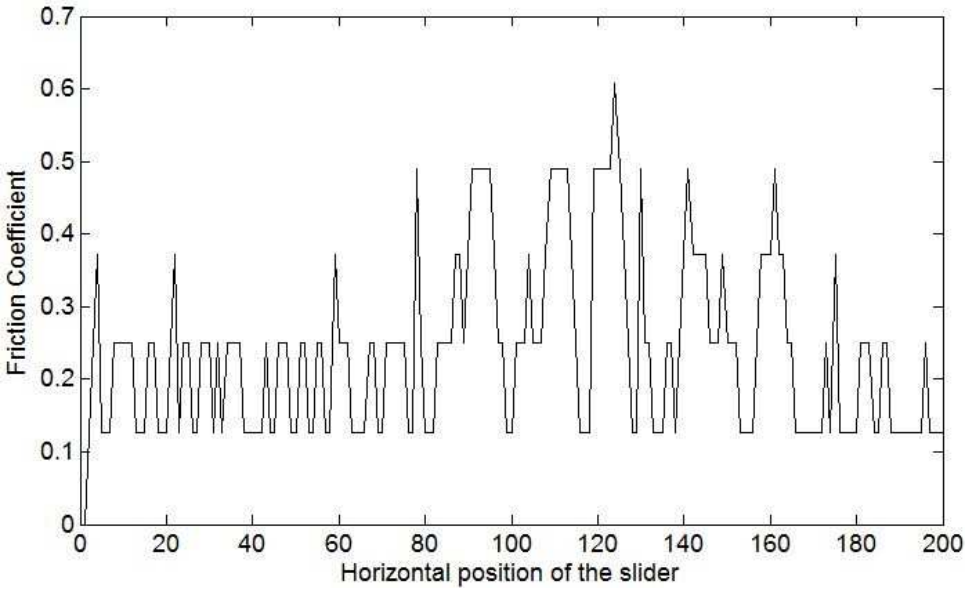

Figure 5-23 – Apparent coefficient of friction

Firstly, it can be seen that both the friction coefficient curve (Figure 5-23) and the energy dissipation diagram (Figure 5-25) show jumps. This is because they can only take discrete values, depending on the number of nano-asperities that are in contact.

Secondly, with a maximum value of about 0.6, the coefficient of friction is much smaller than the coefficient of friction for the single-asperity model described in section 5.2, which had a value of 6.23. This is because, in the current model, the result is a value of the apparent coefficient of friction, whereas in the one-asperity model the result was a value of the 'true' coefficient of friction. In the case of the one-asperity model there is no distinction between the true and the nominal contact area, while in the current model the true contact area is only a fraction of the nominal area. To illustrate this, Figure 5-24 shows the ratio between the number of nano-asperities in contact with the counter-surface and the total number of nano-asperities (in this case 98).

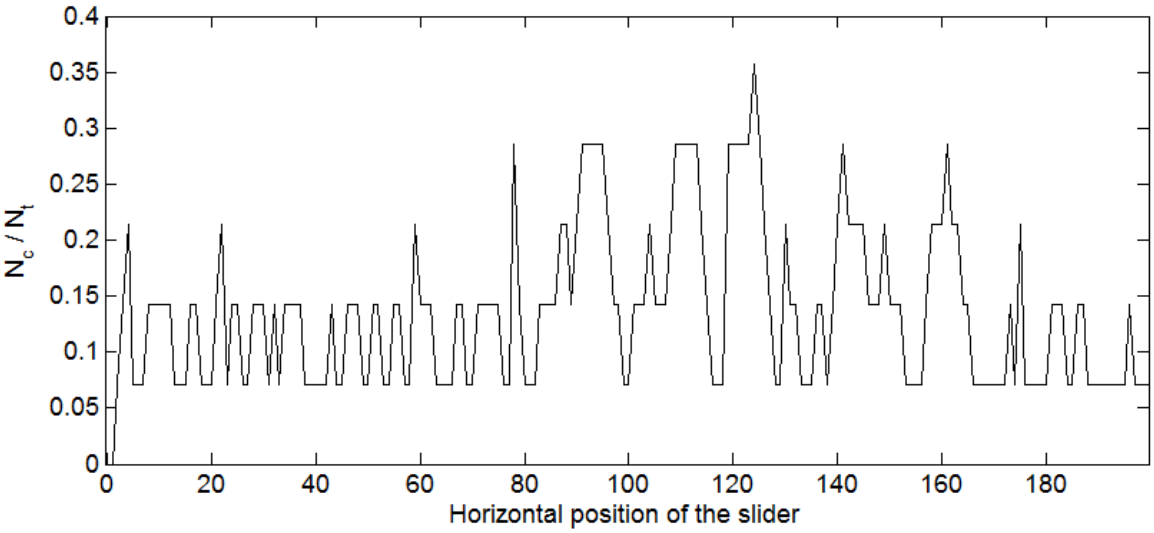

Figure 5-24 – The ratio between the number of nano-asperities in contact and the total number of nano-asperities

The discussion about the magnitude of the friction coefficient brings us to one of the greatest drawbacks of this model: it does not reflect the natural relationship between the normal load and the true contact area. With all nano and micro asperities being at the same level, the increase in the compressive load does not necessarily lead to an increase in the contact area, which contradicts experimental data (Dyson and Hirst 1954, Greenwood and Williamson 1966). If the contact scenario in Figure 5-20 is taken as an example, it can be seen that increasing the load would not increase the contact area. In reality, with a multi-level distribution of the micro-asperities, the contact area could increase upon compression. This makes a discussion about the magnitude of the friction coefficient meaningless. If the friction coefficient is defined as $\mu = \frac{F_f}{N+A} = \frac{U_{dissipated}}{x\,(N+A)}$, it can be seen that, if the amount of the dissipated energy does not change, increasing the normal load would lead to a smaller friction coefficient, which does not make sense.

Figure 5-25 shows the contribution of the different mechanisms of energy dissipation.

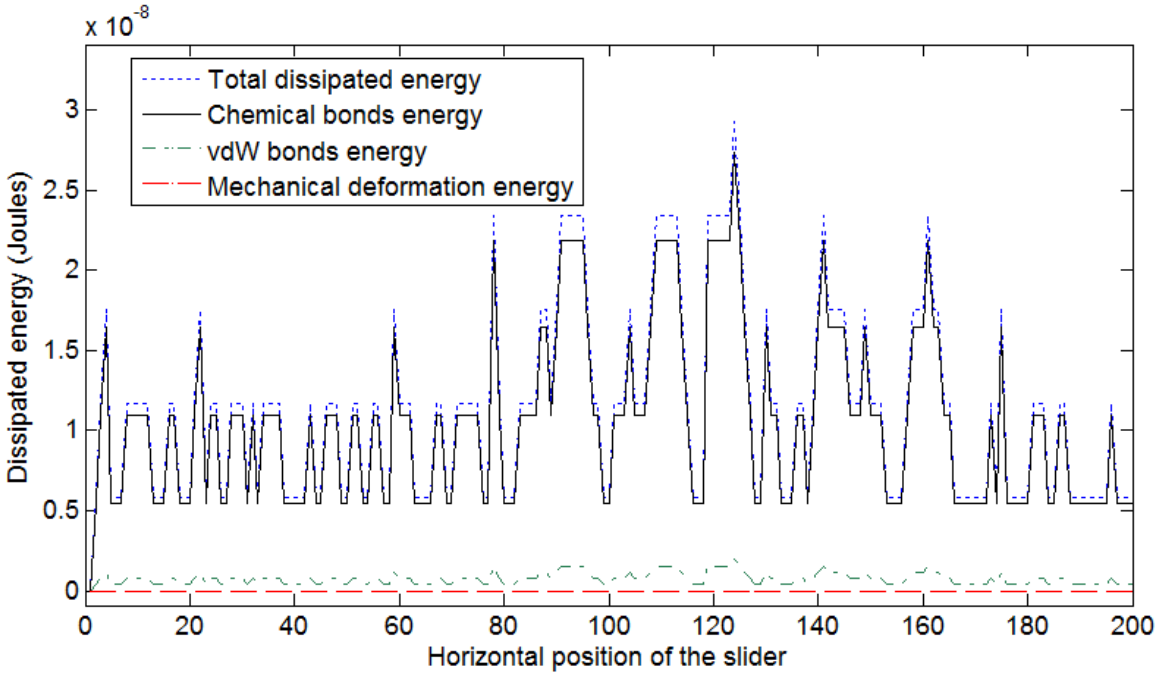

Figure 5-25 - Contribution of the different energy dissipation mechanisms

One can see that the most important energy dissipation mechanism is the dissociation of the chemical bonds. The dissociation of the van der Waals bonds does not bring such a big contribution compared to the breaking of the chemical bonds, but compared to the energy dissipated by mechanical deformation of asperities, it plays quite an important role. The energy lost by elastic deformation is insignificant, compared to the total dissipated energy; it comes to a maximum value of 3×10^{-17} Joules when the simulation begins and the slider is compressed from the undeformed shape.

Even though this model is a multi-scale, hierarchical model, it can be seen that the single-level distribution of asperities is an important drawback. In addition, there is no lateral deformation considered.

5.7 Conclusions

Friction between rough surfaces is a complex phenomenon, involving different mechanisms specific to each length-scale. Among these mechanisms we can mention the chemical interaction, molecular attraction, electrical double-layer effects, capillary effects, elastic-plastic deformation, wave propagation, heat dissipation, etc. Friction models should take into account these phenomena, as they should account for the complex multi-scale, multi-level nature of rough surfaces. In the current chapter we

have discussed models that represent very well different aspects of the friction process.

In the following chapter we introduce a quasistatic multi-scale, multi-level and hierarchical model of dry friction that has resulted by compiling some of the best features of the previously discussed models.

Chapter 6 Simulations of dry friction between rough metallic surfaces using the multi-scale hierarchical models of nominally flat slider

6.1 Introduction

The model presented has some similarities with the multi-scale hierarchical model discussed above, in section 5.6, however it has serious improvements. The model is multi-scale as it incorporates the physical mechanisms described in section Chapter 4. Furthermore, the nano-asperities are generated on top of the micro-asperities, which make the model hierarchical. As a result, the asperities are coupled; the deformation of one asperity affects all other asperities. The model is not only multi-scale and hierarchical, but it is also multi-level with respect to the micro-asperities. The general configuration of the presented model can be seen in Figure 6-1.

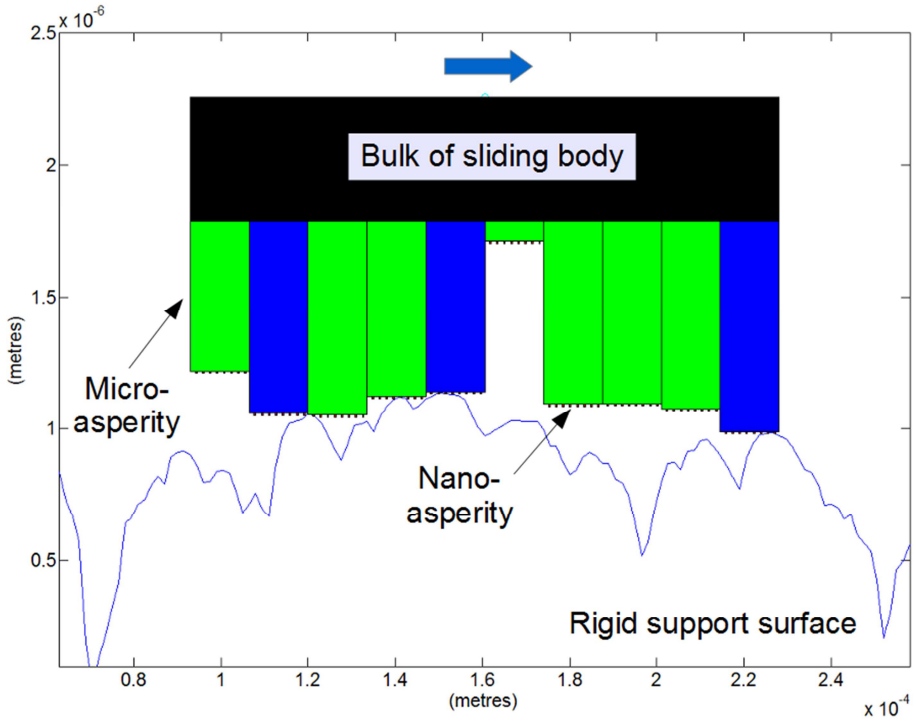

Figure 6-1 – General configuration of the model (notice the different scales of the axes)

The micro-asperities are generated at different heights, according to the real topography of the surface, measured by profilometer, in a fashion very similar to the way Bora et al. (2013) assign the topography to the interface layer. Another important development of the model is that it takes into account the plastic deformation of the

micro-asperities, which have an elastic-perfectly plastic behaviour. This feature allows for a realistic load-area of contact dependence.

The current formulation of the model is quasistatic; therefore it does not take into account the effect of sliding speed. Also, even though the model is multi-scale, in the sense that it models the physical phenomena specific to the different length-scales, it does not consider the different time-scales characterizing these different phenomena. As a consequence, the model is formulated in the time-scale of the fastest process, which in our case is the breaking of the chemical bonds (of the order of the picoseconds).

The model will be described in greater detail in the following section.

6.2 The modelling of surface roughness by a general multi-scale, multi-level, hierarchical model of a nominally flat slider

The tribological system consists of a slider and a support surface. The support surface is represented by a rigid profile of the counter-surface, measured by profilometer. The slider contains all the information regarding the mechanical properties of the counterparts and an approximation of the roughness profile of the measured surface it represents. The way the surface has been interpreted to obtain the geometry of the slider will be described below.

6.2.1 The geometry of the slider

The heights of the micro-asperities were determined by measuring the body's surface at the micro-scale, using a profilometer (profile sample in Figure 6-2, courtesy Weeks (2015)). Similar profiles can be found in the PhD thesis of Weeks (2015), which were measured in 3D using a Taylor Hobson Form Talysurf 2 profilometer with the sample mounted on a y-stage to obtain a series of offset profiles and thus a 3D map of surface height. The height and width of the nano-asperities, as well as the distance between them, were determined by analysing the measurement of the body's surface at nano-level, using an AFM (profile sample in Figure 6-3, courtesy of Dr. Emmanuel Brousseau). The nano-scale roughness was measured using the Park XE-100 AFM from Park Systems. One has to bear in mind that the length scales of these measurements

are significantly different and the tip of the profilometre is not able to 'catch' the asperities at the nano-scale.

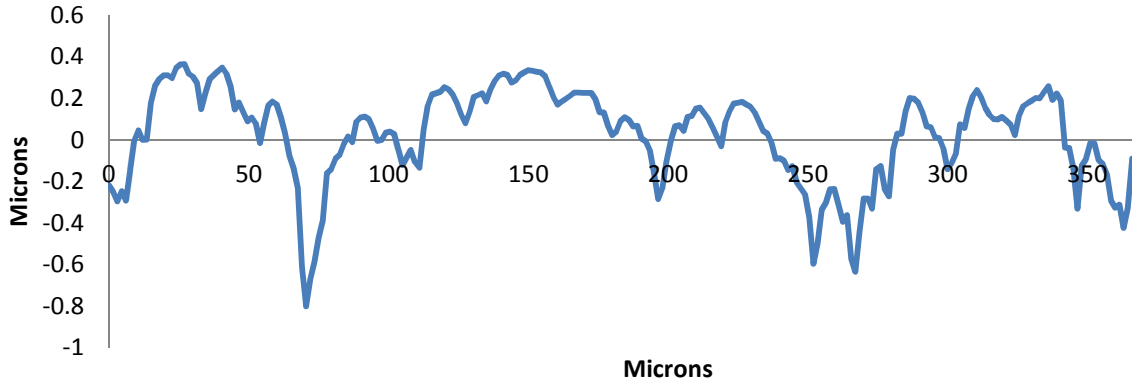

Figure 6-2 - Sample of the copper micro-roughness profile by profilometer

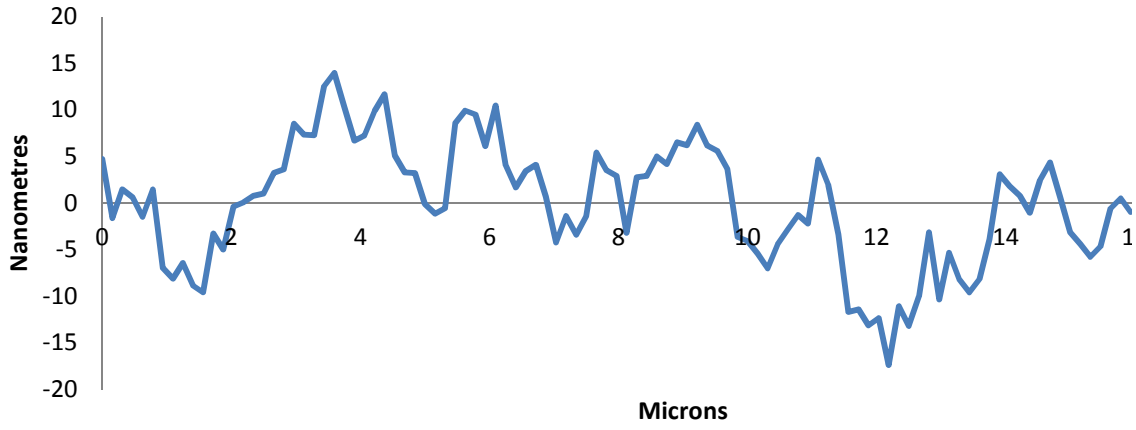

Figure 6-3 - Sample of the copper nano-roughness profile by AFM

The surface profiles may look rough, but one needs to note the different scales of the axes. The natural aspect ratio representation of the first 5 points of both the micro (in Figure 6-4) and the nano (in Figure 6-5) profiles make obvious the fact that the surfaces are very smooth.

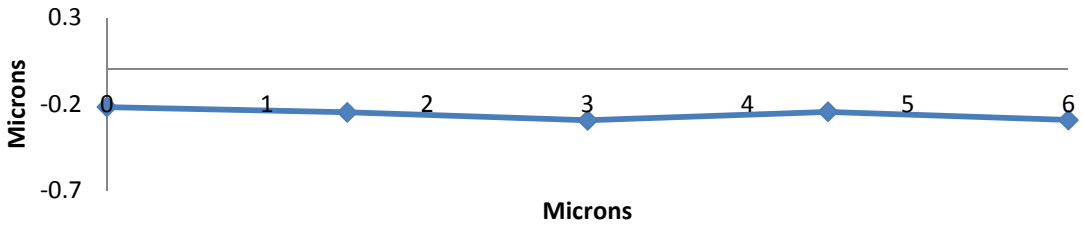

Figure 6-4 –Sample of the micro-roughness profile by profilometer – natural aspect ratio

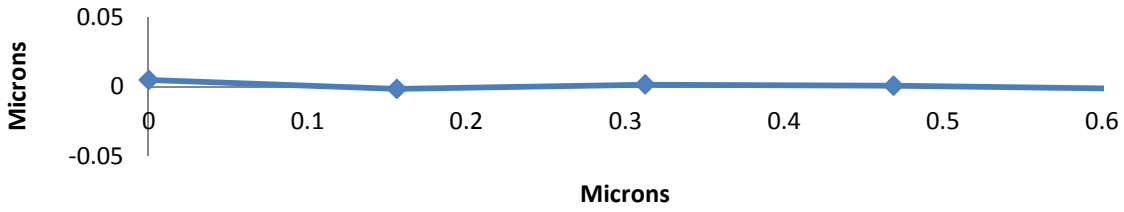

Figure 6-5 –Sample of the nano-roughness profile by AFM – natural aspect ratio

Geometry of the micro-asperities

At the micro-scale, the slider is an approximation of the real surface profile measured by the profilometer. The roughness profile is divided into rods that will represent the micro-asperities (see Figure 6-6).

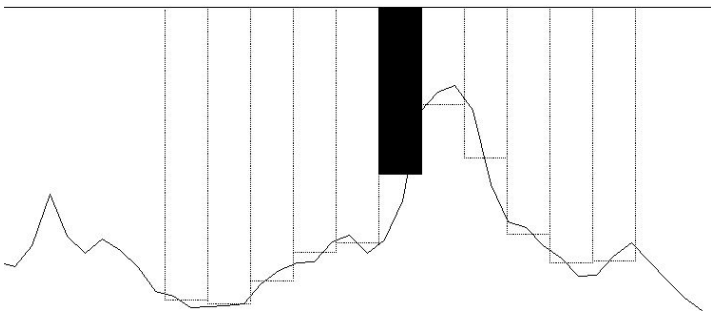

Figure 6-6 - Micro-roughness interpretation - obtaining the geometry of the micro-asperities (horizontally scaled down by a factor of 30)

The width of the micro-asperities can be chosen and their heights will be determined accordingly. Obviously, if micro-asperities are wider, the roughness representation will be coarser. Even though we can choose any discretization size, the width of the micro-asperities should correspond to some statistical property of the roughness profile. This matter will be discussed later.

The micro-asperities will have flat ends (similar to the model of Kragelsky (1948) and their lengths will be given by the arithmetic mean between the sides, hence the micro-asperities will have approximately the same volume as the roughness profile. Let us take as an example the calculation of the height of the hatched micro-asperity in Figure 6-6, magnified in Figure 6-7. The area hatched in Figure 6-7 is the real roughness section corresponding to the approximation hatched in Figure 6-6, that we call micro-asperity. The height of a micro-asperity is calculated as the arithmetic mean of heights *a* and *b*.

$$\mathrm{h} = \frac{a + b}{2} \tag{6-1}$$

The micro-asperities are modelled as elastic - perfectly plastic rods having square cross-section.

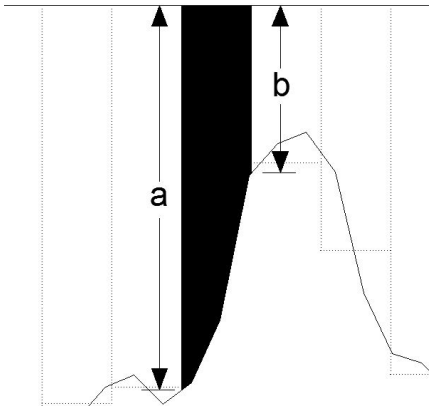

Figure 6-7 - Calculation of micro-asperity height (horizontally scaled down by a factor of 30)

Geometry of the nano-asperities

The nano-asperities are modelled as equally spaced rectangles on the tip of the micro-asperities. Figure 6-8 shows a magnification of the tip of one micro-asperity. In order for the micro-asperity's tip to fit in the figure, it has been scaled down by a factor of 25 in the horizontal direction. In a 1:1 representation, the nano-asperities look wider and reflect the smooth nature of the surface (Figure 6-9).

In our model, the nano-asperity can be engaged in 2 types of contact. If the nano-asperity is within the adhesive layer, then it will establish contact due to van der Waals forces. In this case w_{vdW} is the diameter of adhesive contact and w_{chem} is the diameter

of chemical contact. Due to the nano-asperity modelling both the chemical and the vdW interactions, it has two characteristic widths and two characteristic heights.

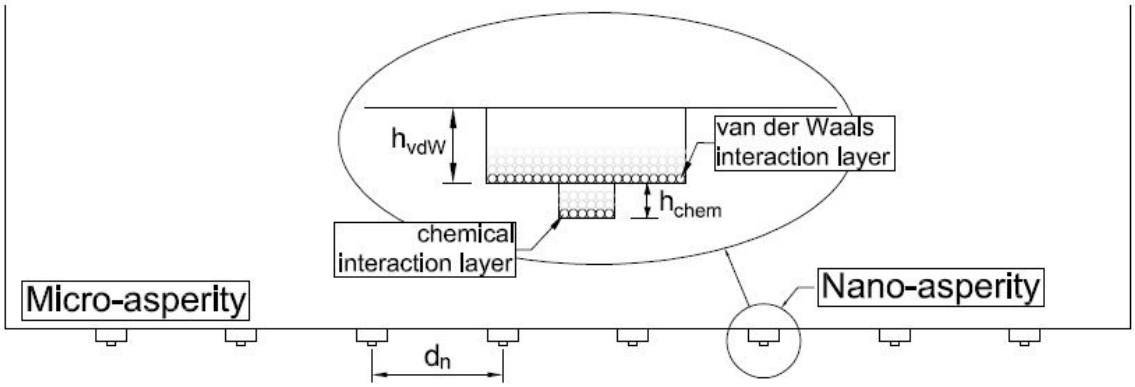

Figure 6-8 - Tip of micro-asperity (horizontally scaled down by a factor of 25)

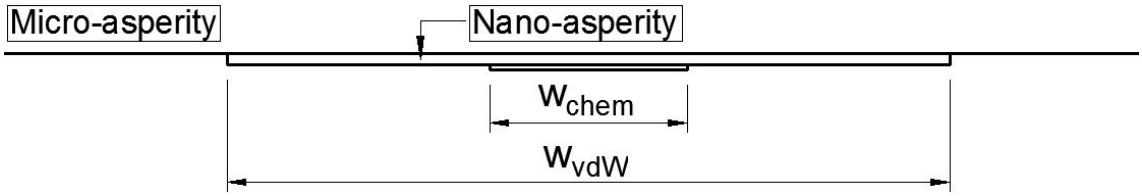

Figure 6-9 - 1:1 representation of one nano-asperity

The geometrical dimensions we need to obtain from the surface measurement are the height of the nano-asperity (h_{vdwl} + h_{chem}), the width of the chemical interaction domain (w_{chem}), the width of the van der Waals interaction domain (w_{vdW}), and the distance between nano-asperities (d_n).

The height of the van der Waals interaction slab was computed using root mean square of all asperity heights with respect to the mean line using equation (5-15).

The width of the van der Waals interaction domain was computed by equally distributing the asperity volume bounded by the mean-line and the height of the van der Waals interaction slab, to the number of asperities in this window. So, as illustrated in Figure 6-10, the hatched area is equally distributed to the number of asperities intersected by the mean-line. The resulting approximation is calculated according to Equation (6-2) and illustrated in Figure 6-11. In this figure the red rods are the approximation of the body of the nano-asperities, which will be engaged in van der Waals interactions. The remaining material (the unhatched area above the mean line in Figure 6-10) will be equally distributed to these rods and will represent the tips of the nano-asperities that will engage in chemical interactions.

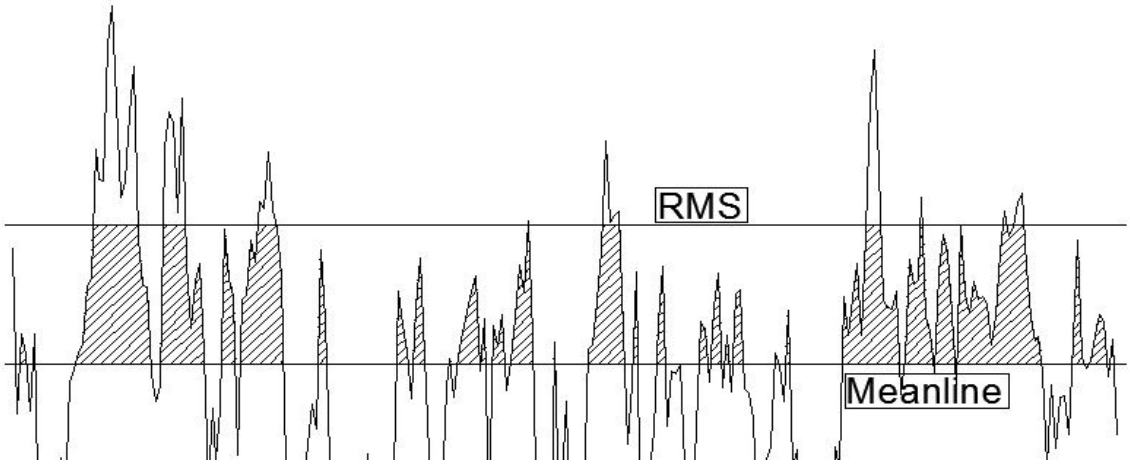

Figure 6-10 - Computation of the width of the van der Waals interaction domain (note the different axis scales)

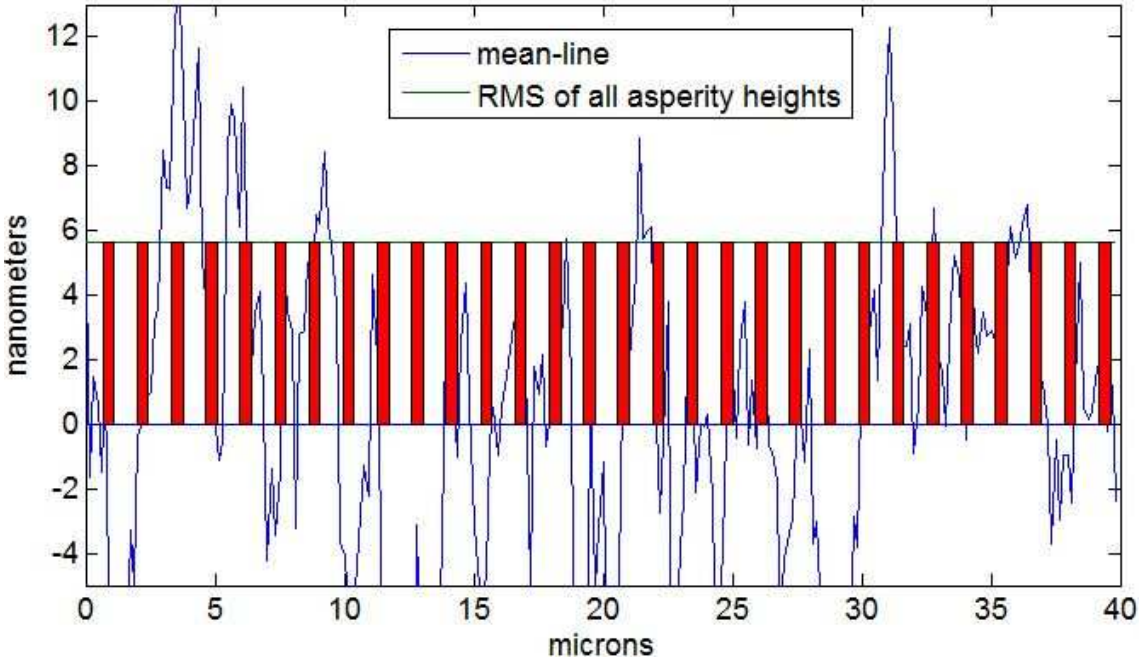

Figure 6-11 - Computation of the width of the van der Waals interaction domain (note the different axis scales)

$$w_{vdW} = \frac{A_{vdW}}{h_{rms}\, n_{mean}} \tag{6-2}$$

Where A_{vdW} is the area hatched in Figure 6-11 – a, h_{rms} is the quadratic mean of all asperity heights and n_{mean} is the number of asperities intersected by the mean-line.

The distance between nano-asperities is computed according to Equation (6-3).

$$\lambda = \frac{L_{nano}}{n_{mean}} \tag{6-3}$$

where L_{nano} is the length of the sampling profile.

The height of the chemical interaction slab was computed as the arithmetic average of all asperity heights above the height of the van de Waals interaction slab (the unhatched area above the mean line in Figure 6-10). It can be seen in Figure 6-12 that the resulting height of the nano-asperities (including both the body and the tip) is 8.2 nm, while the maximum height of the measured profile is 13.9 nm.

The width of the chemical interaction domain is computed in a similar way to the width of the van der Waals interaction domain. The volume of the asperities above the height of the quadratic mean of asperity heights is equally distributed to all nano-asperities. The resulting approximation is illustrated in Figure 6-12, where the red rods represent the body of the asperities, while the black rods on top of them represent their tips. As mentioned above, one should not be deceived by the aspect ratio in these figures as the scales of the axes are different.

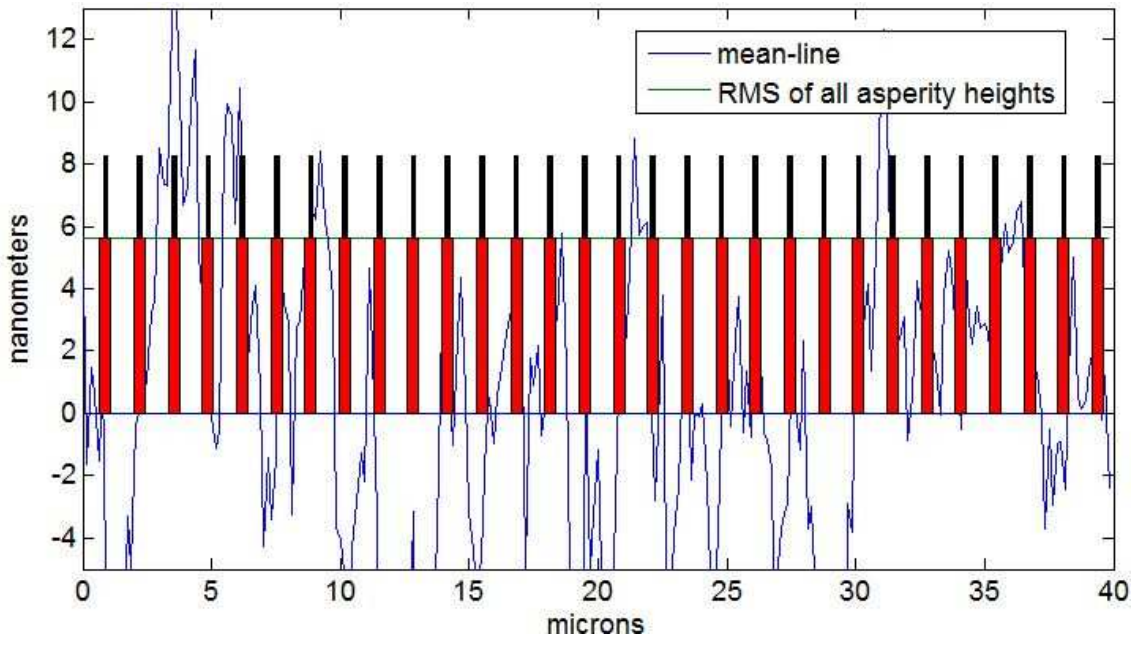

Figure 6-12 - Resulting approximation of the nano-scale roughness (note the different axis scales)

The nano-asperities are considered as having square cross-section, the depth being equal to the width calculated above.

Example of a slider geometry derived from surface measurements

We will here illustrate the configuration of a slider derived from analysing a surface as described above. Our input data are two roughness profiles: one profile obtained by measuring the surface using a profilometer and one roughness profile obtained by measuring the surface by AFM. Samples of these profiles are, in fact, shown in Figure 6-2 and Figure 6-3. The resulting geometry is sketched in Figure 6-13.

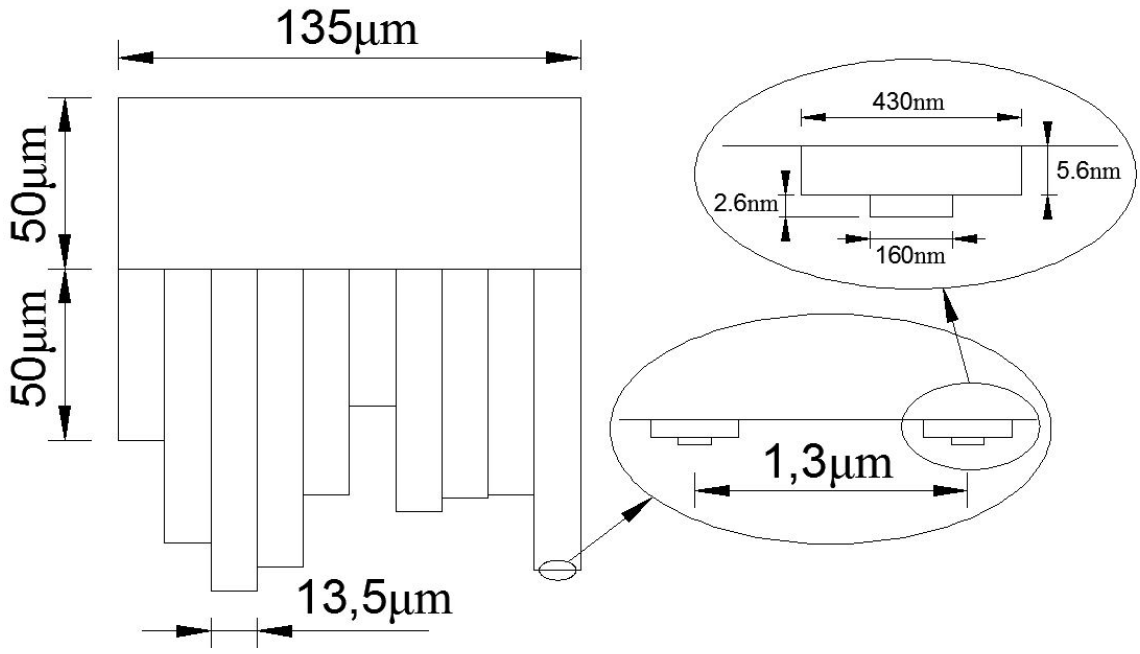

Figure 6-13 - Sketch of a slider geometry derived from measured profiles (note the snippet sketches have been vertically scaled up by a considerable factor to make geometry distinguishable)

6.2.2 The mechanical properties of the rubbing counterparts

The model represents the interaction between two bodies. The top body will be called slider. The body onto which the slider moves is represented solely by the roughness profile and it is considered perfectly rigid. This roughness profile comes from measuring the support surface by the profilometer. Figure 6-2 shows a sample of this measurement.

The slider reflects the mechanical characteristics for the rubbing pair. The model can work with any material characteristics, as it can work with any measured roughness profiles. The part of the slider that represents the body onto which the surface was measured has the mechanical properties of the bulk of the material. The micro

asperities are characterized by the effective elastic modulus for the interacting bodies, which is calculated as follows.

Suppose the elastic rod having cross-sectional area *A*, length L_1 and elastic modulus E_1 is in contact with the elastic rod having cross-sectional area *A*, length L_2 and elastic modulus E_2. The force pressing the rods together is denoted by *P*. The deformations corresponding to each of the elastic rods are:

$$\delta_1 = \frac{PL_1}{E_1 A} \text{ and } \delta_2 = \frac{PL_2}{E_2 A} \tag{6-4}$$

The total deformation for both rods is:

$$\delta_1 + \delta_2 = \frac{P}{A}\left(\frac{L_1}{E_1} + \frac{L_2}{E_2}\right) \tag{6-5}$$

If $L_1 = L_2 = L$,

$$\frac{\delta_1 + \delta_2}{L} = \frac{P}{A}\left(\frac{1}{E_1} + \frac{1}{E_2}\right) \tag{6-6}$$

$$\varepsilon_1 + \varepsilon_2 = \sigma\left(\frac{1}{E_1} + \frac{1}{E_2}\right) \tag{6-7}$$

Relation (6-7) has the form of a stress-strain relation for one dimensional rod in contact with a rigid plane, having the following effective modulus:

$$\frac{1}{E_{eff}} = \frac{1}{E_1} + \frac{1}{E_2} \tag{6-8}$$

The obtained effective contact modulus is used to describe the elasticity of the micro and nano-asperities.

6.2.3 Plastic deformation of micro-asperities

The surface profile changes every time-step if there are any yielding micro-asperities. The amount of plastic deformation of a yielding micro-asperity will be subtracted from its length, and it will be equally distributed to the closest neighbouring micro-asperities which did not deform plastically. The previously yielded asperity will be shorter and its neighbours will be longer.

This is to model a ‘sinking in’ effect, when the yielding asperity becomes shorter, and a ‘pilling up’ effect, when the length of the neighbours increases. It is thus assumed that plastic deformation occurs without changing the volume of the material. This assumption restricts the applicability of our model to crystalline metals.

Of course, in a real contact scenario, the influence of the plastic deformation of an asperity goes beyond its neighbouring asperities. To account for this, future versions of the model will contain a weighting function to define how the dislocated material will be reallocated.

6.3 Simulations for the multi-scale, multi-level, hierarchical slider, under fixed gap (FGM) conditions

In this formulation of the model, the distance between the mean-line of the roughness profile and the top of the slider is constant and set as input data. The calculation gives as results the stress distribution and the force of friction caused by the relative motion between the slider and the rough surface.

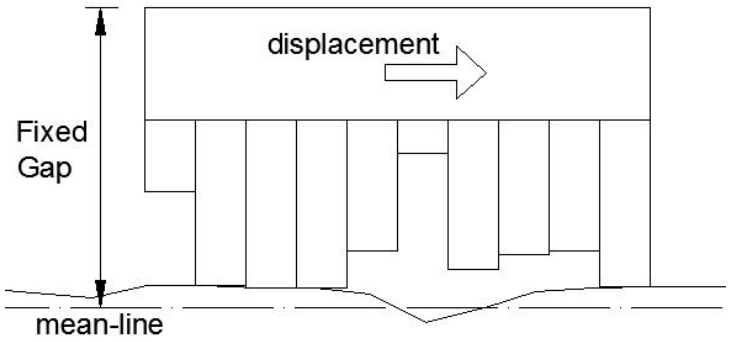

Figure 6-14 - Sketch of the Fixed Gap Model

Formulation of the problem

The problem is quasi-static and it neglects the effect of time and inertial forces. The model calculates the stress distribution and the energy loss if the slider moves a displacement increment under a fixed gap.

Input

- The fixed gap *G* is prescribed.

- The geometry of the slider (height of the micro-asperities H_i, height of the bulk of the body H_B).
- The roughness profile – the heights of the asperities corresponding to each of the micro-asperities h_i.
- The mechanical properties of the slider which give the stiffness for each micro-asperity, $k_i = \frac{EA_i}{L_i}$, where E is the reduced contact modulus for the contacting materials, A_i is the area of the cross-section of the asperity and L_i is the height of the asperity.

Output

- The deformations in the slider based on which the stress distribution is calculated.
- The friction force based on the energy dissipated by elastic-plastic deformation and dissociation of bonds. The energy lost by dissociation of chemical and van der Waals bonds is dependent on the contact area.

Governing equations

- *Equilibrium equations*

The force in the bulk of the slider (F_B) has to be equal to the sum of the forces in the deformed asperities (F_i).

$$F_B = \sum F_i \tag{6-9}$$

This can be written in terms of deformation:

$$\delta_B \frac{E_B A_B}{H_B} = \sum \delta_i \frac{EA}{H_i} \tag{6-10}$$

E_B, A_B, and H_B are the elastic modulus, the cross-sectional area and the height of the bulk of the slider. E and A are the elastic modulus and the cross-sectional area for the micro-asperities. δ_i and H_i are the deformation and the corresponding height of each of the deformed micro-asperity.

- *Compatibility conditions*

For every micro-asperity that comes into contact with the counter-surface, the following must be true:

$$(H_B - \delta_B) + (H_i - \delta_i) + h_i = G \tag{6-11}$$

- *Matrix formulation*

$$\begin{bmatrix} \frac{E_B A_B}{H_B} & -\frac{EA}{H_1} & -\frac{EA}{H_2} & -\frac{EA}{H_3} & \dots \\ 1 & 1 & 0 & 0 & \dots \\ 1 & 0 & 1 & 0 & \dots \\ 1 & 0 & 0 & 1 & \dots \\ \dots & \dots & \dots & \dots & \dots \end{bmatrix} \begin{bmatrix} \delta_B \\ \delta_1 \\ \delta_2 \\ \delta_3 \\ \dots \end{bmatrix} = \begin{bmatrix} 0 \\ h_1 + H_1 + H_B - G \\ h_2 + H_2 + H_B - G \\ h_3 + H_3 + H_B - G \\ \dots \end{bmatrix} \tag{6-12}$$

It can be seen that the resulting system is a determined non-homogeneous linear system of equations and it can be easily solved to obtain the deformations vector. From the state of deformation, both the normal stress distribution and the true contact area are calculated. With the known state of deformation of the micro-asperities, we determine which of the nano-asperities are within the adhesive layer and thus brought into contact by the van der Waals forces. This gives us the true contact area which we can use to find the dissipated energy by breaking of the chemical and van der Waals bonds. The energy spent for mechanically deforming the surfaces can be readily calculated after the state of deformation is found. With the calculated amount of dissipated energy, we can calculate the friction force, by equation (4-1).

6.4 Simulations for the multi-scale, multi-level, hierarchical slider, under a fixed load (FLM)

In this formulation of the model, the slider is loaded by a constant vertical force P. The results of the calculation are the stress distribution, the gap and the force of friction caused by the relative motion between the slider and the rough surface.

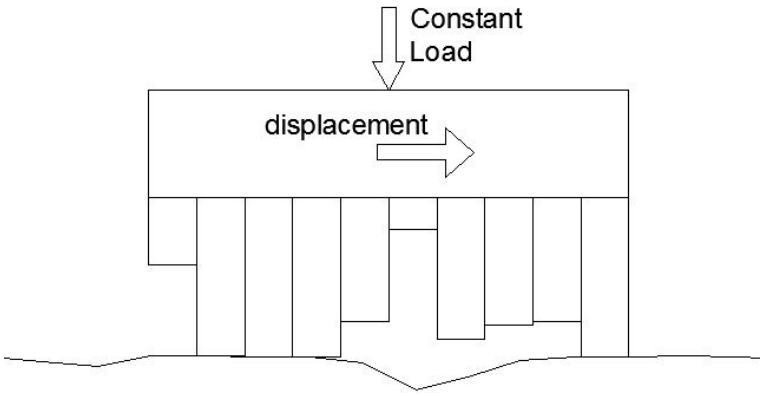

Figure 6-15 - Sketch of the Fixed Force Model

Formulation of the problem

The problem is quasi-static and it neglects the effect of time and inertial forces. The model calculates what the stress distribution and the energy loss are if the slider moves a displacement increment under a fixed load.

Input

- The input is the same as in the fixed gap problem with the only difference that in this model the fixed force *P* pressing on the slider is prescribed and the gap is to be calculated.

Output

- The deformations in the slider based on which the stress distribution is calculated.
- The friction force based on the energy dissipated by elastic-plastic deformation and bonds dissociation. The energy lost by dissociation of chemical and van der Waals bonds is dependent on the contact area.
- The gap between the top of the slider and the mean-line of the surface profile.

Governing equations

- *Equilibrium equations*

The force in the bulk of the slider (F_B) has to be equal to the sum of the forces in the deformed asperities (F_i). The force in the bulk equals the external load to which the slider is subjected. So the equation becomes:

$$P = \sum F_i \tag{6-13}$$

This can be written in terms of deformation:

$$P = \sum \delta_i \frac{EA}{H_i} \tag{6-14}$$

E and *A* are the elastic modulus and the cross-sectional area for the micro-asperities. δ_i and H_i are the deformation and the corresponding height of each of the deformed micro-asperity.

- *Compatiblity conditions*

For every micro-asperity that comes into contact with the counter-surface, the following must be true:

$$(H_B - \delta_B) + (H_i - \delta_i) + h_i = G \tag{6-15}$$

- *Matrix formulation*

$$\begin{bmatrix} 0 & \frac{EA}{H_1} & \frac{EA}{H_2} & \frac{EA}{H_3} & \dots \\ 1 & 1 & 0 & 0 & \dots \\ 1 & 0 & 1 & 0 & \dots \\ 1 & 0 & 0 & 1 & \dots \\ \dots & \dots & \dots & \dots & \dots \end{bmatrix} \begin{bmatrix} G \\ \delta_1 \\ \delta_2 \\ \delta_3 \\ \dots \end{bmatrix} = \begin{bmatrix} P \\ h_1 + H_1 + H_B + \delta_B \\ h_2 + H_2 + H_B + \delta_B \\ h_3 + H_3 + H_B + \delta_B \\ \dots \end{bmatrix} \tag{6-16}$$

It can be seen the resulting system is a determined non-homogeneous linear system of equations and it can be easily solved to obtain the deformations vector that also contains the gap. In the case of the fixed gap setup, once the state of deformation is known we can compute the energy dissipated by mechanical deformation, the true contact area, the energy dissipated by breaking the chemical and inter-molecular bonds and, in the end, the force of friction as the total spent energy over the sliding distance.

6.5 Results of simulations using various parameters of the contact

All calculations in this section are based on the same material samples and roughness profiles that have been used for all the original models presented in the previous chapter (the single asperity model in section 5.2 and the multi-scale hierarchical model

in section 5.6). The same approach to calculate the friction force has been used as described in Chapter 4. The material for both the counter-parts is copper. Samples of the measured roughness are given in Figure 6-2 and Figure 6-3. We will begin with the slider configuration shown in Figure 6-1, i.e. 10 micro-asperities, each being 13.5 microns wide. The support surface is extruded to a depth equal to the width of the micro-asperity (in this case, 13.5 microns). Each micro-asperity then has a square cross-section and is populated by nano-asperities having the geometry and distribution corresponding to the real surface roughness. The procedure used to represent the roughness has been described in section 6.2.1. The geometry of the slider is shown in Figure 6-16.

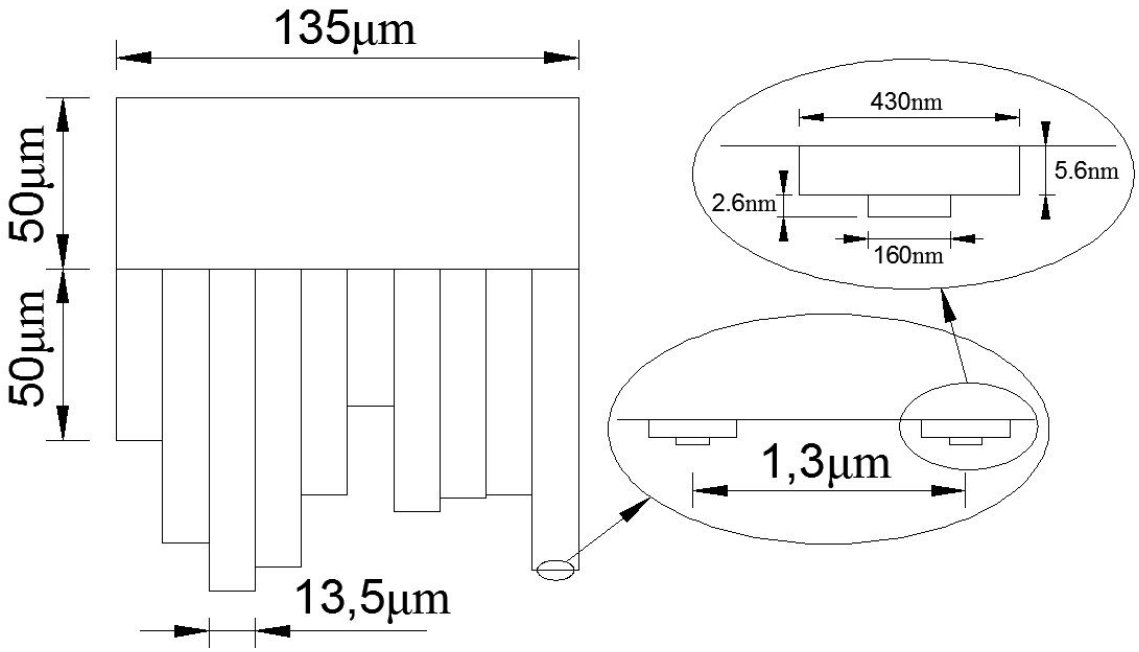

Figure 6-16 - Sketch of a slider geometry derived from measured profiles (note the snippet sketches have been vertically scaled up by a considerable factor to make geometry distinguishable)

6.5.1 The coefficient of friction

Here we present the results obtained when the top body slides over the surface for a distance of 150 microns, under the constant load of 0.18 *N*. Figure 6-17 shows the coefficient of friction (COF) for the configuration described above. The average value of the COF is 0.9. This is in agreement with the value estimated in section 4.4 and with the values of the COF for copper on copper friction given in literature, which are within 0.8 ÷ 1.2, according to Holmberg and Matthews (2009). The average value of the COF

is slightly lower than the value calculated in section 4.4 for one yielded micro-asperity (when all nano-asperities are in contact with the counter-surface), which was estimated at 1.02. The reason for this is that not all nano-asperities on the micro-asperities involved are in contact, therefore Figure 6-17 shows the apparent COF.

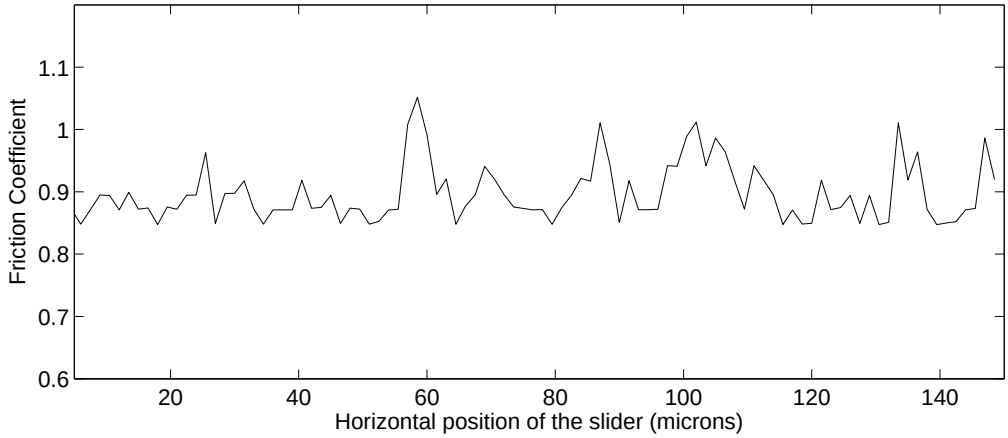

Figure 6-17 – The coefficient of friction (Fixed Load Model)

Dependence of the COF on the external load

Here we study how the normal load (and consequently, plasticity) influences the COF. In the simulation described above the normal force caused 3 micro-asperities to yield. We assume that, when one micro-asperity deforms plastically, all nano-asperities on its tip establish contact with the counter-surface. The breaking of these bonds leads to the dissipation of large amounts of energy which results in large friction force. The graphs presented in Figure 6-18 to Figure 6-31 show the dependence of the friction coefficient and of the dissipated energy on the external load.

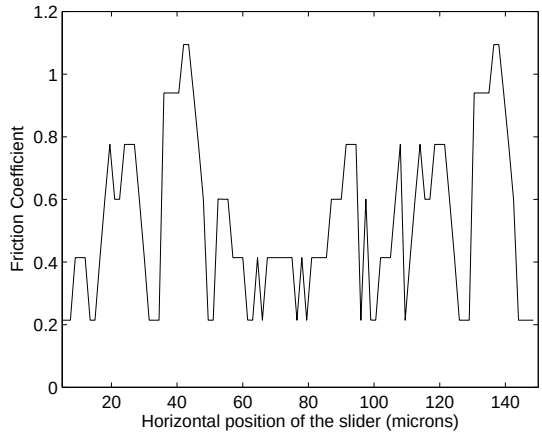

Figure 6-18 – The coefficient of friction in the framework of the fixed load model (FLM) (P_1 = 25mN, elastic deformation)

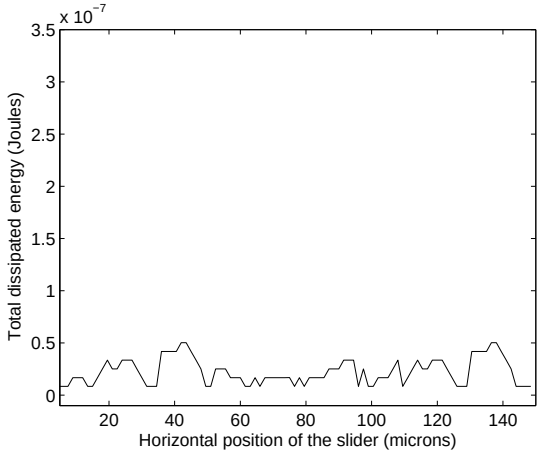

Figure 6-19 – The total dissipated energy in the framework of the fixed load model (FLM) (P_1 = 25mN, elastic deformation)

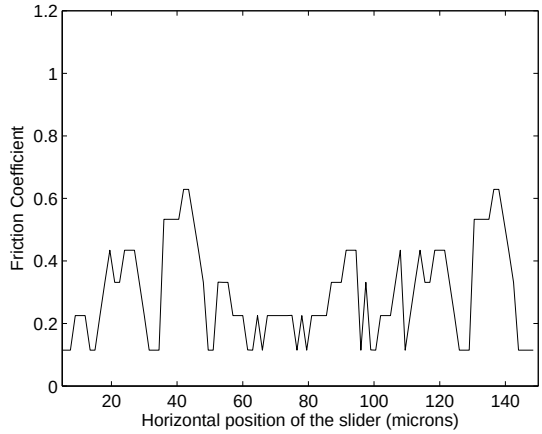

Figure 6-20 – The coefficient of friction (FLM) (P_2 = 48mN, elastic deformation)

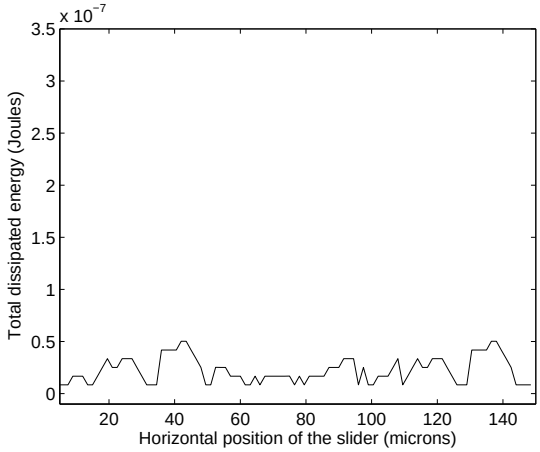

Figure 6-21 – The total dissipated energy (FLM) (P_2 = 48mN, elastic deformation)

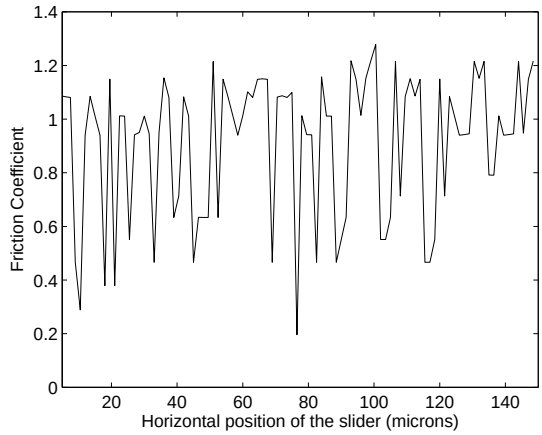

Figure 6-22 – The coefficient of friction (FLM) (P_3 = 55mN, one yielded micro-asperity)

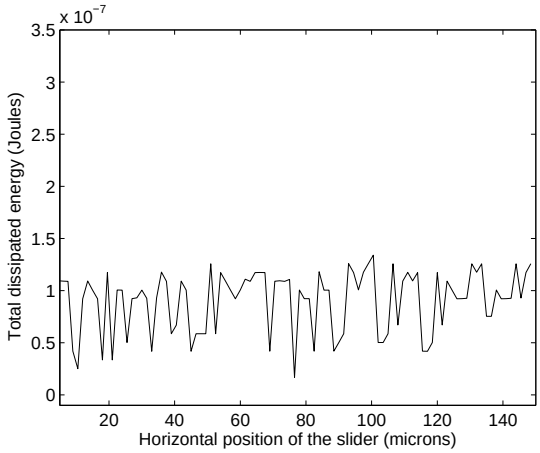

Figure 6-23 – The total dissipated energy (FLM) (P_3 = 55mN, one yielded micro-asperity)

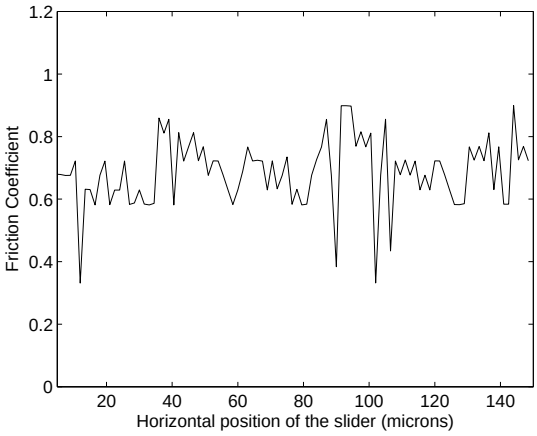

Figure 6-24 – The coefficient of friction (FLM) (P_4 = 96mN, one yielded micro-asperity)

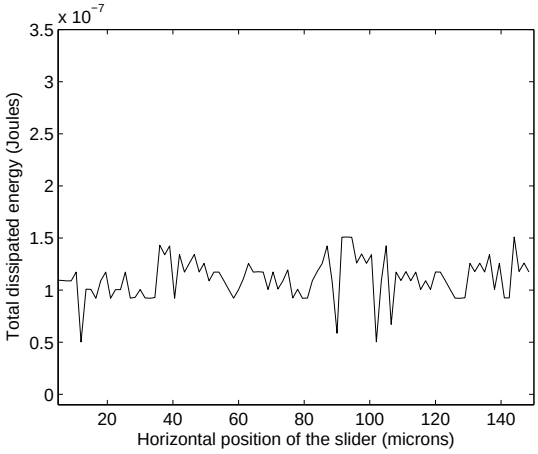

Figure 6-25 – The total dissipated energy (FLM) (P_4 = 96mN, one yielded micro-asperity)

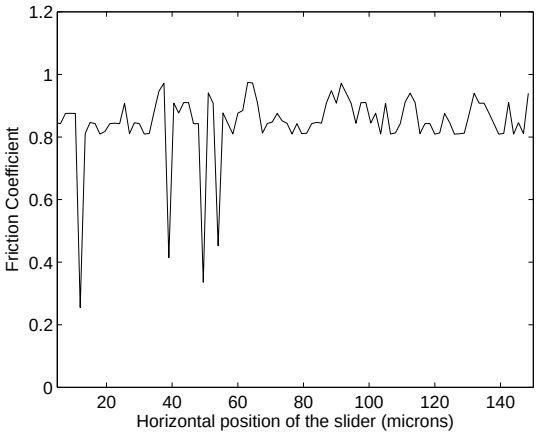

Figure 6-26 – The coefficient of friction (FLM) (P_5 = 126mN, two yielded micro-asperities)

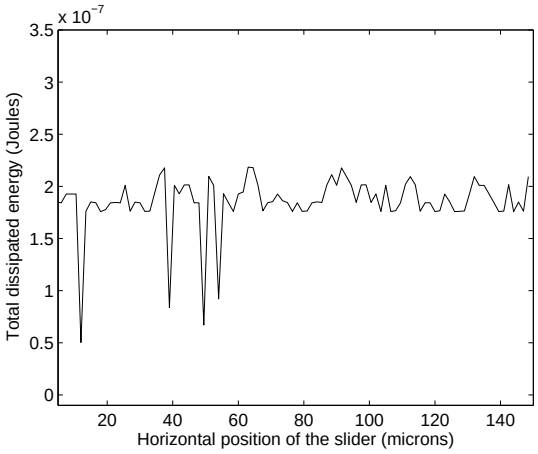

Figure 6-27 – The total dissipated energy (FLM) (P_5 = 126mN, two yielded micro-asperities)

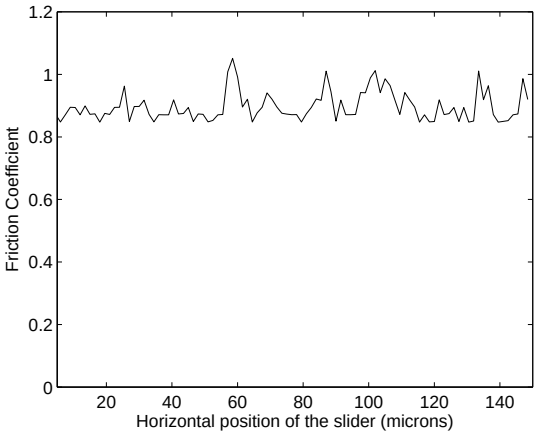

Figure 6-28 – The coefficient of friction (FLM) (P_6 = 176mN, three yielded micro-asperities)

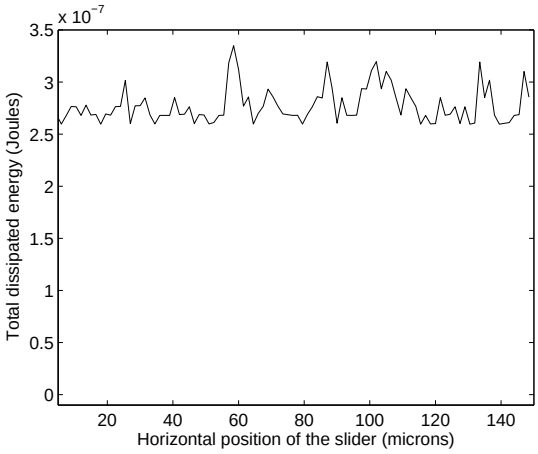

Figure 6-29 – The total dissipated energy (FLM) (P_6 = 176mN, three yielded micro-asperities)

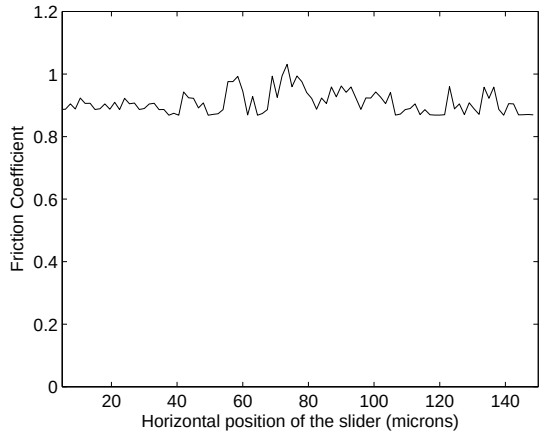

Figure 6-30 – The coefficient of friction (FLM) (P_7 = 226mN, four yielded micro-asperities)

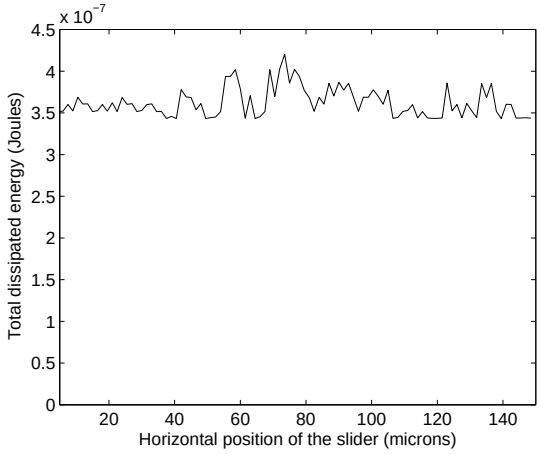

Figure 6-31 – The total dissipated energy (FLM) (P_7 = 226mN, four yielded micro-asperities)

The values of the external load were chosen so that a wanted number of micro-asperities yield. The force was expressed in terms of the elastic limit of the bulk of the slider. Considering we have 10 micro-asperities, the values for the load in the above graphs were obtained as follows (A_n is the nominal area, i.e. the cross-sectional area of the bulk section):

- $P_1 = 0.05\sigma_y A_n = 25mN$, elastic deformation
- $P_2 = 0.095\sigma_y A_n = 48mN$, elastic deformation
- $P_3 = 0.11\sigma_y A_n = 55mN$, one micro-asperity plastically deformed
- $P_4 = 0.19\sigma_y A_n = 96mN$, one micro-asperity plastically deformed
- $P_5 = 0.25\sigma_y A_n = 126mN$, two micro-asperities plastically deformed
- $P_6 = 0.35\sigma_y A_n = 176mN$, three micro-asperities plastically deformed
- $P_7 = 0.45\sigma_y A_n = 226mN$, four micro-asperities plastically deformed

Let us first look at the last 3 cases. The force is P_5 = 126mN, P_6 = 176mN and P_7 = 226mN. These force magnitudes cause 2 asperities to yield for P_5, 3 for P_6, and 4 for P_7. We can see the COF is roughly consistent for the 3 cases. Regarding the dissipated energy, it increases as more micro-asperities yield, leading to a larger contact area.

Another observation is that the aspect of the COF graph is different for the lowest loads than for the higher loads. More precisely, the distinction can be made between the case when we do not have any plastic deformation (for P_1 and P_2) and the case when we have plastic deformation in the micro-asperities (for P_4 to P_7), with the

transition for P_3 in Figure 6-22. At a closer look, the graphs in Figure 6-18 and Figure 6-20 are identical in shape and differ only in the magnitude of the COF. This suggests that we have identical friction force for both P_1 and P_2, which is confirmed by the identical energy dissipation curves in Figure 6-19 and Figure 6-21. This means that we have the same true contact area for both P_1 = 25mN and P_2 = 48mN. The reason for this is that the increase in force from P_1 to P_2 is not enough to change anything in the contact scenario. The contact area is the same; therefore the same amount of energy is dissipated. Consequently, the COF has lower magnitude for the higher load. This is related also to the discretization size of the roughness at the micro-scale.

Let us illustrate this by the contact scenario depicted in Figure 6-32. In the sketched case, the external force is not large enough to compress the micro-asperity to the extent that other micro-asperities come in contact. Small variations in the load would not change the contact area, and therefore would not change the friction force. However, increasing the external force would lower the COF, which we have seen in Figure 6-18 and Figure 6-20. In the current scenario, the contact area would increase if the applied load was large enough to cause the collapse of the asperity in contact, and the excess load to be passed to the next asperity. We can see that this happens in the transition from P_2 to P_3 when the dissipated energy increases drastically due to the increase in the contact area.

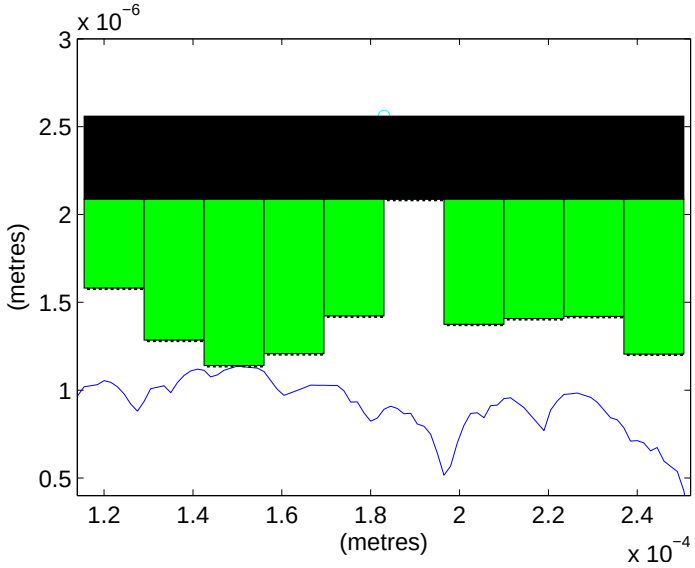

Figure 6-32 – Contact scenario in the framework of the Fixed Load Model (notice the different scales of the axes)

One could suggest that a finer discretization of the micro-surface would make the contacting asperity more compliant, and thus increase the contact area. Let us simulate the interaction between the slider and the surface when the micro-asperities are 9 times narrower.

Influence of the discretization size

Figure 6-33 and Figure 6-34 show the results from running a slider against the counter-surface under a fixed load of *P* = 5mN, in two configurations: coarse discretization (10 micro-asperities 13.5 microns wide, as shown in Figure 6-32) and fine discretization (90 micro-asperities 1.5 microns wide, as shown in Figure 6-35).

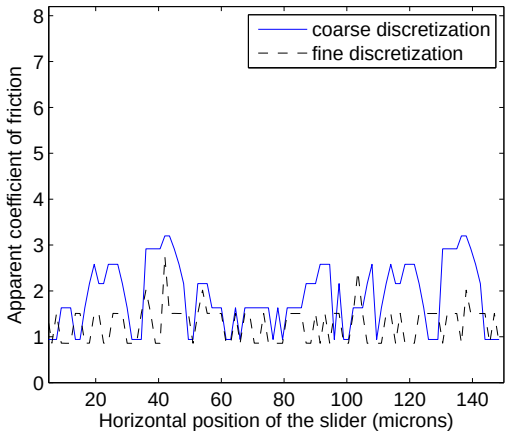

Figure 6-33 – The coefficient of friction (FLM) (P = 5mN, elastic deformation)

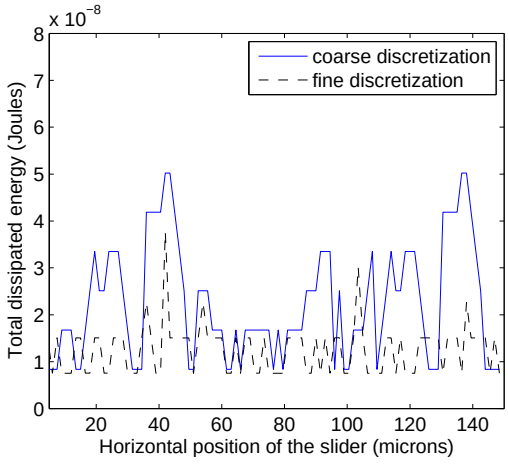

Figure 6-34 – The total dissipated energy (FLM) (P = 5mN, elastic deformation)

It can be seen that a finer discretization shows less energy is dissipated (Figure 6-34), as a consequence of a smaller contact area. This is also reflected in a smaller COF (Figure 6-33). The reason for this is that the profile of the slider becomes rougher under a finer discretization, leading to a smaller contact area. This is clear when Figure 6-32 and Figure 6-35 are compared. They illustrate the same position of the slider, relative to the support surface. It can be seen that in the coarse discretization model, because of the wide, flat micro-asperity in contact, the adhesive forces create a larger contact area. However, this is the case for very small loads, when all deformation is elastic. When the force is slightly increased, some of the micro-asperities in the fine discretization model will yield and the profile of the slider will become more compliant with the counter-surface, leading to an increase in the contact area. A graphical

illustration of this is given in Figure 6-36, and a comparison with the coarse model under the greater load ($P = 15mN$) is given in Figure 6-37 and Figure 6-38. As expected, the yielding of a couple of micro-rods (represented blue in Figure 6-36) has made the slider more compliant and increased the contact area. The dissipated energy is therefore greater and so is the COF.

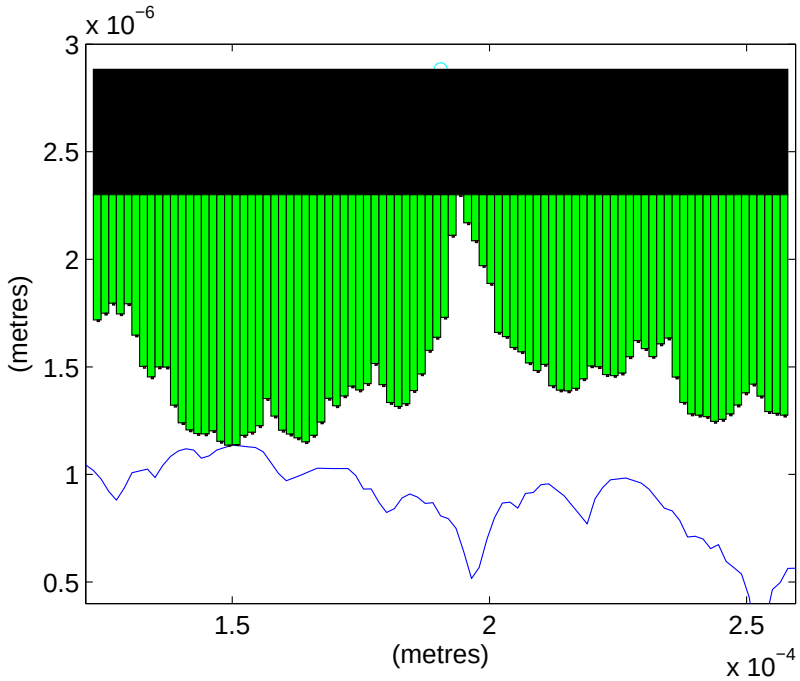

Figure 6-35 – A typical contact scenario for FLM with fine discretization (notice the different scales of the axes). The external load is $P = 5mN$

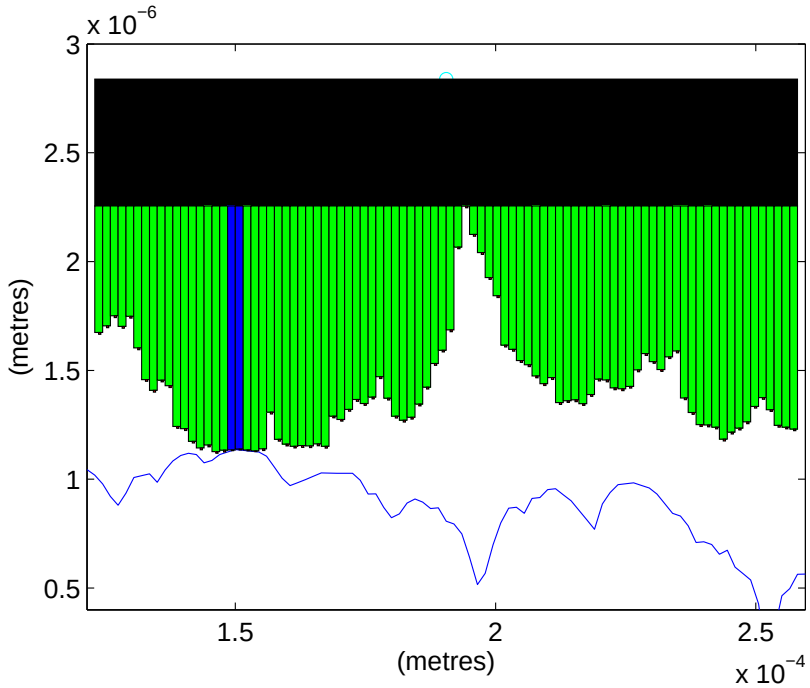

Figure 6-36 – A typical contact scenario for FLM with fine discretization (notice the different scales of the axes). The external load is $P = 15mN$

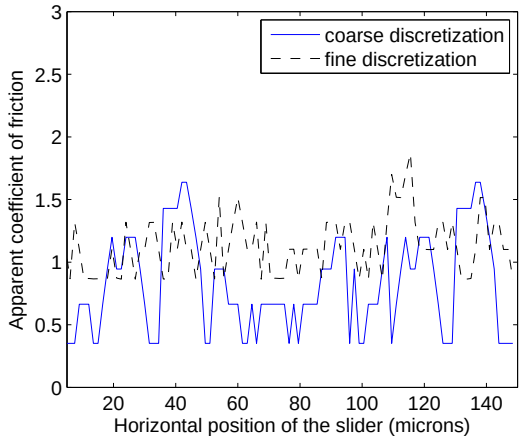

Figure 6-37 – The coefficient of friction (FLM) (P = 15mN)

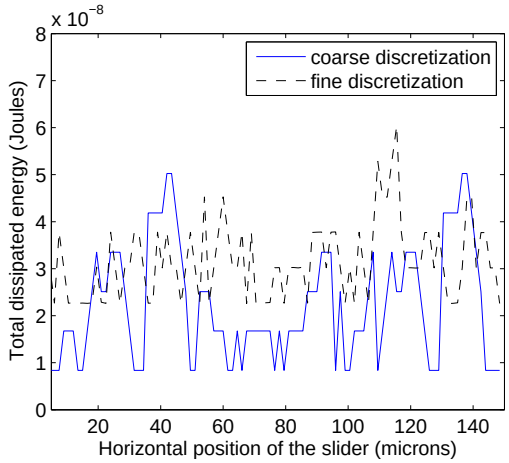

Figure 6-38 – The total dissipated energy (FLM) (P = 15mN)

We can see then that the results depend on the dissipation mechanisms involved, rather than the resolution of the slider, although they are related. Increasing the resolution of the discretization has impact on the results because narrower asperities can reflect the stress concentration at the contact points. The coarse discretization (Figure 6-32) cannot reflect the local contact effects. In real life, the contact would be sharper (closer to the scenario in Figure 6-35) which would lead to the wearing of the contacting asperity, causing an increase in the contact area, much like Figure 6-36 shows.

To test the consistency of the results, let us take the finer slider through the same force progression (from $P_1 = 0.05\sigma_y A_n$ to $P_7 = 0.45\sigma_y A_n$) for the FLM configuration. Figure 6-39 to Figure 6-52 show the COF and the amount of the total dissipated energy.

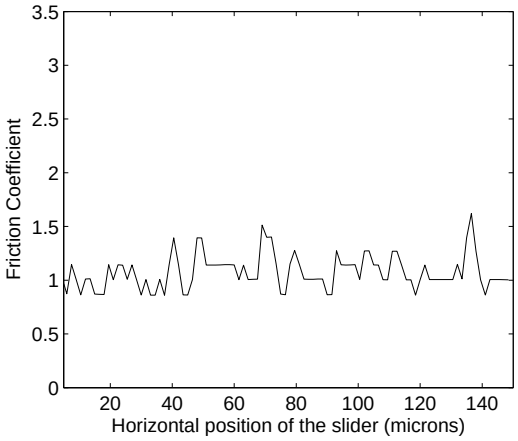

Figure 6-39 – The coefficient of friction in the framework of the Fixed Load Model (FLM) (P_1 = 0.05 σ_y A_n = 25mN)

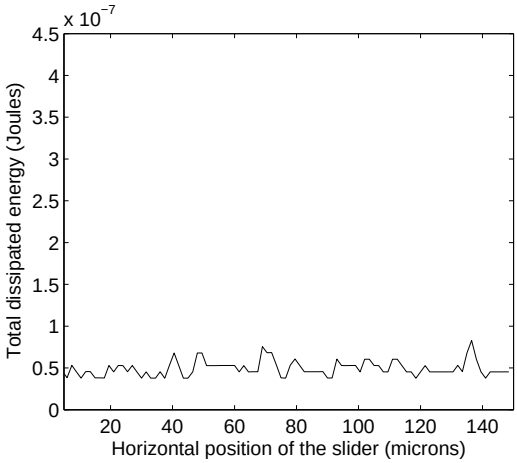

Figure 6-40 – The total dissipated energy (FLM) (P_1 = 0.05 σ_y A_n = 25mN)

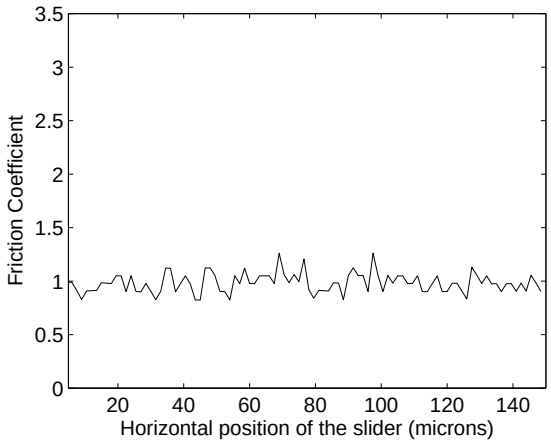

Figure 6-41 – The coefficient of friction (FLM) (P_2 = 0.095 σ_y A_n = 48mN)

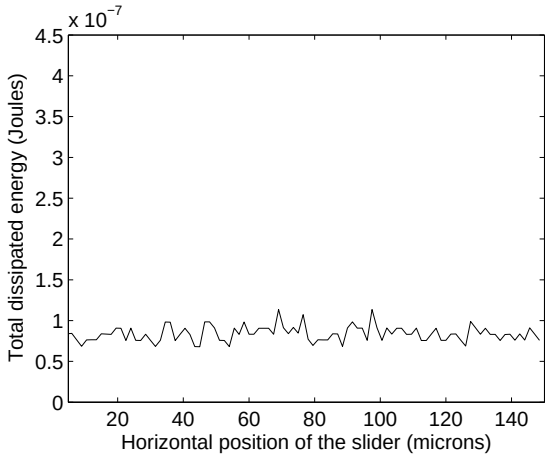

Figure 6-42 – The total dissipated energy (FLM) (P_2 = 0.095 σ_y A_n = 48mN)

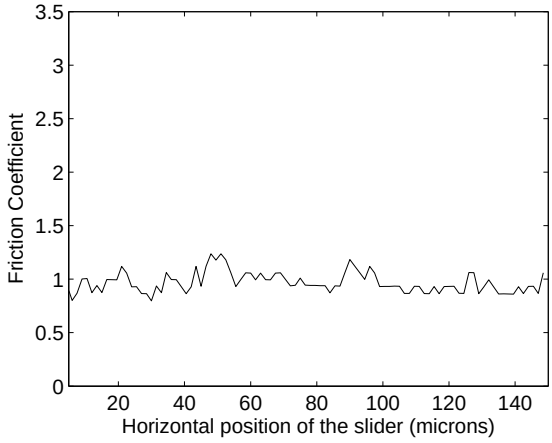

Figure 6-43 – The coefficient of friction (FLM) (P_3 = 0.11 σ_y A_n = 55mN)

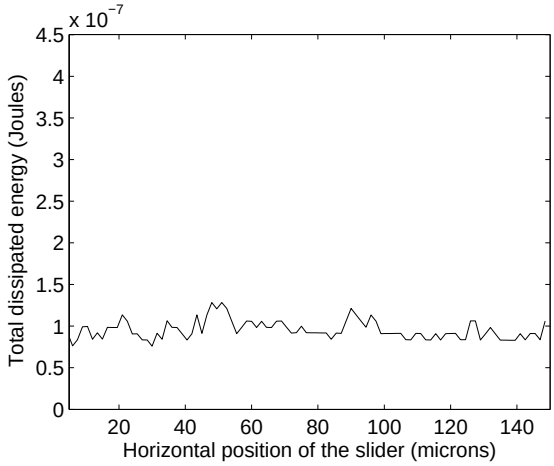

Figure 6-44 – The total dissipated energy (FLM) (P_3 = 0.11 σ_y A_n = 55mN)

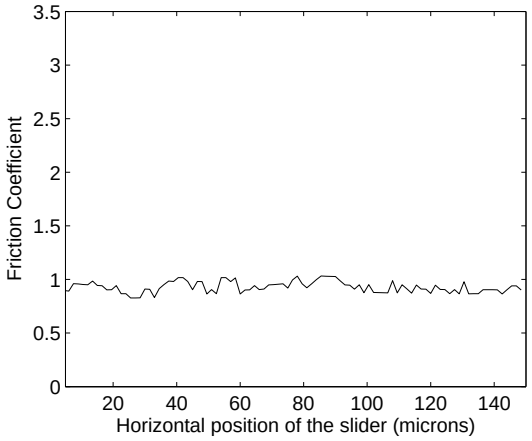

Figure 6-45 – The coefficient of friction (FLM) (P_4 = 0.19 σ_y A_n = 96mN)

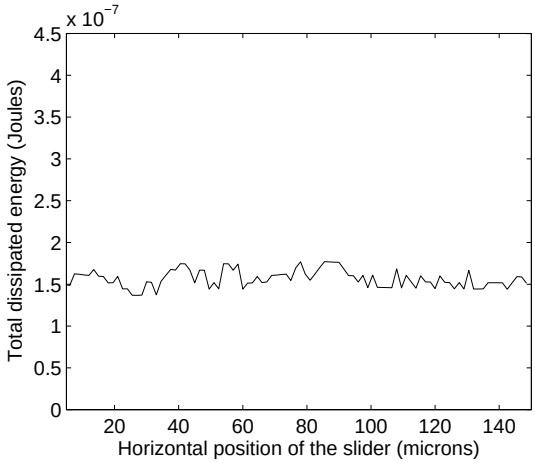

Figure 6-46 – The total dissipated energy (FLM) (P_4 = 0.19 σ_y A_n = 96mN)

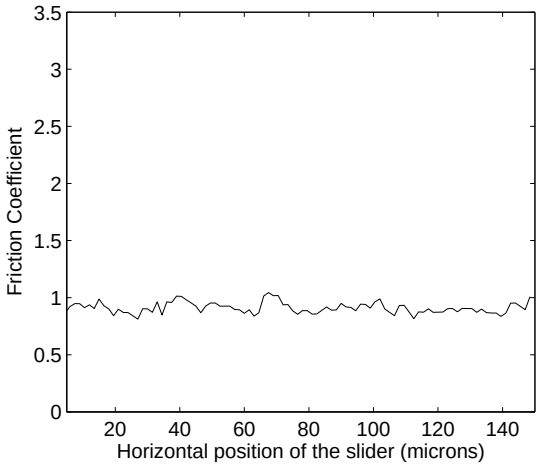

Figure 6-47 – The coefficient of friction (FLM) (P_5 = 0.25 σ_y A_n = 126mN)

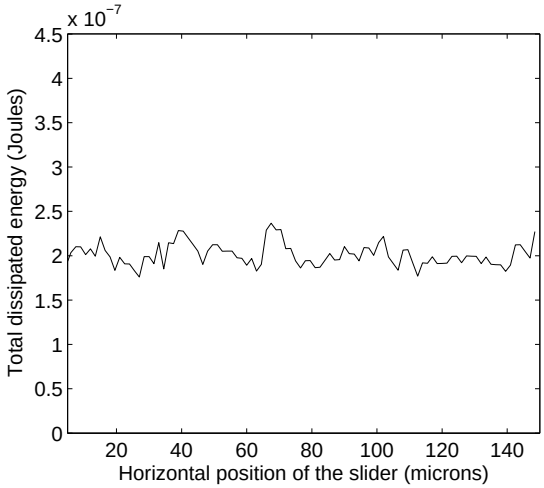

Figure 6-48 – The total dissipated energy (FLM) (P_5 = 0.25 σ_y A_n = 126mN)

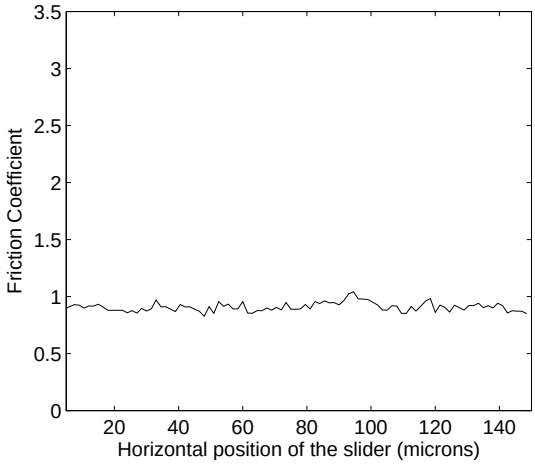

Figure 6-49 – The coefficient of friction (FLM) (P_6 = 0.35 σ_y A_n = 176mN)

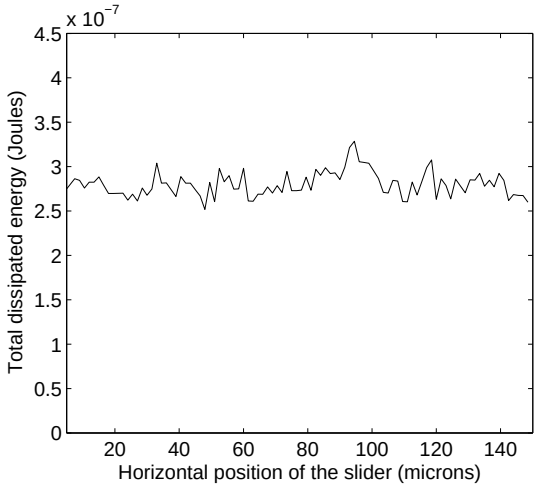

Figure 6-50 – The total dissipated energy (FLM) (P_6 = 0.35 σ_y A_n = 176mN)

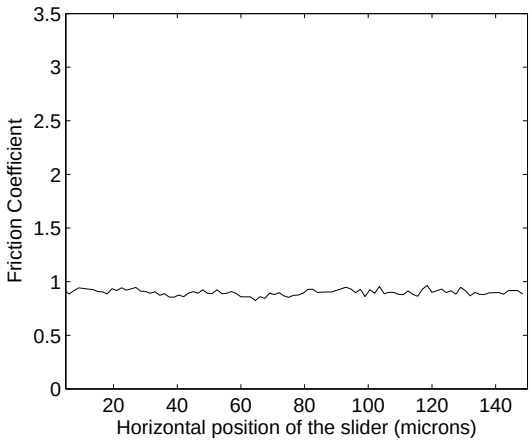

Figure 6-51 – The coefficient of friction (FLM) ($P_7 = 0.45\ \sigma_y\ A_n = 226mN$)

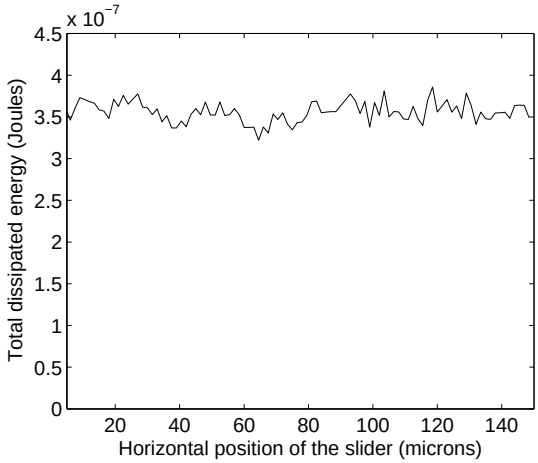

Figure 6-52 – The total dissipated energy (FLM) ($P_7 = 0.45\ \sigma_y\ A_n = 226mN$)

As expected, the total energy spent to slide the surfaces against each other increases as the load increases (see Figure 6-39 to Figure 6-52), while the average COF stays roughly the same. From an amount of 0.5 x 10^{-7} J corresponding to the external load of P_1 = 25mN, the energy reached 5.23 x 10^{-7} J for P_9 = 327mN, rising linearly with load, as shown in Figure 6-54.

Comparing the COF curves from the coarse discretization model (Figure 6-18 to Figure 6-31) to the COF curves from the fine discretization model (Figure 6-39 to Figure 6-52), it is evident that they are smoother when the discretization is finer.

It is also evident that, for both coarser and finer discretization, the COF curve becomes smoother as the load is increased. The explanation for this is that, at higher loads, the contact area is larger (see Figure 6-54 where the increase in the dissipated energy is a direct reflection of the increase of the true contact area) and the contribution of new asperities that come in contact is not so important, relatively speaking. When, for the lower loads, the contact area is smaller, the contribution of new asperities enlarging the contact area, and therefore the force of friction, is greater.

Normal load		Average COF	Average Dissipated Energy (*Joules*)
$P_1 = 0.05\sigma_y A_n$	25*mN*	1.08	0.50 x 10^{-7}
$P_2 = 0.09\sigma_y A_n$	48*mN*	0.98	0.84 x 10^{-7}
$P_3 = 0.11\sigma_y A_n$	55*mN*	0.97	0.91 x 10^{-7}
$P_4 = 0.19\sigma_y A_n$	96*mN*	0.93	1.57 x 10^{-7}
$P_5 = 0.25\sigma_y A_n$	126*mN*	0.91	2.01 x 10^{-7}
$P_6 = 0.35\sigma_y A_n$	176*mN*	0.91	2.80 x 10^{-7}
$P_7 = 0.45\sigma_y A_n$	226*mN*	0.90	3.56 x 10^{-7}
$P_8 = 0.55\sigma_y A_n$	277*mN*	0.91	4.39 x 10^{-7}
$P_9 = 0.65\sigma_y A_n$	327*mN*	0.92	5.23 x 10^{-7}

Table 6-1 - Dependence of the COF on load

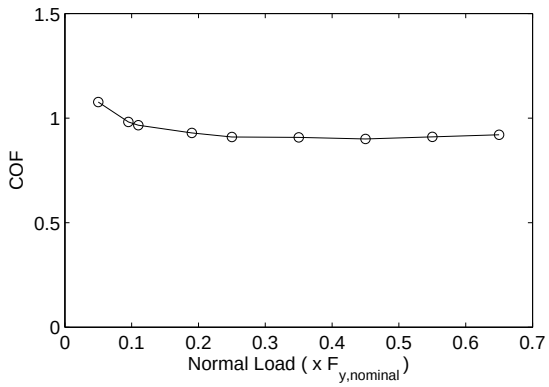

Figure 6-53 – The dependence of the average COF on the normal load (FLM)

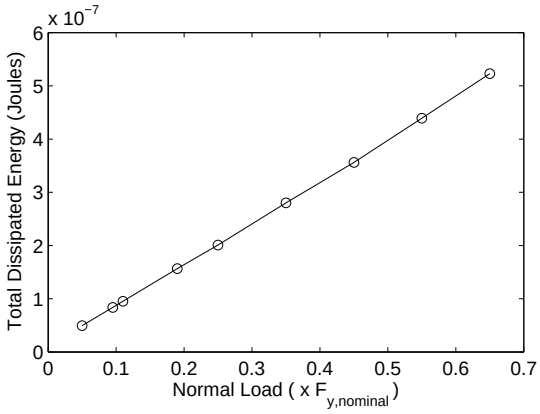

Figure 6-54 – The dependence of the average dissipated energy on the normal load (FLM)

The variation of the COF and the total dissipated energy with the external load, for the fine discretization model, is summarised in Table 6-1, Figure 6-53, and Figure 6-54. As expected from the second Amontons friction law, the friction force is proportional to the external load. It can be seen that more energy is dissipated when the load is increased (see Figure 6-54), leading to a greater friction force.

Dependence of the COF on nominal contact area

Here we study the influence of the increase of the nominal contact area on the COF. The values of the nominal area for which the simulation was performed are given in Table 6-2, and are expressed in terms of the cross-sectional area of a single micro-asperity (A_m = 20.25μm^2). The normal force has been proportionally scaled by the formula:

$P = 0.1\sigma_y A_n$. A snapshot of a contact instance for the widest slider is given in Figure 6-57.

Nominal Area (A_n)		Average COF	Average Dissipated Energy (*Joules*)
$A_1 = 40A_m$	810μm^2	0.99	0.40 x 10^{-8}
$A_2 = 80A_m$	1620μm^2	0.94	0.75 x 10^{-8}
$A_3 = 120A_m$	2430μm^2	0.97	1.16 x 10^{-7}
$A_4 = 160A_m$	3240μm^2	0.96	1.52 x 10^{-7}
$A_5 = 200A_m$	4050μm^2	0.93	1.84 x 10^{-7}
$A_6 = 240A_m$	4860μm^2	0.94	2.23 x 10^{-7}
$A_7 = 280A_m$	5670μm^2	0.96	2.67 x 10^{-7}

Table 6-2 - Dependence of the COF on nominal area

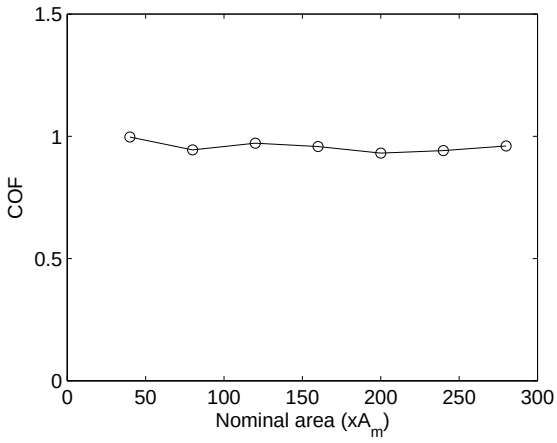

Figure 6-55 – The dependence of the COF on the nominal area (FLM)

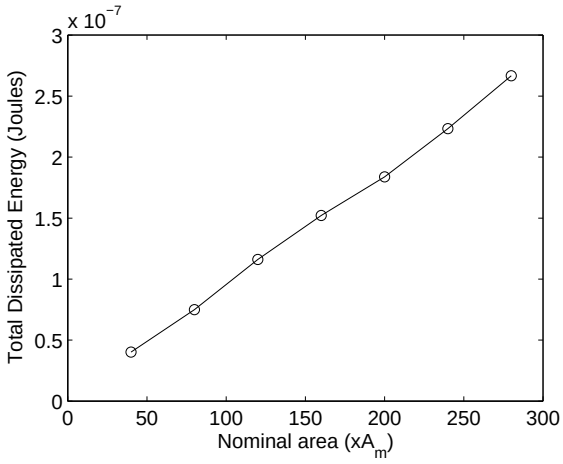

Figure 6-56 – The dependence of the dissipated energy on the nominal area (FLM)

Figure 6-56 shows that more energy is spent to move a wider slider, when the external load increases proportionally to the nominal contact area. The increase in the total dissipated energy is caused by the increase in the total true contact area.

Figure 6-55 suggests that the COF is not dependent on the nominal area of contact, as experimental observations confirm (Bowden and Tabor 1943). This also confirms the first of the Amontons' friction laws saying that 'the polishing force is independent of the dimensions of the lens' (see, for example Kragelsky et al. (1982)). This counterintuitive law was attributed by Akhmatov (1963) to the statistical laws of nature whose apparent simplicity is based on the rather high internal complexity of the phenomenon.

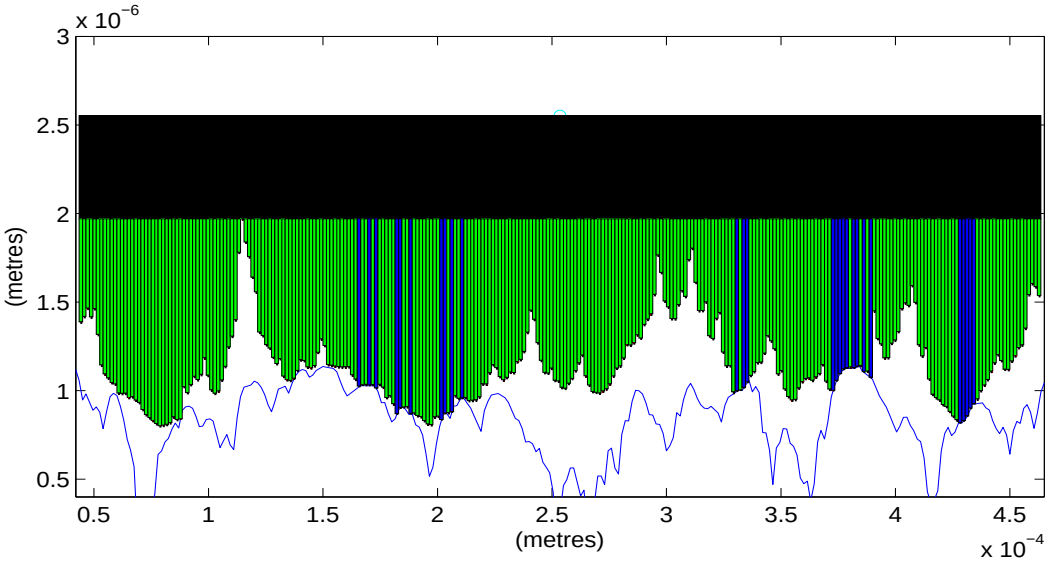

Figure 6-57 – Snapshot of a contact instance in the friction process for the nominal area A_7 (Fixed Load Model)

6.5.2 Influence of different energy dissipation mechanisms on dry friction

Here we will discuss the contribution of the different physical mechanisms to the total dissipated energy. It can be seen in Figure 6-58 that the mechanism causing the greatest energy dissipation is the breaking of chemical bonds.

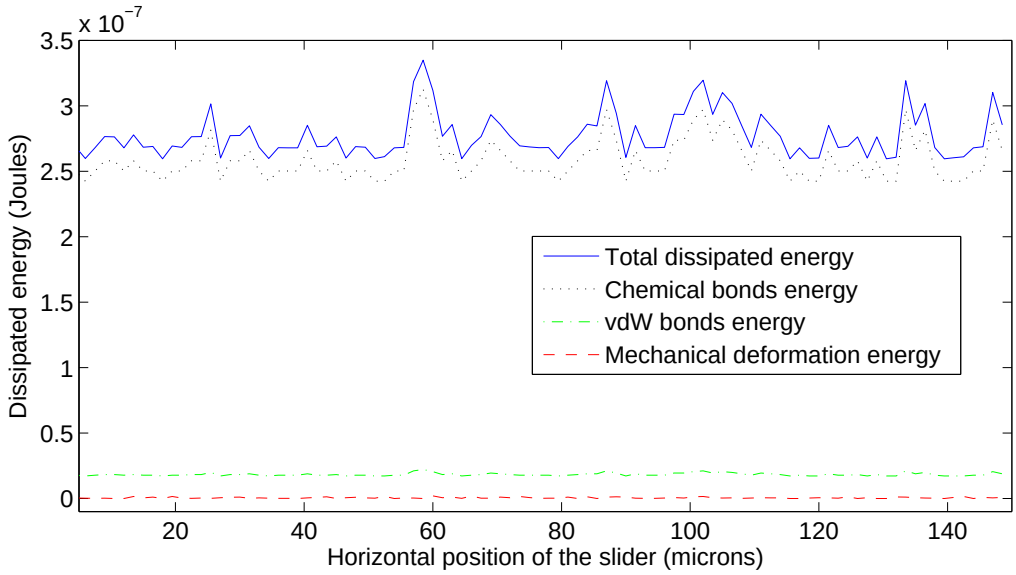

Figure 6-58 – Energy dissipation mechanisms (Fixed Load Model)

As we have explained before (see 4.2), adhesion plays a double role in our model. Firstly, it acts normally to the interface, increasing the true contact area. Secondly, the molecular forces resist the tangential motion when surfaces are sliding, thereby dissipating energy. Figure 6-58 shows strictly the energy spent for overcoming the tangential resistance of the van der Waals interactions. It can be seen that, compared to the energy spent for breaking the chemical bonds, this is very small. However, Figure 6-58 does not show the influence adhesion has in the energy dissipation by chemical interaction due to its role in increasing the true contact area.

To illustrate the role adhesion has normally to the surface and its contribution in increasing the true contact area, Figure 6-59 shows the fraction of the total contact area due solely to the adhesive forces at every step of the simulation.

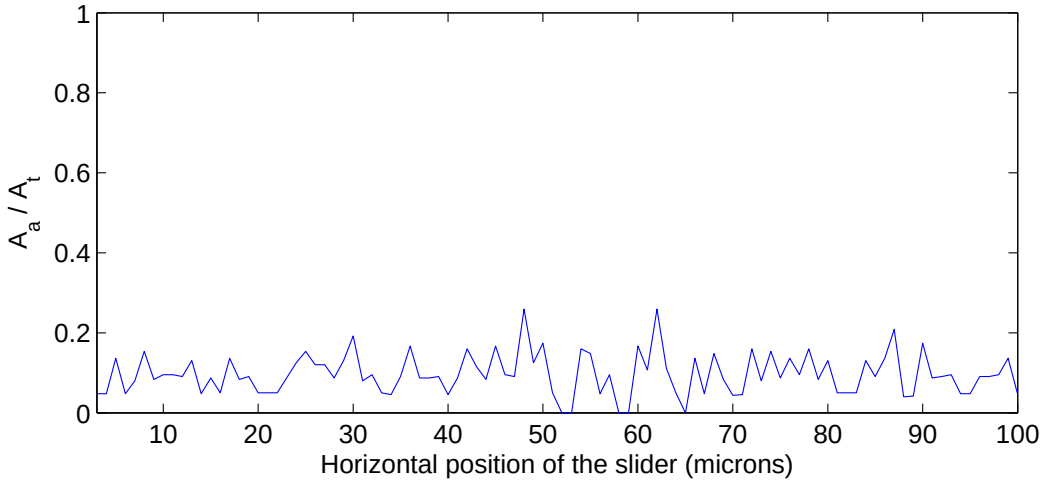

Figure 6-59 – Contact area due to the adhesive forces, as the ratio between the true contact area due to the adhesive forces and the total true contact area (Fixed Load Model)

It can be seen that adhesion is responsible for 10% (in average) of the total true contact area. It is obvious from the way we take into account the adhesive forces (described in section 4.2) that this contribution of adhesion to the true contact area depends on the thickness of the adhesive layer. In this model, the adhesive layer was considered 5*nm* thick, but there are studies that show a range of up to 150nm for the influence of the forces of adhesion (Lessel et al. 2013, Pollock 1992).

6.5.3 Dependence of true contact area on load

Here we will discuss how the contact area depends on the external load. A linear dependence of the contact area on the normal load was already suggested in Figure 6-54. In Figure 6-60 the ratio between the true contact area and the nominal contact area is plotted against the normal compressive force. The true contact area was obtained by multiplying the area of the van der Waals interaction domain of one nano-asperity with the number of nano-asperities in contact. The nominal contact area is the total projected area of the slider.

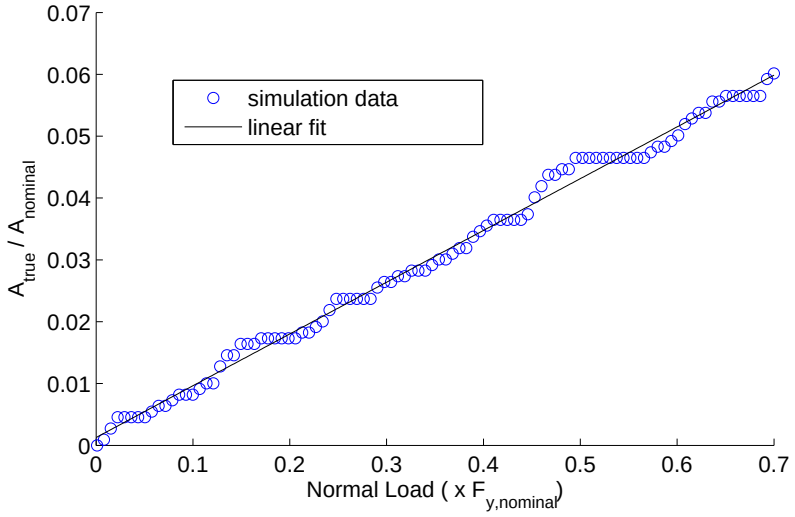

Figure 6-60 – Dependence of the contact area on the normal load (Fixed Load Model)

The 'contact area – normal load' curve shows some plateaus where the contact area is constant for some force intervals. This is due to the fact that the surface of the slider is a discrete domain and the total contact area increases when new nano-asperities establish contact, rather than increasing due to the deformation of the asperities already in contact.

The width, the frequency and the location of these plateaus on the curve is, of course, influenced by the relative position of the surfaces, the size of the roughness discretization, and the thickness of the adhesive layer.

It has to be said that the linear dependence of the contact area on load is a remarkable result. This relation between contact area and load has been observed both experimentally (first by Bowden and Tabor 1939) and in classic theoretical models by Zhuravlev (1940) and Greenwood and Williamson (1966), which use an approach entirely different to the one presented here.

6.5.4 Influence of the micro-roughness discretization size

Although we have addressed the impact of the resolution in section 6.5.1, in the current section we run the simulation for the same normal force and nominal area, over the same distance, for different discretization sizes. The value of the force is fixed at $P = 0.25\sigma_y A_n$. The width of the micro-asperities varies from 1d to 9d, where d is the distance between two measured points on the surface. In our case d = 1.5μm.

The average values of the COF are presented in Table 6-3. One can see that, for the chosen micro-asperity width variation, the diagram of the COF is fairly uniform. It can also be seen that the COF is highest for the finest discretization size.

Let us note also that the curve has a negative slope at the beginning and, after reaching the value of 0.83, it fluctuates about the average value of 0.82. A negative slope when increasing the width of the micro-asperities is most naturally explained by the fact that a more coarse profile is harder to conform with the counter-surface and thus leading to a smaller real contact area compared to the finer profile.

However, this explanation does not seem to make sense for the rest of the curve because, for example, the COF increases from 0.79 to 0.87 when the width of the micro-asperity increases from 6*d* to 7*d*. But there are contact scenarios that can produce a greater COF for a wider micro-asperity, without breaking the above stated general rule. For example, when the micro-asperity on the counter-surface is quite flat, a wider asperity on the slider will establish a larger contact due to the van der Waals forces, rather than a sharper one that can establish very narrow contact.

Width of micro-asperities	Average COF
1*d* = 1.5µm	0.90
2*d* = 3µm	0.91
3*d* = 4.5µm	0.89
4*d* = 6µm	0.83
5*d* = 7.5µm	0.84
6*d* = 9µm	0.79
7*d* = 10.5µm	0.87
8*d* = 12µm	0.79
9*d* = 13.5µm	0.82

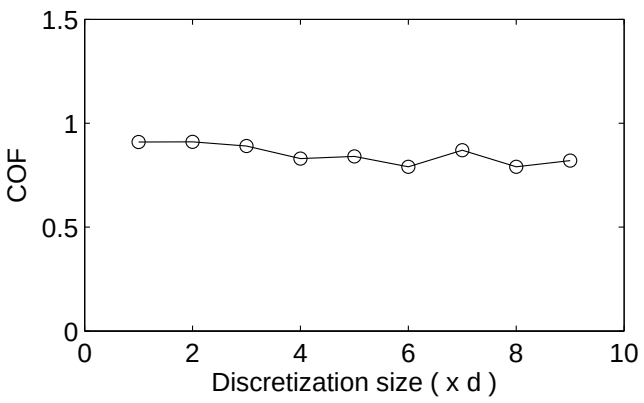

Table 6-3 - Dependence of the COF on the discretization size for $P = 0.25\ \sigma_y\ A_n$

To show that the chosen micro-asperity variation has little impact not only on the average value of the COF but also on the shape of the graph, Figure 6-61 to Figure 6-70 show the plots of the COF and the dissipated energy, corresponding to the following widths: 1*d*, 3*d*, 5*d*, 7*d*, 9*d*. The nominal area and the external load are held constant.

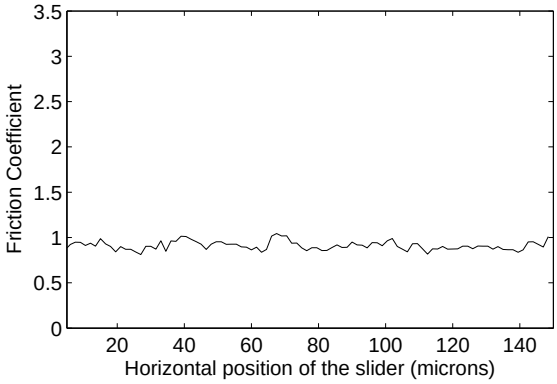

Figure 6-61 – The coefficient of friction in the framework of the Fixed Load Model (FLM) (width of micro-asperity = 1*d*)

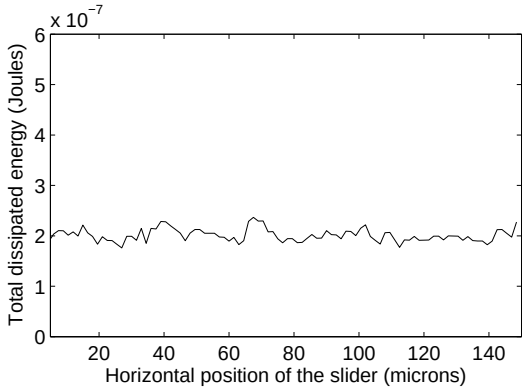

Figure 6-62 – The total dissipated energy in the framework of the Fixed Load Model (FLM) (width of micro-asperity = 1*d*)

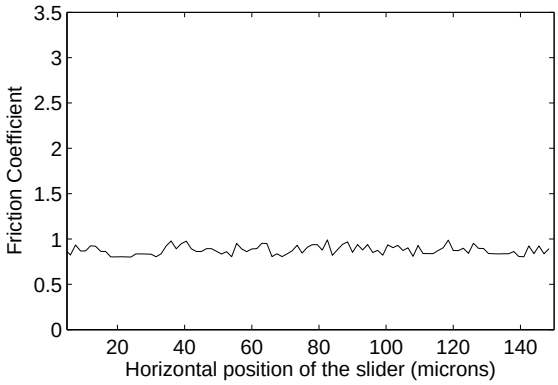

Figure 6-63 – The coefficient of friction (FLM) (width of micro-asperity = 3*d*)

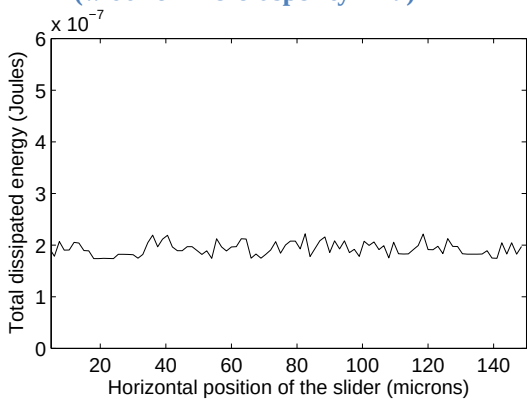

Figure 6-64 – The total dissipated energy (FLM) (width of micro-asperity = 3*d*)

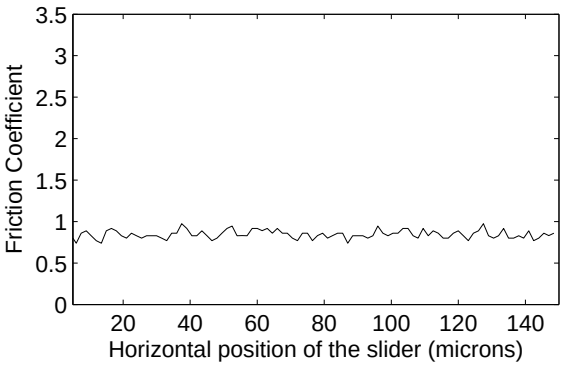

Figure 6-65 – The coefficient of friction (FLM) (width of micro-asperity = 5*d*)

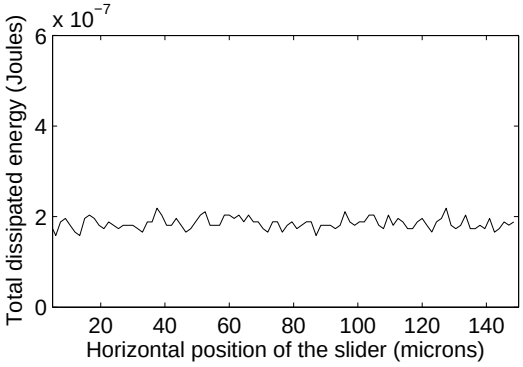

Figure 6-66 – The total dissipated energy (FLM) (width of micro-asperity = 5*d*)

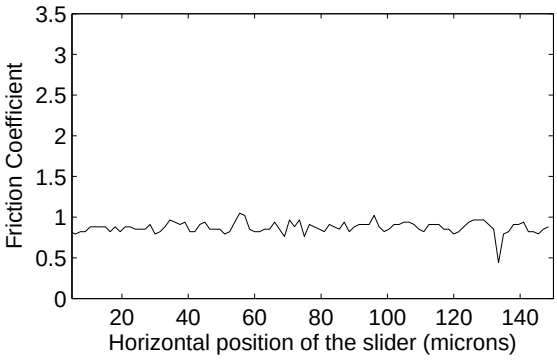

Figure 6-67 – The coefficient of friction (FLM) (width of micro-asperity = 7*d*)

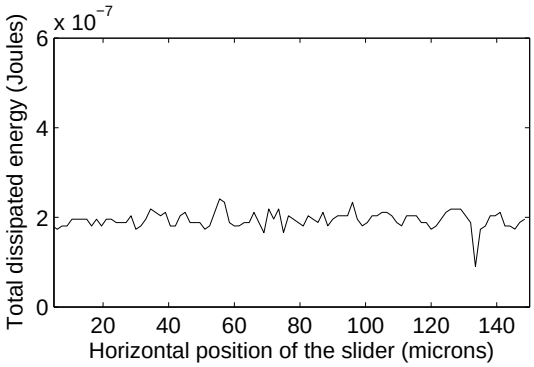

Figure 6-68 – The total dissipated energy (FLM) (width of micro-asperity = 7*d*)

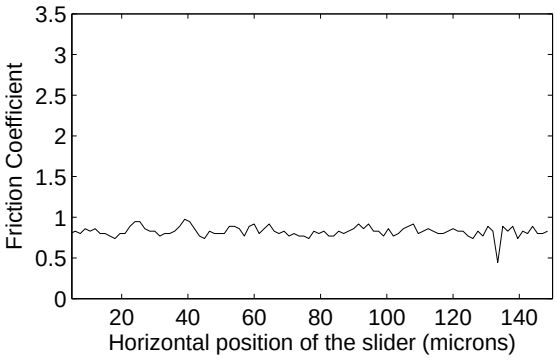

Figure 6-69 – The coefficient of friction (FLM) (width of micro-asperity = 9*d*)

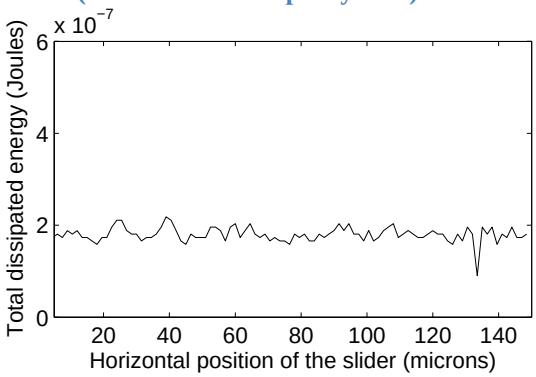

Figure 6-70 – The total dissipated energy (FLM) (width of micro-asperity = 9*d*)

Analysing the above figures, it can be seen that the curves for the first 3 cases (for the 1*d*, 3*d*, and 5*d* wide asperities) are slightly different to the curves for 7*d* and 9*d.* The curves corresponding to the coarser discretization have a steep valley between position 130µm and 140µm of the slider. This is most probably due to some feature of the surface that very wide asperities are unable to 'catch.'

It can also be seen that generally the curves have similar shapes. There is great similarity between the graphs of the first 3 cases and between the graphs of the last 2 cases.

In the discussion in section 6.5.1 about the dependence of the COF on the external load we have seen that the width of the micro-asperities is very important, but for very small loads. When the load is large enough to cause at least one asperity to yield in the coarsest discretization, there is insignificant advantage in considering a finer discretization. The reason for this is that the difference in the true area of contact will

be very small, as the plastically deformed micro-asperities are very compliant and all their nano-asperities are considered to establish contact.

Discussion on choosing the width of the micro-asperity

We have to begin by justifying our choice of the variation of the width of the micro-asperities from 1*d* to 9*d*. A visual representation of the two configurations is shown in Figure 6-71 and Figure 6-72 for comparison.

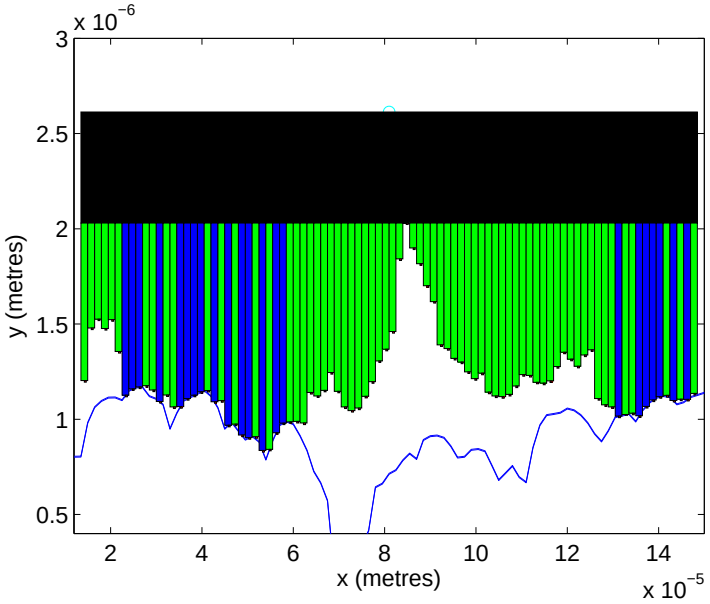

Figure 6-71 – Visual representation of the slider with the finest micro-asperity discretization (width of the micro-asperities is 1*d* = 1.5µm)

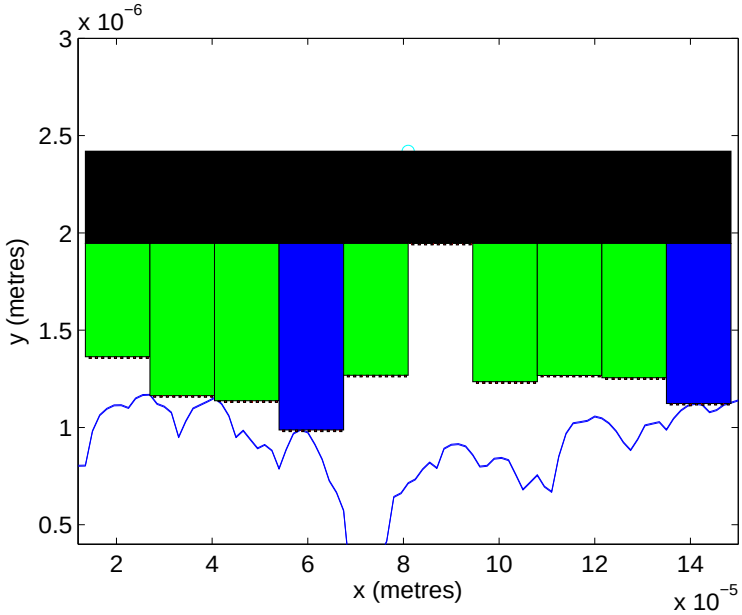

Figure 6-72 – Visual representation of the slider with the coarsest micro-asperity discretization (width of the micro-asperities is 9*d* = 13.5µm)

The lowest of the studied values of the micro-asperity width is directly given by the measurement resolution and it is equal to the horizontal distance between two measured points, which in our case is 1.5µm. It can be seen in Figure 6-71 that such a representation of the asperities fails to model the behaviour of individual micro-asperities, which are wider, because it cannot model appropriately the interlocking between the asperities of the rubbing counter-parts.

On the other hand, a visual examination of the coarse discretization illustrated in Figure 6-72 reveals that the micro-asperities are too wide. Keeping in mind that the surface profiles for the lower surface and for the slider are identical, it can be seen by comparison that the rods of the slider are wider than the micro-asperities they try to represent.

Consequently, the best micro-asperity representation should have a width between the limits of the studied values, i.e. between 1d and 9d. Out of the statistical parameters we can compute to reflect the most appropriate width, the average width of asperities at the height R_q (root mean square of all asperity heights) could be relevant. However, the resulting width is 15.8µm (i.e. 10.5d) which is even larger than the maximum width we have studied. If we calculate the average width of asperities at the height R_a (arithmetic mean of all positive heights), the result is 15.96µm, which is about the same as the previous case.

To conclude the section on the analysis of the influence of the discretization size, we can say that, when at least one micro-asperity is past the elastic limit, there is little impact on the results for the widths we have studied. However, not all of these widths are equally good to model the slider, but the statistical feature to set the width to be used is an open question.

6.6 Discussion of the influence of the environmental conditions on dry friction. Extensions of models to non-crystalline coatings

As it was stated before, the model developed by the author is based on the assumption that the surfaces coming in contact are perfectly clean, i.e. all the atoms on the tip of the nano-asperities engage in chemical interactions. However, the model could be applied to simulate dry friction in non-vacuum conditions due to the fact that the contacting surfaces clean each other after a few sliding cycles. The surface contamination in the form of oxides, water vapours and other impurities can be removed, exposing clean material that will cold-weld to the counter surface.

However, the model could be extended to take into account the contamination of surfaces by considering the statistical features of the contact between them.

Another important factor in the process of dry friction is the coating of surfaces. One example of a widely used class of coatings is the carbon nitride coatings which, under certain conditions, makes attaining COF as low as 0.005 possible (Adachi and Kato 2008). Diamond-like carbon (DLC) coatings are also widely used due to their hardness and wear resistance, in some conditions having a COF as low as 0.02 (see e.g. Bull 1995). Experiments performed by Alanou et al. (2002) show that DLC coatings and boron carbide coatings improve the scuffing resistance of hardened steel disks and gears.

The model presented can be extended to model the interaction between coated surfaces. If the coating is undamaged, the chemical component of friction will reflect the interaction between the atoms of the meeting counter-surfaces, which can be metal-coating, or coating-coating. If material transfer takes place, one can use the statistics of how surfaces change to model the process.

The chemical composition of the gaseous medium where the rubbing between the surfaces takes place also greatly influences the friction mechanisms. For example, as Borodich (2013c) shows for the case of carbon nitride coated surfaces, when the atmosphere contains O_2, some graphitization of asperities takes place and they are removed layer by layer along with the chipping of asperities due to subsurface cracks.

If the atmosphere has a high concentration of O_2, graphitization of asperities is predominant and there is no chipping. However, when the atmosphere is rich in N_2, graphitization is negligible and chipping is dominant. These are mechanisms that have to be taken into account to model the effect of the environment on the tribological processes.

6.7 Conclusions

In the current chapter a hierarchical, multi-scale and multi-level model has been presented. The model takes into account multiple physical mechanisms involved in the frictional process, i.e. the chemical interactions between surfaces at the atomic scale, the adhesive (van der Waals) interactions at the nano-scale, and the mechanical interlocking of asperities and their coupling at the micro and macro-scale.

The results we have obtained are very promising, both quantitatively and qualitatively. The value of the COF for the studied case (~0.9) was as reported in literature (between 0.8 and 1.2 for Cu on Cu dry sliding). The dependence of friction on external load and the dependence of friction on nominal contact area were as expected from Amontons friction laws. The model also reflects a linear dependence between the real contact area and the external load, as experimental observations show.

All the presented results are obtained on the assumption of perfectly clean surfaces, not taking into account effects of the environmental air, like the oxidation layer, water vapours and other impurities which can significantly affect the friction process. Another important assumption is that the crystalline structures of the counter-parts are perfectly aligned, which can hardly be the case for regular sliding surfaces.

We have to also mention that the current formulation of the model is not appropriate for any arbitrary rough profile. The surface we have used in our simulations was from a previously run-in profile, so the rigid surface was already plastically deformed. However, the model can easily be extended to take into account the deformation of the counter-surface, so that the interaction between surfaces with sharper asperities can be modelled as well.

Chapter 7 - Conclusions and Future Work

7.1 Conclusions

This section will draw the conclusions to the work presented in this thesis. As stated before, the concern of the current work is the modelling of dry friction. Two approaches have been used.

Firstly, the rescaling approach introduced by Borodich (1989) was used to describe indentation tests to check whether it can model the mechanical interaction between asperities of interacting surfaces. The findings are presented in section 7.1.1.

Secondly, multi-scale hierarchical models of dry friction were introduced and the main findings are summarized in section 7.1.2.

7.1.1 Scaling approach to indentation tests

1. It has been shown that the bluntness of the nominally sharp indenters greatly influences the force-displacement diagrams.
2. It has been found that the scaling approach is reliable in describing the indentation experiments by a spherical punch, provided the experiment one tries to describe does not break the assumptions of the theory. Most importantly, the materials of the indenter and the sample have to either be identical (have the same hardening exponent) or one of them has to be very hard compared to the other so that it can be considered perfectly rigid.
3. The rescaling approach can be used in modelling dry friction between non-linear elastic materials and surfaces whose asperities are modelled as solids of revolution. The model would be formulated following the straight-forward approach of Zhuravlev (1940) and using the power law punch shape introduced by Galin (1946).
4. In the case of indentation by a nominally sharp indenter, the assumptions of the Hertz problem are broken and the rescaling approach cannot be reliably used to describe the experimental curves.

7.1.2 The simulation of dry friction using a multi-scale, multi-level, hierarchical models

Multi-scale, hierarchical models of dry friction were introduced. Due to the hierarchical nature of their structure, the asperities are coupled at the micro level.

The model reflects physical mechanisms specific to the atomic scale (chemical interactions), the nano-scale (van der Waals interactions), and the micro-scale (mechanical interlocking of micro-asperities). Novel assumptions have been used in modelling adhesion and the deformation of the nano-asperities.

Concerning adhesion, it plays a double role. Normally to the surface, adhesion increases the true contact area, and tangentially to the surface, adhesion opposes the relative sliding thus dissipating energy.

The Polonsky-Keer effect has been modelled in the mechanical behaviour of the nano-asperities, i.e. nano-asperities do not deform plastically.

The geometry of the slider reflects the roughness measured at the micro-scale (by profilometer) and at the nano-scale (by AFM). The width and length of the micro-asperities are approximated directly from the measured profile, while the width and length of the nano-asperities are obtained by statistical analysis of the nano-profile.

The model has been used to simulate the sliding friction between two copper surfaces.

1. The obtained value of the COF was ~0.9, in agreement with experimental findings that report a COF between 0.8 and 1.2.
2. In average, the COF does not depend on the nominal contact area and the external normal load.
3. In general, the force of friction increases linearly with the external load.
4. The true contact area increases linearly with the external load.
5. The results showed that, in the case under consideration (vacuum), the most important energy dissipation mechanism is the breaking of the chemical bonds.
6. For external loads large enough to produce plastic deformation in the micro-asperities, the average value of the COF is not greatly affected by the chosen

width of the micro-rods representing the micro-asperities, provided they reflect reasonably the geometrical aspect of the represented profile.

7.2 Future work

The multi-scale, multi-level hierarchical approach introduced in this work is the first version and is based on many approximating assumptions. Therefore the approach can be developed in many respects.

The way plastic deformation is modelled in the present model is unrealistic and very simplistic. Currently the plastic strain of one yielding micro-asperity is subtracted and equally divided among the closest 2 non-yielded neighbours. Using a weighting function to distribute the dislocated material would be an important improvement as this would affect the way the contact area varies when increasing the external load. Another drawback in the modelling of plastic deformation is that the properties of the material do not change when yielding.

The yielding stress of the asperities depends on the defects orientation in their micro-structure. A future version of the model could take into account the slip orientation of dislocations for every asperity, or it can consider it as a statistical distribution over all asperities.

Another important drawback of the current formulation of the model is that it does not take into account the Poisson effect and thus disregards the transverse strain when the asperities deform. This needs to be addressed in the future version of the model.

A dynamic formulation of the model can describe many physical phenomena observed in friction experimentally. Preliminary dynamic simulations show slider lift with velocity which leads to a decrease in the force of friction, and stick-slip behaviour. In addition the model can be improved to permit lateral deformation which will make it show pre-sliding mechanisms.

As the main source for energy dissipation in vacuum is the dissociation of chemical bonds, a key question is establishing the contact area engaged in chemical interaction, which is closely related to the representation of the asperities at the nano-scale.

Taking this work further would bring important improvements to the model, as would the consideration of other energy dissipation mechanisms, surface contamination and other elements that can change the chemical reactivity of the surface.

References

Abbott, E. J., Firestone, F. A. 1933. Specifying surface quality: a method based on accurate measurement and comparison. *Mechanical Engineering,* 55**,** 569–572

Abuzeid, O. M., Eberhard, P. 2007. Linear viscoelastic creep model for the contact of nominal flat surfaces based on fractal geometry: Standard linear solid (SLS) material. *Journal of Tribology-Transactions of the Asme,* 129**,** 461-466

Adachi, K., Kato, K. 2008. Tribology of Carbon Nitride Coatings. *In:* Donnet, C. & Erdemir, A. (eds.) *Tribology of Diamond-Like Carbon Films.* Springer US**,** 339-361

Agrait, N., Yeyati, A. L., Van Ruitenbeek, J. M. 2003. Quantum properties of atomic-sized conductors. *Physics Reports-Review Section of Physics Letters,* 377**,** 81-279

Akhmatov, A. S. 1963. *Molecular Physics of Boundary Friction,* Moscow.

Akhmatov, A. S. 1966. *Molecular physics of boundary friction,* Jerusalem, Israel Program for Scientific Translations.

Al-Bender, F., De Moerlooze, K., Vanherck, P. 2012. Lift-up Hysteresis Butterflies in Friction. *Tribology Letters,* 46**,** 23-31

Al-Bender, F., Lampaert, V., Swevers, J. 2004. A novel generic model at asperity level for dry friction force dynamics. *Tribology Letters,* 16**,** 81-93

Alanou, M. P., Snidle, R. W., Evans, H. P., Krantz, T. L. 2002. On the performance of thin hard coatings for gearing applications. *Tribology Transactions,* 45**,** 334-344

Amontons, G. 1699. De la resistance causée dans les Machines, tant par les frottemens des parties qui les composent, que par roideur des cordes qu'on y employe, & la maniere de calculer l'un & l'autre. *Histoire de l'Académie royale des sciences***,** 206-222

Archard, J. F. 1957. Elastic deformation and the laws of friction. *Proceedings of the Royal Society of London Series a-Mathematical and Physical Sciences,* 243**,** 190-205

Azo Materials. 2000. *www.azom.com* [Online]. Available: http://www.azom.com/properties.aspx?ArticleID=1203 [Accessed 01 April 2016.

Bartier, O., Hernot, X., Mauvoisin, G. 2010. Theoretical and experimental analysis of contact radius for spherical indentation. *Mechanics of Materials,* 42**,** 640-656

Beghini, M., Bertini, L., Fontanari, V. 2006. Evaluation of the stress-strain curve of metallic materials by spherical indentation. *International Journal of Solids and Structures,* 43**,** 2441-2459

Belyaev, N. M. 1924. Local stresses at compression of elastic solids (1957). *Works on theory of elasticity and plasticity.* Moscow: GITTL (Russian)

Berger, E. J. 2002. Friction modeling for dynamic system simulation. *Appl Mech Rev,* 55**,** 535-577

Berry, M. V., Hannay, J. H. 1978. Topography of random surfaces. *Nature,* 273**,** 573-573

Bertoldi, M., Sglavo, V. M. 2004. Soda-borosilicate glass: normal or anomalous behavior under Vickers indentation? *Journal of Non-Crystalline Solids,* 344**,** 51-59

Bhushan, B. 1995. A fractal theory of the temperature distribution at elastic contacts of fast sliding surfaces - discussion. *Journal of Tribology-Transactions of the Asme,* 117**,** 214-215

Blau, P. J. 2001. The significance and use of the friction coefficient. *Tribology International,* 34**,** 585-591

Bora, C. K., Plesha, M. E., Carpick, R. W. 2013. A Numerical Contact Model Based on Real Surface Topography. *Tribology Letters,* 50**,** 331-347

Borodich, F. M. 1983. Similarity in the problem of contact between elastic bodies. *J. Appl.Math. and Mech. (PMM),* 47**,** 519–521

Borodich, F. M. 1988. Use of the theory of similarity in the nonlinear problem of contact between an indenter and anisotropic metallic foundations. *In:* A. A. Bogatov et al. (ed.) *Abstracts of Reports of All-Union Conference "Metal"-programme's ful llers (September 26-30, 1988).* Abakan: Krasnoyarskii Polytechnical Institute Press**,** 195–196 (Russian)

Borodich, F. M. 1989. Hertz contact problems for an anisotropic physically nonlinear elastic medium. *Problemy Prochnosti,* # 12**,** 47–53.(English transl. in Strength of Materials, 21(12), 1668-1676)

Borodich, F. M. 1992. Self-similarity properties of static and dynamic contact between a punch and anisotropic media. *Abstracts of Reports on 18th Int. Congress of Theoretical and Appl. Mech., Haifa.* 26-27

Borodich, F. M. 1993a. The Hertz frictional contact between nonlinear elastic anisotropic bodies (the similarity approach). *Int. J. Solids Structures,* 30**,** 1513–1526

Borodich, F. M. 1993b. Similarity properties of discrete contact between a fractal punch and an elastic medium. *Comptes Rendus De l'Acad. des Sciences, Paris, Ser. 2,* 316(2)**,** 281-286

Borodich, F. M. 1998a. Parametric homogeneity and non-classical self-similarity. I. Mathematical background. *Acta Mechanica,* 131**,** 27-45

Borodich, F. M. 1998b. Parametric homogeneity and non-classical self-similarity. II. Some applications. *Acta Mechanica,* 131**,** 47-67

Borodich, F. M. 2007. Introduction to Zhuravlev's historical paper: On the question of theoretical justification of the Amontons-Coulomb law for friction of unlubricated surfaces. *Proceedings of the Institution of Mechanical Engineers Part J-Journal of Engineering Tribology,* 221**,** 893-895

Borodich, F. M. 2008. Hertz type contact problems for power-law shaped bodies. *In:* Gladwell, G. L. (ed.) *L.A. Galin, Contact Problems. The legacy of L.A. Galin.* Springer**,** 261-292

Borodich, F. M. 2011. Contact problems at nano/microscale and depth sensing indentation techniques. *Material Science Forum,* 662**,** 53-76

Borodich, F. M. 2013a. Fractal Contact Mechanics. *In:* Wang, Q. J. & Chung, Y.-W. (eds.) *Encyclopedia of Tribology.* Springer, Volume 2, pp. 1249-1258

Borodich, F. M. 2013b. Fractal Nature of Surfaces. *In:* Wang, Q. J. & Chung, Y.-W. (eds.) *Encyclopedia of Tribology.* Springer, Volume 2, pp. 1264-1269

Borodich, F. M. 2013c. Physical and chemical processes affecting performance of super-low friction carbon nitride coatings in various gaseous environments. *World Tribology Congress.* Torino, Italy.

Borodich, F. M. 2014. The Hertz-Type and Adhesive Contact Problems for Depth-Sensing Indentation. *Advances in Applied Mechanics,* 47**,** 225-366

Borodich, F. M., Galanov, B. A., Gorb, S. N., Prostov, Y. I., Suarez-Alvarez, M. M. 2012. An inverse problem for adhesive contact and non-direct evaluation of material properties for nanomechanics applications. *Nanoscale Systems: Mathematical Modeling, Theory and Applications,* 1**,** 80-92

Borodich, F. M., Galanov, B. A., Suarez-Alvarez, M. M. 2014. The JKR-type adhesive contact problems for power-law shaped axisymmetric punches. *Journal of the Mechanics and Physics of Solids,* 68**,** 14-32

Borodich, F. M., Keer, L. M., Korach, C. S. 2003. Analytical study of fundamental nanoindentation test relations for indenters of non-ideal shapes. *Nanotechnology,* 14**,** 803-808

Borodich, F. M., Kryukova, I. V. 1997. Frictional self-oscillations caused by deformation of the irregularities of the contacting surfaces. *Technical Physics Letters,* 23**,** 239-241

Borodich, F. M., Mosolov, A. B. 1991. Fractal contact of solid states. *Zhurnal Tekhnicheskoi Fiziki,* 61**,** 50-54

Borodich, F. M., Mosolov, A. B. 1992. Fractal roughness in contact problems. *Pmm Journal of Applied Mathematics and Mechanics,* 56**,** 681-690

Borodich, F. M., Onishchenko, D. A. 1993. Fractal roughness in contact and friction problems (the simplest models). *Journal of Friction and Wear,* 14**,** 14-19

Borodich, F. M., Onishchenko, D. A. 1999. Similarity and fractality in the modelling of roughness by a multilevel profile with hierarchical structure. *International Journal of Solids and Structures,* 36**,** 2585-2612

Borodich, F. M., Pepelyshev, A., Savencu, O. Micro and nano scale statistical properties of rough surfaces of significance in their friction. Viennano'15, 2015 Wiener Neustadt, Austria.

Bowden, F. P., Leben, L. 1938. Nature of sliding and the analysis of friction. *Nature,* 141**,** 691-692

Bowden, F. P., Leben, L. 1939. The nature of sliding and the analysis of friction. *Proceedings of the Royal Society of London Series a-Mathematical and Physical Sciences,* 169**,** 371-391

Bowden, F. P., Moore, A. J. W., Tabor, D. 1943. The ploughing and adhesion of sliding metals. *Journal of Applied Physics,* 14**,** 80-91

Bowden, F. P., Tabor, D. 1939. The area of contact between stationary and between moving surfaces. *Proceedings of the Royal Society of London Series a-Mathematical and Physical Sciences,* 169**,** 391-413

Bowden, F. P., Tabor, D. 1943. The lubrication by thin metallic films and the action of bearing metals. *Journal of Applied Physics,* 14**,** 141-151

Bowden, F. P., Tabor, D. 1956. *Friction and Lubrication,* London, Methuen.

Bowden, F. P., Tabor, D. 1973. *Friction: An Introduction to Tribology*, R.E. Krieger Publishing Company.

Bradley, R. S. 1932. The cohesive force between solid surfaces and the surface energy of solids. *Philosophical Magazine,* 13**,** 853-862

Brennan, J. K. 2010. *Algorithms for Surface Texture Profiles and Parameters.* Doctor of Philosophy, The University of Huddersfield in collaboration with the National Physical Laboratory.

Brinell, J. A. 1900. Mémoire sur les épreuves a bille en acier. *Communications présentées devant le Congrés international des méthodes d'essai des matériaux de construction, tenu à Paris du 9 au 16 juillet 1900.* Paris: Vve C. Dunod**,** 83**–**94

Brown, S. R., Scholz, C. H. 1985. Closure of random elastic surfaces in contact. *Journal of Geophysical Research-Solid Earth and Planets,* 90**,** 5531-5545

Bull, S. J. 1995. Tribology of carbon coatings: DLC, diamond and beyond. *Diamond and related materials,* 4**,** 827-836

Bull, S. J. 2002. Extracting hardness and Young's modulus from load-displacement curve. *Zeitschrift Fur Metallkunde,* 93**,** 870-874

Bull, S. J. 2003. On the origins and mechanisms of the indentation size effect. *Zeitschrift für Metallkunde,* 94**,** 787-792

Bulychev, S. I., Alekhin, V. P., Shorshorov, M. K., Ternovskii, A. P. 1976. Mechanical properties of materials studied from kinetic diagrams of load versus depth of impression during microimpression. *Strength of Materials,* 8**,** 1084-1089.(Russian)

Bulychev, S. I., Alekhin, V. P., Shorshorov, M. K., Ternovskii, A. P., Shnyrev, G. D. 1975. Determination of Young's modulus according to indentation diagram. *Industrial Laboratory,* 41**,** 1409–1412.(Russian)

Burridge, R., Knopoff, L. 1967. Model and theoretical seismicity. *Bulletin of the Seismological Society of America,* 57**,** 341-&

Bush, A. W., Gibson, R. D., Thomas, T. R. 1975. The elastic contact of a rough surface. *Wear,* 35**,** 87-111

Butt, H.-J., Kappl, M. 2010. *Surface and Interfacial Forces,* Weinheim, Germany, Wiley-VCH Verlag GmbH & Co. KGaA.

Carbone, G., Bottiglione, F. 2008. Asperity contact theories: Do they predict linearity between contact area and load? *Journal of the Mechanics and Physics of Solids,* 56**,** 2555-2572

Carrasco, J., Klimes, J., Michaelides, A. 2013. The role of van der Waals forces in water adsorption on metals. *Journal of Chemical Physics,* 138**,** 9

Chen, J., Bull, S. J. 2009. Modeling of Indentation Damage in Single and Multilayer Coatings. *Iutam Symposium on Modelling Nanomaterials and Nanosystems,* 13**,** 161-170

Chokshi, A. H., Rosen, A., Karch, J., Gleiter, H. 1989. On the validity of the Hall-Petch relationship in nanocrystalline materials. *Scripta Metallurgica,* 23**,** 1679-1683

Chung, Y.-W. 2007. *Introduction to materials science and engineering*, Boca Raton, FL : CRC/Taylor & Francis.

Cocks, M. 1962. Interaction of sliding metal surfaces. *Journal of Applied Physics,* 33**,** 2152-&

Dao, M., Chollacoop, N., Van Vliet, K. J., Venkatesh, T. A., Suresh, S. 2001. Computational modeling of the forward and reverse problems in instrumented sharp indentation. *Acta Materialia,* 49**,** 3899-3918

Darwent, B. D. 1970. *Bond dissociation energies in simple molecules,* [Washington], U.S. National Bureau of Standards; for sale by the Supt. of Docs., U.S. Govt. Print. Off.

De Moerlooze, K., Al-Bender, F., Van Brussel, H. 2011. A novel energy-based generic wear model at the asperity level. *Wear,* 270**,** 760-770

Derjaguin, B. 1934a. Molecular theory of outer friction. *Zeitschrift Fur Physik,* 88**,** 661-675

Derjaguin, B. 1934b. Untersuchungen über die Reibung und Adhäsion, IV. Theorie des Anhaftens kleiner Teilchen. *Kolloid Zeitschrift,* 69**,** 155–164

Derjaguin, B. 1963. *Chto takoe trenie?,* Moscow, USSR Academy of Sciences Publisher.

Derjaguin, B. V., Muller, V. M., Toporov, Y. P. 1975. Effect of contact deformations on adhesion particles. *Journal of Colloid and Interface Science,* 53**,** 314-326

Dinnik, A. N. 1952. Impact and compression of elastic bodies. *Collected works.* Kiev: Izd. Acad. Nauk Ukr. SSR (Russian)

Dowson, D. 1979. *History of Tribology,* New York, Longman.

Dowson, D. 1998. *History of tribology,* London, Professional Engineering Publishers.

Dugdale, D. S. 1960. Yielding of steel sheets containing slits. *Journal of the Mechanics and Physics of Solids,* 8**,** 100-104

Dyson, J., Hirst, W. 1954. The true contact area between solids. *Proceedings of the Physical Society of London Section B,* 67**,** 309-312

Eichenlaub, S., Chan, C., Beaudoin, S. P. 2002. Hamaker constants in integrated circuit metalization. *Journal of Colloid and Interface Science,* 248**,** 389-397

Ferguson, G. S., Chaudhury, M. K., Sigal, G. B., Whitesides, G. M. 1991. Contact adhesion of thin gold-films on elastomeric supports - cold welding under ambient conditions. *Science,* 253**,** 776-778

Filippov, A. E., Popov, V. L. 2007. Fractal Tomlinson model for mesoscopic friction: From microscopic velocity-dependent damping to macroscopic Coulomb friction. *Physical Review E,* 75**,** 4

Fischer-Cripps, A. C. 2011. *Nanoindentation,* New York, Springer.

Gadelrab, K. R., Bonilla, F. A., Chiesa, M. 2012a. Densification modeling of fused silica under nanoindentation. *Journal of Non-Crystalline Solids,* 358**,** 392-398

Gadelrab, K. R., Chiesa, M., Bonilla, F. A. 2012b. Implications of the idea of effective tip shape on nanoindentation unloading curves: AFM measurements and FE simulation. *Journal of Materials Research,* 27**,** 126-131

Galanov, B. A. 1981a. Approximate solution of some contact problems with an unknown contact area under conditions of power law of material hardening. *Dopovidy Akademii Nauk Ukrainskoi RSR,* Series A(6)**,** 35–40

Galanov, B. A. 1981b. Approximate solution to some problems of elastic contact of two bodies. *Mechanics of solids,* 16**,** 61-67

Galanov, B. A. 1993. Development of analytical and numerical methods for study of models of materials. Report for the project 7.06.00/001-92, 7.06.00/015-92. Kiev, Institute for Problems in Material Science. (Ukrainian)

Galanov, B. A., Grigorev, O. N., Milman, Y. V., Ragozin, I. P. 1983. Determination of the hardness and Young's modulus from the depth of penetration of a pyramidal indenter. *Strength of Materials,* 15**,** 1624-1628

Galanov, B. A., Grigorev, O. N., Milman, Y. V., Ragozin, I. P., Trefilov, V. I. 1984. Determination of the hardness and Young's modulus with elastoplastic penetration of indentors into materials. *Dokl. Akad. Nauk SSSR,* 274**,** 815-817

Galin, L. A. 1946. Spatial contact problems of the theory of elasticity for punches of circular shape in planar projection. *PMM J. Appl. Math. Mech.,* 10**,** 425-448

Galin, L. A. 1961. *Contact problems in the theory of elasticity*, Department of Mathematics, School of Physical Sciences and Applied Mathematics, North Carolina State College, 1961.

Galin, L. A. 2008. *Contact problems: The legacy of L.A. Galin*, Springer.

Goldsmith, W., Lyman, P. T. 1960. The Penetration of Hard-Steel Spheres Into Plane Metal Surfaces. *Journal of Applied Mechanics,* 27**,** 717-725

Goryacheva, I. G. 1998. *Contact Mechanics in Tribology*, Springer Netherlands.

Greenwood, J. A., Tripp, J. H. 1967. Elastic contact of rough spheres. *Journal of Applied Mechanics,* 34**,** 153-&

Greenwood, J. A., Williamson, J. B. 1966. Contact of nominally flat surfaces. *Proceedings of the Royal Society of London Series a-Mathematical and Physical Sciences,* 295**,** 300-

Greer, J. R., De Hosson, J. T. M. 2011. Plasticity in small-sized metallic systems: Intrinsic versus extrinsic size effect. *Progress in Materials Science,* 56**,** 654-724

Greer, J. R., Oliver, W. C., Nix, W. D. 2005. Size dependence of mechanical properties of gold at the micron scale in the absence of strain gradients. *Acta Materialia,* 53**,** 1821-1830

Haessig, D. A., Friedland, B. 1991. On the modeling and simulation of friction. *Journal of Dynamic Systems Measurement and Control-Transactions of the Asme,* 113**,** 354-362

Hainsworth, S. V., Chandler, H. W., Page, T. F. 1996. Analysis of nanoindentation load-displacement loading curves. *Journal of Materials Research,* 11**,** 1987-1995

Hamaker, H. C. 1937. The london—Van der waals attraction between spherical particles. *Physica,* 4**,** 1058–1072

Hardy, W., Bircumshaw, I. 1925. Boundary Lubrication - Plane Surfaces and the Limitations of Amontons Law. *Proceedings of the Royal Society a-Mathematical Physical and Engineering Sciences,* 108

Harsono, E., Swaddiwudhipong, S., Liu, Z. S., Shen, L. 2011. Numerical and experimental indentation tests considering size effects. *International Journal of Solids and Structures,* 48**,** 972-978

Hemker, K. J., Nix, W. D. 2008. Nanoscale deformation - Seeing is believing. *Nature Materials,* 7**,** 97-98

Herrmann, K. 2011. *Hardness testing : principles and applications*, Materials Park, Ohio : ASM International.

Hertz, H. 1882a. Ueber die Beruehrung elastischer Koerper (On Contact Between Elastic Bodies). *Gesammelte Werke (Collected Works),* 1

Hertz, H. 1882b. Ueber die Berührung fester elastischer Körper und über die Härte. *Verhandlungen des Vereins zur Beförderung des Gewerbefleißes*.(English translation. Hertz, H. (1896). On the contact of elastic solids and on hardness. In H. Hertz, D. E. Jones, & G. A. Schott (Eds.), Miscellaneous papers. London: Macmillan, pp. 163–183)

Holmberg, K., Matthews, A. 2009. *Coatings Tribology: Properties, Mechanisms, Techniques and Applications in Surface Engineering*, Elsevier Science.

Israelachvili, J. N. 1992. *Intermolecular and surface forces,* New York, USA, Academic Press.

Jayaraman, S., Hahn, G. T., Oliver, W. C., Bastias, P. C. 1998. Determination of monotonic stress-strain curve of hard materials from ultra-low-load indentation tests. *International Journal of Solids and Structures,* 35**,** 365-381

Johnson, K. L. 1958. A note on the adhesion of elastic solids. *British Journal of Applied Physics,* 9**,** 199-200

Johnson, K. L. 1985. *Contact Mechanics,* Cambridge, Cambridge University Press.

Johnson, K. L. 1996. Continuum mechanics modeling of adhesion and friction. *Langmuir,* 12**,** 4510-4513

Johnson, K. L., Kendall, K., Roberts, A. D. 1971. Surface energy and contact of elastic solids. *Proceedings of the Royal Society of London Series a-Mathematical and Physical Sciences,* 324**,** 301-&

Johnson, M. R. 1994. The Galileo high gain antenna deployment anomaly. *NASA. Lewis Research Center, The 28th Aerospace Mechanisms Symposium.*

Kalei, G. N. 1968. Some results of microhardness test using the depth of impression. *Mashinovedenie,* 4**,** 105–107.(Russian)

Kallman, J. S., Hoover, W. G., Hoover, C. G., Degroot, A. J., Lee, S. M., Wooten, F. 1993. Molecular dynamics of silicon indentation. *Physical Review B,* 47**,** 7705-7709

Kelly, S. A., Torres-Verdin, C., Balhoff, M. T. 2015. Anomalous liquid imbibition at the nanoscale: the critical role of interfacial deformations. *Nanoscale,*

Kendall, K. 2001. *Molecular Adhesion and Its Applications - The Sticky Universe,* New York, Kluwer Academic/Plenum Publishers.

Kermouche, G., Barthel, E., Vandembroucq, D., Dubujet, P. 2008. Mechanical modelling of indentation-induced densification in amorphous silica. *Acta Materialia,* 56**,** 3222-3228

Khrushchov, M. M., Berkovich, E. S. 1950. *Devices PMT-2 and PMT-3 for microhardness testing,* Moscow-Leningrad, USSR Academy of Sciences Publisher.

Klein, C. A., Cardinale, G. F. Young's modulus and Poisson's ratio of CVD diamond. 1992. 178-193.

Knoop, F., Peters, C. G., Emerson, W. B. 1939. A sensitive pyramidal-diamond tool for indentation measurements. *National Bureau of Standards,* 23

Koslowski, M., Lee, D. W., Lei, L. 2011. Role of grain boundary energetics on the maximum strength of nanocrystalline Nickel. *Journal of the Mechanics and Physics of Solids,* 59**,** 1427-1436

Kotelnikov, S. K. 1774. *A Book Containing the Doctrine on the Equilibrium and Movement of Bodies,* Saint-Petersburg, Naval Noble Cadet Corps.

Kragelsky, I. V. 1948. Static friction between two rough surfaces. *Bulettin of the Academy of Sciences of the USSR, Technical Sciences Division,* 10**,** 1621-1625

Kragelsky, I. V., Dobychin, M. N., Kombalov, V. S. 1982. *Friction and wear : calculation methods*, Pergamon.

Kragelsky, I. V., Schedrov, V. S. 1956. *Development of the science about friction,* Moscow, USSR Academy of Sciences Press.

Krantz, T. L., Alanou, M. P., Evans, H. P., Snidle, R. W. 2001. Surface Fatigue Lives of Case-Carburized Gears With an Improved Surface Finish. *Journal of Tribology,* 123

Krier, J., Breuils, J., Jacomine, L., Pelletier, H. 2012. Introduction of the real tip defect of Berkovich indenter to reproduce with FEM nanoindentation test at shallow penetration depth. *Journal of Materials Research,* 27**,** 28-38

Kudinov, V. A. 1980. *Vibration in machine-tools. Vibration in Engineering,* Moscow, Mashinostroenie.

Kuhlmann-Wilsdorf, D. 1981. *Dislocation concepts in friction and wear*, ASM International.

Kuhlmann-Wilsdorf, D. 1991. Uses of theory in the design of sliding electrical contacts. *Electrical Contacts - 1991 : Proceedings of the Thirty-Seventh Ieee Holm Conference on Electrical Contracts***,** 1-24

Kuhlmann-Wilsdorf, D. 1996a. Electrical fiber brushes - Theory and observations. *Ieee Transactions on Components Packaging and Manufacturing Technology Part A,* 19**,** 360-375

Kuhlmann-Wilsdorf, D. 1996b. What role for contact spots and dislocations in friction and wear? *Wear,* 200**,** 8-29

Lea, F. C. 1936. *Hardness of Metals,* London, Charles Griffin & Co.

Leite, F. L., Bueno, C. C., Da Roz, A. L., Ziemath, E. C., Oliveira, O. N. 2012. Theoretical Models for Surface Forces and Adhesion and Their Measurement Using Atomic Force Microscopy. *International Journal of Molecular Sciences,* 13**,** 12773-12856

Lessel, M., Loskill, P., Hausen, F., Gosvami, N. N., Bennewitz, R., Jacobs, K. 2013. Impact of van der Waals Interactions on Single Asperity Friction. *Physical Review Letters,* 111**,** 5

Lichinchi, M., Lenardi, C., Haupt, J., Vitali, R. 1998. Simulation of Berkovich nanoindentation experiments on thin films using finite element method. *Thin Solid Films,* 312**,** 240-248

Liu, S. H., Kaplan, T., Gray, L. J. 1986. Theory of the AC Response of Rough Interfaces. *In:* Pietronero, L. & Tosatti, E. (eds.) *Fractals in Physics.* North Holland, Amsterdam**,** 383—392

Longuet-Higgins, M. S. 1957. The statistical analysis of a random, moving surface. *Philosophical transactions of the royal society of London series A - methematical and physical sciences,* 249**,** 321–387

Love, A. E. H. 1939. Boussinesq's problem for a rigid cone. *The Quarterly Journal of Mathematics,* 10**,** 161-175

Lu, P., Loke, Y. C., Tang, X., Kushvaha, S. S., O'shea, S. J. 2011. A Note on the Two-Spring Tomlinson Model. *Tribology Letters,* 43**,** 73-76

Lu, Y., Huang, J. Y., Wang, C., Sun, S. H., Lou, J. 2010. Cold welding of ultrathin gold nanowires. *Nature Nanotechnology,* 5**,** 218-224

Ludwik, P. 1908. *Die Kegelprobe,* Berlin, J. Springer.

Maboudian, R., Ashurst, W. R., Carraro, C. 2002. Tribological challenges in micromechanical systems. *Tribology Letters,* 12**,** 95-100

Majumdar, A., Bhushan, B. 1990. Role of fractal geometry in roughness characterization and contact mechanics of surfaces. *Journal of Tribology-Transactions of the Asme,* 112**,** 205-216

Mandelbrot, B. 1977. *Fractals,* San Francisco, Freeman.

Mata, M., Alcala, J. 2004. The role of friction on sharp indentation. *Journal of the Mechanics and Physics of Solids,* 52**,** 145-165

Matope, S., Van Der Merwe, A. F., Rabinovich, Y. I. 2013. Silver, copper and aluminium coatings for micro-material handling operations. *South African Journal of Industrial Engineering,* 24**,** 69-77

Maugis, D. 1992. Adhesion of spheres - the JKR-DMT transition using a Dugdale model. *Journal of Colloid and Interface Science,* 150**,** 243-269

Maugis, D. 2000. *Contact, Adhesion and Rupture of Elastic Solids,* Berlin, Springer-Verlag Berlin Heidelberg.

Merstallinger, A. 2009. *Assessment of cold welding between separable contact surfaces due to impact and fretting under vacuum*, ESA Communication.

Meyer, E. 1908. Untersuchungen über Härteprüfung und Härte. *Physikalische Zeitschrift,* 9**,** 66–74

Meyers, M. A., Mishra, A., Benson, D. J. 2006. Mechanical properties of nanocrystalline materials. *Progress in Materials Science,* 51**,** 427-556

Moore, A. J. W. 1948. Deformation of Metals in Static and in Sliding Contact. *Proceedings of the Royal Society of London A: Mathematical, Physical and Engineering Sciences,* 195**,** 231-244

Mordehai, D., Rabkin, E., Srolovitz, D. J. 2011. Pseudoelastic Deformation during Nanoscale Adhesive Contact Formation. *Physical Review Letters,* 107**,** 096101

Moreau, P., Raulic, M., P'ng, K. M. Y., Gannaway, G., Anderson, P., Gillin, W. P., Bushby, A. J., Dunstan, D. J. 2005. Measurement of the size effect in the yield strength of nickel foils. *Philosophical Magazine Letters,* 85**,** 339-343

Mott, B. A. 1956. *Micro-indentation hardness testing,* London, Butterworths.

Muller, V. M., Yushchenko, V. S., Derjaguin, B. V. 1980. On the influence of molecular forces on the deformation of an elastic sphere and its sticking to a rigid plane. *Journal of Colloid and Interface Science,* 77**,** 91-101

Nayak, P. R. 1971. Random process model of rough surfaces. *Journal of Lubrication Technology,* 93**,** 398-&

O'neill, H. 1934. *Hardness measurement of metals and alloys,* London, Chapman and Hall.

Paar, A. 2006. Nanoindentation With Spherical Indenters For Characterisation Of Stress-Strain Properties – From CSM Instruments. www.azonano.com.

Parsegian, V. A. 2005. *Van der Waals Forces: A Handbook for Biologists, Chemists, Engineers, and Physicists*, Cambridge University Press.

Pepelyshev, A. 2015.

Perriot, A., Vandembroucq, D., Barthel, E., Martinez, V., Grosvalet, L., Martinet, C., Champagnon, B. 2006. Raman microspectroscopic characterization of amorphous silica plastic behavior. *Journal of the American Ceramic Society,* 89**,** 596-601

Pharr, G. M., Bolshakov, A. 2002. Understanding nanoindentation unloading curves. *Journal of Materials Research,* 17**,** 2660-2671

Pharr, G. M., Oliver, W. C., Brotzen, F. R. 1992. On the generality of the relationship among contact stiffness, contact area, and elastic-modulus during indentation. *Journal of Materials Research,* 7**,** 613-617

Plesha, M. E., Ni, D. 2001. Scaling of geological discontinuity normal load-deformation response using fractal geometry. *International Journal for Numerical and Analytical Methods in Geomechanics,* 25**,** 741-756

Pollock, H. M. 1992. Surface forces and adhesion. *Fundamentals of Friction : Macroscopic and Microscopic Processes,* 220**,** 77-94

Polonsky, I. A., Keer, L. M. 1996a. Scale effects of elastic-plastic behavior of microscopic asperity contacts. *Journal of Tribology-Transactions of the Asme,* 118**,** 335-340

Polonsky, I. A., Keer, L. M. 1996b. Simulation of microscopic elastic-plastic contacts by using discrete dislocations. *Proceedings of the Royal Society a-Mathematical Physical and Engineering Sciences,* 452**,** 2173-2194

Popov, V. L. 2010. *Contact Mechanics and Friction*, Springer-Verlag Berlin Heidelberg.

Prandtl, L. 1928. Mind model of the kinetic theory of solid bodies. *Zeitschrift Fur Angewandte Mathematik Und Mechanik,* 8**,** 85-106.(Translated from German original by Popov, V. L., Gray, J. 2012. Prandtl-Tomlinson model: History and

applications in friction, plasticity, and nanotechnologies. *Z. Angew. Math. Mech.* **92**, 9, 683-708)

Qiu, X., Huang, Y., Wei, Y., Gao, H., Hwang, K. C. 2003. The flow theory of mechanism-based strain gradient plasticity. *Mechanics of Materials,* 35**,** 245-258

Rabinowicz, E. 1951. The nature of the static and kinetic coefficients of friction. *Journal of Applied Physics,* 22**,** 1373-1379

Rabinowicz, E., Tabor, D. 1951. Metallic Transfer between Sliding Metals: An Autoradiographic Study. *Proceedings of the Royal Society of London A: Mathematical, Physical and Engineering Sciences,* 208**,** 455-475

Rockwell, S. P. 1922. Testing metals for hardness. *Transactions of the American Society for Steel Treating,* 2**,** 1013–1033

Roques-Carmes, C., Wehbi, D., Quiniou, J. F., Tricot, C. 1988. Modelling engineering surfaces and evaluating their non-integer dimension for application in material science. *Surface Topography,* 1**,** 435-443

Sayles, R. S., Thomas, T. R. 1978. Surface topography as a nonstationary random process. *Nature,* 271**,** 431-434

Schmittbuhl, J., Vilotte, J. P., Roux, S. 1996. Velocity weakening friction: A renormalization approach. *Journal of Geophysical Research-Solid Earth,* 101**,** 13911-13917

Sergienko, P. V., Bukharov, N. S. 2015. *Noise and Vibration in Friction Systems*, Springer International Publishing.

Shan, Z. W., Adesso, G., Cabot, A., Sherburne, M. P., Asif, S. a. S., Warren, O. L., Chrzan, D. C., Minor, A. M., Alivisatos, A. P. 2008. Ultrahigh stress and strain in hierarchically structured hollow nanoparticles. *Nature Materials,* 7**,** 947-952

Shi, Z., Feng, X., Huang, Y., Xiao, J., Hwang, K. C. 2010. The equivalent axisymmetric model for Berkovich indenters in power-law hardening materials. *International Journal of Plasticity,* 26**,** 141-148

Shorshorov, M. K., Bulychev, S. I., Alekhin, V. P. 1981. Work of plastic and elastic deformation during indenter indentation. *Soviet Physics—Doklady,* 26**,** 769–771.(Russian)

Smith, R. L., Sandland, G. E. 1922. An accurate method of determining the hardness of metals, with particular reference to those of a high degree of hardness. *Proceedings of the Institution of Mechanical Engineers,* 1**,** 623–641

Smith, W. F. 2011. *Foundations of materials science and engineering*, Singapore ; London : McGraw-Hill.

Sneddon, I. N. 1948. Boussinesq's problem for a rigid cone. *Mathematical Proceedings of Cambridge Philosophical Society,* 44**,** 492-507

Spear, K. E., Dismukes, J. P. 1994. *Synthetic diamond: emerging CVD science and technology,* New York, Wiley.

Sperling, G. 1964. *Eine Theorie der Haftung von Feststoffteilchen an festen Körpern.* Doktor-Ingenieurs, Technischen Hochschule Karlsruhe.

Stilwell, N. A., Tabor, D. 1961. Elastic recovery of conical indentations. *Proceedings of the Physical Society of London,* 78**,** 169-&

Tabor, D. 1948. A simple theory of static and dynamic hardness. *Proceedings of the Royal Society of London Series a-Mathematical and Physical Sciences,* 192**,** 247-274

Tabor, D. 1951. *The Hardness of Metals,* Oxford, Oxford University Press.

Tabor, D. 1977. Surface forces and surface interactions. *Journal of Colloid and Interface Science,* 58**,** 2-13

Taljat, B., Zacharia, T., Kosel, F. 1998. New analytical procedure to determine stress-strain curve from spherical indentation data. *International Journal of Solids and Structures,* 35**,** 4411-4426

Taylor, C. R., Malshe, A. P., Salamo, G., Prince, R. N., Riester, L., Cho, S. O. 2005. Characterization of ultra-low-load (mu N) nanoindents in GaAs(100) using a cube corner tip. *Smart Materials & Structures,* 14**,** 963-970

Timoshenko, S. P., Goodier, J. N. 1951. *Theory of Elasticity*, McGraw-Hill.

Tolstoi, D. M. 1967. Significance of normal degree of freedom and natural normal vibrations in contact friction. *Wear,* 10**,** 199-&

Tomlinson, G. A. 1929. A molecular theory of friction. *Philosophical Magazine,* 7**,** 905-939

Uchic, M. D., Dimiduk, D. M., Florando, J. N., Nix, W. D. 2004. Sample dimensions influence strength and crystal plasticity. *Science,* 305**,** 986-989

Volkert, C. A., Roos, B., Kapelle, B., Kelling, A., Epler, E., Richter, G. 2012. Revealing Deformation Mechanisms In Nanoscale Metals. *Microscopy and Microanalysis,* 18**,** 762-763

Warren, T. L., Krajcinovic, D. 1995. Fractal models of elastic perfectly plastic contact of rough surfaces based on the cantor set. *International Journal of Solids and Structures,* 32**,** 2907-2922

Weeks, I. 2015. *An Experimental Investigation into the Mixed Lubrication of Steel Surfaces.* Doctor of Philosophy, Cardiff University.

Weertman, J. R. 1993. Hall-Petch strengthening in nanocrystalline metals. *Materials Science and Engineering a-Structural Materials Properties Microstructure and Processing,* 166**,** 161-167

Wells, A. F. 1984. *Structural inorganic chemistry*, Oxford : Clarendon Press.

Whitehouse, D. J. 1982. The parameter rash - Is there a cure. *Wear,* 83**,** 75-78

Whitehouse, D. J., Archard, J. F. 1970. The Properties of Random Surfaces of Significance in their Contact. *Proceedings of the Royal Society of London A: Mathematical, Physical and Engineering Sciences,* 316**,** 97-121

Williams, S. R. 1942. *Hardness and hardness measurements,* Cleveland, American Society for Metals.

Zhu, T., Li, J. 2010. Ultra-strength materials. *Progress in Materials Science,* 55**,** 710-757

Zhuravlev, V. A. 1940. On question of theoretical justification of the Amontons–Coulomb law for friction of unlubricated surfaces. *Zh. Tekh. Fiz (Journal of Technical Physics),* 10**,** 1447-1452.(Translated in English by Borodich, F.M. 2007. Introduction to V A Zhuravlev's historical paper: 'On the question of theoretical justification of the Amontons-Coulomb law for friction of unlubricated surfaces'. *Proceedings of the Institution of Mechanical Engineers Part J - Journal of Engineering Tribology,* 221, 893-895)